UNIVERSITEIT GENT

FACULTEIT WETENSCHAPPEN

Nuclear Pasta with a touch of Quantum

Towards fully antisymmetrised dynamics for bulk fermion systems

---

Klaas Vantournhout

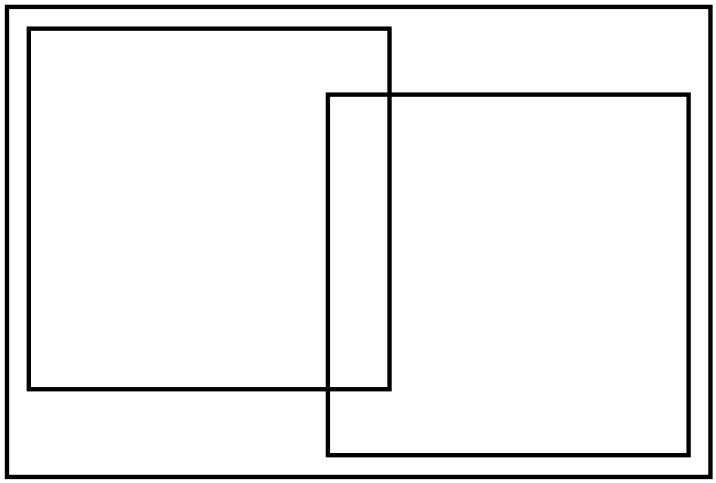

Faculty of Sciences

Proefschrift ingediend tot het behalen van de academische graad van
Doctor in de Wetenschappen: Fysica
Academiejaar 2009-2010

Promotor: Prof. Dr. Jan Ryckebusch
Promotor: Prof. Dr. Natalie Jachowicz

This page intentionally left blank

voor mijn ouders

Philosophy is written in this grand book – I mean the universe – which stands continually open to our gaze, but it cannot be understood unless one first learns to comprehend the language and interpret the characters in which it is written. It is written in the language of mathematics, and its characters are triangles, circles, and other geometrical figures, without which it is humanly impossible to understand a single word of it; without these, one is wandering around in a dark labyrinth.

Galileo Galilei,
Il Saggiatore (The Assayer, 1623)

This page intentionally left blank

DANKWOORD

Mijn proefschrift, 160 bladzijden! Een pad doorheen de werelden van fysica, wiskunde en sterrenkunde; geplaveid met continue, binaire en kwantummechanische tegels. Een zes jaar durende queeste naar vergelijkingen. Bloed, zweet en tranen heeft het gekost. Lezen, schrijven, herschrijven, beschrijven, verschrijven, verwijderen, vergissen, verfrommelen, ontfrommelen, ontrafelen, ontwarren, verwarren, vertalen, hertalen en ook een beetje euforie . . . de eerste print.

Een eindwerk schrijf je niet alleen. Velen hebben bijgedragen aan dit proces. Veel dank ben ik verschuldigd aan mijn beide promotoren, professoren Jan Ryckebusch en Natalie Jachowicz. De wetenschappelijke vrijheid die ik kreeg, jullie steun, vertrouwen en inzicht waren voor deze scriptie heel belangrijk.

I especially would like to express my gratitude to Professor Hans Feldmeier and Doctor Thomas Neff. Your continuous support and interest for this work is greatly appreciated. During the handful of conferences where we met, as well as ones in GSI, you always found the time to discuss my work with a remarkable enthusiasm and deeper knowledge behind the physics of FMD. This often shed a new light on this dissertation and brought its development one step further.

Het is mij ook een eer om professor Kris Heyde te vermelden in dit woord van dank. Uw interesse, steun en onwaarschijnlijk geheugen hebben mij vaak geholpen. Het was een genoegen om ontelbare keren uw bureau plat te lopen, wetende dat daar het antwoord verscholen zat.

Aan de vele collega's en ex-collega's, na zes jaar te veel om op te noemen, een welgemeende dank! Van de oud gedienden wens ik in het bijzonder Stijn en Veerle (meneer en madam), Peter (pière) en Kris (jezus) in de verf te zetten voor de vele wereldveranderende en -verbeterende theoriën die we ontwikkelden tussen pot en pint. Hierbij

staat *een dagje uit in West-Vlaanderen (Vleteren)* centraal met *paters, garres* en ander goddelijk nat. Mijn (ex)bureaugenoten, Wim en Christophe mag ik zeker niet vergeten. Het was een waar genoegen met jullie samen te zuchten, zwoegen en zweten maar ook te genieten, van de winterspelen. Wim, je muziekkeuze is ... Christophe, jammer dat je onze tempel der wetenschappen hebt moeten verlaten, was het door Wim zijn muziekkeuze, of die van mij? In elk geval, met jullie altijd amuzeleute. Ten slotte wens ik ook nog Arne (wombat) te danken. Je bent iemand die ik enorm waardeer. Ernst en leute, altijd tegen de verzuring!

The interest in astronomy and science has always been kept alive thanks to the many friends of the *International Astronomical Youth Camp*. You have given me so much and have supported me in this everlasting quest. I am grateful for that. To Sebastian Bürgel I would like to say the following. You see, I actually finished!

Mijn studies zouden er nooit geweest zijn zonder de inzet en gedrevenheid van Dhr. Baesens. Gerard, het is dankzij u dat ik de grote stap van het technisch onderwijs naar het universitaire heb kunnen maken. Dankzij uw enthousiasme voor wiskunde, uw passie voor het analytische, ontdekte ik de schoonheid van een formule wat zich duidelijk vertaalt in dit werk.

Een bijzonder woord van dank gaat uit naar mijn ouders. Niet enkel hebben jullie met mij moeten samenleven in de soms woelige tijden, maar desondanks alles bleven jullie me steunen. Jullie bijdrage tot deze verhandeling is van onschatbare waarde. Zonder jullie was dit doctoraat nooit af! Zonder jullie was ik nooit wat ik ben.

Puzzles, complex problems and other brainteasers have always attracted me. Monika, you are my true Gordian knot. Not one to be cut, but to cherish and that not only because you helped correcting this work.

Een tevreden promovendus dankt U,

Klaas Vantournhout
27 november 2009

CONTENTS

This page intentionally left blank

1 INTRODUCTION

Preface

Mighty oaks from little acorns grow. This proverb reflects the evolution of the vast and ever-changing panoply presented to us while gazing at the heavens. It represents a cycle of life embracing our own. Massive gas clouds understood as a mere collection of dust and the tiniest of particles are the incubators of stars sprouting towards an active and varied life for millions of years. 'Several billion trillion tons of superhot exploding hydrogen nuclei synthesise into ever-heavier elements, while often rising slowly above a horizon, managing to look small, cold and slightly damp' [Ada82]. Then they collapse and die. In an act of despair, as a last struggle against gravity, they go supernova, one of the most glorious events in the universe. In an unrivalled explosion, they light up in the skies for days and nights on end while seeding ashes into the vast emptiness around, waiting to be used again in a new life cycle of a stellar system. Cocooned within those ashes lies a new type of star dormant. A neutron star, born the moment another star died. One star's breath is another star's death! (Fig. 1.1)

Neutron stars

Neutron stars demonstrate how matter behaves under extreme conditions. Containing roughly 1.5 solar masses of matter within a radius of about 12 km, they reach densities as high as five, ten or even twenty times the nuclear saturation density ρ_0 corresponding to 0.16 nucleons per fermi cubed. Without any doubt, they constitute one of the densest forms of matter in the observable universe. Their discovery started rather unusual. Before their actual theoretical prediction in 1934 by Baade and Zwicky [Baa34a, Baa34b], Landau anticipated the existence of neutron stars in 1931. That was before Chadwick announced in 1932 his discovery of the neutron [Lan32, Cha32, Hae07], the dominant nucleonic component of neutron stars.

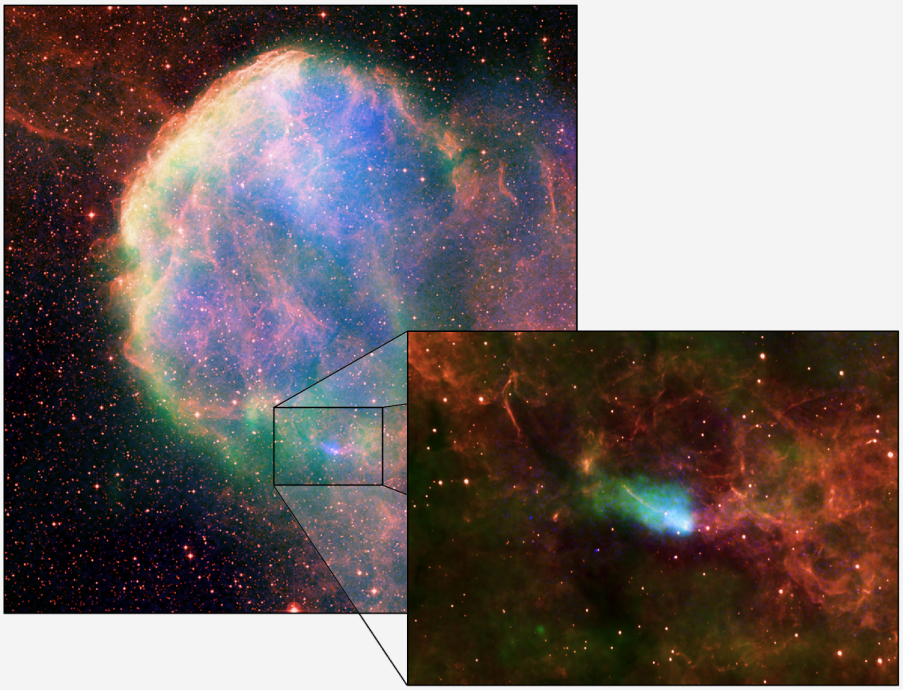

Figure 1.1: This wide-field composite image was made with X-ray (blue/ROSAT & Chandra), radio (green/Very Large Array), and optical (red/Digitized Sky Survey) observations of the supernova remnant IC 443, i.e. the Jellyfish nebula. The pullout, also a composite with a Chandra X-ray close-up, shows a neutron star that is spewing out a comet-like wake of high-energy particles as it races through space. Based on an analysis of the swept-back shape of the wake, astronomers deduced that the neutron star known as CXOU J061705.3 222127, is moving through the multimillion degree Celsius gas in the remnant. (Chandra X-ray: NASA/CXC/B. Gaensler et al.; ROSAT X-ray: NASA/ROSAT/Asaoka & Aschenbach Radio Wide: NRC/DRAO/D. Leahy; Radio Detail: NRAO/VLA Optical: DSS) [Gae06]

Theoretical progress on neutron stars was slow until the first neutron star surveys appeared. Only in 1967, Jocelyn Bell, a graduate student supervised by A. Hewish, discovered the first pulsar PSR B1919+21 [Hew68]. This breaking discovery lead to a somewhat controversial Nobel Prize for Hewish in 1974. The terms “pulsar” and “neutron star” are not to be used equivalently. The name “pulsar” is reserved for an astrophysical object that emits pulsed radiation. A “neutron star”, on the other hand,

refers to the theoretical object and is independent of any observed astrophysical object like a pulsar or a very compact star that is not observed by its pulsed radiation but by other means. Nonetheless, there are good reasons to believe that pulsars represent fast rotating magnetised neutron stars [Gle00], as first suggested by Pacini and Gold [Pac67, Gol68].

As neutron stars are one of the densest manifestations of massive objects in the universe, they represent a stringent test for various theories. Phenomena as hyperon-dominated matter, deconfined quark matter, superfluidity and superconductivity with critical temperatures near 10^{10}K, opaqueness to neutrinos and magnetic fields in excess of 10^{13} Gauss, are a few of the goodies hidden in their layers. According to current theories, a neutron star's layers can be divided into five major regions: the inner and outer cores, the crust, the envelope and the atmosphere as shown in Fig. 1.2 [Lat04, Hae07]. The core of the neutron star, constituting 99 percent of the mass of the star, is the ideal background for a plethora of interesting and exciting physics phenomena. The outer core, with densities ranging from half to double the nuclear saturation density ρ_0, is several kilometres thick and is a mixture of neutrons, protons, electrons and muons behaving as a strongly interacting non-relativistic Fermi-liquid. While the neutrons and protons appear in superfluid states, the superfluidity of the protons is accompanied by superconductivity [Rud91, Yak99]. The composition of the inner core, with densities up to $10\rho_0$, is hardly known. Various hypotheses exist, ranging from hyperonisation [Hae07] over pion [Mig90, Tak93] and kaon condensation [Ram01] to deconfined quark matter [Gle92].

Discussing the physics of a neutron star is interesting to say the least, however beyond the scope of the present work. Various books and review papers deal with the topic. The historical work of Shapiro and Teukolsky [Sha04], reflecting the state of the art by the beginning of the 1980s, as well as the monograph of Glendenning [Gle00] that describes a neutron star through relativistic theories of hadron matter, are excellent starters. A detailed description of the variety of possible models in stellar cores and crusts is given in the work of Haensel, Potekhin and Yakovlev [Hae07]. Other excellent reviews are found in Refs. [Bay79, Pra97, Hei00, Yak01, Yak04, Lat04].

This dissertation aims at introducing a technique for simulating matter in the crust of neutron stars. The next sections will give a short review about the physics of the neutron star crust and its importance in various astrophysical phenomena.

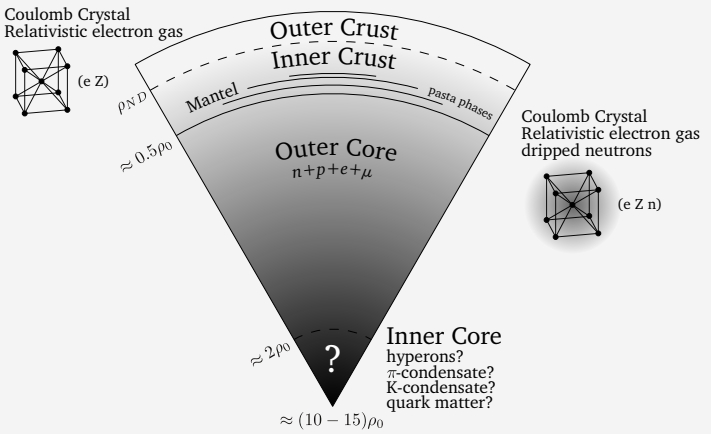

Figure 1.2: Schematic structure of a neutron star. Stellar parameters strongly depend on the equation of state in a neutron star core.

Neutron star crusts and their ground state structure

The stellar evolution of a massive star with mass $M \approx 8-10M_\odot$ ends in a catastrophic gravitational collapse of the degenerate iron core [Jan07]. Because of the very strong gravitational field, nuclei are crushed and compressed such that photodissociation and electron capture neutronises the matter. Hence, the elementary constituents of neutron star matter are neutrons, protons and electrons. Only under the high pressure reigning in the core of the neutron star, these constituents transform into more exotic compounds.

The outer layers of the neutron star with densities lower than the nuclear saturation density are dubbed the crust. Asteroseismology indicates that its thickness is roughly 1.6 km [Str05, Wat06, Wat09]. Hence, it only covers a small portion of the neutron star's mass, but is crucial for many neutron star phenomena. As densities of the crust are subnuclear, one can use the successful terrestrial nuclear-physics models. However, these theories must be applied to extreme physical conditions far from the domains for which they were developed. Although the gravitational field could be seen as one of those extreme conditions, the description of the matter can be decoupled from gravity. The gravitational metric changes by a mere $\approx 10^{-19}$ over the spacing of the nucleons [Gle00].

There are various types of crust possible in a neutron star, all of which result from

differences in their formation or composition. The crusts range from weakly magnetised neutron star surfaces to accreting neutron star surfaces and strongly magnetised crusts [Cha08]. The ground state of neutron star crusts, is one of these crusts.

At zero temperature, a system's entropy is zero and it can be assumed that the system resides in its ground state. For the crust of the neutron star, this implies that its total energy is minimised under the conditions of β-equilibrium ($p + e^- \leftrightarrow n + \nu_e$) and neutrality of electric charge.

The outer crust

The outer crust of a neutron star is defined as the region where matter has densities below the neutron drip value ρ_{ND}. This neutron-drip density marks the border where under the conditions of β-equilibrium and charge neutrality the neutrons drip out of the nuclei. In its ground state, the outer crust is understood as a perfect lattice of nuclear species embedded in an electron gas. The energy density is given by

$$\varepsilon_{tot} = n_N E(A,Z) + \varepsilon_e + \varepsilon_L,$$

with n_N the nuclear-number density, $E(A,Z)$ the energy of the nucleus with Z protons and $A-Z$ neutrons, ε_e the electron-energy density and ε_L the lattice energy [Bay71b]. As the electron Thomas-Fermi screening length is larger than the lattice spacing, electron-screening effects are negligible and the electrons can be treated as an ideal Fermi-gas [Pet95, Wat03a].

Using experimental data for $E(A,Z)$ and model extrapolations, it can be shown that with increasing densities, heavier nuclei with decreasing proton fraction occupy the lattice sites of a body-centred cubic lattice. The nuclei species range from ^{56}Fe to ^{118}Kr. Furthermore, there appears to be a predominance of magic neutron numbers $N = 50, 82$ indicating that shell effects play an important role in the structure of the outer crust [Bay71b, Jog82, Hae94, Rüs06, Hae07, Cha08].

The inner crust

The inner crust of a neutron star starts at densities beyond the neutron drip density ρ_{ND}. This means that neutron rich nuclei are immersed in a gas of neutrons that dripped out of the nuclei. In other words, a fraction of the neutrons are unbound and fill up the energy continuum. Within the crust of a neutron star, it is shown that this neutron drip density is approximately $\rho_{ND} \approx 4 \times 10^{11}$ g cm^{-3} [Bay71b, Hae94, Rüs06].

The structure of the inner crust is similar to that of the outer crust, except that the system is embedded in a neutron gas, representing the dripped neutrons. This kind of system is rather unique and not accessible in laboratories due to the presence of a neutron gas. Furthermore, many-body calculations for this kind of matter are out of reach. This is not only because of the spatial heterogeneities of the nuclear matter, but also due to the complicated bare nucleon-nucleon interaction [Hae07, Cha08]. The models used to study this matter are purely phenomenological. Examples are the compressible liquid drop model having a classical nature [Dou01], or the semi-classical extended Thomas-Fermi calculations [Buc71, Gor05b]. The state-of-the-art calculations are done with self-consistent mean-field methods that are successful in predicting properties of heavy nuclei [Neg73, Ons08].

One of the distinctive features of the inner crust, is the existence of proton shell effects as nuclear clusters with proton numbers $Z = 40$ and $Z = 50$ are strongly favoured.

The mantel

The transition from the crust to the core is generally referred to as the mantle of the neutron star and occurs in the density range from $\rho_0/3$ to $\rho_0/2$, with ρ_0 the nuclear saturation density [Hae07]. It is the region where the spherical nuclear clusters of the inner crust start to outgrow the unit cell of the lattice structure and the crystallised crust transforms into uniform core matter. The equilibrium structure of the nuclear clusters in the neutron star crust are the result of the interplay between the total Coulomb energy and the surface self-energy of the clusters. From these two energies, the Coulomb energy receives contributions from the Coulomb self-energies of the clusters and the Coulomb-lattice energy. For the lower-density regions, i.e. the inner crust, the self-energies of the clusters dominate. This results in spherical clusters. For higher densities, where the Coulomb lattice-energy largely cancels the total Coulomb energy, it is possible to have other geometrical structures that characterise the transition to uniform matter.

In the densest layers of the crust, the Coulomb energy and the nuclear binding energy become comparable. This can be seen from a virial equation stating that the surface self-energy of the clusters is twice the total Coulomb energy, while realising that the total Coulomb energy vanishes in the liquid neutron star core [Rav83, Hae07, Cha08]. At these densities, matter becomes “frustrated”. The system finds itself in a dynamical competition between the short-range nuclear attraction and the long-ranged Coulomb repulsion, making it for the system impossible to minimise all its elementary interactions. This results in a multitude of competing quasi-ground

states from which the system has to choose and leads to complex-shaped nuclei. The work of Liebmann is an excellent introduction to the physics of frustration [Lie86].

The appearance of non-spherical shaped clusters was proposed by Baym, Bethe and Pethick [Bay71a]. They predicted that for cluster-volume fractions exceeding half the volume of the nuclear matter, the structure of the matter would turn inside out. Instead of spherical nuclear clusters appearing in a neutron liquid, spherical neutron bubbles will appear in nuclear matter. Using a liquid drop model, Ravenhall and Pethick as well as Hashimoto and his collaborators discovered that with increasing volume fraction of the clusters more complex clusters appear [Rav83, Has84, Oya84]. The planar, cylindrical and spherical geometries are dubbed nuclear pasta. Starting from the inner crust, the nuclear matter consists of three-dimensional spherical nuclear clusters (meatballs). As the density increases, these spheroids will touch and fuse into two-dimensional cylindrical tubes of dense matter (spaghetti) of varying radii. Similarly, these tubes deform, touch and become one-dimensional slabs interlaid with planar voids filled with neutron liquids (lasagne). At this point, the regime predicted by Baym et al. is reached and the systems turn inside out. While the density grows, the slabs deform and merge, creating two-dimensional cylindrical neutron liquids within the nuclear matter (ziti) who, likewise, transform into the three-dimensional spherical neutron-liquid-bubbles embedded in the nuclear matter (Swiss cheese). As a final step in the transition to the neutron star core, all voids are absorbed and the system transforms into uniform neutron matter (sauce). The pasta phases are shown in Fig. 1.3.

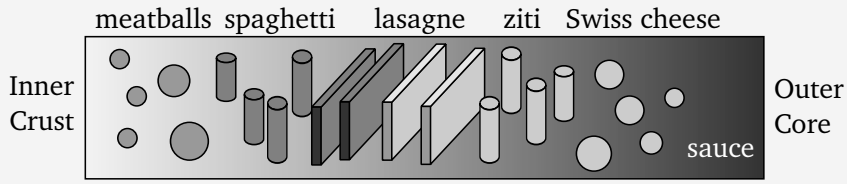

Figure 1.3: Schematic structure of the mantel of a neutron star. Darker colours indicate an increase in baryon density.

The properties of pasta phases have been studied by means of various nuclear models ranging from liquid drop models [Rav83] over semi-classical models [Wil85, Las87, Oya93] towards Hartree-Fock calculations [Sum95] and quantum molecular dynamics simulations [Wat03b, Wat05]. These models predict the same sequence of phases as the density increases, but disagree on the corresponding characteristic

density. All models, except the quantum molecular dynamics simulations, use specific nuclear shapes and determine which phase is energetically more favourable. The quantum molecular dynamics model, on the other hand, has no restrictions regarding the shape of the nuclear clusters. Remarkably, in these simulations, the rod-like and slab-like structures appeared by cooling down hot uniform nuclear matter. Next to the classic pasta phases, intermediate sponge-like structures appeared which could be identified as a bi-continuous double-diamond structure, later identified through a liquid drop model [Nak09].

Importance of the neutron star crust

The study of crustal matter of a neutron star is essential for a thorough understanding of various astrophysical phenomena involving neutron stars. In what follows, a number of these phenomena are sketched.

Supernovae and dense matter physics

The stellar evolution of massive stars with masses ranging from approximately 8 to 20 solar masses is well understood from the initial burning stages of hydrogen until its gravitational collapse, the onset of the explosion of the star. Even the explosion mechanism is understood in fair detail. Nonetheless, in spite of intense numerical efforts, simulations of supernovae still fail to reproduce the stellar explosion. This may indicate that some realistic physics is missing in the current models [MP06].

The main interactions governing the explosion mechanism and the formation of the proto-neutron star are weak-interaction processes and neutrino transport [Lan06]. Simulations generally show that a shock wave is created by the accumulation of sound waves at the sonic point, the region where the infalling matter and the outgoing sound waves have the same speed. When the shock wave has formed, it propagates outwards but hardly succeeds to reach the bifurcation sphere of the star, the radius from where the matter will be expelled. The simulations show that the shock wave dissipates energy through dissociation of nuclei and stalls after moving a few hundred kilometres outwards.

It is strongly believed that a delayed neutrino-heating mechanism is capable of reviving the shock after roughly a hundred milliseconds. For this reason, a thorough study of neutrino interactions with dense matter is crucial for modelling supernovae. The neutrino transport in the supernova heavily depends on the microscopic structure of the matter. Not only the size of the nuclear grains, but also the geometrical shape and topology has an effect on these interactions.

Neutron star cooling

In the proto-neutron star, neutrinos are produced en masse through various processes as electron-positron pair annihilation and plasmon decay in the crust, and Urca processes and bremsstrahlung in the core. The proto-neutron star, however, is opaque for neutrinos because of the high matter densities. The density, however, alters when the shock wave rushes through the proto-neutron star, making the star transparent to neutrinos. Within ten to twenty seconds, the star rapidly cools down because of the neutrino emission and shrinks to a normal neutron star due to pressure loss caused by the deleptonisation. For the first few seconds, the predominant cooling mechanism of the hot proto-neutron star is neutrino cooling. Neutrinos still dominate the cooling of the neutron star for at least the first thousand years, and typically for much longer. Eventually, photon emission takes over when the temperature of the neutron star has sufficiently decreased.

Reviews of neutron star cooling and neutrino production in neutron stars are given in the Refs. [Yak01, Yak04, Bur06, Pag06]. As neutrinos are the main source of cooling for a neutron star, it is evident that a good knowledge of neutrino-nuclear matter interaction is of paramount importance. However, neutrino interactions with nuclear matter are not only important for the cooling of the neutron star but also for supernovae. The interaction with crustal matter shapes up the neutrino signal released during supernovae.

r-process in the decompression of cold neutron star crusts

The r-process, a nucleosynthesis process responsible for the production of many of the neutron-rich nuclei in the universe, entails a succession of rapid neutron captures on seed nuclei. This way the nuclei run up along the neutron drip line until they become highly unstable and decay into stable, neutron-rich nuclei. The location of the astrophysical site for this rapid neutron capture process is still elusive. Well studied scenarios are related to neutrino-driven winds occurring during type-II supernovae or γ-ray bursts [Arn07]. However, the conditions needed for the r-process to be successful are difficult to reach by means of simulations of these scenarios.

Another scenario, proposed by Lattimer [Lat77] suggests that the r-process could occur during the decompression of crustal matter. This is favourable for the r-process as the crust has a high neutron-to-seed ratio as well as a low electron fraction. The idea of decompression of crustal matter is not as weird as it might sound. Recent observations indicate that giant flares of magnetars could eject more than $10^{-9} M_{\odot}$ of matter, while hydrodynamic simulation of neutron star mergers show an ejection

of up to $10^{-2}M_{\odot}$. Not only does it seem possible, it also appears that this could qualitatively reproduce the solar system's r-process abundance pattern. For a current status on crustal decompression, the following works and references therein are of interest [Gor05a, Arn07].

Pulsar glitches

Pulsars are, without a doubt, one of the most precise clocks flouting through the universe. The periods of the 1827 currently discovered pulsars, range from milliseconds up to several seconds. For instance, PSR J1748-2446ad has a period of 1.396 milliseconds while PSR J1841-0456 needs 11.78 seconds for a turn. Although the periods of pulsars are extremely stable, they change measurably. On average, a pulsar slows down roughly 3 seconds in 10^8 years [Gle00]. Although pulsars are clearly stable, some show irregularities in their period. A sudden increase in rotational frequency, referred to as glitches, have been observed in radio and X-ray pulsars. At the time of this writing 170 glitches have been observed in 52 pulsars [Man05].

Since the first observations of glitches, several models have been proposed to explain this erratic behaviour. The starquake model seemed the most convincing one. Due to centrifugal forces, a neutron star is slightly deformed. If the crust would be a liquid, a deceleration of the rotation would entail a readjustment of the stellar shape into a more spherical one. For crystallised crusts on the other hand, the deceleration would inflict a build-up of stress in the crust as its tensile strength prevents the readjustment. When the stress reaches critical levels, the crust cracks and readjusts its shape, this directly leading to a glitch.

Even though crustquake models seem plausible, it remains hard to explain large amplitude glitches. The current leading glitch model involves angular momentum transfer between the crust and the core through superfluidity [And75]. While both the crust and the core are spinning, the crust decelerates through magnetic dipole radiation. The superfluids in the core are weakly coupled to the crustal matter but its rotation rate does not decrease. When the spin difference between both components becomes too large, something breaks releasing a lot of stress by readjusting the spinrates of both components. A short review of this model can be found in [Cha08].

Gravitational waves from pulsars

One of the most fascinating predictions of Einstein's theory of relativity is that massive objects in vehement motion emit radiation, known as gravitational waves [Mis73]. The existence of these waves were confirmed by the discovery of the binary pulsar

PSR 1913+16 by Russel Hulse and Joseph Taylor [Hul75], leading to their Nobel Prize in 1993.

As neutron stars are among the most compact objects in the universe, they are excellent candidates as sources of gravitational waves. Spherical and in general, axially symmetric neutron stars cannot emit gravitational waves. However, a non-axial deformed rotating neutron star can. Mountains on rapidly rotating neutron stars would suffice to radiate gravitational waves efficiently. The question remaining whether the crust can support mountains large enough to create detectable gravitational waves. Current studies show that the breaking strain is large enough to support such mountains [Hor09].

Motivation and outline

As the previous section clearly indicated, the physics of the neutron star crust plays an important role in various astrophysical phenomena related to neutron stars. In order to gain an improved understanding of these phenomena, it is essential to study crustal matter. This dissertation wants to be part of this research effort.

The crust-core interface, i.e. the mantel, may represent a sizable fraction of the crustal mass. After all, it represents the densest regions of the crust. Hence, the mantel plays an important role in the various astrophysical phenomena. Because of frustration, the competition between the interactions leads to a multitude of commensurate, but also incommensurate, phases. With a preponderance of low-energy excitations levels, these pasta phases are susceptible to low-energy dynamics.

As indicated earlier, pasta phases have been investigated with a broad spectrum of computational techniques [Wil85, Las87, Lor93, Oya93, Sum95, Mar05, Wat05]. From all these, molecular dynamics is one of the few techniques that is not biased with regards to the geometry of the nuclear clusters and, thanks to the dynamical aspect, can go beyond the study of ground state structures. This way, the dynamical evolution of the entire crust can be investigated. Classical Molecular Dynamics (CMD) and Quantum Molecular Dynamics (QMD) simulations have been performed by Horowitz et al. [Hor04b, Hor04a, Hor08] and Watanabe et al. [Wat03b, Wat05, Wat07].

As the major interest of Horowitz et al. lied in studying the effect of large density fluctuations on neutrino opacities, he used a simple CMD model. The used interaction provides only the essential physics of frustration, a short-range nuclear attraction and a long-range, but screened, Coulomb repulsion. As the model behaves classically, it

lacks many quantum mechanical features. Nonetheless, the model is fit to reproduce saturation properties at temperatures of 1 MeV.

The QMD model of Watanabe, on the other hand, is more advanced. Even though the potential carries much more quantum mechanical features and stems from a Skyrme interaction, it requires phenomenological potentials to mimic fermion behaviour. The QMD model can be interpreted as a quantum mechanicalised form of CMD as the potential is deduced from quantum mechanics by means of localised wave functions. The potential is able to reproduce various finite-size nuclei properties as well as saturation properties of nuclear matter. As indicated earlier, using this model, Watanabe showed that it is possible to form dynamically the pasta phases within time scales plausible for neutron star formation.

As the QMD model of Watanabe is semi-classical, various quantum mechanical features are missing or phenomenologically incorporated. The antisymmetrisation of the wave function is mimicked through a Pauli potential, spin dynamics is unavailable and a particle's uncertainty is time-independent. All these shortcomings can be remedied by using a technique dubbed "Fermionic Molecular Dynamics" (FMD) [Fel00] but this comes with a cost. As CMD and QMD are N^2 problems, FMD is an N^4 process.

The FMD model is very successful in reproducing ground state properties of nuclei, in particular when combined with the Unitary Correlation Operator Method (UCOM) [Nef08]. Next to ground state properties, the technique can address heavy ion collisions [Ono92b, Ono04]. The use of FMD to simulate properties of bulk fermion systems has not yet been achieved. The main reason for this is that the antisymmetrisation can't be contained within a box-volume when using periodic boundary conditions to mimic bulk matter. The antisymmetry must run over the complete infinite-sized system's wave function. As properties of the neutron star crust are properties of bulk fermion liquids, it is the purpose of this dissertation to demonstrate how an infinite antisymmetrisation can be incorporated in the FMD technique.

The outline of this work is as follows. Chapter 2 introduces the theory behind FMD and gives it a mathematical underpinning. Thereby, all steps in the construction of the FMD formalism are confronted with well known principles in classical and quantum mechanics. Chapter 2 also pays attention towards the choice of the particle representation. As in classical molecular dynamics, particles are point particles, particles in FMD must have quantum mechanical properties.

The FMD formalism of Chapter 2 addresses finite-sized systems. Using this formal-

ism to simulate bulk properties of fermion systems is largely hindered by the amount of particles needed to diminish the surface effects. Chapter 3 is solely devoted to this problem. How can the theory of FMD be applied to bulk systems? As an introduction to classical molecular dynamics, periodic boundary conditions are called to the rescue. By means of well-known theories in solid-state physics, the trial state used in FMD is redefined as a Wannier wave function and used in the FMD formalism introduced in Chapter 2. This results in a viable but computationally cumbersome formalism. The latter problem is resolved by mapping the entire system from Bravais space onto the reciprocal space. To show the effect of periodicity, a single particle system is investigated as well as the momentum densities of a multi-particle system.

The appendices collect the mathematical derivations of various formula used or obtained in this work. They are added to improve on the understanding of the FMD formalism.

This page intentionally left blank

2

Molecular dynamics for Fermions

Abstract

In this chapter, a brief introduction to molecular dynamics for fermions is presented. The time-dependent variational principle is used to obtain the equations of motion for a parameterised trial state. This is used to describe the time evolution of a many-particle fermion system. The trial state, required in the time-dependent variational principle, is created by means of classical ideas and extended such that a full quantum mechanical description of the time-evolution of a fermion system becomes possible.

Section 2.1 Introduction

In quantum physics, the Schrödinger equation [Sch26a, Sch26b, Sch26c, Sch26d],

$$i\frac{\partial \Psi}{\partial t} = \mathcal{H}\Psi,$$

is as essential as Newton's laws [New87] are in classical mechanics. It describes how a quantum state evolves as a function of time when it is subject to a potential. In quantum mechanics, however, it is conventional wisdom to solve this equation in a time-independent way through its static counterpart,

$$E\psi = \mathcal{H}\psi.$$

Strictly speaking, in the study of many quantum phenomena, time-independent methods are preferred over their time-dependent counterparts. Nonetheless, in classical mechanics, time-dependent approaches are rather the rule than the exception. It

stands to reason that, by the correspondence principle, it may be advantageous to use explicitly time-dependent methods for semi-classical problems and even quantum mechanical problems. This is for instance the case when investigating dynamical phenomena in many-body systems where correlations and fluctuations play an important role and mean-field approximations are not sufficient anymore. A technique frequently invoked is molecular dynamics (MD). In this formalism, the constituents of the many-body systems are represented by a few classical degrees of freedom and interact through potentials. In MD simulations, the equations of motion, either Newtonian [New87]

$$m_i \ddot{\boldsymbol{r}}_i = \boldsymbol{F}_i(t),$$

or Hamiltonian [Ham34, Ham35]

$$\dot{\boldsymbol{r}}_i = \frac{\partial H}{\partial \boldsymbol{p}_i}, \qquad \dot{\boldsymbol{p}}_i = -\frac{\partial H}{\partial \boldsymbol{r}_i}, \qquad \text{with} \quad H = \sum_{i=1}^{N} \frac{\boldsymbol{p}_i^2}{2m_i} + \frac{1}{2}\sum_{i,j=1}^{N} V(\boldsymbol{r}_i, \boldsymbol{r}_j),$$

are solved numerically. The interactions that are used range from purely phenomenological to sophisticated ab initio quantal potentials.

One of the major advantages of molecular-dynamics simulations is that they can go beyond quasi-particle interpretations and include both mean-field effects and many-body correlations. For this reason, they can provide insight into complex systems with correlations on different length and time scales. Shortcomings, however arise when investigating quantum mechanical systems. Classical molecular dynamics (CMD) is applicable when the de Broglie wavelength of the constituents is small compared to the length scale of typical variations within the system. When this is not the case, the quantal uncertainties related to the wave character of the constituents start interfering with the classical description [Hei27]. In addition, the statistical many-body correlations, related to the bosonic or fermionic nature of the constituents, are neglected in standard CMD simulations. These correlations are related to the fact that the constituents are indistinguishable and play a negligible role as long as the de Broglie wavelength remains small compared with the typical inter-constituent distances. For instance, the above-mentioned two conditions are not obeyed for nuclear matter near the saturation density. As a matter of fact, CMD is not very suited to study nuclear matter near saturation density.

Quantum molecular dynamics (QMD) [Aic86, Aic91] has been developed as a powerful technique in the study of fragment formation, for instance, in heavy-ion collisions. In QMD a Gaussian wave packet is attributed to each particle, thereby

accounting for their wave character. The total many-body wave function, however, remains a simple direct-product state of the wave-packet states. The equations of motion are classical and the forces act on the centroids of the wave packets. Due to the simple product state, the QMD model lacks the statistical properties inherent to the particles. Actually, even after including a Pauli potential, QMD still describes distinguishable particles.

A technique which was met with great expectations was conceived by Feldmeier and is dubbed fermionic molecular dynamics (FMD) [Fel90, Fel95, Fel00, Nef08]. This technique implements the statistical properties of Fermions in the molecular dynamics formalism through the variation of an antisymmetrised many-body state and allows the dynamical variation of spin-components and wave-packet widths. None of these novelties were present in the previously mentioned models. The various MD models in use might even be considered amended or simplified versions of FMD. Both in fermionic molecular dynamics and antisymmetrised molecular dynamics (AMD) [Ono92a, Ono92b], the overall wave function is antisymmetrised. In AMD, however, the dynamics of the wave-packet width is not taken into account. At the same time, a collision term is added to account for branching into other Slater determinants in a phenomenological way. In the extended quantum molecular dynamics (EQMD) [Mar96] the width is dynamic, but the effects of antisymmetrisation are accounted for approximately by using a Pauli pseudo-potential. Finally, in quantum molecular dynamics (QMD), neither the widths are dynamic, nor antisymmetrisation is carried out explicitly.

In this chapter, the equations of motion for a fermion system will be introduced. This will be done through mathematical derivations and intuitive reasoning. In order to accomplish this, its foundations must be laid, the time-dependent variational method.

Section 2.2 Time-dependent variational methods

In classical physics, time-dependent systems are solved through Hamilton's least action principle. This principle demands that the action

$$S = \int \mathscr{L}\, dt = \int (P\dot{Q} - H) dt, \tag{2.1}$$

is stationary and is implemented by means of variational calculus. Since the dawn of quantum mechanics, variational methods have been employed to find approximate

solutions to the time-dependent Schrödinger equation. Those principles generally lead to practical and accurate time propagation schemes which themselves are useful in a wide variety of problems. The first use of this technique is attributed to Dirac. In his search for a theoretical justification for the Thomas model, Dirac postulated a time-dependent variational method [Dir30]. Later on, Dirac's postulation was generalised by Frenkel leading to the time-dependent Hartree-Fock equations [Fre34]. The Dirac-Frenkel variational principle (DFVP) which states that

$$\left\langle \delta\Psi \middle| i\frac{\partial}{\partial t} - \mathcal{H} \middle| \Psi \right\rangle = 0 \tag{2.2}$$

must hold, is strictly speaking not a variational principle. The DFVP was criticised by McLachlan who pointed out that DFVP does not guarantee a true minimum and might lead to divergent solutions. With this in mind, McLachlan proposed a new variational method by minimisation of the error in the rate of change $\Theta = \partial\Psi/\partial t$ of a state Ψ compared to the exact rate given by Schrödinger's equation, namely $i\Theta = \mathcal{H}\Psi$ [McL64a, McL64b]. Hence the quantity

$$I = \int |i\Theta - \mathcal{H}\Psi|^2 dx, \tag{2.3}$$

should be minimal for all variations of Θ with fixed Ψ. This implies that at all times t [Bro88]

$$\Im\mathrm{m} \left\langle \delta\Psi \middle| i\frac{\partial}{\partial t} - \mathcal{H} \middle| \Psi \right\rangle = 0. \tag{2.4}$$

Even though the initial idea of McLachlan's variational principle (MVP) and DFVP are different, both principles lead to identical results for self-consistent field theories.

Regardless that in molecular physics literature, McLachlan's principle is usually addressed, a different development took place in nuclear physics. There, a variational method based on the principle of least action was devised as a quantum mechanical extension of the classical idea. An effective action based on a quantum mechanical Lagrangian

$$S = \int_{t_1}^{t_2} \mathscr{L}'(\Psi^\star, \Psi) dt, \tag{2.5}$$

is varied. The Lagrange functional $\mathscr{L}'$ is given by

$$\mathscr{L}'(\Psi^\star, \Psi) = \left\langle \Psi \middle| i\frac{\partial}{\partial t} - \mathcal{H} \middle| \Psi \right\rangle. \tag{2.6}$$

The requirement that the effective action S remains stationary, is generally referred to as the time-dependent variational principle (TDVP) [Moc73, Ker76, Kra81]. Analogously to DFVP and MVP, TDVP can be written as

$$\Re\mathrm{e}\left\langle \delta\Psi\middle| i\frac{\partial}{\partial t} - \mathcal{H}\middle|\Psi\right\rangle = 0 \tag{2.7}$$

for all times t [Bro88].

Even though the variational principles have different starting points, similarities are obvious through Eqs. (2.2), (2.4) and (2.7). This means that if DFVP is valid, both MVP and TDVP must hold. The equivalence between the three variational principles was proved by Broeckhove. He indicated that this equivalence occurs when the parameterisation of the state Ψ is such that the variational manifold parameterises in a complementary way. When using a complex parameterisation, it should therefore be analytic [Bro88, Bro89].

Since one would like to utilise the merits of a molecular-dynamics model for indistinguishable particles in the quantum regime, the starting point will be identical to that of CMD. The equations of motion will be derived by means of Hamilton's principle of least action or, quantum mechanically, the time-dependent variational principle.

Various authors have conducted research in time-dependent approximations through variational means. For more considerations on this aspect see Langhoff et al., Heller, Kerman and Koonin, Kramer and Saraceno and various others [Dir30, McL64a, McL64b, Lan72, Hel75, Hel76a, Ker76, Kra81, Sar83, Ger83, Coo86, Coa90, Cor91].

Section 2.3 _ The time-dependent variational principle

As indicated in the previous sections, the time-dependent variational principle will be used to find approximate solutions for the time-dependent Schrödinger equation. Thereby it is assumed that the wave function Ψ adopts a rather simple form. The TDVP is derived starting from the action functional

$$S' = \int_{t_1}^{t_2} \mathscr{L}'(\Psi, \Psi^\star, \dot{\Psi}, \dot{\Psi}^\star)dt, \tag{2.8}$$

where the Lagrange functional $\mathscr{L}'$ is given by

$$\mathscr{L}'(\Psi,\Psi^\star,\dot{\Psi},\dot{\Psi}^\star)=\left\langle \Psi\left| i\frac{\partial}{\partial t}-\mathcal{H}\right|\Psi\right\rangle . \tag{2.9}$$

This Lagrangian functional is appropriate upon varying the wave functions $\Psi(t)$ which are required to be normalised at all times. However, it will turn out convenient to extract the normalisation and the overall time-dependent phase directly from the wave function. If not, they would be inextricably mixed in with the wave function. To this end, this becomes easier by using a complex parameterisation that also makes sure that DFVP, MVP and TDVP become equivalent [Bro88, Bro89]. The extraction can be achieved by introducing the unnormalised wave function $\Phi(t)$ and a time-dependent phase-factor $f(t)$ such that the normalised variational wave function $\Psi(t)$ can be written as

$$|\Psi(t)\rangle = f(t)|\Phi(t)\rangle. \tag{2.10}$$

The extraction of the phase-factor $f(t)$ does not impose any restriction on the functional form of $\Psi(t)$. This ensures that the corresponding time-dependent wave function remains the most general one through the non-normalised wave function $\Phi(t)$. By means of the variation of the action of Eq. (2.8), it is possible to determine this phase-factor $f(t)$. This is done by means of the Euler-Lagrange equations [Lag68] applied to $f(t)$ and its complex conjugate. These equations are given by

$$\frac{d}{dt}\frac{\partial\mathscr{L}'}{\partial\dot{f}}-\frac{\partial\mathscr{L}'}{\partial f}=0, \qquad \frac{d}{dt}\frac{\partial\mathscr{L}'}{\partial\dot{f}^\star}-\frac{\partial\mathscr{L}'}{\partial f^\star}=0.$$

Using the action functional $\mathscr{L}'$ from Eq. (2.9), one can easily obtain the following set of equations

$$\begin{aligned} i\dot{f}\langle\Phi|\Phi\rangle + if\langle\Phi|\dot{\Phi}\rangle &= f\langle\Phi|\mathcal{H}|\Phi\rangle,\\ -i\dot{f}^\star\langle\Phi|\Phi\rangle - if^\star\langle\dot{\Phi}|\Phi\rangle &= f^\star\langle\Phi|\mathcal{H}|\Phi\rangle. \end{aligned}$$

These equations lead, in combination with the normalisation condition for $\Psi(t)$, to the following expression for the time-dependent phase-factor $f(t)$,

$$f(t)=\frac{1}{\sqrt{\langle\Phi|\Phi\rangle}}\cdot\exp\left(i\int_0^t\mathscr{L}(\Phi,\Phi^\star,\dot{\Phi},\dot{\Phi}^\star)dt'\right). \tag{2.11}$$

Here, the Lagrangian $\mathscr{L}$ is given by

$$\mathscr{L}(\Phi,\Phi^\star,\dot{\Phi},\dot{\Phi}^\star)=\frac{i}{2}\frac{\langle\Phi|\dot{\Phi}\rangle-\langle\dot{\Phi}|\Phi\rangle}{\langle\Phi|\Phi\rangle}-\frac{\langle\Phi|\mathcal{H}|\Phi\rangle}{\langle\Phi|\Phi\rangle}=\mathscr{L}_0-\mathscr{H}, \tag{2.12}$$

where $\mathscr{L}_0$ is defined as

$$\mathscr{L}_0 = \frac{i}{2}\frac{\langle\Phi|\dot{\Phi}\rangle - \langle\dot{\Phi}|\Phi\rangle}{\langle\Phi|\Phi\rangle},$$

and $\mathscr{H}$ represents the expectation value of $\mathcal{H}$. Interestingly, the result obtained here can also be deduced by means of DFVP. This was done by Da Providência and is at times referred to as the first occurrence of TDVP [DaP63].

The Lagrangian $\mathscr{L}$ and its parent $\mathscr{L}'$ have a functional relation which will turn out to be useful later on. Inserting Eq. (2.10) into Eq. (2.9) leads to

$$\begin{aligned}\mathscr{L}' &= if^\star\dot{f}\langle\Phi|\Phi\rangle + if^\star f\langle\Phi|\dot{\Phi}\rangle - f^\star f\langle\Phi|\mathcal{H}|\Phi\rangle,\\ &= i\frac{d}{dt}\langle\Psi|\Psi\rangle - i\dot{f}^\star f\langle\Phi|\Phi\rangle - if^\star f\langle\dot{\Phi}|\Phi\rangle - f^\star f\langle\Phi|\mathcal{H}|\Phi\rangle.\end{aligned}$$

The summation of these two equations results in the relation

$$\begin{aligned}\mathscr{L}' &= \frac{i}{2}\frac{d}{dt}\langle\Psi|\Psi\rangle + \frac{i}{2}(f^\star\dot{f} - \dot{f}^\star f)\langle\Phi|\Phi\rangle + \frac{i}{2}f^\star f\left(\langle\Phi|\dot{\Phi}\rangle - \langle\dot{\Phi}|\Phi\rangle\right) - f^\star f\langle\Phi|\mathcal{H}|\Phi\rangle,\\ &= \frac{i}{2}\left(\frac{d}{dt}(f^\star f\langle\Phi|\Phi\rangle) + (f^\star\dot{f} - \dot{f}^\star f)\langle\Phi|\Phi\rangle\right) + f^\star f\langle\Phi|\Phi\rangle\mathscr{L}(\Phi,\Phi^\star,\dot{\Phi},\dot{\Phi}^\star)\end{aligned} \tag{2.13}$$

When inserting the solution $f(t)$ into Eq. (2.13), it evidently leads to $\mathscr{L}' = 0$. Since up to this point no restriction whatsoever with regard to the functional form of $\Phi(t)$ has been made, it indicates that $\mathscr{L}' = 0$ is valid along the wave function's trajectory. All this irrespective of the choice of Φ and its remaining degrees of freedom.

By means of the aforementioned procedure, an overall time-dependent phase-factor has been extracted from the variational wave function Ψ. Through this procedure, a new Lagrangian $\mathscr{L}$ emerged, i.e. Eq. (2.12), which can be used, for variational purposes, with an unnormalised state Φ. This will be shown later on. The overall phase-factor $f(t)$ was obtained by variational means and restores the normalisation conditions of $\Phi(t)$. Furthermore, $f(t)$ plays a similar role as the time-dependent phase-factor obtained from the time-dependent Schrödinger equation for static eigenstates ψ_n from $\mathcal{H}$, i.e. $\exp(-iE_nt)$. In the general case presented here, the Lagrangian $\mathscr{L}$, appearing in Eq. (2.11) for $f(t)$ can be identified as an analogue to energy-level shifts stemming from perturbation theory [Lan72].

The action functional $\mathscr{L}$ can now be used in a variational way by minimising the action

$$S = \int_{t_1}^{t_2} \mathscr{L}(\Phi, \Phi^\star, \dot{\Phi}, \dot{\Phi}^\star) dt. \tag{2.14}$$

One often finds this as the starting point of TDVP. Moreover, it is possible to show that variation of Φ and $\Phi^\star$, completely arbitrary and independent, yield the time-dependent Schrödinger equation for $\Psi(t) = f(t) \cdot \Phi(t)$ [Kra81]. It is worth stressing that the dynamical fields resulting from this Lagrangian generally contain more information than required when only a few macroscopic variables are of interest. Under those circumstances, it is natural to consider approximation schemes for the non-normalised wave function Φ. This can be done by restricting the wave function to a submanifold in the Hilbert space of the Hamiltonian. The submanifold can be represented by a set of variational parameters $x_1, \ldots, x_m$, which are either real or complex. The variational principle provides then the means to determine the optimal time evolution on that submanifold of a given trial-wave function. Hence, the trial state is given by

$$|\Phi(t)\rangle = |\Phi(x_1(t), \ldots, x_m(t))\rangle = |\Phi(\boldsymbol{x}(t))\rangle. \tag{2.15}$$

The equations of motion for the trial state are given by the Euler-Lagrange equations for the variational parameters. It is noteworthy mentioning that the Euler-Lagrange equations stemming from the Lagrangian $\mathscr{L}'$ and those from $\mathscr{L}$ are equivalent. This can easily be seen by means of Eq. (2.13),

$$\begin{aligned}\frac{d}{dt}\frac{\partial \mathscr{L}'}{\partial \dot{x}_i} - \frac{\partial \mathscr{L}'}{\partial x_i} = &\left(\frac{d}{dt}\frac{\partial \mathscr{L}}{\partial \dot{x}_i} - \frac{\partial \mathscr{L}}{\partial x_i}\right) \cdot \left(f^\star f \langle \Phi | \Phi \rangle\right) \\ &+ \frac{i}{2}\left(\frac{d}{dt}\frac{\partial}{\partial \dot{x}_i} - \frac{\partial}{\partial x_i} - 2i\frac{\partial \mathscr{L}}{\partial \dot{x}_i}\right)\left(\frac{d}{dt}\left(f^\star f \langle \Phi | \Phi \rangle\right)\right) \\ &- \frac{i}{2}(f^\star \dot{f} - \dot{f}^\star f - 2i f^\star f \mathscr{L})\frac{\partial \langle \Phi | \Phi \rangle}{\partial x_i}.\end{aligned}$$

When inserting the solution of the phase-factor $f(t)$, i.e. Eq. (2.11), into the above while noting that

$$\dot{f} = -\frac{\langle \dot{\Phi} | \Phi \rangle + \langle \Phi | \dot{\Phi} \rangle}{2\langle \Phi | \Phi \rangle} f + i f \mathscr{L}, \tag{2.16}$$

the equivalence becomes evident. Based on this, it can be concluded that the action in Eq. (2.14) can be used for variational purposes if the trial state Φ is not normalised.

Looking back upon the structure of the Lagrangian $\mathscr{L}$, we had

$$\mathscr{L}(\Phi,\Phi^\star,\dot{\Phi},\dot{\Phi}^\star)=\frac{i}{2}\frac{\langle\Phi|\dot{\Phi}\rangle-\langle\dot{\Phi}|\Phi\rangle}{\langle\Phi|\Phi\rangle}-\frac{\langle\Phi|\mathcal{H}|\Phi\rangle}{\langle\Phi|\Phi\rangle}=\mathscr{L}_0-\mathscr{H}.$$

This expression can be compared to the one for a classical Lagrangian written in a complex format, i.e.

$$\mathscr{L}_C=\frac{i}{2}\sum_{j=1}^{N}(z_j^\star\dot{z}_j-\dot{z}_j^\star z_j)-H=\mathscr{L}_{0,C}-H,$$

in which the real and imaginary parts of z_j are defined as $z_j=(q_j+ip_j)/\sqrt{2}$. The terms $\mathscr{L}_0$ and $\mathscr{L}_{0,C}$ are equivalent and stem from the Legendre transformation. They can be easily connected to the geometry of the system's manifold. The dynamics that the system undergoes on this manifold, is the result of the Hamiltonian. These features will become visible when deriving the equations of motion for the variational parameters.

Since the variational parameters of the trial wave function Φ, namely $x_1,\ldots,x_m$, can be real as well as complex, the complete set of variational parameters of the Lagrangian functional $\mathscr{L}$ is given by $y_1,\ldots,y_n$ containing all variational parameters x_i as well as their complex conjugate in a unique way such that $y_i\neq y_j$. Having this in mind, it becomes convenient to introduce the notations $\bar{y}_1,\ldots,\bar{y}_n$ representing the variational parameters in the ket state, and correspondingly $\bar{y}_1^*,\ldots,\bar{y}_n^*$ for those of the bra state. Note that this is just a new notation to distinguish between the parameter set stemming from the bra and the one from the ket, thus $\bar{y}_k=\bar{y}_k^*=y_k$. With this in mind, the time derivatives of the variational wave functions, appearing in the Lagrangian $\mathscr{L}$, can be written as

$$|\dot{\Phi}\rangle=\sum_{i=1}^{n}\dot{y}_i\frac{\partial}{\partial\bar{y}_i}|\Phi\rangle,\qquad\qquad\langle\dot{\Phi}|=\sum_{i=1}^{n}\dot{y}_i\frac{\partial}{\partial\bar{y}_i^*}\langle\Phi|. \tag{2.17}$$

The equations of motion for the variational parameters y_i can now be deduced from the Euler-Lagrange equations stemming from $\mathscr{L}$. One obtains

$$i\frac{\partial}{\partial\bar{y}_i^*}\left(\frac{\langle\Phi|\dot{\Phi}\rangle}{\langle\Phi|\Phi\rangle}\right)-i\frac{\partial}{\partial\bar{y}_i}\left(\frac{\langle\dot{\Phi}|\Phi\rangle}{\langle\Phi|\Phi\rangle}\right)=\frac{\partial\mathscr{H}}{\partial y_i}, \tag{2.18}$$

which can be written in the more convenient form by means of Eqs. (2.17) as

$$i\left(\frac{\partial^2\ln\langle\Phi|\Phi\rangle}{\partial\bar{y}_i^*\partial\bar{y}_j}-\frac{\partial^2\ln\langle\Phi|\Phi\rangle}{\partial\bar{y}_i\,\partial\bar{y}_j^*}\right)\dot{y}_j=\frac{\partial\mathscr{H}}{\partial y_i}. \tag{2.19}$$

The equations of motion obtained here are in their most general form and can easily be related to the equations given in various other works [Ker76, Kra81, Cau82, Fel00].

When investigating the equations of motion of Eq. (2.19), it is clear that, when the trial wave function consists of only one real variational parameter, the equations lead to the static condition with the energy of the system as an extremum. Then, the description of dynamical processes becomes impossible. Hence, in order to treat collective motion, one requires at least two real variables or one complex variable in the parameterisation of Φ [Ker76]. Furthermore, it is visible that the antisymmetric tensor η defined by

$$\eta_{ij} = i\left(\frac{\partial^2 \ln\langle\Phi|\Phi\rangle}{\partial \bar{y}_i^* \partial \bar{y}_j} - \frac{\partial^2 \ln\langle\Phi|\Phi\rangle}{\partial \bar{y}_i \partial \bar{y}_j^*}\right), \tag{2.20}$$

represents the geometrical structure of the variational manifold. Throughout the deduction of the equations of motion, it is clearly visible that this metric originates from the term $\mathscr{L}_0$ as we indicated previously.

As mentioned in the previous section, the three variational principles become equivalent when the parameterisation is complex analytic. This is achieved when the wave function Φ is parameterised by complex variational parameters. Denoting the set of complex variables by $z_1, \ldots, z_m$, the equations governing their time-dependence, can be derived from Eq. (2.19). They adopt the simple form

$$i\mathbf{C}_{ij}\dot{z}_j = \frac{\partial \mathscr{H}}{\partial \dot{z}_i^\star}, \qquad -i\mathbf{C}_{ij}^\star \dot{z}_j^\star = \frac{\partial \mathscr{H}}{\partial z_i}. \tag{2.21}$$

Here, the matrix $\mathbf{C}$ is defined as

$$\mathbf{C}_{ij} = \frac{\partial^2 \ln\langle\Phi|\Phi\rangle}{\partial z_i^\star \partial z_j}, \tag{2.22}$$

representing the Hermitian metric of the manifold.

The equations of motion, which have been derived, bear a strong resemblance with those from classical Hamiltonian dynamics. First of all, Eq. (2.19) reveals a generalised Poisson structure. Provided that the antisymmetric tensor η is not singular, and the tensor ξ is the inverse of η, a bracket $\{.,.\}$ for two functions f and g on the manifold can be defined as

$$\{f, g\} = \frac{\partial f}{\partial y_i}\xi_{ij}\frac{\partial g}{\partial y_j}.$$

It is possible to show that this bracket is bilinear, skew-symmetric and satisfies Leibniz' rule as well as the Jacobi identity [Kra81, Hai06]. This means that the bracket is a general Poisson bracket. With these observations, the equations of motion of Eq. (2.19) may be written as

$$\dot{y}_i = \{y_i, \mathscr{H}\}.$$

Through this, the time evolution of an observable $\mathscr{B} = \langle\Phi|\mathcal{B}|\Phi\rangle / \langle\Phi|\Phi\rangle$ that does not possess any explicit time dependence, can be determined by

$$\dot{\mathscr{B}} = \dot{y}_i \frac{\partial \mathscr{B}}{\partial y_i} = \frac{\partial \mathscr{B}}{\partial y_i} \xi_{ij} \frac{\partial \mathscr{H}}{\partial y_j} = \{\mathscr{B}, \mathscr{H}\}.$$

The formula reflects the time evolution of the observable along a trajectory on the manifold which is generated by the Hamiltonian $\mathcal{H}$. It also directly states that the expectation value $\mathscr{H}$ of the Hamiltonian operator $\mathcal{H}$ is conserved as time goes by.

A second resemblance with Hamiltonian dynamics emerges when rewriting Eq. (2.21) in block notation,

$$i \begin{pmatrix} 0 & -\mathbf{C}^\star \\ \mathbf{C} & 0 \end{pmatrix} \begin{pmatrix} \dot{\boldsymbol{z}} \\ \dot{\boldsymbol{z}}^\star \end{pmatrix} = \begin{pmatrix} \dfrac{\partial \mathscr{H}}{\partial \boldsymbol{z}} \\ \dfrac{\partial \mathscr{H}}{\partial \boldsymbol{z}^\star} \end{pmatrix}. \tag{2.23}$$

The equivalence with the classical Hamiltonian equations of motion is now evident. With $\mathbf{C}$ the unit matrix, the equations of motion of Eq. (2.23) reduce to the complex form of the classical Hamiltonian equations of motion. The generalised Poisson bracket becomes the complex counterpart of the standard Poisson bracket governing the dynamics of a classical Hamiltonian system. Having this in mind, it can be stated that the real and imaginary parts of the variational variables play the role of canonical pairs [Sar83, Fel97, Fel00].

In this section, it has been shown that by abandoning the idea of generalised variational fields, the restriction of the wave functions to a parameterised manifold lead to equations of motion governing the time evolution of the variational parameters. A strong resemblance between the time-dependent variational principle and the classical principle of least action, has been identified. The time-dependent variational principle transformed the Hilbert space into a generalised phase space where the motion is described by a classical Poisson bracket. Accordingly, the complete apparatus of classical Hamiltonian dynamics can be used in TDVP. When the wave function is parameterised as an analytic function with complex variables, the equations of motion

reduce to a block form revealing its similarities with classical Hamiltonian dynamics even further. It is also of interest to recall that under these conditions the three variational principles are equivalent. It is beyond the scope of this work to study the geometrical properties of these equations, their connection to canonical variables or to investigate the conservation laws within these generalised Poisson systems. For further information, I refer to the extensive works of Kerman and Koonin, Kramer and Saraceno and others [Ker76, Kra81, Bro88, Bro89, Fel00, Hai06].

Section 2.4 The motion of a single particle

The discussion in the previous section demonstrated that by employing the time-dependent variational principle on a complex parameterised variational trial state, equations of motion for the parameters can be derived. These equations of motion, bearing strong resemblances with classical Hamiltonian mechanics, could be used to determine the time evolution of a trial state. Accordingly, in order to describe the dynamical evolution of Fermi liquids, it is of paramount importance to represent the fermion system by a properly parameterised trial state. Despite the fact that a fermion system requires anti-symmetrisation, a property inherited by the Pauli exclusion principle [Pau25] with no classical counterpart, the point of departure to obtain this trial state will be the quantum analogue to the classical point particle, i.e. wave packets. Strictly speaking, wave packets can have a certain degree of localisation in phase space making them an appropriate representation of a constituent for MD purposes.

In his book, Dirac succinctly stated the starting point of this discussion. For any dynamical system with a classical analogue, a wave packet represents a quantum-mechanical state for which the classical description is valid as an approximation. The numerical values of the coordinates and momenta have accuracies limited by Heisenberg's uncertainty principle. He also pointed out that the Schrödinger equation determines how such a wave packet varies with time. Therefore, in order for the classical description to remain valid, the wave packet should remain a wave packet and should move according to the laws of classical dynamics [Dir67].

Wave packets, portraying particles confined in phase space, can easily be linked with the correspondence principle. When investigating the propagation of a wave packet for a free and heavy particle with an initial state given by

$$\Psi(\boldsymbol{x}, 0) = e^{i\boldsymbol{p}\cdot\boldsymbol{x}}\psi(\boldsymbol{x}),$$

the heavy-mass limit of the wave packet's time-evolution, can be approximated by

$$\Psi(\boldsymbol{x},t) \approx e^{i\boldsymbol{p}\cdot(\boldsymbol{x}-\boldsymbol{v}_p t)}\psi(\boldsymbol{x}-\boldsymbol{v}_g t) + \mathcal{O}\left(\tfrac{t}{m}\right).$$

By defining $\boldsymbol{v}_p$ as the phase velocity $\boldsymbol{p}/2m$ and $\boldsymbol{v}_g$ the group velocity $\boldsymbol{p}/m$, the classical behaviour of the propagation becomes evident through the expectation value, $|\Psi(\boldsymbol{x},t)|^2 \approx |\Psi(\boldsymbol{x}-\boldsymbol{v}_g t)|^2$ and $\langle\hat{\boldsymbol{x}}(t)\rangle \approx \langle\hat{\boldsymbol{x}}(0)\rangle + \boldsymbol{v}_g t$ [Lub08]. When the heavy particle moves within a potential $\mathcal{V}(\hat{x})$, its propagation also displays classical behaviour. The time evolution of the wave packet is denoted as

$$\Psi(\boldsymbol{x},t) = e^{-i\mathcal{H}t}\Psi(\boldsymbol{x},0) = e^{-i(\mathcal{T}+\mathcal{V})t}\Psi(\boldsymbol{x},0),$$

and can, for a short time-scale Δt, be approximated by means of the Lie-Trotter-Suzuki formula [Suz85], i.e.

$$e^{-i\mathcal{H}\Delta t} \approx e^{-i\mathcal{V}\Delta t/2}e^{-i\mathcal{T}t}e^{-i\mathcal{V}\Delta t/2}.$$

Under the assumption that the wave packet $\psi(\boldsymbol{x})$ is localised around $\boldsymbol{r} \equiv \langle\hat{\boldsymbol{x}}\rangle$, the above approximation combined with a Taylor expansion of $\mathcal{V}$ around $\boldsymbol{r}$ leads to the following set of equations [Lub08],

$$\begin{aligned}
\boldsymbol{p}_{\Delta t/2} &= \boldsymbol{p}_0 - \boldsymbol{\nabla}V(\boldsymbol{r}_0)\cdot\Delta t/2,\\
\boldsymbol{r}_{\Delta t} &= \boldsymbol{r}_0 + \Delta t\cdot\boldsymbol{p}_{\Delta t/2}/m,\\
\boldsymbol{p}_{\Delta t} &= \boldsymbol{p}_{\Delta t/2} - \boldsymbol{\nabla}V(\boldsymbol{r}_{\Delta t})\cdot\Delta t/2.
\end{aligned}$$

Here the initial state was defined through $\boldsymbol{r}_0$ and $\boldsymbol{p}_o$. This is the Strömer-Verlet integration scheme for numerical solutions of the Newtonian equations of motion. This integration scheme is one of the most frequently used numerical integration methods in classical molecular dynamics. More information on this subject can be found in Hairer et al. and Lubich [Hai06, Lub08].

Notwithstanding the fact that the above discussion alludes to classical behaviour, the full transition from quantum mechanics to classical mechanics is given by Ehrenfest's theorem [Ehr27]. The theorem states that the equations of classical Hamiltonian dynamics are satisfied by the expectation values of the corresponding quantum mechanical operators, or

$$\frac{d}{dt}\langle\hat{\boldsymbol{x}}\rangle = \left\langle\frac{\partial\mathcal{H}}{\partial\hat{\boldsymbol{k}}}\right\rangle, \qquad \frac{d}{dt}\langle\hat{\boldsymbol{k}}\rangle = -\left\langle\frac{\partial\mathcal{H}}{\partial\hat{\boldsymbol{x}}}\right\rangle.$$

At a more formal level, the classical equations could be obtained by means of a Taylor expansion of $\mathcal{H}(\boldsymbol{p},\boldsymbol{q})$ around the expectation values $\boldsymbol{r} \equiv \langle\hat{\boldsymbol{x}}\rangle$ and $\boldsymbol{p} \equiv \langle\hat{\boldsymbol{k}}\rangle$. This

introduces an error term depending on the variance of the wave packet and the third derivative of the potential. One obtains [Got89]

$$\frac{d}{dt}\langle\hat{\boldsymbol{x}}\rangle \approx \quad \frac{\partial}{\partial \boldsymbol{p}}\mathcal{H}(\boldsymbol{r},\boldsymbol{p}) + \mathcal{O}\left(\left\langle(\hat{\boldsymbol{k}}-\boldsymbol{p})\otimes(\hat{\boldsymbol{k}}-\boldsymbol{p})\right\rangle \frac{\partial^3\mathcal{H}}{\partial \boldsymbol{p}\partial \boldsymbol{p}\partial \boldsymbol{p}}\right), \tag{2.24a}$$

$$\frac{d}{dt}\langle\hat{\boldsymbol{k}}\rangle \approx -\frac{\partial}{\partial \boldsymbol{r}}\mathcal{H}(\boldsymbol{r},\boldsymbol{p}) + \mathcal{O}\left(\langle(\hat{\boldsymbol{x}}-\boldsymbol{r})\otimes(\hat{\boldsymbol{x}}-\boldsymbol{r})\rangle \frac{\partial^3\mathcal{H}}{\partial \boldsymbol{r}\partial \boldsymbol{r}\partial \boldsymbol{r}}\right). \tag{2.24b}$$

From these expressions, it can be concluded that for up to quadratic potentials, the error term vanishes and the classical Ehrenfest equations are exact. For more general potentials, the classical trajectories are followed when the wave packet is sufficiently narrow or the potential is smooth and nearly harmonic. This hints at the use of Gaussian trial states as a single particle state. The argumentation goes that some of the exact solutions of the time-dependent Schrödinger equation with a quadratic Hamiltonian are general Gaussian wave packets having only a few seemingly classical parameters. This will be demonstrated later on.

Consider a Gaussian wave function in the form of a coupled multidimensional Gaussian wave packet written as

$$\langle \boldsymbol{x}|\mathbf{A}\boldsymbol{b}\rangle = \exp\left\{-\frac{1}{2}(\boldsymbol{x}-\boldsymbol{b})\cdot\mathbf{A}^{-1}\cdot(\boldsymbol{x}-\boldsymbol{b})\right\}. \tag{2.25}$$

The variable $\boldsymbol{b}$ represents the complex phase-space vector while the complex symmetrical positive-definite matrix $\mathbf{A}$ controls the spread of the packet in phase space and the direct correlations between different spatial coordinates. Gaussian wave packets are the obvious choice for a single-particle trial state as they represent the best quantum analogue of a classical particle. Their mean position and momentum is given by $\boldsymbol{r}$ and $\boldsymbol{p}$ via

$$\boldsymbol{r} = \frac{\langle\mathbf{A}\boldsymbol{b}|\widehat{\boldsymbol{x}}|\mathbf{A}\boldsymbol{b}\rangle}{\langle\mathbf{A}\boldsymbol{b}|\mathbf{A}\boldsymbol{b}\rangle} = \mathbf{A}(\mathbf{A}^\dagger+\mathbf{A})^{-1}\boldsymbol{b}^\star + \mathbf{A}^\dagger(\mathbf{A}^\dagger+\mathbf{A})^{-1}\boldsymbol{b},$$

$$\boldsymbol{p} = \frac{\langle\mathbf{A}\boldsymbol{b}|\widehat{\boldsymbol{k}}|\mathbf{A}\boldsymbol{b}\rangle}{\langle\mathbf{A}\boldsymbol{b}|\mathbf{A}\boldsymbol{b}\rangle} = i(\mathbf{A}^\dagger+\mathbf{A})^{-1}(\boldsymbol{b}^\star-\boldsymbol{b}),$$

indicating that the phase-space vector can be defined as $\boldsymbol{b} = \boldsymbol{r} + i\mathbf{A}\boldsymbol{p}$. The uncertainties in the phase space are given by

$$(\Delta\boldsymbol{r})^2 = \frac{\langle\mathbf{A}\boldsymbol{b}|(\widehat{\boldsymbol{x}}-\boldsymbol{r})^2|\mathbf{A}\boldsymbol{b}\rangle}{\langle\mathbf{A}\boldsymbol{b}|\mathbf{A}\boldsymbol{b}\rangle} = \mathrm{Tr}\left(\mathbf{A}^\dagger(\mathbf{A}^\dagger+\mathbf{A})^{-1}\mathbf{A}\right),$$

$$(\Delta\boldsymbol{p})^2 = \frac{\langle\mathbf{A}\boldsymbol{b}|(\widehat{\boldsymbol{k}}-\boldsymbol{p})^2|\mathbf{A}\boldsymbol{b}\rangle}{\langle\mathbf{A}\boldsymbol{b}|\mathbf{A}\boldsymbol{b}\rangle} = \mathrm{Tr}\left((\mathbf{A}^\dagger+\mathbf{A})^{-1}\right).$$

This demonstrates that the particle doesn't violate Heisenberg's uncertainty principle [Hei27] and its wave function is at minimum uncertainty when $\mathbf{A} = a\mathbf{I}$ with a a real positive definite variable [Fel95].

As is pointed out in appendix C, the equations of motion of the time-dependent variational principle (2.21), lead to the following time propagation of the Gaussian wave packet

$$i\dot{\boldsymbol{b}} = (\mathbf{A}^\dagger + \mathbf{A})\frac{\partial \mathscr{H}}{\partial \boldsymbol{b}^\star} - \dot{\mathbf{A}}\boldsymbol{p}, \tag{2.26a}$$

$$i\dot{\mathbf{A}} = (\mathbf{A}^\dagger + \mathbf{A})\left(2\sum_\alpha \frac{\partial \mathscr{H}}{\partial A^\star_\alpha}\mathbf{S}^\alpha - i\frac{\partial \mathscr{H}}{\partial \boldsymbol{b}^\star}\otimes\boldsymbol{p} - i\boldsymbol{p}\otimes\frac{\partial \mathscr{H}}{\partial \boldsymbol{b}^\star}\right)(\mathbf{A}^\dagger + \mathbf{A}). \tag{2.26b}$$

These mathematically challenging expressions are correct for any Hamiltonian. The underlying physical meaning, however, is rather ill defined. A better understanding is obtained by Taylor expanding the Hamiltonian as is indicated in appendix C. The true physical nature of the above expressions reveals itself as

$$\dot{\boldsymbol{r}} = \left\langle \frac{\partial \mathcal{H}}{\partial \hat{\boldsymbol{k}}} \right\rangle, \tag{2.27a}$$

$$\dot{\boldsymbol{p}} = -\left\langle \frac{\partial \mathcal{H}}{\partial \hat{\boldsymbol{x}}} \right\rangle, \tag{2.27b}$$

$$i\dot{\mathbf{A}} = \mathbf{A}\left\langle \frac{\partial^2 \mathcal{H}}{\partial \hat{\boldsymbol{x}}\partial \hat{\boldsymbol{x}}} \right\rangle \mathbf{A} - \left\langle \frac{\partial^2 \mathcal{H}}{\partial \hat{\boldsymbol{k}}\partial \hat{\boldsymbol{k}}} \right\rangle + i\mathbf{A}\left\langle \frac{\partial^2 \mathcal{H}}{\partial \hat{\boldsymbol{x}}\partial \hat{\boldsymbol{k}}} \right\rangle + i\left\langle \frac{\partial^2 \mathcal{H}}{\partial \hat{\boldsymbol{k}}\partial \hat{\boldsymbol{x}}} \right\rangle \mathbf{A}. \tag{2.27c}$$

Surprisingly, it appears that the original set of equations, for which no direct physical interpretation seems possible, merely represent a translation of Ehrenfest's theorem into the language of the time-dependent variational principle. The third equation, not obtainable through the standard equation of motion of the expectation value of an operator, leads to correct results when using it in the time derivative of any operator's expectation value and comparing it with the result obtained through its standard evolution equation. Remark that the Eqs. (2.26) and (2.27) are mapped onto the symmetrical positive definite description of the variance. Another structure will create other equations of motion.

Despite the fact that the Eqs. (2.27) are reflections of Ehrenfest's theorem and valid for general Hamiltonians, a Gaussian wave packet is no solution to the time-dependent Schrödinger equation after embedding the time-dependent phase-factor $f(t)$ conform Eq. (2.11). The time-dependence of the phase factor $f(t)$, according to Eq. (2.16), provides a defect in the normalised state $f|\mathbf{A}\boldsymbol{b}\rangle$, determined by Eq. (2.16),

so that this state represents no solution to the Schrödinger equation. The normalised state, however, answers to the expectation value of the Schrödinger operator to be zero. In short

$$i\frac{d}{dt}f(t)\langle \boldsymbol{x}|\mathbf{A}\boldsymbol{b}\rangle \neq \mathcal{H}f(t)\langle \boldsymbol{x}|\mathbf{A}\boldsymbol{b}\rangle, \qquad \left\langle f(t)\mathbf{A}\boldsymbol{b}\middle| i\frac{d}{dt}-\mathcal{H}\middle| f(t)\mathbf{A}\boldsymbol{b}\right\rangle = 0.$$

The reason for this difference are local effects which tamper with the phase-factor making it a function of $\boldsymbol{x}$ and t, i.e. $f(\boldsymbol{x},t)$. Thus, if the phase-factor corrects for the deficiency of the Gaussian wave packets, only then will the Schrödinger equation hold. Exceptions to this are quadratic Hamiltonians. The motion of a normalised wave packet $f(t)|\mathbf{A}\boldsymbol{b}\rangle$ governed by the Hamiltonian for a damped oscillator

$$\mathcal{H} = \frac{\hat{\boldsymbol{k}}^2}{2m} + C + \boldsymbol{\Gamma}\cdot\hat{\boldsymbol{x}} + \frac{1}{2}\hat{\boldsymbol{x}}\cdot\mathbf{K}\cdot\hat{\boldsymbol{x}},$$

is described by

$$i\dot{\boldsymbol{b}} = \mathbf{A}\boldsymbol{\Gamma} + \mathbf{A}\mathbf{K}\boldsymbol{b}, \tag{2.28a}$$

$$i\dot{\mathbf{A}} = \mathbf{A}\mathbf{K}\mathbf{A} - \frac{1}{m}\mathbf{I}, \tag{2.28b}$$

$$i\dot{f} = C + \boldsymbol{\Gamma}\cdot\boldsymbol{b} + \frac{1}{2}\boldsymbol{b}\cdot\mathbf{K}\cdot\boldsymbol{b} - \frac{1}{2m}\operatorname{Tr}(\mathbf{A}^{-1}). \tag{2.28c}$$

Here, the mass of the particle is determined by m while the strength of the oscillator is given by the symmetrical matrix $\mathbf{K}$. The damping term is introduced as $\boldsymbol{\Gamma}$. The time evolution dictated by these equations is identical to those proposed by Heller in his excellent papers on Gaussian wave packet dynamics [Hel75, Hel76a, Hel76b]. In these papers, the evolution of the normalised wave packet is derived through the time-dependent Schrödinger equation, indicating that any Gaussian wave packet is an exact solution for oscillator potentials. Furthermore, from the above equations it is clear that the mean position and momentum are determined according to Hamilton's equations. This is in agreement with Ehrenfest's theorem. In addition to these classical equations, a new equation for the time-dependent matrix $\mathbf{A}$ emerges. This equation describes the evolution of the variance of the wave packet in phase space and provides the first non-classical degree of freedom in the parameter manifold. The effect of the quantum mechanical parameter is best understood in the one-dimensional situation assuming that $\mathbf{A} = a\mathbf{I}$ while investigating the phase space of the wave packet through its Wigner representation. The mathematical details can be found in appendix D and its result is presented in Fig. 2.1. It shows that a wave packet in a one-dimensional harmonic oscillator undergoes a rigid rotation throughout a scaled

phase space. This rotation is the result of the time-evolution of the variance. The projection of the Wigner distribution on the spatial or momentum coordinate shows the distribution functions. Even though the rotation is the result of the equation of motion of the variance, it must be indicated that an analogue result can be obtained by classically evolving a distribution of point particles throughout phase space.

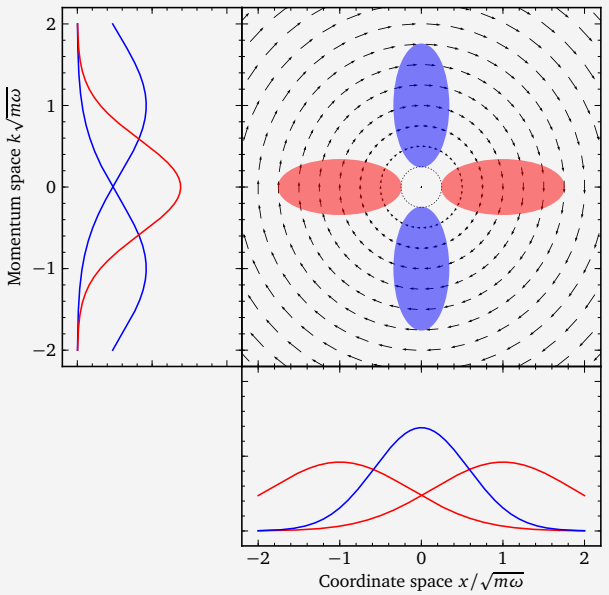

Figure 2.1: The Wigner distribution of a Gaussian wave packet in a harmonic oscillator is presented in combination with its projection on the spatial coordinate as well as the momentum coordinate. Four equidensity contours are shown with their individual projection. From this, it is visible that a wide wave packet in coordinate space depicts as a small wave packet in moment space, and vice versa. In combination with the equidensity contours, the flow in phase space is also represented.

When extrapolating this idea to an arbitrary momentum-independent potential $\mathcal{V}(\hat{x})$, it should be stressed that, as indicated by Eq. (2.27c), the time-evolution of the

variance can be written as

$$i\dot{a} = a^2 \left\langle \frac{d^2\mathcal{V}(x)}{dx^2} \right\rangle - \frac{1}{m}. \tag{2.29}$$

The structure of this equation is, for potentials not restricted to a quadratic form, identical to the one for a harmonic oscillator. Because of the higher orders of the potential, however, the equations of motion, Eqs. (2.27), are all intertwined. The mixing of these equations dictates that the variance influences the path in phase space and causes it to deviate from the classical path leaning towards the exact quantum mechanical solution. This is understood given that the classical path, as indicated by Eqs. (2.24a) and (2.27), can be constructed by a local quadratic approximation of the potential surface in the mean phase-space position. The exact quantum mechanical solution, however, cannot be reached since, as mentioned earlier, the phase factor is not in agreement with the Schrödinger equation. As for the distribution within phase space, the variation of a allows the wave packet to twirl around in phase space squeezing and expanding itself as if it was breathing on its potential surface which is seen by the variance as a time-dependent harmonic oscillator.

To summarise the above, although wave packets show classical behaviour, it becomes clearly more advantageous to propagate a Gaussian wave packet forward in time by variational means. Those packets exhibit classical behaviour on Hamiltonians of quadratic form. For higher order Hamiltonians, they deviate from the classical trajectory and move towards a real quantum mechanical solution via the time-dependent variational principle. Furthermore, through the variation of the variance, a first quantum mechanical parameter is introduced. This allows the particle to breathe on its potential surface by gaining and loosing uncertainty in coordinate and momentum space. With this, it can be concluded that the Gaussian wave packet is a good quantum mechanical analogue to the classical particle. Not only does it allow taking fluctuations in the classical parameters, like position and momentum, into account. It offers the possibility to incorporate the uncertainty principle.

Section 2.5 The dynamics of a fermion system

The focus of this chapter is on obtaining equations of motion for a fermion system. To this end, it is quintessential to construct a good trial state. Previously, it was stressed that a Gaussian wave packet is a good quantum mechanical representation of the classical point particle. Its evolution in time, dictated by the time-dependent variational principle, gives rise to quantum mechanical deviations from the classical

picture. The Gaussian description can be adopted to describe fermions. In order to accomplish this, it will be necessary to dress the Gaussian wave packet with more quantum mechanical properties. Adding spin and weak isospin allows to describe leptons while the combination of spin and isospin describes some composite fermions, like baryons. The quantum dressed Gaussian is described by

$$|\mathbf{A}\boldsymbol{b}\rangle \otimes |\chi\rangle \otimes |\zeta\rangle,$$

a product state of a Gaussian wave packet with spin and isospin. In this description χ and ζ denote the fermion's spin and isospin respectively. Even though this description introduces quantum properties, it only maps a spatially localised particle to its quantum features. Interference effects and tunnelling, for instance, could not be described by this type of wave packet, rendering the total model as semi-quantal. An improved fermion wave function can be constructed by a superposition of Gaussian wave packets, spin states and isospin states, i.e.

$$|q_p\rangle = \sum_{klm} c_{klmp} |\mathbf{A}_{klmp}\boldsymbol{b}_{klmp}\rangle \otimes |\chi_{klmp}\rangle \otimes |\zeta_{klmp}\rangle. \tag{2.30}$$

Through the complex amplitudes c, this superposition allows to construct tailed wave packets, as well as separate spatial localisations per spin and isospin state. The latter is necessary to explain, for instance, the Stern-Gerlach experiment [Ger22a, Ger22b].

Using this, the fermion system can be described in terms of Gaussian wave packets propagating in concert under the influence of an antisymmetric operator. The antisymmetrisation is necessary to incorporate the Pauli exclusion principle [Pau25]. This resulting total fermion trial state is often the starting point of self-consistent mean-field theories like the time-dependent Hartree and Hartree-Fock methods [Dir30, Fre34, McL64a, Lan72, Ker76, Lub08]. Thereby, the A-body Hilbert space is seen as the direct product of one-body Hilbert spaces, i.e. $\mathcal{H}_A = \mathcal{H}_1 \otimes \cdots \otimes \mathcal{H}_1$ with a wave function given by $\langle x_1|\phi_1\rangle \cdots \langle x_A|\psi_A\rangle$. Herein, the variable x denotes all coordinates in phase space, including spin and isospin space. Since fermions live in the antisymmetric subspace of this Hilbert space, their representation is obtained by the projection of the wave function by means of the antisymmetric operator

$$\mathcal{A} = \frac{1}{\sqrt{A!}} \sum_{\mathcal{P}} \mathrm{sgn}(\mathcal{P})\mathcal{P}.$$

The operator $\mathcal{P}$ performs a permutation among the one-body wave functions. The

result can be written as a Slater determinant [Sla29],

$$\langle x_1,\ldots,x_A|\Psi\rangle = \frac{1}{\sqrt{A!}}\det\begin{pmatrix}\langle x_1|\psi_1\rangle & \cdots & \langle x_1|\psi_A\rangle\\ \vdots & \ddots & \vdots\\ \langle x_A|\psi_1\rangle & \cdots & \langle x_A|\psi_A\rangle\end{pmatrix}. \tag{2.31}$$

In combination with the fermion wave functions, this gives rise to a good trial state for the description of a fermion system,

$$|Q\rangle = \mathcal{A}|q_1\rangle\otimes\cdots\otimes|q_A\rangle. \tag{2.32}$$

An important feature of this quantum dressed Gaussian wave-packet basis is that various symmetry operations like parity, rotations, translations, boosts and time reversal do not alter the Slater determinant structure and hence map an FMD trial state onto another [Nef08]. The parity operation on a quantum dressed Gaussian is given by

$$\mathcal{P}|\mathbf{A}\boldsymbol{b}\rangle\otimes|\chi\rangle\otimes|\zeta\rangle = |\mathbf{A},-\boldsymbol{b}\rangle\otimes|\chi\rangle\otimes|\zeta\rangle, \tag{2.33a}$$

while a translation over $\boldsymbol{\ell}$ is written as

$$\mathcal{T}(\boldsymbol{\ell})|\mathbf{A}\boldsymbol{b}\rangle\otimes|\chi\rangle\otimes|\zeta\rangle = |\mathbf{A},\boldsymbol{b}+\boldsymbol{\ell}\rangle\otimes|\chi\rangle\otimes|\zeta\rangle. \tag{2.33b}$$

When boosting a system with a momentum $\boldsymbol{p}$, an extra normalisation correction needs to be introduced. This guarantees a balance in the amplitudes of the proposed fermion trial state. The boost results in

$$\mathcal{B}(\boldsymbol{p})|\mathbf{A}\boldsymbol{b}\rangle\otimes|\chi\rangle\otimes|\zeta\rangle = |\mathbf{A},\boldsymbol{b}+i\mathbf{A}\boldsymbol{p}\rangle\otimes|\chi\rangle\otimes|\zeta\rangle \times\exp\left\{i\boldsymbol{b}\cdot\boldsymbol{p}-\frac{1}{2}\boldsymbol{p}\cdot\mathbf{A}\cdot\boldsymbol{p}\right\}. \tag{2.33c}$$

Upon rotation, it is not only required to rotate the phase-space vector $\boldsymbol{b}$, but also the spin components through its SU(2) symmetry. This results in

$$\mathcal{R}(\Omega)|\mathbf{A}\boldsymbol{b}\rangle\otimes|\chi\rangle\otimes|\zeta\rangle = |R_3^{-1}(\Omega)\mathbf{A}R_3(\Omega),R_3(\Omega)\boldsymbol{b}\rangle\otimes R_2(\Omega)|\chi\rangle\otimes|\zeta\rangle. \tag{2.33d}$$

Finally, the time-reversal operator acts as

$$\mathcal{T}|\mathbf{A}\boldsymbol{b}\rangle\otimes|\chi\rangle\otimes|\zeta\rangle = |\mathbf{A}^\dagger\boldsymbol{b}^\star\rangle\otimes|-\chi_\downarrow^\star,\chi_\uparrow^\star\rangle\otimes|\zeta\rangle, \tag{2.33e}$$

which has the property, due to the spin, that $\mathcal{T}^2|q\rangle = -|q\rangle$.

Despite the non-orthogonality of the single-particle wave packets $|q_p\rangle$ and the apparent cumbersome structure of the system's trial state, the calculation of matrix

elements and their derivatives lead to fairly simple expressions. Detailed calculations can be found in appendix E. Defining the single-particle overlap matrix $\mathbf{n}$ and its inverse $\mathbf{o}$ as

$$\mathbf{n}_{pq} = \langle q_p | q_q \rangle, \qquad \mathbf{o}_{pq} = (\mathbf{n}^{-1})_{pq},$$

the norm of the trial state is given by

$$\langle Q|Q\rangle = \det \mathbf{n}. \tag{2.34}$$

This determinant has as direct consequence that one- and two-body operators are written as a function of the inverse overlap matrix $\mathbf{o}$. The expectation value of a one-body operator $\mathcal{B}_I$ is given by

$$\mathscr{B}_I = \frac{\langle Q|\mathcal{B}_I|Q\rangle}{\langle Q|Q\rangle} = \sum_{pq=1}^{A} \langle q_p|\mathcal{B}_I|q_q\rangle \mathbf{o}_{qp}, \tag{2.35a}$$

while the two-body operator $\mathcal{B}_{II}$ has the expectation value

$$\mathscr{B}_{II} = \frac{\langle Q|\mathcal{B}_{II}|Q\rangle}{\langle Q|Q\rangle} = \frac{1}{2}\sum_{pqrs=1}^{A} \langle q_p q_r|\mathcal{B}_{II}|q_q q_s\rangle (\mathbf{o}_{qp}\mathbf{o}_{sr} - \mathbf{o}_{qr}\mathbf{o}_{sp}). \tag{2.35b}$$

The final step towards the development of the evolution equations for the fermion system, involves the determination of the gradients of these expectation values as well as the metric $\mathbf{C}$. To this end, not only the gradients of the matrix elements are required, but also the gradients of the inverse matrix elements. The latter can be derived via the unity matrix and becomes

$$\frac{\partial \mathbf{o}_{pq}}{\partial z_i^\star} = \frac{\partial \mathbf{o}_{pq}}{\partial z_{\mu a}^\star} = -\sum_{r=1}^{A} \mathbf{o}_{pa} \cdot \frac{\partial \mathbf{n}_{ar}}{\partial z_{\mu a}^\star} \cdot \mathbf{o}_{rq}. \tag{2.36}$$

With this expression, the gradients read

$$\frac{\partial \mathscr{B}_I}{\partial z_i^\star} = \frac{\partial \mathscr{B}_I}{\partial z_{\mu a}^\star} = \sum_{q=1}^{A} \frac{\partial}{\partial z_{\mu a}^\star} \langle q_a^\partial |\mathcal{B}_I|q_q\rangle \mathbf{o}_{qa} - \sum_{pqr=1}^{A} \langle q_p|\mathcal{B}_I|q_q\rangle \mathbf{o}_{qa} \cdot \frac{\partial \mathbf{n}_{ar}}{\partial z_{\mu a}^\star} \cdot \mathbf{o}_{rp}, \tag{2.37a}$$

$$\begin{aligned}\frac{\partial \mathscr{B}_{II}}{\partial z_i^\star} = \frac{\partial \mathscr{B}_{II}}{\partial z_{\mu a}^\star} = &\sum_{qrs=1}^{A} \frac{\partial}{\partial z_{\mu a}^\star} \langle q_a^\partial q_r|\mathcal{B}_{II}|q_q q_s\rangle (\mathbf{o}_{qa}\mathbf{o}_{sr} - \mathbf{o}_{qr}\mathbf{o}_{sa}) \\ &- \sum_{pqrst=1}^{A} \langle q_p q_r|\mathcal{B}_{II}|q_q q_s\rangle \mathbf{o}_{qa} \cdot \frac{\partial \mathbf{n}_{at}}{\partial z_{\mu a}^\star} \cdot (\mathbf{o}_{tp}\mathbf{o}_{sr} - \mathbf{o}_{tr}\mathbf{o}_{sp}),\end{aligned} \tag{2.37b}$$

while the metric, easily found through the use of Eq. (2.37a), results in

$$\mathbf{C}_{ij} = \mathbf{C}_{\mu a,\nu b} = \frac{\partial^2 \ln\langle Q|Q\rangle}{\partial z^\star_{\mu a}\partial z_{\nu b}} = \left(\frac{\partial^2 \mathbf{n}_{ab}}{\partial z^\star_{\mu a}\partial z_{\nu b}} - \sum_{pq=1}^{A} \frac{\partial \mathbf{n}_{ap}}{\partial z^\star_{\mu a}} \cdot \mathbf{o}_{pq} \cdot \frac{\partial \mathbf{n}_{qb}}{\partial z_{\nu b}} \right) \cdot \mathbf{o}_{ba}. \quad (2.38)$$

In these equations, Latin indices refer to single-particle wave functions $|q_p\rangle$. The Greek indices are used in combination with a Latin one and refer to a single-particle quantum number. The indices i and j are exceptions and represent a parameter of the entire parameter set of Q. The superscript $^\partial$ indicates on what single-particle wave function the partial derivative works.

At the current point, all ingredients for the equation of motion are known. As it is clear, overlap matrix elements of fermion states will appear throughout these calculations. With this in mind, the following notations can be introduced. The single particle overlap is denoted as

$$\mathbf{n}_{pq} = \langle q_p|q_q\rangle = \sum_{\substack{k_p l_p m_p \\ k_q l_q m_q}} c^\star_{k_p l_p m_p p} c_{k_q l_q m_q q} \mathscr{R}_{k_p l_p m_p, k_q l_q m_q} \mathscr{S}_{k_p l_p m_p, k_q l_q m_q} \mathscr{T}_{k_p l_p m_p, k_q l_q m_q}, \quad (2.39)$$

where the spatial overlap is introduced as $\mathscr{R}_{pq}$ and is given by (see appendix C)

$$\begin{aligned}\mathscr{R}_{pq} = \left\langle \mathbf{A}_p \boldsymbol{b}_p | \mathbf{A}_q \boldsymbol{b}_q \right\rangle = &\sqrt{\det(2\pi \mathbf{A}_p^\dagger (\mathbf{A}_p^\dagger + \mathbf{A}_q)^{-1} \mathbf{A}_q)} \\ &\times \exp\left\{ -\frac{1}{2} (\boldsymbol{b}_p^\star - \boldsymbol{b}_q) \cdot (\mathbf{A}_p^\dagger + \mathbf{A}_q)^{-1} \cdot (\boldsymbol{b}_p^\star - \boldsymbol{b}_q) \right\}. \quad (2.40)\end{aligned}$$

The spin-space overlap is denoted as $\mathscr{S}_{pq}$ and can be obtained through the complex components of the spin-spinor $|\chi\rangle$ as

$$\mathscr{S}_{pq} = \langle \chi_p | \chi_q \rangle = \chi^\star_{p\uparrow}\chi_{q\uparrow} + \chi^\star_{p\downarrow}\chi_{q\downarrow}. \quad (2.41)$$

The isospin overlap is denoted by $\mathscr{T}_{pq}$. It is important to stress that the spin and isospin components are not required to be normalised. This will, however, result in an extra amount of degrees of freedom which will make the metric $\mathbf{C}$ singular.

With the above derivations, the introduction of the FMD formalism can be concluded. Still, its mathematical elegance should be stressed. By mapping the description of a many-body fermion system onto a Slater determinant of single-particle states $|q_p\rangle$, a synergy between linear algebra and the single-particle description of fermion systems emerges. The determinant structure makes that all operators can be written as functions of the inverse single-particle overlap matrix. This is not possible for boson

systems. For bosons, the single-particle description can be mapped on a permanent, the symmetric counterpart of the determinant, i.e.

$$\det \mathbf{A} = \sum_{\mathcal{P}} \mathrm{sgn}(\mathcal{P}) \prod_{i=1}^{n} A_{i,\mathcal{P}(i)}, \qquad \mathrm{perm}\, \mathbf{A} = \sum_{\mathcal{P}} \prod_{i=1}^{n} A_{i,\mathcal{P}(i)}.$$

with $\mathcal{P}$ the permutation operator. For the expectation values of the operators, this leads to identical structures as those for fermions presented in Eqs. (2.37a) and (2.37b). Unfortunately, due to this permanent, the connection with the inverse single-particle overlap matrix vanishes. As a consequence, the symmetric structure, i.e. the permanents, must be explicitly calculated. This calculation would even be more tedious than a brute force calculation for the antisymmetrised system. This is due to the lack of linear-algebraic properties connected to permanents. Nonetheless, for fermion systems it is not necessary to calculate the antisymmetrisation rigorously. It becomes naturally embedded in the calculation of expectation values through the inverse single-particle overlap matrix.

Section 2.6 Final remark on FMD

The forthcoming chapter builds upon the derivations of previous sections. Here, a few interesting properties of FMD are sketched. These properties, however, are not essential for the remainder of this work but will sooner or later be crucial for the continuation of this research.

When investigating low-density fermion systems, the equations of motion of FMD can be written in a classical form. This is directly visible from Eqs. (2.37) and (2.38) when realising that the overlap matrix **n** is diagonal and assuming that the variance and spin are time-independent. The effect of antisymmetrisation gains in importance with increasing densities and has been studied in the works of Saraceno, Feldmeier as well as Corianò [Sar83, Fel90, Cor91, Fel97, Fel00]. By studying a two-body fermion system, it was seen that in addition to the energy of distinguishable particles, the total energy of the system contains an extra potential depending on the phase-space distance between both fermions. This extra potential is attributed to Pauli repulsion and is referred to as a Pauli potential. The Hamiltonian of a two-fermion system can be written as

$$\mathscr{H} = H_{classical} + V_{uncertainty} + V_{Pauli}.$$

Even though potentials of this form lead to successful energy calculations, it is important to realise that the Pauli repulsion is not a two-body effect. Even though two-body

interactions can produce N-body correlations, they cannot reproduce typical fermion behaviour [Mul03]. The Pauli repulsion should not be seen as a force, but as a geometrical consequence of the antisymmetrisation.

Initially, FMD was devised to describe heavy-ion reactions in a time-dependent framework. Thereby, it is important to evaluate ground states of nuclei that are constructed from the fermion trial states described in section 2.5. Whereas the time-dependent framework is based on the time-dependent variational principle, the Rayleigh-Ritz variational principle is used for finding the ground state [Rit08, Mac33, Fel95]. The latter reads

$$\delta(\mathscr{H} - \mathscr{T}_{CM}) = \delta\left(\frac{\langle Q|\mathcal{H} - \mathcal{T}_{CM}|Q\rangle}{\langle Q|Q\rangle}\right) = 0,$$

where the kinetic energy of the centre-of-mass motion is subtracted. This is done because only the properties of the intrinsic state are of interest. This variational approach translates itself in to the search of the extrema of the multivariate Hamiltonian expectation value $\mathscr{H} - \mathscr{T}_{CM}$. This technique has been shown to be successful in the study of nuclear structure and is often combined with the Unitary Correlation Operator Method (UCOM) [Fel98, Nef03] as well as parity and angular momentum projection [KE01]. A nice overview of nuclear-structure studies using FMD and AMD is given in Refs. [KE03, Nef08].

Even though these days FMD is often used to study nuclear structure, and disregards the dynamics of the problem, AMD is still used for the study of heavy-ion collisions. Thereby, effects as quantum branching and multifragmentation play an important role. These effects will also influence crustal matter and have been studied in Refs. [Fel95, Ono96, Kid97, Ono04].

As FMD is a deterministic microscopic transport theory, it is of great interest to know how thermodynamic properties can be extracted from such a dynamical quantum simulation. The usual approach would be to perform time averages and to rely on the ergodic assumption, i.e. time averages are equivalent to ensemble averages. The validity of this depends on the statistical and ergodic properties of the dynamical model. Various authors have investigated this for FMD and AMD [Ohn93, Ohn95, Sch96, Fel00, Ono04] and came to the following conclusion. Since the antisymmetric many-body states of single-particle Gaussian wave packets form an overcomplete set and provide a complete representation of the unit operator, the statistical mechanical properties obtained through the partition function $Z(T) = \mathrm{Tr}\left\{\exp(-\mathcal{H}/T)\right\}$ are correct. In addition, it was shown that the system is ergodic. This was done by posi-

tioning a system in a harmonic oscillator potential.

As described above, FMD is very promising in various fields. For fermions, it is more satisfactory than classical models as it takes antisymmetrisation into account. However, within FMD, the evaluations of expectation values of operators and the solution of the equations of motion are computationally very demanding problems due to the antisymmetry constraints. Antisymmetry brings along another problem in the study of bulk matter. Large systems lead to large matrices and this is computationally not acceptable. The next chapter addresses this problem.

This page intentionally left blank

3

FERMION MATTER IN BULK

ABSTRACT

The study of bulk liquids is well established within classical molecular dynamics using periodic boundary conditions. This chapter introduces dynamical simulations of bulk fermion systems and incorporates periodic boundary conditions into fermionic molecular dynamics. In order to achieve this, a new boundary technique dubbed truncated antisymmetrised periodic boundary conditions (TAPBC) is introduced.

Section 3.1 Introduction

Molecular dynamics is widely used for studying many-particle systems but has its limitations. Simulations are generally performed with a small number of constituents due to limits on the availability of computational memory as well as on the execution speed of the simulation program. For CMD simulations of N constituents, the latter is proportional to N^2, while for an equivalent FMD model execution time scales with N^4.

Computationally, there is no problem when adopting molecular dynamic techniques in the study of very small systems. For instance, small liquid drops or microcrystals are simulated in a straightforward fashion, only paying attention to the evaporation of the system. The latter occurs when the cohesive forces between the constituents cannot keep the system together while simulation time goes by. This evaporation can be counteracted by means of an external potential container to reach confinement.

When investigating the phenomena of bulk liquids by means of large systems, a simulation suffers from surface effects. A large fraction of constituents lie on the

surface of any relatively small simulation sample and are governed by considerable different potentials than those in bulk. As an example, for a 1000 particles arranged in a $10\times10\times10$ lattice, not less than 488 particles appear on the surface. The study of enormously large systems would minimise the influence of the surface to bulk properties, but this becomes numerically challenging and often unmanageable. As a way to eliminate the surface effects, the system is modelled as if it was part of a larger system by means of periodic boundary conditions (PBC) [Bor12]. In its simplest form, a cubic unit cell, containing a set of constituents, is replicated creating a tessellation of space. In this way, each constituent has images periodically placed throughout space that are part of a copy of the unit cell. In the course of the simulation, each image of the constituent has identical properties as the original and evolves in exactly the same way. Therefore, if a particle leaves the unit cell, one of its images will emerge on the opposite side with identical properties. At that point, attention may be switched to the image just entering the unit cell, creating the illusion as if the particle itself resurfaced. A two dimensional version of such a periodic system is presented in Fig. 3.1.

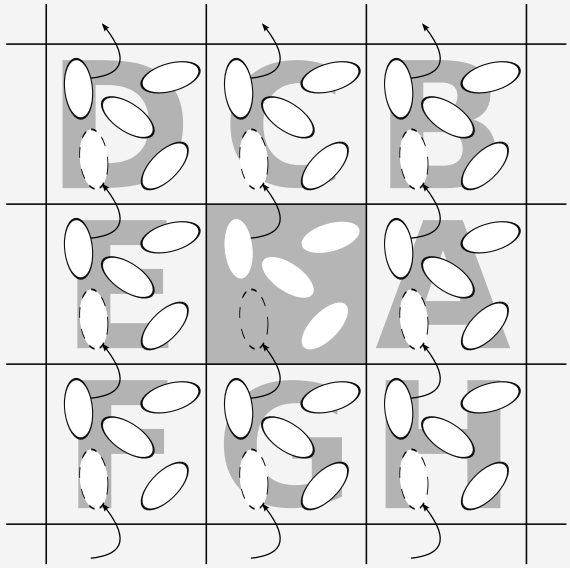

Figure 3.1: A two-dimensional periodic system. The centre cell with its constituents is periodically replicated to tessellate the two-dimensional space. The constituents can travel in the two-dimensional space crossing any of the four borders of the unit cells.

An important question concerns the equivalence of the properties of the small periodic system and the macroscopic system. The periodicity imposes that PBC inhibit long wavelength fluctuations as any fluctuations with wavelengths greater than the box length are suppressed. Other artefacts introduced through PBC will not only depend on the range of the interaction but also on the phenomenon under investigation. The unit cell should be sufficiently larger than the range of the interaction such that a particle is unaware of the geometry and symmetry of the unit cell. This is a particular problem for long-range interactions but can be resolved by applying various tricks, for instance the Ewald sum for Coulomb interactions [Ewa21, dL80]. Furthermore, PBC introduce other artefacts like anisotropies in the fluid structure [Man76] and the cube-corner effect in which the fluid structure is distorted from a radial symmetric structure into a cubic one [Ada79]. The latter is the result of combining PBC with the minimal image convention, a technique introduced by Metropolis et al. to truncate short-range interactions [Met53]. Despite these imperfections, the PBC have little effect on the thermodynamic properties of fluids in equilibrium, as well as their structure if the fluids are far from a phase transition and its interactions behave short-ranged [All91].

The cubic honeycomb is ubiquitous within molecular dynamics as well as Monte Carlo simulations of liquids in bulk, however it is not the only space-filling tessellation used. In total there are fourteen possible honeycombs created from a replication of a single unit cell. These honeycombs, all representations of Bravais lattices [Bra50], can be used in molecular dynamics simulations to study next to equilibria also out-of-equilibrium situations as pressure changes and shear viscosity or any other phenomena that requires volume changes [All91]. Even though most of these phenomena can be studied by means of a cubic unit cell, or by slightly adapting the cubes PBC [All91], it should be stressed that more complex honeycombs can show some advantages. Disregarding that they bring along more complex implementations of PBC. Examples of the unit-cells of these honeycombs are depicted in Fig. 3.2.

When studying correlation functions, the functional range of the correlation function that can be covered, is limited by the properties of the simulation box. The evaluation of the pair-correlation function $g(r)$ in a cubic unit cell limits the range of r to half the box length. This is consistent with the minimal image convention and prevents that periodicity renders into correlation function. Consequently, the cubic unit-cell has a disadvantage. Only a mere fraction of its volume contains particle pairs that can be addressed, resulting in a lot of computational overhead. Other tessellations provide an answer to this problem. The rhombic dodecahedron [Wan72] and truncated octahedron [Ada79] tessellate space in a more spherical way than the

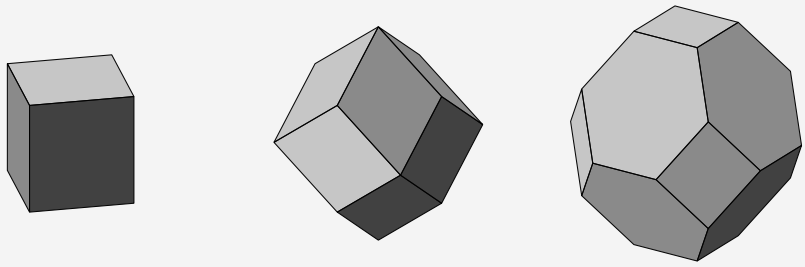

Figure 3.2: Cubic and non-cubic simulation boxes. From left to right, the cube, the rhombic dodecahedron and the truncated octahedron. These boxes tessellate space uniformly as the cubic honeycomb, rhombic dodecahedral honeycomb or the bi-truncated cubic honeycomb respectively. Because of their geometrical structure, it is obvious that the implementation of the boundary conditions is more tedious for all but the cubic honeycomb.

cubic unit cells. Therefore, a larger portion of the particle pairs plays a role in the correlation function. Using these cells thus extends the range of the correlation function. This is understood when comparing different unit-cells for a given density, for the non-cubic unit cells, the distance between the periodic images is larger.

Even though PBC is a well-established technique in molecular dynamics, there is no account of a technique that applies PBC to FMD. A first report of the momentum distribution of one-dimensional nuclear matter by means of equidistant antisymmetrised Gaussian wave packets can be found in the dissertation of Schnack [Sch93]. In that work an adaptation of spherical boundary conditions was used to eliminate surface effects. Thereby, the constituents are placed on the surface of a sphere [Han79] for two-dimensional simulations or a glome [Kra80, Kra82] for three dimensions, hence creating a space without physical boundaries but introducing a non-Euclidean geometry.

The goal of this chapter is to introduce periodic boundary conditions into the fermion molecular dynamics formalism. However, before blindly stepping into the unknown one needs to pave the way.

Section 3.2 — Lattices and periodic quantum systems

Before describing how periodic boundary conditions are introduced in FMD, it is useful to survey some of the most important geometrical properties of periodic arrays in three-dimensional space. These fundamental concepts, well known in crystallography and solid stated physics, will be the key to a better understanding of how periodicity is introduced in FMD.

One of the most fundamental concepts of lattice systems is that of a Bravais lattice. A Bravais lattice is an infinite array of points periodically placed throughout space. This placement is done such that the lattice appears identical from whichever of the points the array is viewed. In total, for three-dimensional space, there are fourteen such a lattice structures [Bra50, Ash76]. Each of these lattice points can be referred to through a Bravais lattice vector $\boldsymbol{R}$, generated by a set of primitive vectors $\boldsymbol{a}_m$ as

$$\boldsymbol{R} = n_1\boldsymbol{a}_1 + n_2\boldsymbol{a}_2 + n_3\boldsymbol{a}_3,$$

where the values n_m are all integers and the set of lattice vectors $\boldsymbol{a}_m$ span the Euclidean space.

When a volume of space can be translated throughout all the Bravais lattice vectors without either overlapping a copy or leaving voids, it is referred as a primitive cell of the Bravais lattice. Such a cell tessellates space perfectly and only contains one lattice point per cell. The most common choice for a primitive cell is the Wigner-Seitz cell, a region of space that is closer to one lattice point than to any other preserving the symmetry of the lattice. Hence, these Wigner-Seitz cells are the preferred choice as a unit-cell within molecular dynamics. A number of constituents are confined within the volume of a Wigner-Seitz cell and replicated according to the Bravais lattice vectors, creating a perfect periodic structure. The lattice structures and their Wigner-Seitz cells which are of interest to this work, are depicted in Fig. 3.3.

Periodicity stands synonym to Fourier series. With this in mind, a new Bravais lattice can be constructed in Fourier space. This lattice, referred to as the reciprocal lattice of the Bravais lattice, is generated through a set of lattice vectors $\boldsymbol{K}$ satisfying

$$e^{i\boldsymbol{K}\cdot\boldsymbol{R}} = 1,$$

and this for all Bravais lattice vectors $\boldsymbol{R}$. The primitive vectors of the reciprocal lattice, denoted as $\boldsymbol{b}_m$ are in three-dimensional Euclidean space related to those of the Bravais

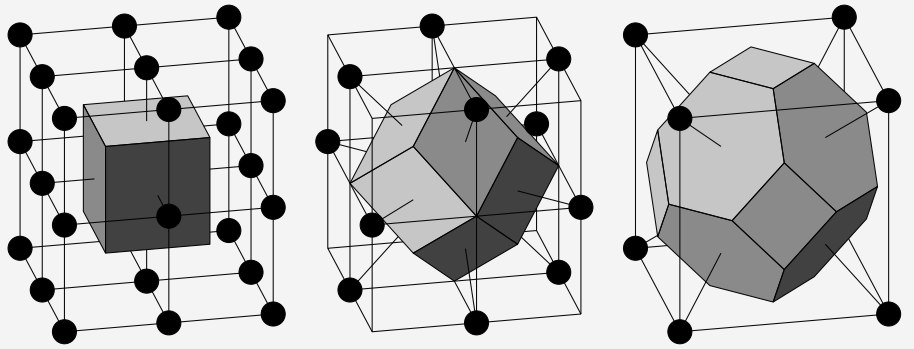

Figure 3.3: The Wigner-Seitz cells for the three most important cubic Bravais lattices are represented here. From left to right, the simple cubic Bravais lattice with its cubic Wigner-Seitz cell, the face-centred cubic Bravais lattice with its rhombic dodecahedron Wigner-Seitz cell and the body-centred cubic Bravais lattice with its truncated octahedron as Wigner-Seitz cell. The surrounding cube is taken such that a lattice point is located in the centre of the cube. This indicates that the Wigner-Seitz cell only contains one lattice point. The Wigner-Seitz cells are perfect volumes to tessellate space through translation over the Bravais lattice vectors.

lattice through

$$\boldsymbol{b}_1 = 2\pi \frac{\boldsymbol{a}_2 \times \boldsymbol{a}_3}{\boldsymbol{a}_1 \cdot (\boldsymbol{a}_2 \times \boldsymbol{a}_3)},$$
$$\boldsymbol{b}_2 = 2\pi \frac{\boldsymbol{a}_3 \times \boldsymbol{a}_1}{\boldsymbol{a}_1 \cdot (\boldsymbol{a}_2 \times \boldsymbol{a}_3)},$$
$$\boldsymbol{b}_3 = 2\pi \frac{\boldsymbol{a}_1 \times \boldsymbol{a}_2}{\boldsymbol{a}_1 \cdot (\boldsymbol{a}_2 \times \boldsymbol{a}_3)}.$$

Similarly to Bravais lattices, it is also possible to define a Wigner Seitz cell of the reciprocal lattice. This cell is generally known as the first Brillouin zone of the Bravais lattice in coordinate space.

From a quantum mechanical perspective, it is interesting to know how particles behave in periodic lattice structures. In the independent particle model, when a Wigner-Seitz cell confines a number of particles and tessellates space through perfect replicas, a single particle behaves as if it was under influence of a periodic potential $\mathcal{V}(\hat{\boldsymbol{x}})$ with its periodicity determined by the underlying Bravais lattice, i.e.

$$\mathcal{V}(\hat{\boldsymbol{x}} + \boldsymbol{R}) = \mathcal{V}(\hat{\boldsymbol{x}}),$$

and this for all Bravais lattice vectors. The stationary eigenstates of such a particle satisfy the following important property inherent to the periodic structure. All eigenstates of a periodic quantum mechanical problem can be written as

$$\psi_{n\boldsymbol{k}}(\boldsymbol{r}) = e^{i\boldsymbol{k}\cdot\boldsymbol{r}} u_{n\boldsymbol{k}}(\boldsymbol{r}),$$

where $u(\boldsymbol{r})$ obtains the same periodicity as the Bravais lattice. This theorem is generally referred to as Floquet's theorem or Bloch's theorem and gives rise to the well-known band-structure in metals and semi-conductors [Flo83, Blo29, Ash76] through the quantum number n. The lattice momentum $\boldsymbol{k}$ is restricted to the first Brillouin zone. The above condition is alternatively stated as

$$\psi_{n\boldsymbol{k}}(\boldsymbol{r}+\boldsymbol{R}) = e^{i\boldsymbol{k}\cdot\boldsymbol{R}}\psi_{n\boldsymbol{k}}(\boldsymbol{r})$$

for every Bravais lattice vector $\boldsymbol{R}$.

From the above theorem, it is clear that Bloch states are understood as perturbations on the plane-wave description of free particles. However, in order to combine FMD and PBC, it is more interesting to work with Wannier states, a set of wave states that are closely related to the single particle states of a single unit cell [Wan37, Ash76]. The Wannier functions $\phi_n(\boldsymbol{r}-\boldsymbol{R})$ form a complete set and are closely related to the Bloch states through a Fourier transformation

$$\psi_{n\boldsymbol{k}}(\boldsymbol{r}) = \sum_{\boldsymbol{R}} \phi_n(\boldsymbol{r}-\boldsymbol{R}) e^{i\boldsymbol{k}\cdot\boldsymbol{R}}, \tag{3.1a}$$

$$\phi_n(\boldsymbol{r}-\boldsymbol{R}) = \frac{1}{V_{BZ}} \int_{BZ} e^{-i\boldsymbol{R}\cdot\boldsymbol{k}} \psi_{n\boldsymbol{k}}(\boldsymbol{r}) d\boldsymbol{k}. \tag{3.1b}$$

The integration in the latter is done over the volume of the first Brillouin zone.

Section 3.3 Truncated antisymmetrised periodic boundary conditions

In the introduction of this chapter, it was shown that PBC provide a way to embed a numerically manageable set of particles, confined in a unit cell, in a larger macroscopic system. This way the surface effects resulting from the finite-size simulation cancel and the study of liquids in bulk becomes feasible. The macroscopic system itself is created as a tessellation of space by means of replicas of the initial unit cell. When the unit cell is only subject to translation, the replicas are placed on well-known

Bravais lattice sites. Despite the fact that the unit cell can have various shapes, the natural choice is the Wigner-Seitz cell of the corresponding Bravais lattice $\mathfrak{B}$.

The idea of PBC is well known in CMD. When, however, framing this fairly simple scheme into a quantum mechanical picture like FMD, there is much more to it than meets the eye because of the antisymmetrisation of the wave function. Periodic boundary conditions have been introduced in quantum mechanics as an adaptation of the Born-von Kármán boundary conditions of classical wave mechanics [Bor12, Ash76]. The Born-von Kármán boundary conditions dictate that a quantum mechanical state remains identical after displacement over a Bravais lattice vector $\boldsymbol{R}$, or

$$\Psi(\boldsymbol{x}+\boldsymbol{R}) = \Psi(\boldsymbol{x}), \qquad \forall \boldsymbol{R} \in \mathfrak{B}.$$

When enforcing these boundary conditions onto the fermion trial state, it is not sufficient to merely copy the antisymmetrised state and translate it over the Bravais lattice vectors. This is consistent with the classic idea of PBC but generates deficiencies with regard to the antisymmetrisation of the complete wave function. A particle would only be antisymmetrised with the particles of its own Wigner-Seitz cell, but not with those from the replicas. This should be corrected as antisymmetrisation of the wave function is a fundamental property of fermions. By copying the single-particle states periodically throughout space, the macroscopic system becomes antisymmetrised through the antisymmetry operator $\mathcal{A}$, embracing this endless structure.

When applying the idea of periodically copying the single-particle states in the FMD formalism and more specific the calculation of the expectation values of one- and two-body operators in accordance with Eqs. (2.35):

$$\mathscr{B}_I = \frac{\langle Q|\mathcal{B}_I|Q\rangle}{\langle Q|Q\rangle} = \sum_{pq=1}^{A} \langle q_p|\mathcal{B}_I|q_q\rangle \mathbf{o}_{qp},$$

$$\mathscr{B}_{II} = \frac{\langle Q|\mathcal{B}_{II}|Q\rangle}{\langle Q|Q\rangle} = \frac{1}{2}\sum_{pqrs=1}^{A} \langle q_p q_r|\mathcal{B}_{II}|q_q q_s\rangle (\mathbf{o}_{qp}\mathbf{o}_{sr} - \mathbf{o}_{qr}\mathbf{o}_{sp}),$$

an infinite dimensional problem arises on the account that an infinite number of particles are addressed. As the FMD expressions are governed by the knowledge of the overlap matrix of the infinite system and its inverse, it is paramount to understand the structure these matrices acquire due to the periodicity. To this end, periodic boundary conditions and the structure of these matrices are introduced by gradually adding unit cells. The basic idea is straightforward. Under the assumption that A single-particle states are confined within a Wigner-Seitz cell of a Bravais lattice $\mathfrak{B}$, consider $(2m+1)^3$ copies of that cell placed on the Bravais lattice vectors $\boldsymbol{R} = n_1\boldsymbol{a}_1 + n_2\boldsymbol{a}_2 + n_3\boldsymbol{a}_3$ with

$n_1, n_2, n_3 \in \{-m, \ldots, m\}$. This way, a volume of $(2m+1)^3$ times the volume of the Wigner-Seitz cell is tessellated in a symmetrical way with a single Wigner-Seitz cell in the centre. As mentioned earlier, when using MD techniques on such a construction, surface effects will interfere with the bulk properties of the system. While the central cell feels the effect of all possible neighbours, the surface cells are only affected by a few. This is clearly visualised in Fig. 3.4 for a two-dimensional system with $m = 1$.

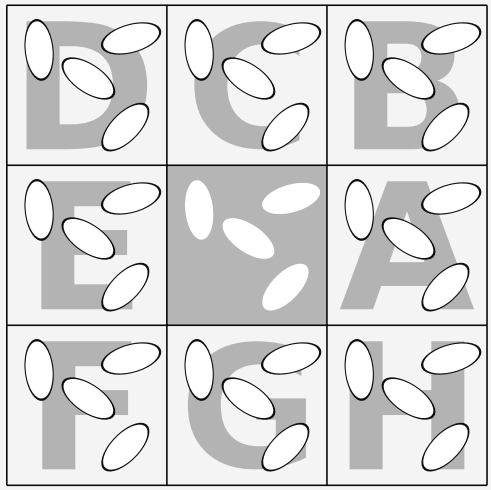

Figure 3.4: In a two-dimensional lattice, nine identical copies of a unit cell are placed symmetrically on the Bravais lattice sites of $\{\mathfrak{B}\}_m$. It is evident that because of this construction, surface effects will play a crucial role. While the centre cell feels the effect of the eight copies, the unit-cells on the corners, i.e. B, D, F and H, only feel three close neighbours. The central border cells A, C, E and G feel the effect of five nearest unit-cells.

To counteract the imprint of this in FMD, the single particle states in such a cell are subject to the Born-von Kármán boundary conditions with a period of $2m+1$ times the size of the Bravais lattice vectors. In this way, the surface cells not only feel the effect of their closest neighbours but also of the opposing surface cells. In short, due to the Born-von Kármán boundary conditions, each cell feels the effect of the same amount of cells, disregarding its position. A one-dimensional representation for first order TAPBC is given in Fig. 3.5 and a two-dimensional representation of TAPBC of order one is given in Fig. 3.6.

This combination of nearest image convention (NIC) on the configuration and the

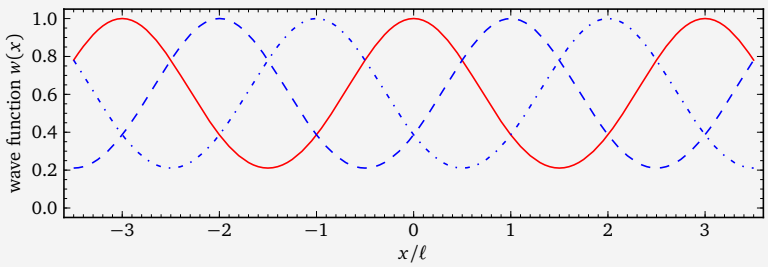

Figure 3.5: Three single particle wave functions used in TAPBC of the first order are represented for a one-dimensional problem. The unit cell has length ℓ. The three wave functions are each shifted over the unit length of the unit cell.

Born-von Kármán boundary conditions on the single-particle wave packets introduces in FMD a truncated antisymmetry in the system. Hence, the technique is dubbed truncated antisymmetrical boundary conditions (TAPBC) with m the order. By using TAPBC with FMD, the notion of an infinite system is created. Remark that, as the result of the Born-von Kármán boundary conditions on the single-particle wave functions, this seemingly infinite system only contains a finite set of particles. Using this finite set in FMD simulations creates thus the illusion to work with an infinite set of particles, however, antisymmetrisation will only encapsulate the finite set. Wave functions which are displaced $2m+1$ unit-cells apart are not antisymmetrised since they represent the same particle. It is evident FMD will simulate an infinite set of particles if the TAPBC has infinite order. Under this condition the truncation is lifted and the antisymmetrisation embedded in FMD will encapsulate an infinite set of particles.

If a single unit-cell contains A particles and the Bravais lattice $\mathfrak{B}$ has primitive vectors $\boldsymbol{a}_1$,$\boldsymbol{a}_2$ and $\boldsymbol{a}_3$, then the FMD trial state is written as

$$|W\rangle = \mathcal{A} \bigotimes_{\boldsymbol{R}\in\{\mathfrak{B}\}_m} \mathcal{T}(\boldsymbol{R}) \left\{ |w_1\rangle \otimes \cdots \otimes |w_A\rangle \right\}. \tag{3.2}$$

It consists thus of a direct product state of sub-systems, periodically translated over the primitive vectors of Bravais lattice $\mathfrak{B}$. The set $\{\mathfrak{B}\}_m$ represents the Bravais lattice vectors of $\mathfrak{B}$ confined within the volume described earlier, namely the Bravais lattice vectors $\boldsymbol{R} = n_1\boldsymbol{a}_1 + n_2\boldsymbol{a}_2 + n_2\boldsymbol{a}_3$ with $n_1, n_2, n_3 \in \{-m, \ldots, m\}$. The A single-particle states $|w_i\rangle$ are subject to the Born-von Kármán boundary conditions with periods

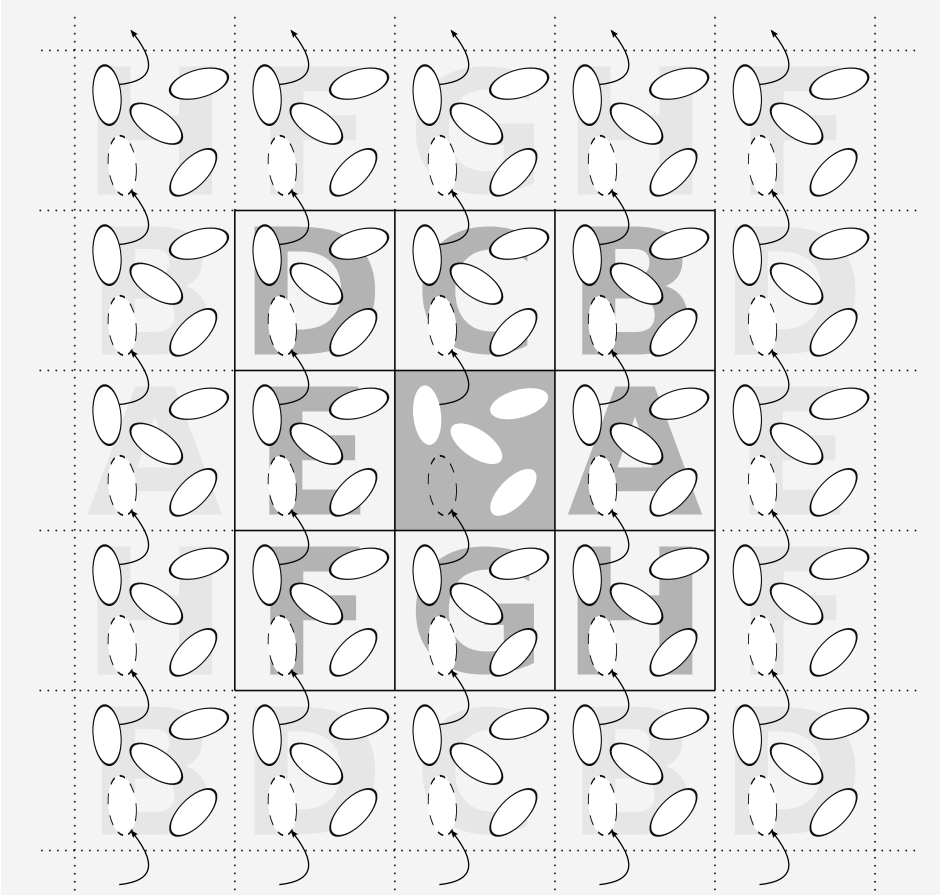

Figure 3.6: In a two-dimensional lattice, nine identical copies of a unit cell are placed symmetrically on Bravais lattice sites. The constituents in those unit-cells have periodic wave functions with periodicity $3L$ in both directions (L is the box size). Because of this periodicity, the constituents in the surface cells not only feel the effect of the particles in the neighbouring cells but also of all the other cells through the periodicity. For instance, the particles in cell A feel the effect of the particles in the central cell and the cells B, C, G and H directly, while an indirect interaction is given through the periodicity of the wave functions of the cells D, E and F.

$\boldsymbol{\ell}_i = (2m+1)\boldsymbol{a}_i$, i.e.

$$\langle \boldsymbol{r} + \boldsymbol{\ell}_1 | w \rangle = \langle \boldsymbol{r} + \boldsymbol{\ell}_2 | w \rangle = \langle \boldsymbol{r} + \boldsymbol{\ell}_3 | w \rangle = \langle \boldsymbol{r} | w \rangle. \tag{3.3}$$

Up to this point, the Born-von Kármán boundary condition is the only condition the single-particle wave functions $|w_i\rangle$ must fulfil. As was indicated in the previous chapter, the single-particle trial states $|q\rangle$ constructed from quantum dressed Gaussian wave packets are ideal for FMD, hence logic states to construct the states $|w\rangle$ from the quantum dressed Gaussian fermion states as

$$|w\rangle = \sum_{n_1 n_2 n_3 = -\infty}^{\infty} \mathcal{T}(n_1\boldsymbol{\ell}_1 + n_2\boldsymbol{\ell}_2 + n_3\boldsymbol{\ell}_3)|q\rangle, \qquad \boldsymbol{\ell}_j = (2m+1)\boldsymbol{a}_j. \tag{3.4}$$

Repeatedly stated so far, since the single particle states are periodic, the FMD trial state $|W\rangle$ will only contain a finite set of $(2m+1)^3 A$ particles.

As was indicated in the previous chapter, the overlap matrix created by the single particle states and its inverse are the key elements in the FMD formalism. Due to the proposed choice of the FMD trial state $|W\rangle$ in accordance with Eq. (3.2), the overlap matrix $\mathbf{N}$ shows a peculiar structure reflecting the double periodicity embedded in the trial state. Due to the systems translational invariance over the Bravais lattice vectors of $\mathfrak{B}$ and the periodicity of the single-particle quantum states, the overlap matrix of the particles in two different Wigner-Seitz cells only depends on their relative displacement. This is seen when investigating the overlap of two systems located on the Bravais lattice points $\boldsymbol{P}$ and $\boldsymbol{Q}$. The block of the overlap matrix which stems from these systems is given by $\mathbf{N}_{\boldsymbol{PQ}}$ and has elements

$$\mathbf{N}_{\boldsymbol{PQ},pq} = \langle w_p|\mathcal{T}^\dagger(\boldsymbol{P})\mathcal{T}(\boldsymbol{Q})|w_q\rangle = \langle w_p|\mathcal{T}(\boldsymbol{Q}-\boldsymbol{P})|w_q\rangle, \tag{3.5}$$

where the spatial overlap is calculated within the Wigner-Seitz cell of the Bravais lattice $\mathfrak{B}_m$ constructed from primitive vectors $\boldsymbol{\ell}_i$. When combining this with the Born-von Kármán boundary conditions, the overlap matrices stemming from cells with an equal modulo displacement become identical and can thus be written as

$$\begin{aligned}\mathbf{N}_{\boldsymbol{PQ},pq} = \mathbf{n}_{\boldsymbol{P}-\boldsymbol{Q},pq} &= \langle w_p|\mathcal{T}(\boldsymbol{Q}-\boldsymbol{P})|w_q\rangle = \langle w_p|\mathcal{T}\left(\boldsymbol{Q}-\boldsymbol{P}\pm\boldsymbol{\ell}_1\right)|w_q\rangle \\ &= \langle w_p|\mathcal{T}\left(\boldsymbol{Q}-\boldsymbol{P}\pm\boldsymbol{\ell}_2\right)|w_q\rangle = \langle w_p|\mathcal{T}\left(\boldsymbol{Q}-\boldsymbol{P}\pm\boldsymbol{\ell}_3\right)|w_q\rangle.\end{aligned} \tag{3.6}$$

Hence, the overlap matrix $\mathbf{N}$, a $(2m+1)^3 \times (2m+1)^3$ block matrix with $A \times A$ blocks, has a single, double or triple block-circulant structure, depending on the number of spatial dimensions. The circulant structure is best understood for one-dimensional TAPBC. The overlap matrix can then be constructed from the sequence of matrices $\{\mathbf{n}_r, r = -m, \ldots, m\}$ with $\mathbf{n}_r$ a complex $A \times A$ matrix representing the overlap of the

unit cell with a replica translated over $\boldsymbol{R} = r\boldsymbol{a}_1$. The matrix $\mathbf{n}_r$ is thus equivalent to $\mathbf{n}_{\boldsymbol{R}}$ and $\mathbf{n}_r \equiv \mathbf{n}_{\boldsymbol{R}} = \mathbf{n}_{\boldsymbol{R}\pm\ell_1}$ because of the Born-von Kármán boundary conditions. Due to the symmetry of the problem, the overlap is bidirectional within its block structure, indicating that the block indices reach both positive and negative values. The overlap matrix $\mathbf{N}$ is represented by

$$\mathbf{N} = \begin{pmatrix} \mathbf{n}_0 & \mathbf{n}_{-1} & \cdots & \mathbf{n}_{1-m} & \mathbf{n}_{-m} & \mathbf{n}_m & \cdots & \mathbf{n}_2 & \mathbf{n}_1 \\ \mathbf{n}_1 & \mathbf{n}_0 & \mathbf{n}_{-1} & \cdots & \mathbf{n}_{1-m} & \mathbf{n}_{-m} & \mathbf{n}_m & \cdots & \mathbf{n}_2 \\ \vdots & \mathbf{n}_1 & \mathbf{n}_0 & \ddots & \vdots & \mathbf{n}_{1-m} & \mathbf{n}_{-m} & \ddots & \vdots \\ \mathbf{n}_{m-1} & \vdots & \ddots & \ddots & \mathbf{n}_{-1} & \vdots & \ddots & \ddots & \mathbf{n}_m \\ \mathbf{n}_m & \mathbf{n}_{m-1} & \cdots & \mathbf{n}_1 & \mathbf{n}_0 & \mathbf{n}_{-1} & \cdots & \mathbf{n}_{1-m} & \mathbf{n}_{-m} \\ \mathbf{n}_{-m} & \mathbf{n}_m & \mathbf{n}_{m-1} & \cdots & \mathbf{n}_1 & \mathbf{n}_0 & \mathbf{n}_{-1} & \cdots & \mathbf{n}_{1-m} \\ \vdots & \mathbf{n}_{-m} & \mathbf{n}_m & \ddots & \vdots & \mathbf{n}_1 & \mathbf{n}_0 & \ddots & \vdots \\ \mathbf{n}_{-2} & \vdots & \ddots & \ddots & \mathbf{n}_{m-1} & \vdots & \ddots & \ddots & \mathbf{n}_{-1} \\ \mathbf{n}_{-1} & \mathbf{n}_{-2} & \cdots & \mathbf{n}_{-m} & \mathbf{n}_m & \mathbf{n}_{m-1} & \cdots & \mathbf{n}_1 & \mathbf{n}_0 \end{pmatrix}. \quad (3.7)$$

The construction of the overlap for higher dimensional TAPBC is explained in Fig. 3.7. Where for one-dimensional TAPBC the Wigner-Seitz cell is periodically displaced, for two-dimensional TAPBC it becomes an entire one-dimensional lattice that is periodically translated. This means that the overlap matrix for two-dimensional TAPBC is created analogously as the one for one-dimensional TAPBC but the block matrices are now $(2m+1)A \times (2m+1)A$ matrices instead of the $A \times A$ blocks for one-dimensional TAPBC. The block matrices for two-dimensional TAPBC themselves will inherit the circulant structure from the one-dimensional TAPBC. Analogous reasoning holds for higher dimensional TAPBC and thus the overlap matrix attains a nested block-circulant structure. Despite the fact that with increasing dimensionality of the problem, the block matrices become larger and larger, $(2m+1)^2A \times (2m+1)^2A$ for a three-dimensional problem, a clear relation exists between the $A \times A$ blocks and a Bravais lattice vector $\boldsymbol{R}$. For the $A \times A$ block $\mathbf{n}_{ijk}$, the index k indicates the k^{th} $(2m+1)^2A$ $\times(2m+1)^2A$ block of the third circulant structure, the index j states that within this block a reference is made to the j^{th} sub-block of dimension $(2m+1)A \times (2m+1)A$. The last index i selects then to the $A \times A$ block within the latter block. Having the construction of the overlap matrix $\mathbf{N}$ in mind, the link is directly made. Block $\mathbf{n}_{ijk}$ refers to the overlap between the particles of the unit-cell and those of a displaced cell over $\boldsymbol{R} = i\boldsymbol{a}_1 + j\boldsymbol{a}_2 + k\boldsymbol{a}_3$ and thus $\mathbf{n}_{ijk} \equiv \mathbf{n}_{\boldsymbol{R}}$.

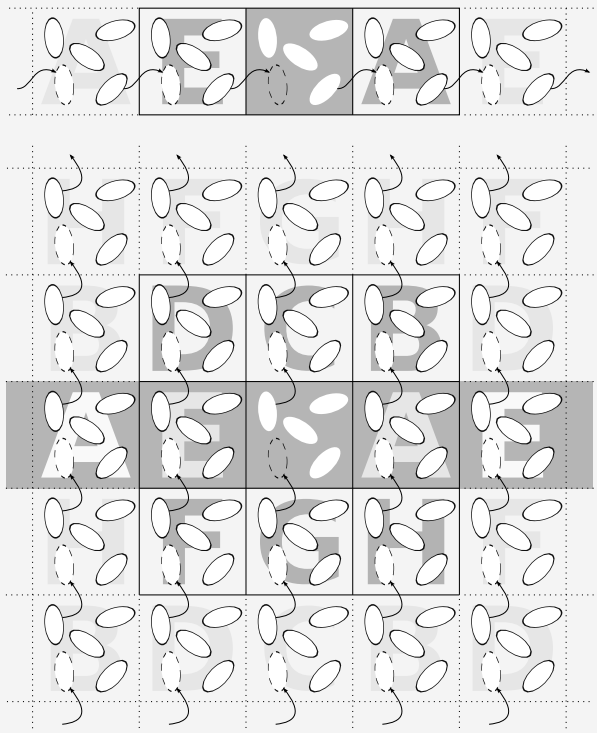

Figure 3.7: In order to create the overlap matrix for two-dimensional TAPBC of first order, it is important to create one-dimensional TAPBC system by translating the Wigner-Seitz cell marked in grey in the top figure. This one-dimensional lattice structure is then used as the seed for the two-dimensional TAPBC where the one-dimensional structure, marked in grey in the lowest figure, is translated over the second primitive lattice vector.

The appearance of such a circulant system, a common special case of Toeplitz systems, is not unexpected. These type of matrices have close connections to Fourier series, see Grenander and Szegö [Gre84] as well as Gray [Gra06], and it is this Fourier-connection which is called for through the periodic structure of the system. The question raised now is how to tackle the problem of inverting this circulant matrix. Inverting the overlap matrix **N** using classic inversion schemes through various matrix decompositions is forcefully discouraged as m tends to infinity for a proper FMD simulation of bulk matter.

Toeplitz systems [Toe11] arise in a variety of application in mathematics, scien-

tific computing as well as engineering and have been meticulously studied. As an analytic scheme to invert Toeplitz matrices is unknown, various algorithms have been devised such that finite linear Toeplitz systems can be solved in an adequate and fast way [Gol96, Cha07]. These algorithms are however not of any interest to this work. Circulant matrices are well known for their analytical properties and can straightforwardly be inverted. In this section, the inversion is introduced by exploiting the periodicity. A meticulous mathematical deduction can be found in appendix F.

As was indicated earlier, the overlap matrix is constructed out of a set of $A \times A$ matrices and has a nested circulant structure. Although each $A \times A$ block of the overlap matrix can be identified by a single integer r or three separate integers i, j, k for a three dimensional problem, it is more convenient to associate with each block an appropriate Bravais lattice vector $\boldsymbol{R}$ of $\mathfrak{B}$. The block related to a Bravais lattice vector $\boldsymbol{R}$ then represents the overlap of the particles from two Wigner-Seitz cells displaced over $\boldsymbol{R}$ as indicated by Eq. (3.6). As the overlap matrix reflects a periodic system, presuppose the existence of a set of matrices $\mathscr{N}_{\boldsymbol{k}}$ representing the discrete Fourier transform (DFT) of the sequence $\{\mathbf{n}_{\boldsymbol{R}}, \boldsymbol{R} \in \{\mathfrak{B}\}_m\}$. As a consequence of the DFT, the vectors $\boldsymbol{k}$ are scaled lattice vectors of the reciprocal lattice $\mathfrak{R}$ of Bravais lattice $\mathfrak{B}$. They are scaled by a factor $2m+1$. The DFT of both sequences can then be written as

$$\mathscr{N}_{\boldsymbol{k}} = \sum_{\boldsymbol{R}\in\{\mathfrak{B}\}_m} \mathbf{n}_{\boldsymbol{R}} e^{-i\boldsymbol{k}\cdot\boldsymbol{R}}, \qquad \mathbf{n}_{\boldsymbol{R}} = \frac{1}{(2m+1)^3} \sum_{\boldsymbol{k}\in\{\mathfrak{R}\}'_m} \mathscr{N}_{\boldsymbol{k}} e^{i\boldsymbol{k}\cdot\boldsymbol{R}}. \tag{3.8}$$

Here $\{\mathfrak{R}\}'_m$ is the set of scaled vectors $\boldsymbol{k}$ confined to the Brillouin zone of $\mathfrak{B}$. In conjunction to the DFT of the overlap matrices and as shown in appendix F, the inverse of $\mathbf{N}$, being $\mathbf{O}$, has an identical nested circulant structure. Hence, a DFT sequence is also known and is related to the original inverse blocks through the relations

$$\boldsymbol{\mathscr{O}}_{\boldsymbol{k}} = \sum_{\boldsymbol{R}\in\{\mathfrak{B}\}_m} \mathbf{o}_{\boldsymbol{R}} e^{-i\boldsymbol{k}\cdot\boldsymbol{R}}, \qquad \mathbf{o}_{\boldsymbol{R}} = \frac{1}{(2m+1)^3} \sum_{\boldsymbol{k}\in\{\mathfrak{R}\}'_m} \boldsymbol{\mathscr{O}}_{\boldsymbol{k}} e^{i\boldsymbol{k}\cdot\boldsymbol{R}}. \tag{3.9}$$

That $\mathbf{N}$ and $\mathbf{O}$ are each others inverse, can readily be confirmed:

$$\begin{aligned}(\mathbf{NO})_{\boldsymbol{PR}} &= \sum_{\boldsymbol{Q}\in\{\mathfrak{B}\}_m} \mathbf{n}_{\boldsymbol{P}-\boldsymbol{Q}} \mathbf{o}_{\boldsymbol{Q}-\boldsymbol{R}} \\ &= \frac{1}{(2m+1)^6} \sum_{\boldsymbol{Q}\in\{\mathfrak{B}\}_m} \sum_{\boldsymbol{k}\boldsymbol{k}'\in\{\mathfrak{R}\}'_m} \mathscr{N}_{\boldsymbol{k}} \boldsymbol{\mathscr{O}}_{\boldsymbol{k}'} e^{i\boldsymbol{k}\cdot(\boldsymbol{P}-\boldsymbol{Q})} e^{i\boldsymbol{k}'\cdot(\boldsymbol{Q}-\boldsymbol{R})} \\ &= \frac{1}{(2m+1)^3} \sum_{\boldsymbol{k}\in\{\mathfrak{R}\}'_m} \mathscr{N}_{\boldsymbol{k}} \boldsymbol{\mathscr{O}}_{\boldsymbol{k}} e^{i\boldsymbol{k}\cdot(\boldsymbol{P}-\boldsymbol{R})} = \mathbf{I}\delta_{\boldsymbol{P},\boldsymbol{R}},\end{aligned} \tag{3.10}$$

where the following relations were used

$$\begin{aligned}
&\mathbf{n}_R = \mathbf{n}_{R\pm\ell_1} = \mathbf{n}_{R\pm\ell_2} = \mathbf{n}_{R\pm\ell_3},\\
&\mathbf{o}_R = \mathbf{o}_{R\pm\ell_1} = \mathbf{o}_{R\pm\ell_2} = \mathbf{o}_{R\pm\ell_3},\\
&\frac{1}{(2m+1)^3}\sum_{\boldsymbol{Q}\in\{\mathfrak{B}\}_m} e^{i\boldsymbol{k}\cdot\boldsymbol{Q}} = \sum_{\boldsymbol{K}\in\mathfrak{K}} \delta_{\boldsymbol{k},\boldsymbol{K}}.
\end{aligned}$$

The last step in Eq. (3.10) only holds when $\mathscr{N}_{\boldsymbol{k}}$ and $\boldsymbol{\mathscr{O}}_{\boldsymbol{k}}$ are each others inverse as shown in appendix F. This can also be verified as

$$\begin{aligned}
\mathscr{N}_{\boldsymbol{k}}\boldsymbol{\mathscr{O}}_{\boldsymbol{k}} &= \sum_{\boldsymbol{P}\boldsymbol{Q}\in\{\mathfrak{B}\}_m} \mathbf{n}_{\boldsymbol{P}}\mathbf{o}_{\boldsymbol{Q}} e^{-i\boldsymbol{k}\cdot(\boldsymbol{P}+\boldsymbol{Q})}\\
&= \sum_{\boldsymbol{P}'\boldsymbol{Q}\in\{\mathfrak{B}\}_m} \mathbf{n}_{\boldsymbol{P}'-\boldsymbol{Q}}\mathbf{o}_{\boldsymbol{Q}} e^{-i\boldsymbol{k}\cdot\boldsymbol{P}'} = \sum_{\boldsymbol{P}'\in\{\mathfrak{B}\}_m} \mathbf{I}\delta_{\boldsymbol{P}',\mathbf{0}} e^{-i\boldsymbol{k}\cdot\boldsymbol{P}'} = \mathbf{I}. \qquad (3.11)
\end{aligned}$$

Thus concluding, the inverse of the overlap matrix $\mathbf{N}$ has an identical circulant structure and can be obtained through their respective reciprocal matrices $\mathscr{N}_{\boldsymbol{k}}$ and $\boldsymbol{\mathscr{O}}_{\boldsymbol{k}}$ which are each other's inverse, i.e.

$$\mathscr{N}_{\boldsymbol{k}}\boldsymbol{\mathscr{O}}_{\boldsymbol{k}} = \boldsymbol{\mathscr{O}}_{\boldsymbol{k}}\mathscr{N}_{\boldsymbol{k}} = \mathbf{I}. \qquad (3.12)$$

The only requirement for this is that all $\mathscr{N}_{\boldsymbol{k}}$ are invertible. Inverting the overlap matrix thus becomes a straightforward procedure. For all $\boldsymbol{k}$ in $\{\mathfrak{K}\}'_m$ calculate the matrices $\mathscr{N}_{\boldsymbol{k}}$ through a DFT of the set $\mathbf{n}_{\boldsymbol{R}}$. Invert each of these matrices creating the sequence $\boldsymbol{\mathscr{O}}_{\boldsymbol{k}}$ and do an inverse DFT to create the $A\times A$ blocks $\mathbf{o}_{\boldsymbol{R}}$ of the inverse overlap matrix $\mathbf{O}$.

As the overlap matrix of the truncated antisymmetric fermion system and its inverse are known, it is easy to obtain expectation values of operators using Eqs. (2.35). Although the complete system contains only a finite set of particles, it is more interesting to exploit the block structure of the matrices that is the result of the periodic tessellation. Translating Eqs. (2.35) into the principle of block multiplication [Gol96], the expectation value of a one-body operator is given by

$$\mathscr{B}_I = \frac{\langle W|\mathcal{B}_I|W\rangle}{\langle W|W\rangle} = \sum_{\boldsymbol{P}\boldsymbol{Q}\in\{\mathfrak{B}\}_m}\sum_{pq=1}^{A} \langle w_p|\mathcal{T}^\dagger(\boldsymbol{P})\mathcal{B}_I\mathcal{T}(\boldsymbol{Q})|w_q\rangle \mathbf{o}_{\boldsymbol{Q}-\boldsymbol{P},qp}. \qquad (3.13)$$

Up to this point, it was tacitly assumed that there are no external fields within the simulation. However when an external field is available, it must have the same periodicity of the system's underlying Bravais lattice $\mathfrak{B}$ otherwise TAPBC cannot be applied. Furthermore, expectation values are independent of the coordinate system of

choice. This means that

$$\begin{aligned}\langle w_p|\mathcal{T}^\dagger(\boldsymbol{P})\mathcal{B}_I\mathcal{T}(\boldsymbol{Q})|w_q\rangle &= \langle w_p|\mathcal{B}_I\mathcal{T}(\boldsymbol{Q}-\boldsymbol{P})|w_q\rangle = \langle w_p|\mathcal{B}_I\mathcal{T}(\boldsymbol{Q}-\boldsymbol{P}\pm\boldsymbol{\ell}_1)|w_q\rangle \\ &= \langle w_p|\mathcal{B}_I\mathcal{T}(\boldsymbol{Q}-\boldsymbol{P}\pm\boldsymbol{\ell}_2)|w_q\rangle = \langle w_p|\mathcal{B}_I\mathcal{T}(\boldsymbol{Q}-\boldsymbol{P}\pm\boldsymbol{\ell}_3)|w_q\rangle, \quad (3.14)\end{aligned}$$

and hence

$$\mathscr{B}_I = \frac{\langle W|\mathcal{B}_I|W\rangle}{\langle W|W\rangle} = \sum_{\boldsymbol{PQ}\in\{\mathfrak{B}\}_m}\sum_{pq=1}^{A}\langle w_p|\mathcal{B}_I\mathcal{T}(\boldsymbol{Q})|w_q\rangle\mathbf{o}_{\boldsymbol{Q},qp}. \quad (3.15)$$

As expected, the expectation values should be expressed per unit-cell. An exception to this reasoning is field operators that depend on the coordinate. For instance the spatial-density operator $\hat{\rho}_{\boldsymbol{x}}$, is such an operator. For these, the density is not expressed per volume cell. There $\langle w_p|\hat{\rho}_{\boldsymbol{x}}|w_q\rangle = \langle \boldsymbol{x}|w_q\rangle\langle w_p|\boldsymbol{x}\rangle$, the full summation must be performed. The density then reads,

$$\begin{aligned}\rho(\boldsymbol{x}) = \frac{\langle W|\hat{\rho}_{\boldsymbol{x}}|W\rangle}{\langle W|W\rangle} &= \sum_{\boldsymbol{PQ}\in\{\mathfrak{B}\}_m}\sum_{pq=1}^{A}\langle \boldsymbol{x}-\boldsymbol{Q}|w_q\rangle\langle w_p|\boldsymbol{x}-\boldsymbol{P}\rangle\mathbf{o}_{\boldsymbol{Q}-\boldsymbol{P},qp}, \\ &= \sum_{\boldsymbol{PQ}'\in\{\mathfrak{B}\}_m}\sum_{pq=1}^{A}\langle \boldsymbol{x}-\boldsymbol{Q}'-\boldsymbol{P}|w_q\rangle\langle w_p|\boldsymbol{x}-\boldsymbol{P}\rangle\mathbf{o}_{\boldsymbol{Q}',qp}. \quad (3.16)\end{aligned}$$

One of the main reasons why the sum over $\boldsymbol{P}$ does not vanish is that the operator is coordinate dependent and thus is influenced by translating the coordinate system.

A similar reasoning can be done regarding the two-body operator even though the periodicity of the operator is created through the periodicity of the single-particle states. The final results for the expectation values of the one- and two-body operators per unit-cell, noted respectively as $\mathscr{B}_{\rho,I}$ and $\mathscr{B}_{\rho,II}$, read

$$\mathscr{B}_{\rho,I} = \sum_{\boldsymbol{Q}\in\{\mathfrak{B}\}_m}\sum_{pq=1}^{A}\langle w_p|\mathcal{B}_I\mathcal{T}(\boldsymbol{Q})|w_q\rangle\mathbf{o}_{\boldsymbol{Q},qp}, \quad (3.17a)$$

$$\begin{aligned}\mathscr{B}_{\rho,II} = \frac{1}{2}\sum_{\boldsymbol{QRS}\in\{\mathfrak{B}\}_m}\sum_{pqrs=1}^{A}&\langle w_p w_r|\mathcal{T}_2^\dagger(\boldsymbol{R})\mathcal{B}_{II}\mathcal{T}_1(\boldsymbol{Q})\mathcal{T}_2(\boldsymbol{R}+\boldsymbol{S})|w_q w_s\rangle \\ &\times(\mathbf{o}_{\boldsymbol{Q},qp}\mathbf{o}_{\boldsymbol{S},sr} - \mathbf{o}_{\boldsymbol{Q}-\boldsymbol{R},qr}\mathbf{o}_{\boldsymbol{R}+\boldsymbol{S},sp}). \quad (3.17b)\end{aligned}$$

Here, in the two-body expectation value, the indices for the translation operators indicate the translation operator acts on the bra- ket-state, w_p or w_q, or on the second,

w_r or w_s. The displacement over $\boldsymbol{R}$ reflects upon the inter-particle distance and truncation would mimic the idea of the nearest image convention in CMD.

To understand how TAPBC manifests itself in the equations of motion of a truncated antisymmetric fermion system, the A particles of the unit-cell and their copies are formally considered as different particles. The entire system is then described by a set of variational parameters given by $\{\boldsymbol{z}_{\boldsymbol{R},1},\ldots,\boldsymbol{z}_{\boldsymbol{R},A};\forall \boldsymbol{R}\in\{\mathfrak{B}\}_m\}$. When evaluating the elements of the metric $\mathbf{C}$ for the variational parameters $\boldsymbol{z}_{\boldsymbol{P},p}$ and $\boldsymbol{z}_{\boldsymbol{Q},q}$, Eq. (2.38) shows that the nested block-circulant structure of the overlap matrix and its inverse is mapped on the metric. The elements of $\mathbf{C}$ are given by

$$\mathbf{C}_{\boldsymbol{PQ},pq}=\left(\frac{\partial^2\mathbf{n}_{\boldsymbol{P}-\boldsymbol{Q},pq}}{\partial\boldsymbol{z}^\star_{\boldsymbol{P},p}\partial\boldsymbol{z}_{\boldsymbol{Q},q}}-\sum_{\boldsymbol{RS}\in\{\mathfrak{B}\}_m}\sum_{rs=1}^{A}\frac{\partial\mathbf{n}_{\boldsymbol{P}-\boldsymbol{R},pr}}{\partial\boldsymbol{z}^\star_{\boldsymbol{P},p}}\cdot\mathbf{o}_{\boldsymbol{R}-\boldsymbol{S},rs}\cdot\frac{\partial\mathbf{n}_{\boldsymbol{S}-\boldsymbol{Q},sq}}{\partial\boldsymbol{z}_{\boldsymbol{Q},q}}\right)\cdot\mathbf{o}_{\boldsymbol{Q}-\boldsymbol{P},qp}. \tag{3.18}$$

As a result of the translational invariance of the system over any Bravais lattice vector of $\mathfrak{B}$, this leads to $\mathbf{C}_{\boldsymbol{PQ},pq}=\mathbf{C}_{\boldsymbol{P}'\boldsymbol{Q}',pq}\equiv\mathbf{C}_{\boldsymbol{P}-\boldsymbol{Q},pq}$, with $\boldsymbol{P}-\boldsymbol{Q}=\boldsymbol{P}'-\boldsymbol{Q}'$. The equations of motion now become

$$i\sum_{\boldsymbol{R}\in\{\mathfrak{B}\}_m}\mathbf{C}_{\boldsymbol{P}-\boldsymbol{R}}\dot{\boldsymbol{z}}_{\boldsymbol{R}}=\frac{\partial\mathscr{H}}{\partial\boldsymbol{z}^\star_{\boldsymbol{P}}}\qquad\forall\boldsymbol{P}\in\{\mathfrak{B}\}_m, \tag{3.19}$$

in which $\mathbf{C}_{\boldsymbol{R}}=\mathbf{C}_{\boldsymbol{R}\pm\boldsymbol{\ell}_1}=\mathbf{C}_{\boldsymbol{R}\pm\boldsymbol{\ell}_2}=\mathbf{C}_{\boldsymbol{R}\pm\boldsymbol{\ell}_3}$.

Given that the system is created with two periodicities that complement each other, a finite one in the configuration and an infinite one in the single-particle states, the system is translational invariant. This translational invariance manifests itself into the metric $\mathbf{C}$, but should also appear in the Hamiltonian force of the system. Combining Eqs. (3.14) and (3.17) it is readily seen that

$$\frac{\partial\mathscr{H}}{\partial\boldsymbol{z}^\star_{\boldsymbol{P},p}}=\frac{\partial\mathscr{H}}{\partial\boldsymbol{z}^\star_{\boldsymbol{P}',p}}\equiv\frac{\partial\mathscr{H}_\rho}{\partial\boldsymbol{z}^\star_p},$$

confirming the translational invariance of the system. When evaluating Eq. (3.19) for all lattice vectors $\boldsymbol{P}$, the set of equation only holds when $\dot{\boldsymbol{z}}_{\boldsymbol{P}}=\dot{\boldsymbol{z}}_{\boldsymbol{P}'}\equiv\dot{\boldsymbol{z}}$. This equivalence implicates that when a fermion system is subjected to TAPBC, the motion of a single particle matches that of its images.

When embedding these equivalences in the equation of motion, the system's evolution can be described by a new reduced equation of motion,

$$i\mathbf{C}_\rho\cdot\dot{\boldsymbol{z}}=\frac{\partial\mathscr{H}_\rho}{\partial\boldsymbol{z}^\star}, \tag{3.20}$$

where the metric of the periodic fermion system $\mathbf{C}_\rho$ is given by

$$\begin{aligned}\mathbf{C}_{\rho,pq} &= \sum_{\boldsymbol{Q}\in\{\mathfrak{B}\}_m} \mathbf{C}_{\boldsymbol{Q},pq} \\ &= \sum_{\boldsymbol{Q}\in\{\mathfrak{B}\}_m} \left(\frac{\partial^2 \mathbf{n}_{-\boldsymbol{Q},pq}}{\partial \boldsymbol{z}_p^\star \partial \boldsymbol{z}_q} - \sum_{\boldsymbol{RS}\in\{\mathfrak{B}\}_m} \sum_{rs=1}^{A} \frac{\partial \mathbf{n}_{-\boldsymbol{R},pr}}{\partial \boldsymbol{z}_p^\star} \cdot \mathbf{o}_{\boldsymbol{R}-\boldsymbol{S},rs} \cdot \frac{\partial \mathbf{n}_{\boldsymbol{S}-\boldsymbol{Q},sq}}{\partial \boldsymbol{z}_q} \right) \cdot \mathbf{o}_{\boldsymbol{Q},qp}.\end{aligned} \tag{3.21}$$

The gradients of the system can then be deduced from Eqs. (3.17) and read

$$\frac{\partial \mathscr{B}_I}{\partial z_i^\star} = \frac{\partial \mathscr{B}_I}{\partial z_{\mu a}^\star} = \sum_{q=1}^{A} \frac{\partial}{\partial z_{\mu a}^\star} \langle q_a^\partial | \mathcal{B}_I | q_q \rangle \mathbf{o}_{qa} - \sum_{pqr=1}^{A} \langle q_p | \mathcal{B}_I | q_q \rangle \mathbf{o}_{qa} \cdot \frac{\partial \mathbf{n}_{ar}}{\partial z_{\mu a}^\star} \cdot \mathbf{o}_{rp}, \tag{3.22a}$$

$$\begin{aligned}\frac{\partial \mathscr{B}_{II}}{\partial z_i^\star} = \frac{\partial \mathscr{B}_{II}}{\partial z_{\mu a}^\star} &= \sum_{qrs=1}^{A} \frac{\partial}{\partial z_{\mu a}^\star} \langle q_a^\partial q_r | \mathcal{B}_{II} | q_q q_s \rangle (\mathbf{o}_{qa}\mathbf{o}_{sr} - \mathbf{o}_{qr}\mathbf{o}_{sa}) \\ &\quad - \sum_{pqrst=1}^{A} \langle q_p q_r | \mathcal{B}_{II} | q_q q_s \rangle \mathbf{o}_{qa} \cdot \frac{\partial \mathbf{n}_{at}}{\partial z_{\mu a}^\star} \cdot (\mathbf{o}_{tp}\mathbf{o}_{sr} - \mathbf{o}_{tr}\mathbf{o}_{sp}).\end{aligned} \tag{3.22b}$$

In chapter 2, it was shown that the overlap matrix **N** and its inverse **O** carry the information about the wave-mechanical and statistical properties of the fermions. Periodic boundary conditions are fundamental for the study of bulk properties of fermions but lead to infinite structures. To resolve this infinite problem and achieve a better understanding of the effects of periodic boundary conditions, this section introduced the concept of truncated antisymmetric periodic boundary conditions. A configuration of single-particles was periodically placed in a known volume and antisymmetrised. The antisymmetrised state itself was then used to tessellate space. This construction shows a perfect tessellation of space by means of the single-particle states. However, the antisymmetrisation itself only acts within a small region of space, hence appearing to be truncated. The overlap matrix of such a system reflects a nested block-circulant structure and is easily inverted by means of discrete Fourier transforms. Using block multiplications, the cell structure of the system was preserved in the calculations of expectation values of operators as well as in the equations of motion of the system. For the latter it was also shown that each copy behaves identically.

Obtaining the inverse overlap matrix is straightforward but computationally intensive. Two multidimensional DFTs require a lot of computational effort, even when using fast Fourier transforms. In order to reduce the overhead, the inverse matrix

elements must be stored in memory. This way, the same overlap matrices are not reevaluated repeatedly. Unfortunately, the amount of available memory is also finite and grows gradually with increasing order of TAPBC. As will be indicated later, the higher the order, the closer the TAPBC comes to PBC but the more memory is needed and hence the smaller the number of particles that can be used in the simulation. Moreover, more computation time is needed for the calculation of the inverse overlap matrix. As always, from a numerical point of view, a choice between the devil and the deep blue sea has to be made, that is to say speed versus memory consumption. A way to get out of this treacherous behaviour is by performing the evaluations in the Bloch representation.

Section 3.4 The Bloch representation of TAPBC

As was indicated earlier, periodic problems in quantum mechanics are described using Bloch states or Wannier states. These dual states can address questions concerning the behaviour of periodic systems in lattice-momentum (or reciprocal) space as well as lattice-coordinate (or Bravais) space. When assuming that $|w\rangle$ are unnormalised representations of Wannier states, it is easily shown that $|\omega_{\boldsymbol{k}}\rangle$ constructed as

$$|\omega_{\boldsymbol{k}}\rangle = \sum_{\boldsymbol{R}\in\{\mathfrak{B}\}_m} e^{i\boldsymbol{k}\cdot\boldsymbol{R}}\mathcal{T}(\boldsymbol{R})|w\rangle, \tag{3.23}$$

fulfils the Bloch condition for Bravais lattice vectors of $\mathfrak{B}$. As a result of the Born-von Kármán boundary conditions, the lattice momenta $\boldsymbol{k}$ are quantised as the reciprocal lattice vectors of $\mathfrak{B}_m$. The overlap of two such Bloch states constructed from Wannier states can be calculated within the Wigner-Seitz cell of $\mathfrak{B}_m$ and is given by

$$\langle \boldsymbol{k}, \omega_p|\boldsymbol{k}, \omega_q\rangle = \sum_{\boldsymbol{R}\in\{\mathfrak{B}\}_m} e^{i\boldsymbol{k}\cdot\boldsymbol{R}}\langle w_p|\mathcal{T}(\boldsymbol{R})|w_q\rangle = \sum_{\boldsymbol{R}\in\{\mathfrak{B}\}_m} e^{i\boldsymbol{k}\cdot\boldsymbol{R}}\mathbf{n}_{-\boldsymbol{R},pq}. \tag{3.24}$$

From this it can be concluded that the matrices $\mathcal{N}_{\boldsymbol{k}}$ represent the overlap of Bloch states built up as running waves from periodic single-particle states.

As evaluating expectation values, metrics and Hamiltonian forces in the classic FMD way is computationally demanding, it is favourable if one of the DFTs can be avoided. To accomplish this, discrete Fourier transforms are calculated from the operators and are representations of expectation values of the Bloch states. When $\mathscr{B}_{I,\boldsymbol{k}}$ and $\mathscr{B}_{II,\boldsymbol{k}_1\boldsymbol{k}_2,\boldsymbol{R}}$ are defined as the expectation values of single-particle Bloch states

obtained through

$$\mathscr{B}_{I,\boldsymbol{k},pq} = \sum_{\boldsymbol{Q}\in\{\mathfrak{B}\}_m} \langle w_p|\mathcal{B}_I\mathcal{T}(\boldsymbol{Q})|w_q\rangle e^{i\boldsymbol{k}\cdot\boldsymbol{Q}}, \tag{3.25a}$$

$$\mathscr{B}_{II,\boldsymbol{k}_1\boldsymbol{k}_2,\boldsymbol{R},pqrs} = \sum_{\boldsymbol{QS}\in\{\mathfrak{B}\}_m} \langle w_p w_r|\mathcal{T}_2^\dagger(\boldsymbol{R})\mathcal{B}_{II}\mathcal{T}_1(\boldsymbol{Q})\mathcal{T}_2(\boldsymbol{R}+\boldsymbol{S})|w_q w_s\rangle e^{i\boldsymbol{k}_1\cdot\boldsymbol{Q}} e^{i\boldsymbol{k}_2\cdot\boldsymbol{S}}, \tag{3.25b}$$

the matrix elements in the Wannier representation are regained through the inverse DFT and hence

$$\langle w_p|\mathcal{B}_I\mathcal{T}(\boldsymbol{Q})|w_q\rangle = \frac{1}{(2m+1)^3} \sum_{\boldsymbol{k}\in\{\mathfrak{R}\}'_m} \mathscr{B}_{I,\boldsymbol{k},pq} e^{-i\boldsymbol{k}\cdot\boldsymbol{Q}}, \tag{3.26a}$$

$$\langle w_p w_r|\mathcal{T}_2^\dagger(\boldsymbol{R})\mathcal{B}_{II}\mathcal{T}_1(\boldsymbol{Q})\mathcal{T}_2(\boldsymbol{R}+\boldsymbol{S})|w_q w_s\rangle = \frac{1}{(2m+1)^6} \sum_{\boldsymbol{k}_1\boldsymbol{k}_2\in\{\mathfrak{R}\}'_m} \mathscr{B}_{II,\boldsymbol{k}_1\boldsymbol{k}_2,\boldsymbol{R},pqrs} e^{-i\boldsymbol{k}_1\cdot\boldsymbol{Q}} e^{-i\boldsymbol{k}_2\cdot\boldsymbol{S}}. \tag{3.26b}$$

When combining Eqs. (3.9) and Eqs. (3.26) into Eqs. (3.17) a more elegant result is found for the expectation value per unit cell. After merging the exponents together into the Fourier-decomposition of the periodic delta,

$$\sum_{\boldsymbol{R}\in\{\mathfrak{B}\}_m} e^{i\boldsymbol{k}\cdot\boldsymbol{R}} = (2m+1)^3 \sum_{\boldsymbol{K}\in\mathfrak{R}} \delta_{\boldsymbol{K},\boldsymbol{k}},$$

the expectation values per volume unit-cell are given by

$$\mathscr{B}_{\rho,I} = \frac{1}{(2m+1)^3} \sum_{\boldsymbol{k}\in\{\mathfrak{R}\}'_m} \sum_{pq=1}^{A} \mathscr{B}_{I,\boldsymbol{k},pq} \boldsymbol{\mathcal{O}}_{\boldsymbol{k},qp}, \tag{3.27a}$$

$$\mathscr{B}_{\rho,II} = \frac{1}{2(2m+1)^6} \sum_{\boldsymbol{k}_1\boldsymbol{k}_2\in\{\mathfrak{R}\}'_m} \sum_{\boldsymbol{R}\in\{\mathfrak{B}\}_m} \sum_{pqrs=1}^{A} \mathscr{B}_{II,\boldsymbol{k}_1\boldsymbol{k}_2,\boldsymbol{R},pqrs} \times \left[\boldsymbol{\mathcal{O}}_{\boldsymbol{k}_1,qp}\boldsymbol{\mathcal{O}}_{\boldsymbol{k}_2,sr} - \boldsymbol{\mathcal{O}}_{\boldsymbol{k}_1,qr}\boldsymbol{\mathcal{O}}_{\boldsymbol{k}_2,sp} e^{i\boldsymbol{R}\cdot(\boldsymbol{k}_2-\boldsymbol{k}_1)}\right]. \tag{3.27b}$$

As was indicated earlier, one-body field operators are not expressed per unit cell. Disregarding this, an analogous Bloch representation is obtained. With respect to the spatial density according to Eq. (3.16), the Bloch-like representation $\boldsymbol{\varrho}_{\boldsymbol{x},\boldsymbol{P},\boldsymbol{k},pq}$ can be defined as

$$\boldsymbol{\varrho}_{\boldsymbol{x},\boldsymbol{P},\boldsymbol{k},pq} = \sum_{\boldsymbol{Q}\in\{\mathfrak{B}\}_m} \langle \boldsymbol{x}-\boldsymbol{P}-\boldsymbol{Q}|w_q\rangle\langle w_p|\boldsymbol{x}-\boldsymbol{P}\rangle e^{i\boldsymbol{k}\cdot\boldsymbol{Q}}, \tag{3.28a}$$

and leads to the density

$$\rho(\boldsymbol{x}) = \frac{1}{(2m+1)^3} \sum_{\boldsymbol{k}\in\{\mathfrak{R}\}'_m} \sum_{\boldsymbol{P}\in\{\mathfrak{B}\}_m} \sum_{pq=1}^{A} \boldsymbol{\varrho}_{\boldsymbol{x},\boldsymbol{P},\boldsymbol{k},pq} \boldsymbol{\mathcal{O}}_{\boldsymbol{k},qp}. \tag{3.28b}$$

An identical reduction can be performed for the metric of the system and the Hamiltonian forces. They transform into

$$\mathbf{C}_{\rho,pq} = \frac{1}{(2m+1)^3} \sum_{\boldsymbol{k}\in\{\mathfrak{R}\}'_m} \left(\frac{\partial^2 \mathcal{N}_{\boldsymbol{k},pq}}{\partial \boldsymbol{z}_p^\star \partial \boldsymbol{z}_q} - \sum_{rs=1}^{A} \frac{\partial \mathcal{N}_{\boldsymbol{k},pr}}{\partial \boldsymbol{z}_p^\star} \cdot \boldsymbol{\mathcal{O}}_{\boldsymbol{k},rs} \cdot \frac{\partial \mathcal{N}_{\boldsymbol{k},sq}}{\partial \boldsymbol{z}_q} \right) \cdot \boldsymbol{\mathcal{O}}_{\boldsymbol{k},qp}. \tag{3.29}$$

and

$$\begin{aligned} \frac{\partial \mathscr{B}_{\rho,I}}{\partial \boldsymbol{z}_a^\star} = {} & \frac{1}{(2m+1)^3} \sum_{\boldsymbol{k}\in\{\mathfrak{R}\}'_m} \sum_{q=1}^{A} \frac{\partial}{\partial \boldsymbol{z}_a^\star} \mathscr{B}_{I,\boldsymbol{k},aq} \boldsymbol{\mathcal{O}}_{\boldsymbol{k},qa} \\ & - \frac{1}{(2m+1)^3} \sum_{\boldsymbol{k}\in\{\mathfrak{R}\}'_m} \sum_{pqr=1}^{A} \mathscr{B}_{I,\boldsymbol{k},pq} \boldsymbol{\mathcal{O}}_{\boldsymbol{k},qa} \cdot \frac{\partial \mathcal{N}_{\boldsymbol{k},ar}}{\partial \boldsymbol{z}_a^\star} \cdot \boldsymbol{\mathcal{O}}_{\boldsymbol{k},rp}, \end{aligned} \tag{3.30a}$$

$$\begin{aligned} \frac{\partial \mathscr{B}_{\rho,II}}{\partial \boldsymbol{z}_a^\star} = {} & \frac{1}{(2m+1)^6} \sum_{\boldsymbol{k}_1\boldsymbol{k}_2\in\{\mathfrak{R}\}'_m} \sum_{\boldsymbol{R}\in\{\mathfrak{B}\}_m} \sum_{qrs=1}^{A} \frac{\partial}{\partial \boldsymbol{z}_a^\star} \mathscr{B}_{II,\boldsymbol{k}_1\boldsymbol{k}_2,\boldsymbol{R},aqrs} \\ & \times \left(\boldsymbol{\mathcal{O}}_{\boldsymbol{k}_1,qa} \boldsymbol{\mathcal{O}}_{\boldsymbol{k}_2,sr} - \boldsymbol{\mathcal{O}}_{\boldsymbol{k}_1,qr} \boldsymbol{\mathcal{O}}_{\boldsymbol{k}_2,sa} e^{i\boldsymbol{R}\cdot(\boldsymbol{k}_2-\boldsymbol{k}_1)} \right) \\ & - \frac{1}{(2m+1)^6} \sum_{\boldsymbol{k}_1\boldsymbol{k}_2\in\{\mathfrak{R}\}'_m} \sum_{\boldsymbol{R}\in\{\mathfrak{B}\}_m} \sum_{pqrst=1}^{A} \mathscr{B}_{II,\boldsymbol{k}_1\boldsymbol{k}_2,\boldsymbol{R},pqrs} \boldsymbol{\mathcal{O}}_{\boldsymbol{k}_1,qa} \cdot \frac{\partial \mathcal{N}_{\boldsymbol{k}_1,at}}{\partial \boldsymbol{z}_a^\star} \\ & \times \left(\boldsymbol{\mathcal{O}}_{\boldsymbol{k}_1,tp} \boldsymbol{\mathcal{O}}_{\boldsymbol{k}_2,sr} - \boldsymbol{\mathcal{O}}_{\boldsymbol{k}_1,tr} \boldsymbol{\mathcal{O}}_{\boldsymbol{k}_2,sp} e^{\boldsymbol{R}\cdot(\boldsymbol{k}_2-\boldsymbol{k}_1)} \right). \end{aligned} \tag{3.30b}$$

Hence, evaluating expectation values, the metric and the various Hamiltonian gradients is computationally more favourable in the Bloch representation than in the Wannier representation introduced in the previous section. As it is not necessary to calculate the inverse overlap rigorously, the inverse DFT does not need to be performed. This has as consequence that calculations of the metric and one-body operators can be done straightforwardly without the need to evaluate the same block from the inverse overlap several times. For the two-body operators, it is still required to evaluate inverse overlap matrices in Bloch space several times, however, the calculation is more manageable than in the Wannier representation. The Bloch representation is therefore preferred over the Wannier representation.

Section 3.5 Periodic boundary conditions in FMD

In the previous sections, TAPBC was introduced as a finite set of periodically placed single particle states that were antisymmetrised. This antisymmetrisation acted only in a limited volume of space. The antisymmetrised state itself is periodically replicated throughout the entire space. When studying the equations of motion of this peculiar fermion system, it became evident that each particle and all its clones undergo an identical time-evolution. Although a straightforward adaptation of the FMD technique seemed possible, it resulted in a procedure in which a lot of computational overhead is created. This was largely resolved by evaluating the relevant quantities in the Bloch representation.

In contrast to TAPBC of finite order m, there is no truncation of the antisymmetry in perfect PBC and the unit-cell does not tessellate a finite volume but entire space. In PBC, if the underlying Bravais lattice of the tessellation is $\mathfrak{B}$, the FMD trial state of the infinite fermion system can be written as

$$|Q\rangle = \mathcal{A} \bigotimes_{\boldsymbol{R}\in\mathfrak{B}} \mathcal{T}(\boldsymbol{R})|q_1\rangle \otimes \cdots \otimes |q_A\rangle. \tag{3.31}$$

Comparing this with Eqs. (3.2) and (3.4) it is obvious that the FMD trial states of PBC and TAPBC of infinite order are equivalent. Since the single particle states can be normalised, they are asymptotically zero in coordinate space, that is to say

$$\lim_{\boldsymbol{x}\to\infty} \langle \boldsymbol{x}|q\rangle = 0,$$

which indicates that

$$\lim_{m\to\infty} |w\rangle = |q\rangle, \qquad \text{and} \qquad \lim_{m\to\infty} |W\rangle = |Q\rangle.$$

This equivalence could be argued against since $|w\rangle$ is periodic for finite m. The reasoning, however, is similar to that of obtaining Fourier transformations as the limit of Fourier series where the latter is done on periodic functions and the former not. Finally, in TAPBC the normalisation of the single particle states was done in the Wigner-Seitz cell of $\mathfrak{B}_m$. In the limit for m representing infinity, however, this volume equals the complete coordinate space.

Even though the FMD trial states created by PBC or TAPBC are equivalent, the structure of the overlap matrix is slightly different. In contrast to TAPBC where the overlap matrix has a nested block-circulant structure it now obtains a nested block-Toeplitz structure. In truncated form for the one-dimensional case, for which the FMD

trial state is given by

$$|Q\rangle = \mathcal{A} \bigotimes_{\boldsymbol{R}\in\{\mathfrak{B}\}_m} \mathcal{T}(\boldsymbol{R})|q_1\rangle \otimes \cdots \otimes |q_A\rangle,$$

the overlap matrix can be represented as

$$\mathbf{N} = \begin{pmatrix}
\mathbf{n}_0 & \mathbf{n}_{-1} & \cdots & \mathbf{n}_{1-m} & \mathbf{n}_{-m} & \mathbf{n}_{-m-1} & \cdots & \mathbf{n}_{-2m+1} & \mathbf{n}_{-2m} \\
\mathbf{n}_1 & \mathbf{n}_0 & \mathbf{n}_{-1} & \cdots & \mathbf{n}_{1-m} & \mathbf{n}_{-m} & \mathbf{n}_{-m-1} & \cdots & \mathbf{n}_{-2m+1} \\
\vdots & \mathbf{n}_1 & \mathbf{n}_0 & \ddots & \vdots & \mathbf{n}_{1-m} & \mathbf{n}_{-m} & \ddots & \vdots \\
\mathbf{n}_{m-1} & \vdots & \ddots & \ddots & \mathbf{n}_{-1} & \vdots & \ddots & \ddots & \mathbf{n}_{-m-1} \\
\mathbf{n}_m & \mathbf{n}_{m-1} & \cdots & \mathbf{n}_1 & \mathbf{n}_0 & \mathbf{n}_{-1} & \cdots & \mathbf{n}_{1-m} & \mathbf{n}_{-m} \\
\mathbf{n}_{m+1} & \mathbf{n}_m & \mathbf{n}_{m-1} & \cdots & \mathbf{n}_1 & \mathbf{n}_0 & \mathbf{n}_{-1} & \cdots & \mathbf{n}_{1-m} \\
\vdots & \mathbf{n}_{m+1} & \mathbf{n}_m & \ddots & \vdots & \mathbf{n}_1 & \mathbf{n}_0 & \ddots & \vdots \\
\mathbf{n}_{2m-1} & \vdots & \ddots & \ddots & \mathbf{n}_{m-1} & \vdots & \ddots & \ddots & \mathbf{n}_{-1} \\
\mathbf{n}_{2m} & \mathbf{n}_{2m-1} & \cdots & \mathbf{n}_{m+1} & \mathbf{n}_m & \mathbf{n}_{m-1} & \cdots & \mathbf{n}_1 & \mathbf{n}_0
\end{pmatrix}. \tag{3.32}$$

Here, each block $\mathbf{n}_R$ is a complex $A\times A$ matrix representing the overlap of the unit cell with a copy translated over $\boldsymbol{R} = R\boldsymbol{a}_1$. A clear discrepancy between the overlap matrices from truncated PBC and TAPBC in one dimension is visible near the upper right and lower left corners of the matrix when comparing Eqs. (3.7) and (3.32). In order to obtain the overlap matrix for higher dimensional periodicity, an identical approach is taken as with the nested circulant structure where each block is referenced by a Bravais lattice vector. Remark that the truncated form is of no interest to this work and only the limit for m going to infinity is.

The problem of inverting such a matrix arose in the work of Brink and Castro in their study of an Alpha-cluster model for nuclear matter [Bri73]. Gaussian wave packets, depicting the alpha particles are placed on a well-defined lattice. By exploiting the extensive symmetry of this lattice, translational and rotational, and handling only nearest neighbours, the inversion problem was reduced to a finite-sized tractable approximate computation. Unfortunately this approach cannot be used here as in the FMD approach a set of particles is placed in a lattice cell, loosing rotational symmetry and the particular one-body description.

As was indicated earlier, Toeplitz systems in general have no specific analytical solution. However, because of the infinite limit, it can be confirmed that the overlap matrix of the FMD trial state subject to PBC or TAPBC of infinite order have identical inverses. To confirm this, a slight adaptation to the formula regarding the overlap matrix and its inverse of TAPBC, i.e. Eqs. (3.8), (3.9) and (3.12), is required. The overlap matrix in the Wannier representation and the ones in the Bloch representation are related as

$$\mathcal{N}(\boldsymbol{k}) = \sum_{\boldsymbol{R}\in\mathfrak{B}} \mathbf{n}_{\boldsymbol{R}} e^{-i\boldsymbol{k}\cdot\boldsymbol{R}}, \qquad \mathbf{n}_{\boldsymbol{R}} = \frac{1}{V_{BZ}} \int_{BZ} \mathcal{N}(\boldsymbol{k}) e^{i\boldsymbol{k}\cdot\boldsymbol{R}} d\boldsymbol{k}, \tag{3.33}$$

and is nothing more than taking the limit for $m \to \infty$ of Eqs. (3.8). The integration is contained within the first Brillouin zone of the lattice. Here, the overlap $\mathbf{n}_{\boldsymbol{R},pq}$ is given by Eq. (3.8) as $\langle q_p|\mathcal{T}(-\boldsymbol{R})|q_q\rangle$. The inverse overlap matrix can then be obtained through

$$\mathbf{o}_{\boldsymbol{R}} = \frac{1}{V_{BZ}} \int_{BZ} \boldsymbol{\mathcal{O}}(\boldsymbol{k}) e^{i\boldsymbol{k}\cdot\boldsymbol{R}} d\boldsymbol{k} \qquad \text{with} \qquad \boldsymbol{\mathcal{O}}(\boldsymbol{k}) = \mathcal{N}(\boldsymbol{k})^{-1}. \tag{3.34}$$

In these formulae, as a result of the infinite order of TAPBC, the lattice momenta $\boldsymbol{k}$ are not quantised anymore but allowed to have all values within the first Brillouin zone of the Bravais lattice $\mathfrak{B}$.

Using these equations, it can be confirmed that $\mathbf{N}$ and $\mathbf{O}$ are each others inverse

$$\begin{aligned}
(\mathbf{NO})_{\boldsymbol{PR}} &= \sum_{\boldsymbol{Q}\in\mathfrak{B}} \mathbf{N}_{\boldsymbol{PQ}} \mathbf{O}_{\boldsymbol{QR}} = \sum_{\boldsymbol{Q}\in\mathfrak{B}} \mathbf{n}_{\boldsymbol{P}-\boldsymbol{Q}} \mathbf{o}_{\boldsymbol{Q}-\boldsymbol{R}} \\
&= \frac{1}{V_{BZ}^2} \iint_{BZ\otimes BZ} \sum_{\boldsymbol{Q}\in\mathfrak{B}} \mathcal{N}(\boldsymbol{k}) \boldsymbol{\mathcal{O}}(\boldsymbol{k}') e^{i\boldsymbol{k}\cdot(\boldsymbol{P}-\boldsymbol{Q})} e^{i\boldsymbol{k}'\cdot(\boldsymbol{Q}-\boldsymbol{R})} d\boldsymbol{k} d\boldsymbol{k}' \\
&= \frac{1}{V_{BZ}} \int_{BZ} \mathcal{N}(\boldsymbol{k}) \boldsymbol{\mathcal{O}}(\boldsymbol{k}) e^{i\boldsymbol{k}\cdot(\boldsymbol{P}-\boldsymbol{R})} d\boldsymbol{k} \\
&= \mathbf{I}\delta_{\boldsymbol{P},\boldsymbol{R}}.
\end{aligned}$$

It is thus straightforward that in order to accomplish PBC in FMD the formula of TAPBC must be obtained for TAPBC of infinite order. All formula can thus be adjusted by means of the following transformations

$$\sum_{\boldsymbol{R}\in\{\mathfrak{B}\}_m} \to \sum_{\boldsymbol{R}\in\mathfrak{B}}, \qquad \frac{1}{(2m+1)^3} \sum_{\boldsymbol{k}\in\{\mathfrak{R}\}'_m} \to \frac{1}{V_{BZ}} \int_{BZ} d\boldsymbol{k}. \tag{3.35}$$

In this way the expectation values of operators per unit cell are obtained as

$$\mathscr{B}_{\rho,I} = \frac{1}{V_{BZ}} \int_{BZ} \sum_{pq=1}^{A} \mathscr{B}_{I,pq}(\boldsymbol{k}) \boldsymbol{\mathcal{O}}_{qp}(\boldsymbol{k}) d\boldsymbol{k}, \tag{3.36a}$$

$$\begin{aligned}\mathscr{B}_{\rho,II} = \frac{1}{2V_{BZ}^2} \iint_{BZ\otimes BZ} \sum_{\boldsymbol{R}\in\mathfrak{B}} \sum_{pqrs=1}^{A} \mathscr{B}_{II,\boldsymbol{R},pqrs}(\boldsymbol{k}_1,\boldsymbol{k}_2) \\ \times \left[\boldsymbol{\mathcal{O}}_{qp}(\boldsymbol{k}_1)\boldsymbol{\mathcal{O}}_{sr}(\boldsymbol{k}_2) - \boldsymbol{\mathcal{O}}_{qr}(\boldsymbol{k}_1)\boldsymbol{\mathcal{O}}_{sp}(\boldsymbol{k}_2) e^{i\boldsymbol{R}\cdot(\boldsymbol{k}_2-\boldsymbol{k}_1)}\right] d\boldsymbol{k}_1 d\boldsymbol{k}_2.\end{aligned} \tag{3.36b}$$

In order to accomplish this, the expectation values of the Bloch states are required. These are obtained by means of lattice summations and are written as

$$\mathscr{B}_{I,pq}(\boldsymbol{k}) = \sum_{\boldsymbol{Q}\in\mathfrak{B}} \langle q_p|\mathcal{B}_I \mathcal{T}(\boldsymbol{Q})|q_q\rangle e^{i\boldsymbol{k}\cdot\boldsymbol{Q}}, \tag{3.37a}$$

$$\mathscr{B}_{II,\boldsymbol{R},pqrs}(\boldsymbol{k}_1,\boldsymbol{k}_2) = \sum_{\boldsymbol{QS}\in\mathfrak{B}} \langle q_p q_r|\mathcal{T}_2^{\dagger}(\boldsymbol{R})\mathcal{B}_{II}\mathcal{T}_1(\boldsymbol{Q})\mathcal{T}_2(\boldsymbol{R}+\boldsymbol{S})|q_q q_s\rangle e^{i\boldsymbol{k}_1\cdot\boldsymbol{Q}} e^{i\boldsymbol{k}_2\cdot\boldsymbol{S}}. \tag{3.37b}$$

With the proper choice of the volume size of the Wigner-Seitz cells and the spatial spread of the particles, these Bloch representations converge quickly.

As was already mentioned in the previous section, the above one-body definitions do not hold for expectation values of fields like the spatial density. These are given, as the infinite limit of the order m of Eq. (3.28), by

$$\rho(\boldsymbol{x}) = \frac{1}{V_{BZ}} \sum_{\boldsymbol{P}\in\mathfrak{B}} \int_{BZ} \sum_{pq=1}^{A} \boldsymbol{\varrho}_{\boldsymbol{x},\boldsymbol{P},pq}(\boldsymbol{k}) \boldsymbol{\mathcal{O}}_{qp}(\boldsymbol{k}) d\boldsymbol{k}, \tag{3.38a}$$

with

$$\boldsymbol{\varrho}_{\boldsymbol{x},\boldsymbol{P},pq}(\boldsymbol{k}) = \sum_{\boldsymbol{Q}\in\mathfrak{B}} \langle \boldsymbol{x}-\boldsymbol{P}-\boldsymbol{Q}|q_q\rangle\langle q_p|\boldsymbol{x}-\boldsymbol{P}\rangle e^{i\boldsymbol{k}\cdot\boldsymbol{Q}}. \tag{3.38b}$$

A similar adaptation can be obtained for the equations of motion in FMD. Without much difficulty, the result reads

$$i\mathbf{C}_\rho \cdot \dot{\boldsymbol{z}} = \frac{\partial \mathscr{H}_\rho}{\partial \boldsymbol{z}^\star}, \tag{3.39}$$

where the metric of the periodic fermion system $\mathbf{C}_\rho$ is given by

$$\mathbf{C}_{\rho,ab} = \frac{1}{V_{BZ}} \int_{BZ} \left(\frac{\partial^2 \mathscr{N}_{ab}(\boldsymbol{k})}{\partial \boldsymbol{z}_a^\star \partial \boldsymbol{z}_b} - \sum_{pq=1}^{A} \frac{\partial \mathscr{N}_{ap}(\boldsymbol{k})}{\partial \boldsymbol{z}_a^\star} \cdot \boldsymbol{\mathcal{O}}_{pq}(\boldsymbol{k}) \cdot \frac{\partial \mathscr{N}_{qb}(\boldsymbol{k})}{\partial \boldsymbol{z}_b} \right) \cdot \boldsymbol{\mathcal{O}}_{ba}(\boldsymbol{k}) d\boldsymbol{k}. \tag{3.40}$$

The Hamiltonian forces of the system are then obtained directly from the expectation values obtained earlier or by means of the equations of TAPBC. They are represented by

$$\begin{aligned} \frac{\partial \mathscr{B}_{\rho,I}}{\partial \boldsymbol{z}_a^\star} = \frac{1}{V_{BZ}} \int_{BZ} \sum_{q=1}^{A} \frac{\partial}{\partial \boldsymbol{z}_a^\star} \boldsymbol{\mathscr{B}}_{I,aq}(\boldsymbol{k}) \boldsymbol{\mathcal{O}}_{qa}(\boldsymbol{k}) d\boldsymbol{k} \\ - \frac{1}{V_{BZ}} \int_{BZ} \sum_{pqr=1}^{A} \boldsymbol{\mathscr{B}}_{I,pq}(\boldsymbol{k}) \boldsymbol{\mathcal{O}}_{qa}(\boldsymbol{k}) \cdot \frac{\partial \mathscr{N}_{ar}(\boldsymbol{k})}{\partial \boldsymbol{z}_a^\star} \cdot \boldsymbol{\mathcal{O}}_{rp}(\boldsymbol{k}) d\boldsymbol{k}, \end{aligned} \tag{3.41a}$$

$$\begin{aligned} \frac{\partial \mathscr{B}_{\rho,II}}{\partial \boldsymbol{z}_a^\star} = \frac{1}{V_{BZ}^2} \iint_{BZ \otimes BZ} \sum_{\boldsymbol{R} \in \mathfrak{B}} \sum_{qrs=1}^{A} \frac{\partial}{\partial \boldsymbol{z}_a^\star} \boldsymbol{\mathscr{B}}_{II,\boldsymbol{R},aqrs}(\boldsymbol{k}_1, \boldsymbol{k}_2) \\ \times \left(\boldsymbol{\mathcal{O}}_{qa}(\boldsymbol{k}_1) \boldsymbol{\mathcal{O}}_{sr}(\boldsymbol{k}_2) - \boldsymbol{\mathcal{O}}_{qr}(\boldsymbol{k}_1) \boldsymbol{\mathcal{O}}_{sa}(\boldsymbol{k}_2) e^{i\boldsymbol{R} \cdot (\boldsymbol{k}_2 - \boldsymbol{k}_1)} \right) d\boldsymbol{k}_1 d\boldsymbol{k}_2 \\ - \frac{1}{V_{BZ}^2} \iint_{BZ \otimes BZ} \sum_{\boldsymbol{R} \in \mathfrak{B}} \sum_{pqrst=1}^{A} \boldsymbol{\mathscr{B}}_{II,\boldsymbol{R},pqrs}(\boldsymbol{k}_1, \boldsymbol{k}_2) \boldsymbol{\mathcal{O}}_{qa}(\boldsymbol{k}_1) \cdot \frac{\partial \mathscr{N}_{at}(\boldsymbol{k}_1)}{\partial \boldsymbol{z}_a^\star} \\ \times \left(\boldsymbol{\mathcal{O}}_{tp}(\boldsymbol{k}_1) \boldsymbol{\mathcal{O}}_{sr}(\boldsymbol{k}_2) - \boldsymbol{\mathcal{O}}_{tr}(\boldsymbol{k}_1) \boldsymbol{\mathcal{O}}_{sp}(\boldsymbol{k}_2) e^{i\boldsymbol{R} \cdot (\boldsymbol{k}_2 - \boldsymbol{k}_1)} \right) d\boldsymbol{k}_1 d\boldsymbol{k}_2, \end{aligned} \tag{3.41b}$$

The theory developed in the foregoing shows how PBC are incorporated into FMD. An idea similar to PBC in CMD was introduced as the limit of truncated antisymmetric periodic boundary conditions. Through Fourier series, it became possible to reduce the infinite dimensional equations into finite sized matrix operations. The overlap matrices, operators, Hamiltonian forces and geometrical metrics of the periodic fermion system can all be understood as representations in Wannier space and are generated through the Bloch representations. These Bloch representations symbolise the object in question in reciprocal space of the Bravais lattice and transforms the infinite dimensional equations in Bravais space into a finite dimensional set in reciprocal space. These contain all information with respect to the periodicity in coordinate space. Herewith, the implementation of PBC into FMD can be concluded.

Section 3.6 The Bloch overlap in PBC

In the preceding sections, a formalism dubbed TAPBC is introduced with periodic boundary conditions as its limit for infinite order. As it is based on FMD, no restrictions were made with regard to the single-particle trial states employed in the formalism and only the Slater determinant was its prerequisite. Using the proposed single-particle wave packet of the previous chapter, being Eq. (2.30),

$$|q_p\rangle = \sum_{klm} c_{klmp} |\mathbf{A}_{klmp}\boldsymbol{b}_{klmp}\rangle \otimes |\chi_{klmp}\rangle \otimes |\zeta_{klmp}\rangle,$$

it is interesting to look into the mathematical implications it has on this new formalism. This especially on the overlap of two particles defined by Eq. (2.39)

$$\mathbf{n}_{pq} = \sum_{\substack{k_p l_p m_p \\ k_q l_q m_q}} c^{\star}_{k_p l_p m_p p} c_{k_q l_q m_q q} \mathscr{R}_{k_p l_p m_p, k_q l_q m_q} \mathscr{S}_{k_p l_p m_p, k_q l_q m_q} \mathscr{T}_{k_p l_p m_p, k_q l_q m_q}.$$

Since the boundary conditions presented in this chapter only affect the spatial components $|\mathbf{A}\boldsymbol{b}\rangle$ of the single-particle state $|q\rangle$, it is evident that only the adaptation to the spatial part has to be addressed. As was indicated earlier, it is the overlap in the Bloch representation that is of interest. Using the definitions of the Bloch representation and the overlap of Gaussian wave packets, i.e. Eqs. (3.33) and (2.39), the Bloch overlap reads

$$\mathscr{N}(\boldsymbol{k})_{pq} = \sum_{\substack{k_p l_p m_p \\ k_q l_q m_q}} c^{\star}_{k_p l_p m_p p} c_{k_q l_q m_q q} \mathscr{R}(\boldsymbol{k})_{k_p l_p m_p, k_q l_q m_q} \mathscr{S}_{k_p l_p m_p, k_q l_q m_q} \mathscr{T}_{k_p l_p m_p, k_q l_q m_q}. \quad (3.42)$$

Here the spatial overlap differs from the one of the single-particle state through a modulation factor. It is simply written as

$$\begin{aligned} \mathscr{R}(\boldsymbol{k})_{pq} &= \sum_{\boldsymbol{R}\in\mathfrak{B}} \langle \mathbf{A}_p \boldsymbol{b}_p | \mathcal{T}(\boldsymbol{R}) | \mathbf{A}_q \boldsymbol{b}_q \rangle e^{i\boldsymbol{k}\cdot\boldsymbol{R}}, \\ &= \mathscr{R}_{pq} \vartheta\{\boldsymbol{z}(\boldsymbol{k})_{pq} | \mathbf{T}_{pq}\}, \end{aligned} \quad (3.43)$$

with the values of $\boldsymbol{z}(\boldsymbol{k})_{pq}$ and $\mathbf{T}_{pq}$ defined through

$$\boldsymbol{z}(\boldsymbol{k})_{pq} = \frac{1}{2i}\mathbf{B}^T(\mathbf{A}_p^{\dagger} + \mathbf{A}_q)^{-1}(\boldsymbol{b}_p^{\star} - \boldsymbol{b}_q) - \frac{1}{2}\mathbf{B}^T\boldsymbol{k} = \frac{1}{2}\mathbf{B}^T\left(\boldsymbol{k} - \boldsymbol{p}_{pq}\right), \quad (3.44a)$$

$$\mathbf{T}_{pq} = \frac{i}{2\pi}\mathbf{B}^T(\mathbf{A}_p^{\dagger} + \mathbf{A}_q)^{-1}\mathbf{B}. \quad (3.44b)$$

The matrix $\mathbf{B}$ is the generator of the Bravais lattice vectors $\boldsymbol{R}$ such that $\boldsymbol{R} = \mathbf{B}\boldsymbol{n}$ with $\boldsymbol{n}$ an integer vector. The columns of $\mathbf{B}$ are the primitive vectors of the Bravais lattice. For a simple cubic honeycomb, the generating matrix is given by $\mathbf{B}_{sc} = \frac{\ell}{2}\mathbf{I}$. with ℓ the lattice constant. For the face-centred cubic and body-centred cubic honeycombs, the matrix is given by

$$\mathbf{B}_{fcc} = \frac{\ell}{2}\begin{pmatrix} 0 & 1 & 1 \\ 1 & 0 & 1 \\ 1 & 1 & 0 \end{pmatrix}, \qquad \mathbf{B}_{bcc} = \frac{\ell}{2}\begin{pmatrix} -1 & 1 & 1 \\ 1 & -1 & 1 \\ 1 & 1 & -1 \end{pmatrix}. \tag{3.45}$$

The lattice constant ℓ is chosen to be the size of the conventional cube of sc, fcc and bcc lattices.

A representation of $\mathscr{R}_{pq}(\boldsymbol{k})$ for one dimension is visualised in Fig. 3.8. It is seen

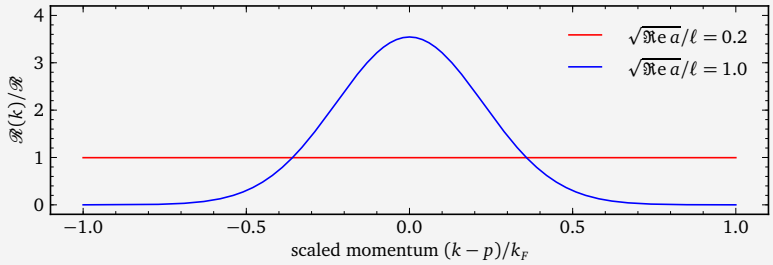

Figure 3.8: A one-dimensional representation of the Bloch overlap of Gaussian wave packets. The lattice size is taken to be ℓ and $k_F = \pi/\ell$. For Gaussian wave packets with a small width, $\mathscr{R}(k) \approx \mathscr{R}$, while for larger widths this is clearly not the case.

that for wave packets with a variance much smaller than the size of the Wigner-Seitz cell, the Bloch overlap $\mathscr{R}_{pq}(\boldsymbol{k})$ and the standard overlap $\mathscr{R}_{pq}$ are almost identical. When the width of the Gaussian wave packet becomes of the same order of magnitude of the cell size, corrections appear.

From the above it is thus obvious that approximations are in place. In the light of CMD, analogues to the nearest image convention (NIC) and minimal image convention (MIC) are introduced as the nearest antisymmetry convention (NAC) and the minimal antisymmetry convention (MAC). As was indicated in the introduction, the effect of the periodicity should be as small as possible and thus the size of the

wave packets should be smaller than the Wigner-Seitz cell. With this in mind, NAC is introduced as

$$\mathscr{R}(\boldsymbol{k})_{pq} \approx \mathscr{R}_{pq} \sum_{n_1 n_2 n_3 = -1}^{1} \exp\left\{ i\pi \boldsymbol{n} \cdot \mathbf{T}_{pq} \cdot \boldsymbol{n} + 2i\boldsymbol{n} \cdot \boldsymbol{z}(\boldsymbol{k})_{pq} \right\}. \tag{3.46}$$

The contribution from higher order terms, those stemming from non-neighbouring unit cells, will be much smaller as a result of the relative size of the wave packets compared to the cell size, i.e.

$$\Re\mathrm{e}\left[\boldsymbol{a}_i \cdot (\mathbf{A}_p^\dagger + \mathbf{A}_q)^{-1} \cdot \boldsymbol{a}_i \right] \gg 1, \qquad i = 1,2,3.$$

That being the case, a last approximation is introduced as MAC. The largest contribution to $\mathscr{R}(k)_{pq}$ comes from the closest neighbour of all images of particles q to a single image of particle p. The MAC approximation reads then

$$\mathscr{R}(\boldsymbol{k})_{pq} \approx \mathscr{R}_{pq} \exp\left\{ i\pi \boldsymbol{n}_M \cdot \mathbf{T}_{pq} \cdot \boldsymbol{n}_M + 2i\boldsymbol{n}_M \cdot \boldsymbol{z}(\boldsymbol{k})_{pq} \right\}, \tag{3.47}$$

where $\boldsymbol{n}_M$ is the vector of the set $\{\boldsymbol{n}, n_i = -1,0,1\}$ that minimises the norm of $\langle \mathbf{A}_p \boldsymbol{b}_p | \mathbf{A}_q, \boldsymbol{b}_q + \mathbf{B}\boldsymbol{n} \rangle$. The latter translates itself in minimising the inter-particle distance, that is to say $||\boldsymbol{r}_p - \boldsymbol{r}_q - \mathbf{B}\boldsymbol{n}_M||$ is minimal. This is in line with the CMD MIC picture according to Metropolis [Met53]. A representation of NAC and MAC is given in Fig. 3.9.

Even though the wave packets should be smaller than the Wigner-Seitz cell, it is interesting to investigate what approximations are in place when the wave packets are larger than the cell. Considering the modular transformation for Riemann theta functions conform Eq. (B.25), the Bloch overlap is given by

$$\mathscr{R}(\boldsymbol{k})_{pq} \approx \mathscr{R}_{pq} \sqrt{\det(-i\mathbf{T}_{pq})} \exp\left\{ -\frac{1}{2} (\boldsymbol{k} - \boldsymbol{p}_{pq}) \cdot (\mathbf{A}_p^\dagger + \mathbf{A}_q) \cdot (\boldsymbol{k} - \boldsymbol{p}_{pq}) \right\} \times \vartheta\left\{ \mathbf{T}_{pq}^{-1} \boldsymbol{z}(\boldsymbol{k})_{pq} \middle| -\mathbf{T}^{-1} \right\}. \tag{3.48}$$

For wave packets larger than the cell size, a modular form of NAC (MFNAC) and of MAC (MFMAC) can be attained. Thus if

$$\Re\mathrm{e}\left[\boldsymbol{a}_i \cdot (\mathbf{A}_p^\dagger + \mathbf{A}_q)^{-1} \cdot \boldsymbol{a}_i \right] \ll 1, \qquad i = 1,2,3;$$

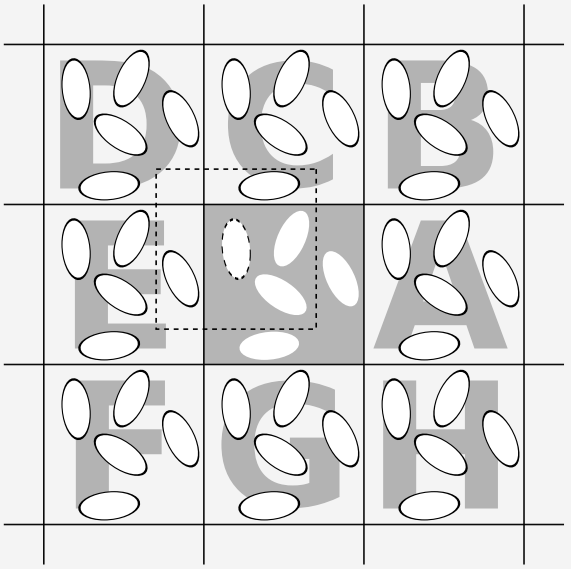

Figure 3.9: The nearest antisymmetry convention and the minimal antisymmetry convention in a two-dimensional system. While for the NAC the contributions of the cells A, ..., H are taken into account in the calculation of the Bloch overlap function, MAC only addresses the particles laying in a box volume with in its centre the particle under investigation. Due to translation invariance, the amount of particles in the dashed box and the original box is identical.

the Bloch overlap is approximated by MFNAC as

$$\mathscr{R}(\boldsymbol{k})_{pq} \approx \frac{\mathscr{R}_{pq}}{\sqrt{\det(-i\mathbf{T}_{pq})}} \exp\left\{-\frac{1}{2}(\boldsymbol{k}-\boldsymbol{p}_{pq})\cdot(\mathbf{A}_p^{\dagger}+\mathbf{A}_q)\cdot(\boldsymbol{k}-\boldsymbol{p}_{pq})\right\} \times \sum_{n_1 n_2 n_3=-1}^{1} \exp\left\{-i\pi\boldsymbol{n}\cdot\mathbf{T}_{pq}^{-1}\cdot\boldsymbol{n}+2i\boldsymbol{n}\cdot\mathbf{T}_{pq}^{-1}\cdot\boldsymbol{z}(\boldsymbol{k})_{pq}\right\}. \quad (3.49)$$

Where MFMAC leads to

$$\mathscr{R}(\boldsymbol{k})_{pq} \approx \frac{\mathscr{R}_{pq}}{\sqrt{\det(-i\mathbf{T}_{pq})}} \exp\left\{-\frac{1}{2}(\boldsymbol{k}-\boldsymbol{p}_{pq})\cdot(\mathbf{A}_p^{\dagger}+\mathbf{A}_q)\cdot(\boldsymbol{k}-\boldsymbol{p}_{pq})\right\} \times \exp\left\{-i\pi\boldsymbol{n}_M\cdot\mathbf{T}_{pq}^{-1}\cdot\boldsymbol{n}_M+2i\boldsymbol{n}_M\cdot\mathbf{T}_{pq}^{-1}\cdot\boldsymbol{z}(\boldsymbol{k})_{pq}\right\}, \quad (3.50)$$

with $\boldsymbol{n}_M$ maximising the norm of the last exponential.

Section 3.7 — Fermionic behaviour of a particle in one dimension

Up to this point, this chapter introduced the theoretical background of PBC within the concept of FMD. The remaining question is whether this theory reproduces fermionic effects. Schnack and Feldmeier indicated that a hundred equally displaced Gaussian wave packets showed identical properties as a free Fermi gas, establishing the validity of FMD [Sch93, Fel95, Fel00]. These results can now be mathematically confirmed by means of PBC in FMD.

With this in mind, properties of a one-dimensional free single particle in a box are investigated. As indicated in the previous sections, the overlap in the Bloch representation is essential. Under the assumption that the single-particle state is given by $|ab\rangle$ and the box-size is ℓ, this overlap is written as

$$\mathscr{R}(k) = \langle ab|ab\rangle \vartheta_3\{z(k)|\tau\}, \tag{3.51}$$

where the values for $z(k)$ and τ are

$$z(k) = \frac{\ell(k-p)}{2}, \qquad \tau = \frac{i\ell^2}{2\pi(a+a^\star)}.$$

For brevity, the value of τ will not be specified and z is assumed to be k-dependent.

In the course of this section, the following expressions are useful and can easily be deduced from the formulae presented in appendix B:

$$\frac{\ell}{2\pi}\int_{-\frac{\pi}{\ell}}^{\frac{\pi}{\ell}} \frac{\vartheta_3'(z)}{\vartheta_3(z)}dk = 0,$$
$$\frac{\ell}{2\pi}\int_{-\frac{\pi}{\ell}}^{\frac{\pi}{\ell}} \frac{\vartheta_3''(z)}{\vartheta_3(z)}dk = \frac{\ell}{2\pi}\int_{-\frac{\pi}{\ell}}^{\frac{\pi}{\ell}} \left(\frac{\vartheta_3'(z)}{\vartheta_3(z)}\right)^2 dk = 8\sum_{n=1}^{\infty}\frac{e^{2ni\pi\tau}}{(1-e^{2ni\pi\tau})^2}.$$

The kinetic energy of this system is well defined and readily obtained by means of the formula in appendix B.5. To obtain the kinetic energy per unit-cell according

to Eq. (3.36a), the Bloch expectation value of the kinetic energy operator is required. Using Eq. (3.37a) this reads

$$\begin{aligned}\mathscr{T}(k) &= \frac{1}{2m}\sqrt{\frac{aa^\star}{a+a^\star}}\sum_{n=-\infty}^{\infty}\left(\frac{1}{a+a^\star}-\frac{(b^\star-b-n\ell)^2}{(a+a^\star)^2}\right)\\ &\qquad\qquad\times\exp\left\{-\frac{1}{2}\frac{(b^\star-b-n\ell)^2}{a+a^\star}+ikn\ell\right\},\\ &= \left\{\left(\frac{1}{a+a^\star}+p^2\right)\vartheta_3(z)-\frac{p\ell}{a+a^\star}\vartheta_3'(z)+\frac{\ell^2}{4(a+a^\star)^2}\vartheta_3''(z)\right\}\frac{\langle ab|ab\rangle}{2m}.\end{aligned} \tag{3.52}$$

The kinetic energy per unit-cell is then given by

$$\begin{aligned}\mathscr{T}_\rho &= \frac{1}{2m}\left(\frac{1}{a+a^\star}+p^2+\frac{2\ell^2}{(a+a^\star)^2}\sum_{n=1}^{\infty}\frac{e^{2ni\pi\tau}}{(1-e^{2ni\pi\tau})^2}\right), \qquad (3.53)\\ &= \frac{1}{2m}\left(\frac{1}{a+a^\star}+p^2+\frac{\ell^2}{12(a+a^\star)^2}\left(\frac{\vartheta_1'''(0)}{\vartheta_1'(0)}+1\right)\right),\end{aligned}$$

which is obtained by means of Eqs. (B.22). The last comparison is obtained from Whittaker and Watson [Whi63]. As $\mathscr{T}_\rho$ represents the kinetic energy per unit-cell and only one particle is available in this cell, it is equivalent to the kinetic energy per particle of the periodic system.

When comparing the kinetic energy of the periodic system, i.e. the particle in the box, with the one of a single free particle,

$$\mathscr{T} = \langle ab|\mathcal{T}|ab\rangle = \frac{1}{2m}\left(\frac{1}{a+a^\star}+p^2\right),$$

the effect of antisymmetry clearly pops up. In the case of distinguishable particles, the kinetic energy per particle would be identical to that of a single particle. In Eq. (3.53), however, an extra term is added to this energy to account for the antisymmetry of the system. This can be best understood when investigating Fig. 3.10. The kinetic energy per particle is shown as a function of the scaled variance which is compared with the box size ℓ. When the variance is small compared to the box, the kinetic energy per particle is similar to that of a single particle:

$$\mathscr{T}_\rho \approx \frac{1}{2m}\left(\frac{1}{a+a^\star}+p^2\right), \qquad \frac{\sqrt{a+a^\star}}{\ell}\ll 1. \tag{3.54a}$$

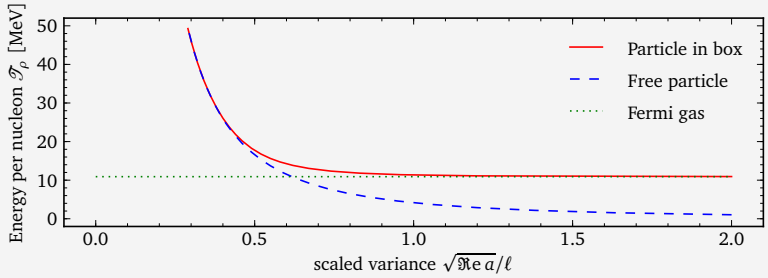

Figure 3.10: The kinetic energy per neutron is presented as a function of the scaled variance $\sqrt{\mathfrak{Re}\, a}/\ell$. The box size is taken to be $|\ell| = 2.5$ fm. The figure presents the comparison of the periodic system with a single particle and a free Fermi gas.

This is easy to understand as, due to the small overlap between two neighbouring states, each particle acts as if it was on its own. The effect of antisymmetry is thus negligible.

For large values of the variance, Fig. 3.10 shows that antisymmetry starts to influence the kinetic energy rendering it constant. Under the assumption that the particles have initial zero momentum, $p = 0$, the energy can be approximated by

$$\mathscr{T}_\rho \approx \frac{1}{2m}\sum_{n=1}^{\infty}\frac{2}{\ell^2 n^2} = \frac{1}{6m}\left(\frac{\pi}{\ell}\right)^2, \qquad \frac{\sqrt{a+a^\star}}{\ell} \gg 1. \tag{3.54b}$$

This value is equal to the one of a free one-dimensional Fermi gas with particle density $\rho = 1/\ell$ and, hence, Fermi momentum $k_F = \pi/\ell$. This result is a typical example of the fermion character of the system. When the variance of the wave packets becomes large, they render into plane waves. Therefore, the above result was expected.

Given this effect in the kinetic energy, a similar result should be obtained in the density distributions in coordinate and momentum space. The density distribution operators $\hat{\rho}_x$ and $\hat{\rho}_k$ are given by

$$\langle a_p b_p|\hat{\rho}_x|a_q b_q\rangle = \langle x|a_q b_q\rangle\langle a_p b_p|x\rangle, \qquad \langle a_p b_p|\hat{\rho}_k|a_q b_q\rangle = \langle k|a_q b_q\rangle\langle a_p b_p|k\rangle.$$

The Bloch expectation value $\varrho_k(k')$ of the one-dimensional system, are then, accord-

ing to Eq. (3.37a), written as

$$\varrho_k(k') = \frac{2\pi}{\ell}\sqrt{aa^\star}\exp\left\{-\frac{a+a^\star}{2}k^2 - i(b^\star - b)k\ell\right\}\sum_{m=-\infty}^{\infty}\delta\left(k' - k + \frac{2\pi m}{\ell}\right), \quad (3.55)$$

and leads by means of Eqs. (3.36), to the momentum density

$$\rho(k) = \sqrt{\frac{a+a^\star}{2\pi}}\frac{\exp\left\{-\frac{a+a^\star}{2}(k-p)^2\right\}}{\vartheta_3(z(k))}. \quad (3.56)$$

The spatial density is evaluated directly by means of the limit of Eq. (3.13), to conserve mathematical symmetry, and reads

$$\rho(x) = \frac{\ell}{2\pi}\sqrt{\frac{a+a^\star}{2\pi aa^\star}}\cdot\exp\left\{-\frac{a+a^\star}{2aa^\star}(x-r)^2\right\} \times\int_{-\frac{\pi}{\ell}}^{\frac{\pi}{\ell}}\frac{\vartheta_3\left(\frac{(x-r)\ell}{2ia} + z(k)\middle|\frac{i\ell^2}{2\pi a}\right)\vartheta_3\left(\frac{(x-r)\ell}{2ia^\star} - z(k)\middle|\frac{i\ell^2}{2\pi a^\star}\right)}{\vartheta_3(z(k)|\tau)}dk. \quad (3.57)$$

A representation of these densities can be found in Fig. 3.11. There the densities in coordinate space and momentum space are depicted for an infinite set of periodic Gaussian wave packets with real variance a and mean momentum p set to zero. When the variance $\sqrt{a}$ is 0.2ℓ, the densities in coordinate space and momentum space remain unaltered. This is due to the small overlap between individual wave packets. Antisymmetry has no effect on these densities. When the overlap between neighbouring wave packets is more significant, antisymmetry starts to play a fundamental role with increasing overlap. A more uniform distribution is attained in the coordinate space while the momentum density tends towards a Fermi distribution. When comparing the momentum distribution of the infinite system with the one of a single particle in Fig. 3.11 (d), it is remarkable to notice that, even though the single particle has zero momentum density around $k = 0.8k_F$, the density is pulled up to one. This is merely the result of the inverse overlap matrix. These results are in agreement with those obtained by Schnack and Feldmeier in the early stages of FMD [Sch93, Fel00], however , in these works, a total of a hundred equally spaced wave packets were used as initial trial state.

From a more theoretical point of view, a comparison with the Fermi distribution can be made by evaluating the density equation Eq. (3.56) for broad wave packets with zero momenta. The modular transformation of the Jacobi-theta function by

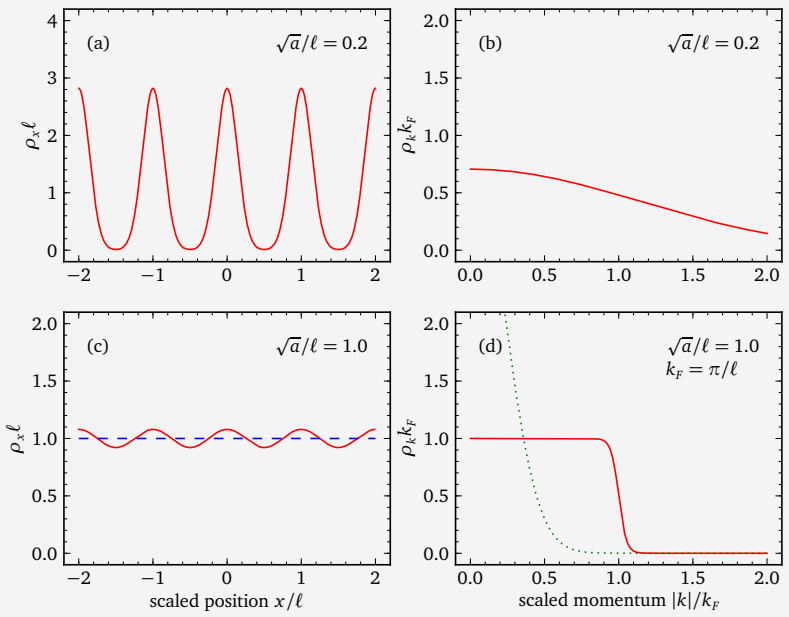

Figure 3.11: The momentum density and spatial density of an infinite system of Gaussian wave packets periodically displaced over ℓ with zero mean momentum and real variance a. The evaluations of the densities are done by means of periodic boundary conditions for two ratios of $\sqrt{a}/\ell$. It is clearly visible that a small overlap of the wave packets creates a distinguishable particle picture while a large overlap, or wide wave packets show Fermi gas behaviour. The dashed line indicates the spatial density of a plane wave distribution or an ideal Fermi gas. The dotted line shows the momentum distribution of a single free particle.

means of Eq. (B.20) and a first order approximation of the theta function leads to

$$\rho(k) \approx \frac{\pi}{2k_F} \cdot \frac{1}{1 + \exp\left\{\frac{k^2 - k_F^2}{2mT}\right\} \exp\left\{-\frac{(|k| - k_F)^2}{2mT}\right\}}, \tag{3.58}$$

where $k_F = \pi/\ell$ and $a + a^\star = 1/2mT$. The obtained result is that of a Fermi distribution with a modulation factor. Even though the variance a hints to the temperature of the system, it is not the real temperature of the system as known in statistical mechanics. The momentum density owes its shape to the ground state fluctuations.

There is no actual motion within the system as the momenta of the ground state wave functions are zero.

Finally, the equations of motion of a single particle in a box are investigated. Using the differential equation where all Jacobi Theta functions answer to, i.e. Eq. (B.17)

$$\frac{1}{4}\pi i\frac{\partial^2\vartheta_n(z|\tau)}{\partial z^2}+\frac{\partial\vartheta_n(z|\tau)}{\partial\tau}=0,$$

and the equalities from the beginning of this chapter, it can be shown that the metric of the periodic system and the single free particle system are identical. Comparing the structure of the equations of motion for a system with periodic boundary conditions, Eq. (3.39), with those of a general TDVP problem Eq. (2.21) and combining them with the equations of motion of a single Gaussian conform Eq. (2.26), the equations of motion become

$$\dot{r}=\frac{p}{m}, \tag{3.59a}$$

$$\dot{p}=0, \tag{3.59b}$$

$$\dot{a}=\frac{i}{m}\left\{1-\frac{4\ell^4}{(a+a^\star)^2}\cdot\frac{\displaystyle\sum_{n=1}^{\infty}\frac{ne^{2ni\pi\tau}(1+e^{2ni\pi\tau})}{(1-e^{2ni\pi\tau})^2}}{2+\dfrac{4\ell^2}{a+a^\star}\displaystyle\sum_{n=1}^{\infty}\frac{e^{2ni\pi\tau}}{1-e^{2ni\pi\tau}}}\right\}. \tag{3.59c}$$

Comparing this result with the one of a free one-dimensional Gaussian wave packet adapted from Eq. (2.28), it is visible that PBC have no effect on the motion of the system. The particle behaves as if it were free. The PBC only affects the rate of change of the variance of the Gaussian wave packet. From Eq. (3.59c) it is clear that $\dot{a}$ is purely imaginary and hence the real part of a remains unchanged. In Fig. 3.12 the rate of change of a is presented as a function of the box size ℓ. The PBC have as effect that it counteracts the rate of change of the variance of a free particle. If the overlap of neighbouring particles is weak, PBC have hardly any influence on the time-evolution of the variance a and the particle behaves as if it was completely free. With increasing overlap, however, the time derivative of a diminishes and vanishes. The latter occurs when the particles in the system are described as plane waves or when the system used zero box length.

The results presented in this section epitomise how localised single-particle states with zero mean momentum reproduce fermion properties by means of PBC and antisymmetrisation of wave functions. When trying to obtain these results by means of

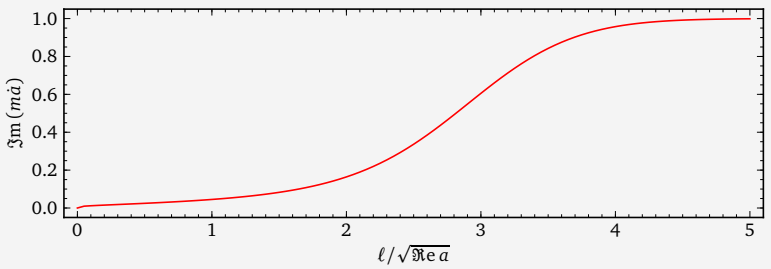

Figure 3.12: The rate of change of the variance a. When the box size increases, the rate of change resembles that of a free single particle while with decreasing box size, that effect is counteracted.

Pauli potentials and classical mechanics, as is indicated by Dorso et al., the resulting ground state momentum distributions are unsatisfactory [Dor87].

Section 3.8 Fermions and Brillouin zones

In the course of this chapter, a theoretical model was introduced to study fermions in bulk. The previous section provided evidence that various fermionic properties are present for a single particle in one dimension subject to this model. The question remaining now, is whether these properties are genuine fermionic effects or artefacts resulting from the boundary conditions. This section will try to answer that question.

The most conclusive evidence from the previous section was the comparison between the momentum distribution and the Fermi-distribution. For a Gaussian wave packet, relatively large in comparison to the box size, Fig. 3.11 and Eq. (3.58) indicated that the momentum distribution is similar to that of a free Fermi gas. A further investigation of the momentum density is essential, and this for various lattice structures. The lattices under investigation will be the two dimensional square and hexagonal Bravais lattices and the three dimensional simple cubic, face-centred cubic and body-centred cubic Bravais lattices, as presented in Fig. 3.13.

As always, the system under investigation, is created by placing a number of fermions in a unit cell and replicating this cell to tessellate space according to a Bra-

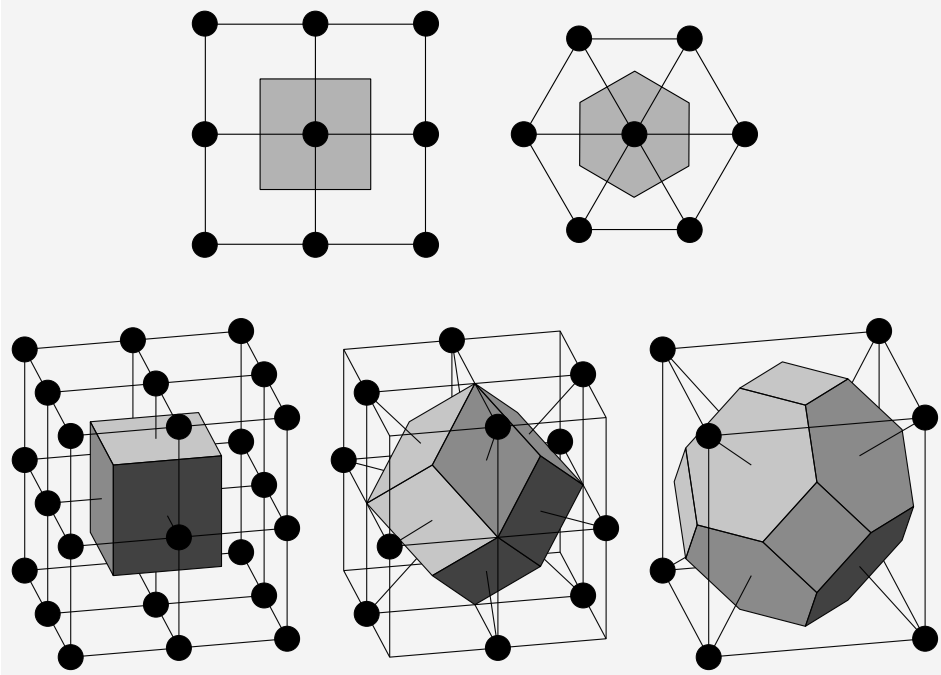

Figure 3.13: The two and three-dimensional Bravais lattices which will be investigated. The top row from left to right the square lattice and the hexagonal lattice. The bottom row from left to right the simple cubic, face-centred cubic and body-centred cubic lattice. The unit length ℓ for the two-dimensional lattices is given by the distance between two lattice points, while for the three dimensional lattices it refers to the cube size of the conventional cube.

vais lattice with primitive lattice vectors $\boldsymbol{a}_1, \ldots, \boldsymbol{a}_d$ for a d-dimensional system. The generating lattice matrix $\mathbf{B}$ is then given by $\mathbf{B} = \left[\boldsymbol{a}_1 \ldots \boldsymbol{a}_d\right]$. The matrices $\mathbf{B}$ for the three-dimensional lattices are given by Eq. (3.45) while the two-dimensional matrices are represented by

$$\mathbf{B}_{sqr} = \ell \begin{pmatrix} 0 & 1 \\ 1 & 0 \end{pmatrix}, \qquad \mathbf{B}_{hex} = \ell \begin{pmatrix} 1 & \frac{1}{2} \\ 0 & \frac{\sqrt{3}}{2} \end{pmatrix}, \tag{3.60}$$

for a square and hexagonal lattice with ℓ the length of a side. The first system under investigation is created by placing a single Gaussian wave packet $|\mathbf{A}\boldsymbol{b}\rangle$ in the unit cell. The wave packet has zero momentum. A straightforward calculation of the momentum distribution by means of Eqs. (3.36) and the modular transformation of

the Riemann theta function according to (B.25), leads to

$$\rho(\boldsymbol{k})V_{BZ} = \frac{1}{\vartheta\left\{\pi i\mathbf{B}^{-1}(\mathbf{A}+\mathbf{A}^{\dagger})\boldsymbol{k}|2\pi i\mathbf{B}^{-1}(\mathbf{A}+\mathbf{A}^{\dagger})(\mathbf{B}^{T})^{-1}\right\}}. \tag{3.61}$$

For a spherical wave packet with $\mathbf{A} = a\mathbf{I}$ for real a, this reduces to

$$\rho(\boldsymbol{k})V_{BZ} = \frac{1}{\vartheta\left\{2\pi ia\mathbf{B}^{-1}\boldsymbol{k}|4\pi ia(\mathbf{B}^{T}\mathbf{B})^{-1}\right\}}. \tag{3.62}$$

This normalised momentum density is shown in Fig. 3.14 for the square Bravais lattice and Fig. 3.15 for the hexagonal Bravais lattice. With increasing ratio $\sqrt{a}/\ell$, the momentum distribution transforms from a Gaussian to the first Brillouin zone of the Bravais lattice in question. With larger values of $\sqrt{a}/\ell$, the wave function in the box more and more resembles a plane wave. The increasing ratio corresponds to an increase in overlap between the neighbouring wave packets.

According to the Heisenberg uncertainty principle [Hei27], a particle occupies a phase-space volume of $h = 2\pi$ per dimension. As a result of the antisymmetrisation, a single particle state will be restricted to the Wigner-Seitz cell in coordinate space. Hence, the volume the momenta should occupy in momentum space, is that of the first Brillouin zone $V_{BZ} = (2\pi)^d/V_{WSC}$. For free particles, this volume is spherically shaped. However, since the particles are placed on a lattice, they are restricted by Bloch's theorem resulting in the shape of the first Brillouin zone.

Another more intuitive way, is to investigate the ground state of a free fermion system using the principle of box-normalisation. For a one-dimensional box of size ℓ, the wave vector of a plane wave is quantised according to

$$k = \frac{2\pi}{\ell}m,$$

for integral m. When adding a single free particle to the box and bringing it to the ground state, it will occupy the state $m = 0$. When expanding the volume of the box by a factor three, the quantisation of the wave vector will be as

$$k = \frac{2\pi}{3\ell}m.$$

Placing three fermions in the ground state of this box, they will occupy the states $m = -1, 0, 1$. A box of size $(2N+1)\ell$ will have a quantisation of the wave vector as

$$k = \frac{2\pi}{(2N+1)\ell}m,$$

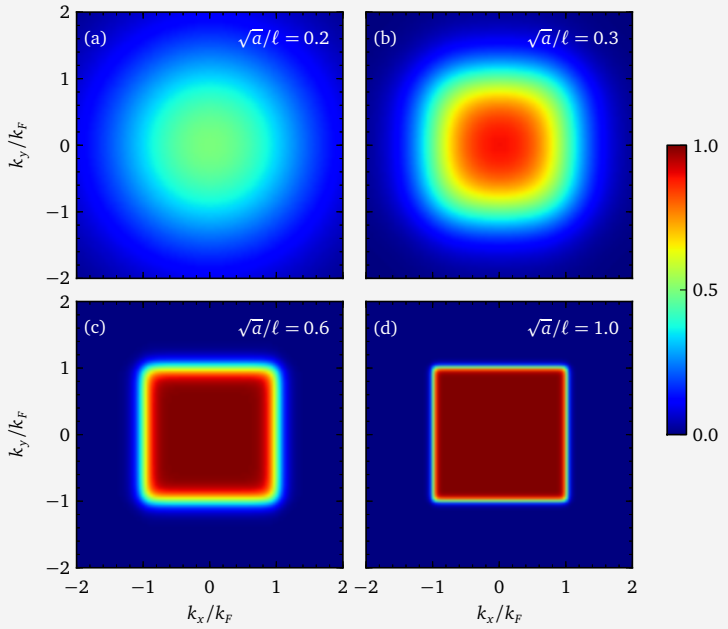

Figure 3.14: The momentum distribution of a fermion system created by placing a single Gaussian wave packet $|a\boldsymbol{b}\rangle$ on a two-dimensional square Bravais lattice with lattice constant ℓ for various values of $\sqrt{a}/\ell$. With increasing overlap, the momentum distribution evolves towards the first Brillouin zone of the square Bravais lattice. The value k_F is given by π/ℓ.

and thus $2N+1$ free fermions will occupy the levels $m = -N, \ldots, N$ in the system's ground state. The highest levels have the value $k = \pm\frac{2\pi N}{(2N+1)\ell}$ and in the limit for N tending to infinity, which resembles the simulation in Fig. 3.11 for large overlap, that value reaches $k = \pm\frac{\pi}{\ell}$. In the limit, the values the wave vector can reach will not be quantised but continuous, covering all values between $k = -\frac{\pi}{\ell}$ and $k = \frac{\pi}{\ell}$. This is the first Brillouin zone of the lattice.

Analogue arguments can be made for higher dimensional Bravais lattices. If the vectors $\boldsymbol{b}_j$ represent the primitive reciprocal lattice vectors of the Bravais lattice, then

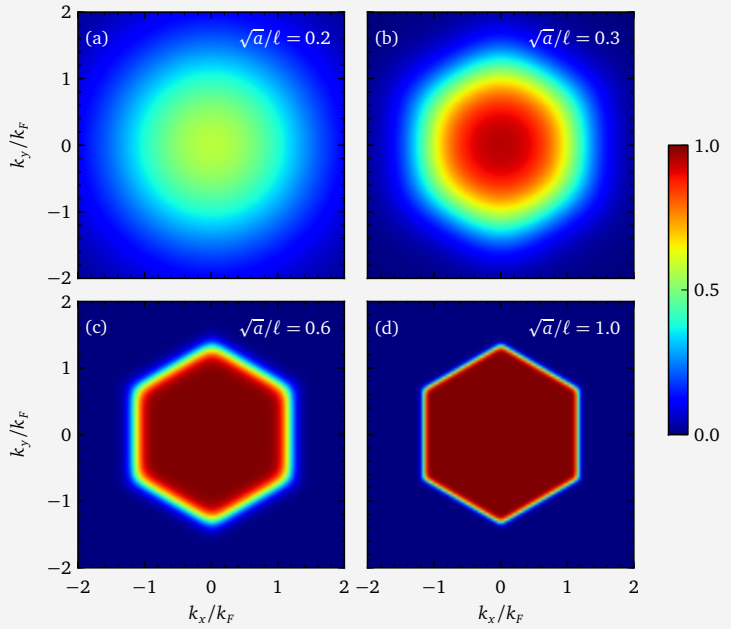

Figure 3.15: The momentum distribution of a fermion system created by placing a single Gaussian wave packet $|a\boldsymbol{b}\rangle$ on a two-dimensional hexagonal Bravais lattice with lattice constant ℓ for various values of $\sqrt{a}/\ell$. With increasing overlap, the momentum distribution evolves towards the first Brillouin zone of the hexagonal Bravais lattice. The value k_F is given by π/ℓ.

the lattice wave vector is quantised as

$$\boldsymbol{k} = \frac{m_1}{2N+1}\boldsymbol{b}_1 + \cdots + \frac{m_d}{2N+1}\boldsymbol{b}_d,$$

for integral m_j. The occupied wave vectors $\boldsymbol{k}$ for the ground state will always be all the possible wave vectors contained within the first Brillouin zone of the Bravais lattice. For free fermions in the ground state, the momenta would be contained in a sphere. However, according to Bloch's theorem, the lattice momenta $\boldsymbol{k}$ and $\boldsymbol{k}+\boldsymbol{K}$, with $\boldsymbol{K}$ a reciprocal lattice vector, are equivalent [Ash76]. Hence, the sphere in momentum space would contain regions representing equivalent states with different energies. Only the first Brillouin zone represents the lowest energy state.

A three-dimensional representation of the first Brillouin zones of the simple cubic, face-centred cubic and body-centred cubic Bravais lattice is shown in Fig. 3.16. The isosurface represents the value $\rho(k)V_{BZ} = \frac{1}{2}$ which reflects border and is shaped in the first Brillouin zone.

As is shown, the momentum density of a system with spatial density $1/V_{WSC}$ is the first Brillouin zone in the plane-wave limit. When increasing the density of the system by adding more fermions per unit-cell, the momentum distribution cannot be contained anymore within the first Brillouin zone and higher order Brillouin zones fill up [Ash76]. Using PBC combined with FMD, this is visualised by Figs. 3.17 and 3.18. The spatial and momentum distribution of a system is represented with one, five, thirteen and twenty-five fermions in the unit cell. Each of the fermions has a variance $\sqrt{a} = \ell/5$ that is not large enough to represent a plane wave. Hence, for a single particle, the momentum distribution does not represent the first Brillouin zone as is seen in panel b of Fig. 3.17. The figures clearly show that with increasing density, the momentum distribution grows out of the first Brillouin zones. Simultaneously it is seen that the spatial distribution tends to become more uniform.

Figs. 3.17 and 3.18 visualise the expansion of the momentum distribution and corroborate the reasoning behind the appearance of the first Brillouin zone given earlier. The sequence can be seen as filling a square Bravais lattice with lattice constant $\ell/5$. For this Bravais lattice, the variance of the wave packets is large enough such that the fermions appear as plane waves. While the lattice becomes filled, the momentum distribution fills up the Brillouin zone of the Bravais lattice. The momentum distribution does not exceed the first Brillouin zone. This becomes possible when the density becomes higher than a single particle per lattice site.

When investigating the spatial distributions in Figs. 3.17 and 3.18 it is seen that the distribution becomes more and more uniform when the lattice is filled. At the fully filled lattice, panel c in Fig. 3.18, it is clear that the system obtains a more or less uniform distribution.

The previous section described various properties of a single fermion placed in a one-dimensional lattice cell. For a broad Gaussian wave packet, the kinetic energy, spatial distribution and momentum distribution resemble those of a free fermion system. This section however conclusively identified that this fermionic behaviour reflects the ground state of a fermion system on a lattice and not a free fermion system. It is thus clear that wave packets clearly feel the effect of the lattice structure and this is unacceptable. The main idea of PBC was to simulate bulk properties but in a way

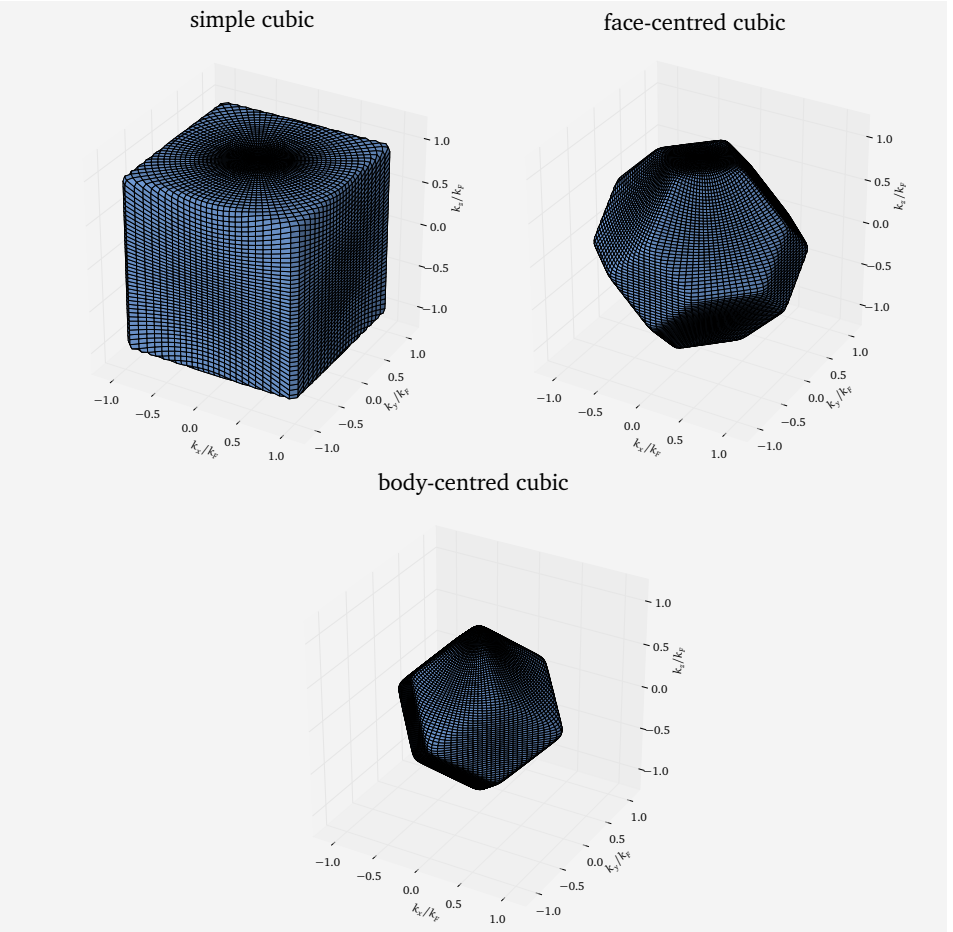

Figure 3.16: The isosurfaces $\rho(k)V_{BZ} = \frac{1}{2}$ from the momentum distributions of fermion systems created by placing a single fermion in a primitive cell of three-dimensional Bravais lattices. Presented here are the simple cubic, face-centred cubic and body-centred cubic Bravais lattice. The isosurface clearly contains the first Brillouin zone of the respective lattice. The value of k_F is given by $k_F = \frac{\pi}{\ell}$ where ℓ is the size of the conventional cube representing the Bravais lattice in question.

that the artefacts resulting from PBC are minimal. The question remaining thus is whether it is possible to model a set of free fermions?

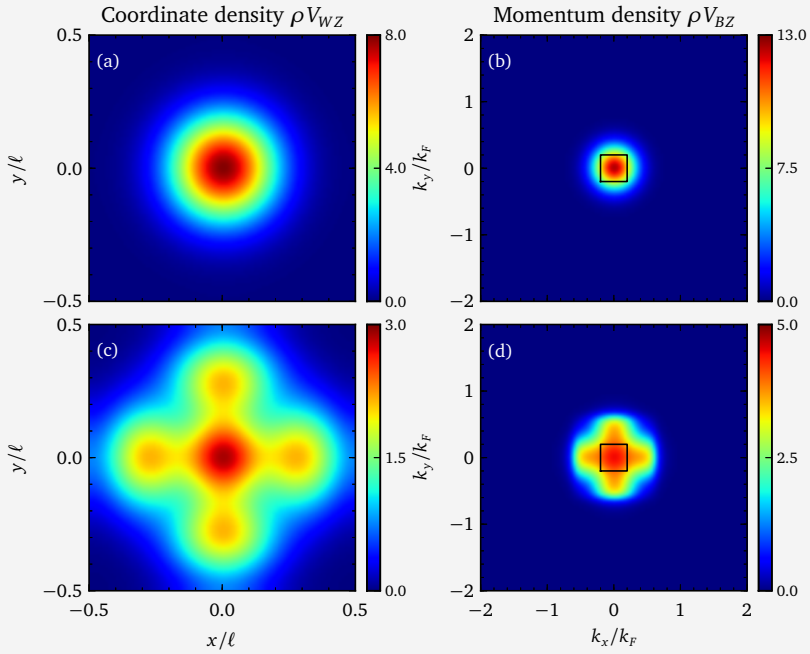

Figure 3.17: The spatial and momentum distribution of a single and five fermions in a square Bravais lattice. The variance of each wave packet is $\sqrt{a} = \ell/5$ and the value k_F is given by $k_F = 5\pi/\ell$. The value presented for the momentum distribution is $25\rho V_{BZ}$. The square in the momentum distribution represents the size of the first Brillouin zone of the square Bravais lattice.

On a side note, from a mathematical point of view, it is also remarkable to see how the solutions of the equation $\rho(\boldsymbol{k}) = 1/2$ where $\rho(\boldsymbol{k})$ represents a fully continuous function, reflect regular polygons.

Section 3.9 Free fermions and periodic boundary conditions

In the introduction of this chapter, it was indicated that periodic boundary conditions are introduced as a way to eliminate surface effects. One of the questions raised

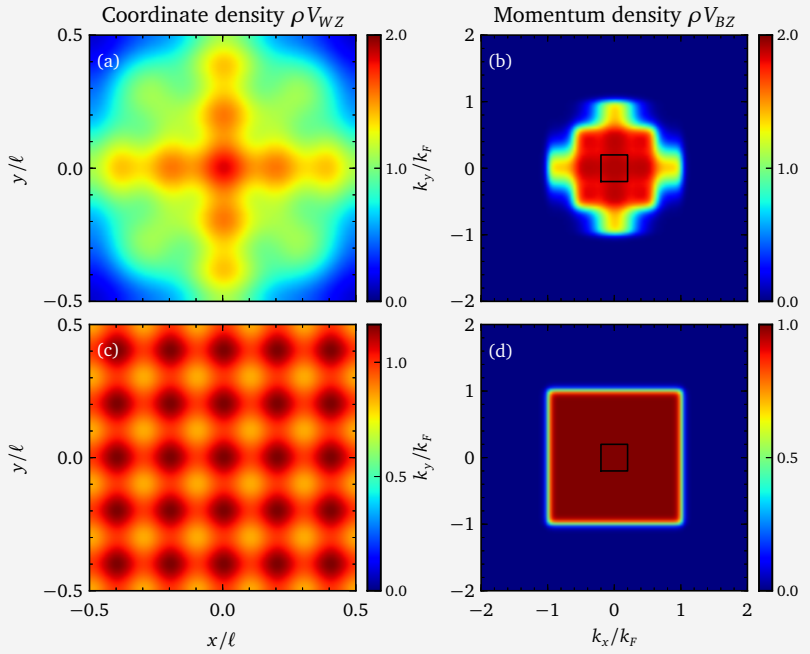

Figure 3.18: The spatial and momentum distribution of thirteen and twenty-five fermions in a square Bravais lattice. The variance of each wave packet is $\sqrt{a} = \ell/5$ and the value k_F is given by $k_F = 5\pi/\ell$. The value presented for the momentum distribution is $25\rho V_{BZ}$. The square in the momentum distribution represents the size of the first Brillouin zone of the square Bravais lattice.

concerned the equivalence of the properties of the small periodic system and the macroscopic system. The previous section clearly indicated that the particles sense the geometry of the boundary conditions as the momentum distribution reflects the first Brillouin zone. However, the momentum distribution of free particles should be spherical. If a set of N indistinguishable fermions are placed in a unit-cell with volume V_{WSC}, their momentum should be restricted to a volume Ω in momentum space, given by

$$V_{WSC}\Omega = (2\pi)^d N.$$

As the energy is proportional to the squared wave vector of the particles, this volume Ω represents an n-sphere for the ground state of the system.

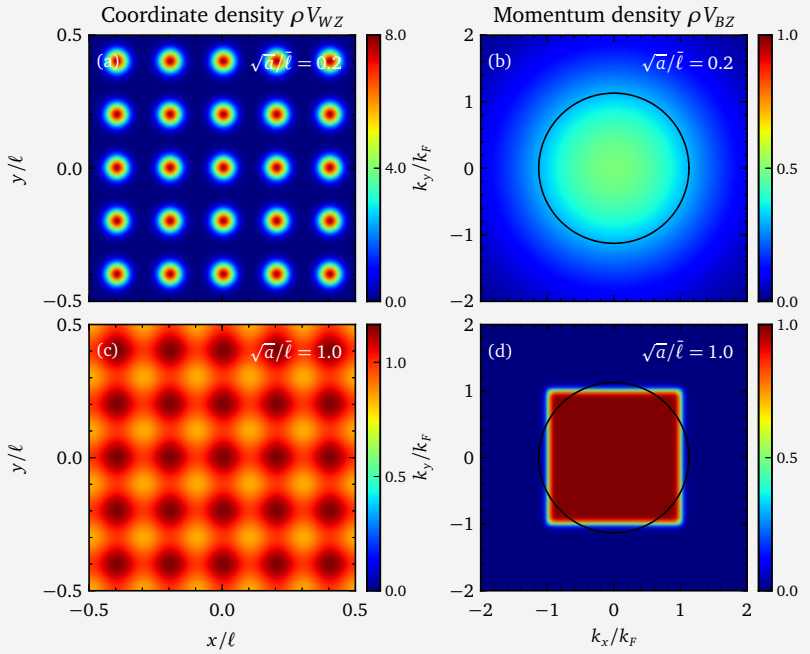

Figure 3.19: The spatial and momentum distributions for square Bravais lattices containing twenty-five particles placed on a sublattice. The lattice constant of the Bravais lattices is given by ℓ. The distributions are presented for a low-density system, i.e. $\sqrt{a}/\bar{\ell} = 0.2$ and a high-density system where $\sqrt{a}/\bar{\ell} = 1.0$. Here $\bar{\ell} = \ell/5$. The value k_F is determined on the sublattice as $k_F = \pi/\bar{\ell}$. The black circle in the momentum distribution represents the Fermi sphere for a system of free particles with the same density.

In order to see whether FMD with PBC can simulate a system of free particles, a comparison is made between two systems with identical densities, i.e. square Bravais lattices with twenty-five fermions per unit-cell. In one system, the particles are ordered on a sublattice while in the other they are placed randomly in the unit-cell. Their spatial and momentum distributions are presented in Fig. 3.19 and Fig. 3.20 for small and large overlap, or low and high density.

In the low-density representations, there is hardly any difference. The spatial

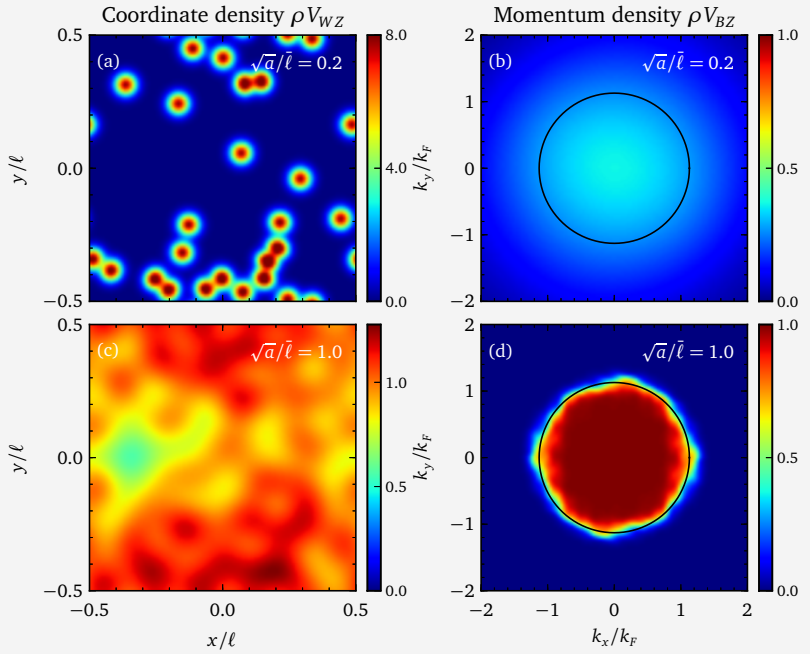

Figure 3.20: The spatial and momentum distributions for square Bravais lattices containing twenty-five particles randomly placed in the unit cell. The lattice constant of the Bravais lattices is given by ℓ. The distributions are presented for a low-density system, i.e. $\sqrt{a}/\bar{\ell} = 0.2$ and a high-density system where $\sqrt{a}/\bar{\ell} = 1.0$. Here $\bar{\ell} = \ell/5$. The value k_F is determined as $k_F = \pi/\bar{\ell}$. The black circle in the momentum distribution represents the Fermi sphere for a system of free particles with the same density.

distribution clearly shows where the particles are located, that is on the sublattice or randomly within the unit cell. The momentum distribution on the other hand is roughly the same. The main reason for this is that the overlap between separate particles is very low, hence they behave as if they were distinguishable. The momentum density can easily be approximated by that of a single particle.

The high-density situation is an other story. The spatial density is roughly uniform, but in the randomised system larger fluctuations are observed. The momentum distribution shows a clear difference. For the sublattice, the momentum distribution again reflects the first Brillouin zone, while in the randomised system a clear circular

distribution with the size of the Fermi-sphere can be identified.

It can thus be concluded that FMD with PBC has the ability to simulate a set of free fermions at high density. In the examples used here, the width of the wave packets was given by $\sqrt{a} = (V_{WSC}/N)^{1/d}$. This, however, is not a sufficient condition to eliminate the effects from periodic boundary conditions. A lot will depend on the range of the interaction under investigation.

This page intentionally left blank

4

Conclusion and Outlook

Among the myriad of phenomena in the universe, a neutron star is one of the most interesting objects that one can encounter. As an "oversized nucleus", it is one of the most dense and compact objects floating in the vast reaches of the universe. Due to their high mass and densities, neutron stars not only wrap the fabric of space-time, but also have an intriguing composition. While particle physicists rejoice when contemplating about the composition of the core, the neutron-star crust is the playground of nuclear physicists. A sound description of the material in the crust can enhance the understanding of various astrophysical phenomena related to neutron stars. Composed of neutron-rich nuclear matter, a nuclear physicist's toolbox can be used to examine the crust.

Unlike terrestrial matter that is composed of nuclear clusters with spherical shapes, the crust harbours various kinds of clusters. It is evident that it is important to study this form of matter with techniques that are unbiased in regards to the geometry of the nuclear clusters. Molecular dynamic (MD) techniques are suitable for this purpose. Because the material in the crust is dominated by fermions, the MD technique of choice is fermionic molecular dynamics (FMD).

This dissertation addresses FMD. The second chapter is devoted to its mathematical formalism, while the third chapter is dedicated to the question how FMD can be used in the study of infinite fermion systems.

FMD describes the evolution of a fermion system through a set of equations of motion stemming from the time-dependent variational principle (TDVP). This is done by applying the TDVP on a well-chosen trial state. For the simulation of an N-body fermion system, the trial state is given by a Slater determinant of N quantum dressed Gaussian wave packets, each representing a single particle. In this way, the equations of motion trace the particles individually while keeping the antisymmetry intact. This

way, the FMD description can be seen as an extension of the classical molecular dynamics approach where each particle is presented as a point particle that can be traced individually. Within the context of FMD, it is not only the position in phase-space that is dynamical, but also spin, isospin and quantum uncertainty are dynamical variables. The Slater determinant not only introduces the fermionic character in the system's description, but also converts the equations of motion into a set of matrix equations. The metric of the system's manifold and the expectation values of the operators can be calculated in terms of the overlap matrix and its inverse. Although spin, isospin and uncertainty are still manageable as extra dynamical variables, the antisymmetry increases the complexity of simulations compared to CMD. While CMD is an N^2-problem, FMD becomes an N^4-problem for two-body operators. This is due to the traces of $N \times N$ matrices in the equations of motion. When investigating bulk properties of fermionic matter, this becomes problematic. Large systems diminish surface effects but lead to large matrices making the problem computationally very expensive.

The third chapter addresses some specific problems that arise when studying bulk fermion matter with the FMD formalism. When using periodic boundary conditions (PBC) in the classical sense, the FMD description becomes infinite dimensional. The main reason for this is that the antisymmetrisation does not stop at the border of the unit-cell. It must be applied to the infinite system. Using well-known theories from solid-state physics, the following steps were taken to address this issue:

- The Gaussian wave packets are replaced with Wannier states with a periodic character. A finite number of these Wannier states are copied periodically over a finite set of Bravais lattice vectors such that the periodicity of the Wannier states is a multiple of the periodicity of the Bravais lattice. The number of copies is chosen such that both periodicities are complementary.

- The overlap matrix is evaluated and shows a block-circulant character. Because of the close connection between circulant systems and Fourier series, many Fourier properties were used to invert the overlap matrix keeping the block-circulant structure. This way, the block-circulant structure translates into the FMD matrix formalism.

- Due to the block structure, where each block reflects the original set of particles translated over a Bravais-lattice vector, the equations of motion can be rewritten in block notation. This way, the infinite-dimensional matrix formalism was reduced to a finite one.

- Although of finite size, the matrix formalism involves a number of infinite sums. These can be avoided by translating the entire problem in the Bloch represen-

tation. The infinite sums are thus transformed into a set of finite sums in reciprocal space.

- As a last step, the doubly periodic system was translated into a single periodic system by taking the limit in which the period of the Wannier states goes to infinity and the wave packets transform into the known single-particle states from a finite FMD problem, i.e. Gaussian wave packets. This transformation reformats the finite sums in reciprocal space into integrations over the first Brillouin zone of the Bravais lattice.

As is seen from these steps, the infinite-dimensional matrix formalism arising from the antisymmetry of a periodic system is recast into a finite-dimensional one. The structure of this new formalism is similar to that of finite-sized FMD, albeit integrated in the reciprocal space.

The validity of this description was evaluated with a study of the spatial and momentum distribution of various lattice systems. The one-dimensional single-particle lattice showed the appearance of a Fermi distribution for high-density systems. Simulations of systems in two and three dimensions, on the other hand, showed that this momentum distribution in fact represented the first Brillouin zone of the lattice in question. This is typical behaviour for fermions placed in a lattice potential and we consider this as a proof of principle for our proposed technique. However, it also indicates that the lattice structure influences the behaviour of the system. To describe bulk properties, it is important that box effects are as small as possible. When deviating from a perfect lattice, these effects could be shown to vanish. This was demonstrated by placing a set of particles randomly in a unit cell. The width of the wave packets is small compared to the box size, but the particles have a considerable overlap. Under these conditions, the system behaves as a free fermion system: the momentum distribution is spherical and the spatial distribution becomes more or less uniform.

This work shows that the bulk properties of fermion systems can be reproduced by the proposed FMD technique. The next steps to be taken, is the further investigation of a number of extensions and applications that we deem important.

With respect to FMD as a computational technique, it is essential to investigate a geometrical integrator that conserves energy, as the Strömer-Verlet algorithm does in CMD. Faou and Lubich proposed a time-reversible Poisson integrator for Gaussian wave packets based on a variational splitting of the Hamiltonian [Fao06, Hai06]. This integrator has the Strömer-Verlet algorithm as its classical limit and shows long-time energy conservation. Since quantum molecular dynamics is based on Gaussian wave

packets, this integrator is suitable for this simulation technique. However, because of the antisymmetrisation, the Faou-Lubich integrator is not applicable for FMD. The variational-splitting method shows to be most promising to FMD. Nonetheless, in contrast to the Strömer-Verlet and Faou-Lubich scheme that stem from the variational-splitting method by separating the potential from the kinetic energy [Lub08], the dynamics resulting from the kinetic energy cannot be integrated analytically.

As was indicated at the end of chapter two, the FMD has ergodic statistical properties. This leads directly to the question how temperature might be measured in such a system. The classical virial theorem is clearly not valid anymore, as fermions are anything but classic. Another classical approach is the demon algorithm that introduces an extra degree of freedom for which the system acts as a heath bath [Cre83, Gou07]. Unfortunately, due to its use of Boltzmann statistics, this technique is inapplicable for quantum systems [Fel00]. A promising way out of this problem is given by Schnack and Feldmeier [Sch97]. The demon added to the system is a weakly interacting harmonic oscillator system of distinguishable particles. Through Boltzmann statistics, it is possible to relate the energy distribution of this "thermometer" to the temperature of the system.

Another computational issue that should be addressed is the implementation of long-range interactions. These interactions are particularly treacherous in periodic systems as they quickly introduce periodic artefacts to the system. An example of such an interaction is the Coulomb interaction that also plays a crucial role in the frustration of nuclear pasta. In the classical picture, the conditional convergence of the lattice sums of the Coulomb interaction is addressed by the Ewald summation [Ewa21, dL80]. An adaptation of this summation should be done for the Gaussian particle-picture.

All the previous ideas were proposed improvements on FMD as a computational technique. The aim of this dissertation was, however, to devise a technique that can be used to study the neutron star crust. At the current point, the technique is ready to investigate the ground state of the neutron star crust, and this for a wide range of densities. The technique which should be employed here is the Rayleigh-Ritz variational principle [Rit08, Mac33] as was indicated at the end of chapter two. The effects of frustration can be investigated by means of potentials containing the basics of frustration. These could be very similar to those used by Horowitz [Hor04b, Hor04a]. Other simple potentials with Gaussian terms are very suitable for FMD. Examples for the study of nuclear matter are the Brink-Boeker potential [Bri67], Malfliet-Tjon [Mal69] or the Volkov potential [Vol65].

Although the ground state properties are interesting, a dynamical evolution contains much more information. Pair correlations and structure functions would allow the investigation of neutrino transport. Cooling schemes and phase transitions can be investigated as well as the effect of strong magnetic fields on the neutron star crust. A full FMD, however, is computationally very demanding. Even though the dynamics of spin, isospin and uncertainty are interesting, the problem becomes more tractable when those are fixed in time. Actually, it is advisable to start studying fermion liquids in the AMD approach. Systematically, more dynamics can be incorporated afterwards.

Notwithstanding the fact that FMD is computationally challenging and despite its complexity and the problems that might be encountered while using it, it shows to be a very promising technique.

This page intentionally left blank

A

Notations and conventions

Section A.1 Units and conversion factors

Throughout this work, all quantities are expressed in natural units. The magnitude of the speed of light, the Planck constant and the Boltzmann constant are all equal to unity, i.e.

$$[c] = [\hbar] = [k] = 1.$$

These units are often used in the calculations of cross sections and other reaction quantities making their expressions easier. Since natural units are constructed from four different units – time, distance, energy and temperature – it is possible to choose one of these units to be equal to the SI unit. Unlike for reaction quantities, where the unit of choice is the MeV, the preference for this work is the unit of length expressed in fm. These are the conversion factors

$$1\ \mathrm{L} = \ell\ \mathrm{fm} \qquad 1\Delta = \frac{\ell}{[c]_{\mathrm{fm/s}}}\ \mathrm{s}$$

$$1\ \mathrm{E} = \frac{[\hbar c]_{\mathrm{MeV\,fm}}}{\ell}\ \mathrm{MeV} \qquad 1\ \mathrm{T} = \frac{[\hbar c]_{\mathrm{fm/s}}}{\ell \cdot [k]_{MeV/K}}\ \mathrm{K}$$

Section A.2 Abbreviations

AMD	Antisymmetrised Molecular Dynamics
bcc	Body-Centred Cubic Bravais lattice
BZ	Brillouin Zone
CFT	Continuous Fourier Transform
CMD	Classical Molecular Dynamics

DFT	Discrete Fourier Transform
DFVP	Dirac-Frenkel Variational Principle
EQMD	Extended Quantum Molecular Dynamics
fcc	Face-Centred Cubic Bravais lattice
FMD	Fermionic Molecular Dynamics
hex	Hexagonal Bravais lattice
MAC	Minimal Antisymmetry Convention
MD	Molecular Dynamics
MFMAC	Modular Form of Minimal Antisymmetry Convention
MFNAC	Modular Form of Nearest Antisymmetry Convention
MIC	Minimal Image Convention
MVP	McLachlan's Variational Principle
NAC	Nearest Antisymmetry Convention
NIC	Nearest Image Convention
PBC	Periodic Boundary Conditions
QMD	Quantum Molecular Dynamics
sc	Simple Cubic Bravais lattice
sqr	Square Bravais lattice
TAPBC	Truncated Antisymmetrised Periodic Boundary conditions
TDVP	Time-Dependent Variational Principle
UCOM	Unitary Correlation Operator Method
WSC	Wigner Seitz Cell

Section A.3 – Math notations, operations and functions

notations

$a, b, c, \ldots$	scalar
$\boldsymbol{a}, \boldsymbol{b}, \boldsymbol{c}, \ldots$	column vector
$\mathbf{A}, \mathbf{B}, \mathbf{C}, \ldots$	matrix
$\square^{\star}$	Complex conjugate of $\square$
$\square^{T}$	Transpose of $\square$
$\square^{\dagger}$	Hermitian transpose of $\square$
$\dot{\square}$	complete time-derivative of $\square$

vector derivatives

$$\frac{f(\boldsymbol{u}, \boldsymbol{v}, \ldots)}{\partial \boldsymbol{u}} \qquad \boldsymbol{w},\ w_p = \frac{f(\boldsymbol{u}, \boldsymbol{v}, \ldots)}{\partial u_p}$$

$\dfrac{f(\boldsymbol{u},\boldsymbol{v},\ldots)}{\partial\boldsymbol{u}\partial\boldsymbol{v}}$ $\qquad$ $\mathbf{A}, A_{pq} = \dfrac{f(\boldsymbol{u},\boldsymbol{v},\ldots)}{\partial u_p \partial v_q}$

operations

$\boldsymbol{u}\cdot\boldsymbol{v}$	$\sum_p u_p v_p$	inner vector product
$\boldsymbol{u}\otimes\boldsymbol{v}$	$\boldsymbol{u}\boldsymbol{v}^T$	outer vector product
$\boldsymbol{u}^2$	$\boldsymbol{u}\cdot\boldsymbol{u}$	
$\boldsymbol{u}\cdot\mathbf{A}\cdot\boldsymbol{v}$	$\sum_{pq} u_p A_{pq} v_q$	
$\mathbf{A}\otimes\mathbf{B}$		Kronecker product

functions

$\mathcal{D}_n(z)$	The parabolic cylinder function
$\mathrm{erf}(z)$	The complex error function
$H_n(z)$	The Hermite polynomial
$\vartheta_n(z\|\tau)$, $\vartheta_n(z,q)$	The Jacobi-theta function
$\vartheta(\boldsymbol{z}\|\mathbf{T})$	The Riemann-theta function

Section A.4 Other notations

wave functions, wave packets and overlaps

$\|\Phi\rangle$	Φ	unnormalised time-dependent N-particle wave function
$\|\phi\rangle$	ϕ	unnormalised time-independent N-particle wave function
$\|\Psi\rangle$	Ψ	normalised time-dependent N-particle wave function
$\|\psi\rangle$	ψ	normalised time-independent N-particle wave function
$\|Q\rangle$	Q	unnormalised N-particle FMD trial state
$\|q\rangle$	q	quantum dressed Gaussian wave packet
$\|w\rangle$	w	quantum dressed wave packet subject to Born-von Kármán boundary conditions
$\|\mathbf{A}\boldsymbol{b}\rangle$	$(\|a\boldsymbol{b}\rangle)$	unnormalised (spherical) Gaussian wave packet
$\|\chi\rangle$	χ	spin state
$\|\zeta\rangle$	ζ	isospin state
$\mathbf{n}_{pq}$		$\langle q_p \| q_q\rangle$
$\mathscr{R}_{pq}$		$\langle \mathbf{A}_p\boldsymbol{b}_p \| \mathbf{A}_q\boldsymbol{b}_q\rangle$, $\quad \langle a_p\boldsymbol{b}_p \| a_q\boldsymbol{b}_q\rangle$
$\mathscr{S}_{pq}$		$\langle \chi_p \| \chi_q\rangle$
$\mathscr{T}_{pq}$		$\langle \zeta_p \| \zeta_q\rangle$

operators and expectation values

$\mathcal{A}, \mathcal{B}, \mathcal{C}, \ldots$		operators
$\mathscr{A}, \mathscr{B}, \mathscr{C}, \ldots$		expectation values of the corresponding operator
$\mathscr{A}_\rho, \mathscr{B}_\rho, \mathscr{C}_\rho, \ldots$		expectation values per unit of volume
$\mathcal{A}$		antisymmetry operator
$\mathcal{B}(\boldsymbol{p})$		boost operator
$\mathcal{B}_I$	$\mathscr{B}_I$	a general one-body operator and its expectation value
$\mathcal{B}_{II}$	$\mathscr{B}_{II}$	a general two-body operator and its expectation value
$\mathcal{H}$	$\mathscr{H}$	Hamiltonian operator and its expectation value
$\mathcal{P}$		parity operator
$\mathcal{R}(\Omega)$		rotation operator
$\mathcal{T}$		time-reversal operator
$\mathcal{T}$		kinetic energy operator
$\mathcal{T}(\boldsymbol{\ell})$		translation operator
$\hat{\boldsymbol{x}}$	$\boldsymbol{r}$	position operator and its expectation value
$\hat{\boldsymbol{k}}$	$\boldsymbol{p}$	momentum operator and its expectation value

lattice notations

$\mathfrak{B}$	a Bravais lattice
$\mathfrak{R}$	a Reciprocal lattice
$\boldsymbol{a}_1, \ldots, \boldsymbol{a}_d$	primitive Bravais-lattice vectors
$\boldsymbol{b}_1, \ldots, \boldsymbol{b}_d$	primitive reciprocal-lattice vectors
$\{\mathfrak{B}\}_m$	a set of Bravais-lattice vectors contained in a $2m+1$ times scaled Wigner-Seitz cell of $\mathfrak{B}$.
$\{\mathfrak{R}\}'_m$	a set of reciprocal-lattice vectors, scaled with a factor $2m+1$, and contained in the first Brillouin zone of $\mathfrak{B}$
$\boldsymbol{R}$	a Bravais-lattice vector
$\boldsymbol{K}$	a reciprocal-lattice vector

special matrices

$\mathbf{n}$	$\mathbf{o}$	the overlap matrix and its inverse
$\mathbf{N}$	$\mathbf{O}$	the overlap matrix and its inverse of a periodic system
$\mathcal{N}_{\boldsymbol{k}}$	$\boldsymbol{\mathcal{O}}_{\boldsymbol{k}}$	the overlap matrix in Bloch representation and its inverse
$\mathcal{N}(\boldsymbol{k})$	$\boldsymbol{\mathcal{O}}(\boldsymbol{k})$	the overlap matrix in Bloch representation and its inverse
$\mathbf{C}$	$\mathbf{C}_\rho$	the metric of a fermion system and a periodic one

B

Reference Formulae

Abstract

In this appendix, some properties of a selection of special functions and expressions for integrals are provided. These expressions are most useful to this work and are used in the analytic derivations of the various chapters and appendices of this dissertation.

Section B.1 Parabolic cylinder functions

The parabolic cylinder functions are the solutions to the Weber differential equation

$$\frac{d^2u}{dz^2} + \left(p + \frac{1}{2} - \frac{z^2}{4}\right)u = 0, \qquad z \in \mathbb{C}.$$

The solutions are written as $u = \mathcal{D}_p(z), \mathcal{D}_p(-z), \mathcal{D}_{-p-1}(iz)$ and $\mathcal{D}_{-p-1}(-iz)$, which are linearly dependent through

$$\mathcal{D}_p(z) = \frac{\Gamma(p+1)}{\sqrt{2\pi}}\left[e^{p\pi i/2}\mathcal{D}_{-p-1}(iz) + e^{-p\pi i/2}\mathcal{D}_{-p-1}(-iz)\right], \tag{B.1a}$$

$$= e^{-p\pi i}\mathcal{D}_p(-z) + \frac{\sqrt{2\pi}}{\Gamma(-p)}e^{-\pi(p+1)i/2}\mathcal{D}_{-p-1}(iz), \tag{B.1b}$$

$$= e^{p\pi i}\mathcal{D}_p(-z) + \frac{\sqrt{2\pi}}{\Gamma(-p)}e^{\pi(p+1)i/2}\mathcal{D}_{-p-1}(-iz). \tag{B.1c}$$

Furthermore they obey the following recursion formulae

$$\mathcal{D}_{p+1}(z) - z\mathcal{D}_p(z) + p\mathcal{D}_{p-1}(z) = 0, \tag{B.2a}$$

$$\frac{d}{dz}\mathcal{D}_p(z) + \frac{1}{2}z\mathcal{D}_p(z) - p\mathcal{D}_{p-1}(z) = 0, \tag{B.2b}$$

$$\frac{d}{dz}\mathcal{D}_p(z) - \frac{1}{2}z\mathcal{D}_p(z) + \mathcal{D}_{p+1}(z) = 0. \tag{B.2c}$$

For integer values of p, $\mathcal{D}_p(z)$ can be related to Hermite polynomials and error functions.

$$\mathcal{D}_n(z) = 2^{-n/2}e^{-z^2/4}H_n\left(\frac{z}{\sqrt{2}}\right), n \geq 0,$$

$$\mathcal{D}_{-1}(z) = e^{z^2/4}\sqrt{\frac{\pi}{2}}\left[1 - \operatorname{erf}\left(\frac{z}{\sqrt{2}}\right)\right].$$

Further information on the parabolic cylinder function can be found in Whittaker and Watson [Whi63], Gradshteyn and Ryzhik [Gra07] as well as Abramowitz and Stegun [Abr72].

Section B.2 Gaussian integrals

Gaussian integrals are common throughout this work. This section collects the most crucial ones. The main reference for these integrals are Eqs. (GR 3.462) in Gradshteyn and Ryzhik [Gra07].

$$\int_0^\infty x^{\nu-1}e^{-\beta x^2 - 2\gamma x}dx = (2\beta)^{-\nu/2}\Gamma(\nu)\exp\left(\frac{\gamma^2}{2\beta}\right)\mathcal{D}_{-\nu}\left(\frac{2\gamma}{\sqrt{2\beta}}\right) \tag{B.3}$$

$$[\mathfrak{Re}\,\beta > 0, \mathfrak{Re}\,\nu > 0].$$

Defining I_n and J_n, for integer $n \geq 0$, as

$$I_n = \int_0^\infty x^n e^{-\beta x^2 - 2\gamma x}dx, \qquad J_n = \int_{-\infty}^\infty x^n e^{-\beta x^2 - 2\gamma x}dx,$$

Eq. (B.3) gives

$$I_n = n!(2\beta)^{-(n+1)/2}\exp\left(\frac{\gamma^2}{2\beta}\right)\mathcal{D}_{-n-1}\left(\frac{2\gamma}{\sqrt{2\beta}}\right), \tag{B.4a}$$

$$J_n = \sqrt{2\pi}e^{n\pi i/2}(2\beta)^{-(n+1)/2}\exp\left(\frac{\gamma^2}{2\beta}\right)\mathcal{D}_n\left(\frac{2i\gamma}{\sqrt{2\beta}}\right). \tag{B.4b}$$

After making use of Eq. (B.2a), the following recursion relations can be obtained :

$$I_{n+1} - \frac{\gamma}{\beta} I_n + \frac{n}{2\beta} I_{n-1} = 0, \tag{B.5a}$$

$$J_{n+1} + \frac{\gamma}{\beta} J_n - \frac{n}{2\beta} J_{n-1} = 0. \tag{B.5b}$$

Section B.3 Multivariate Gaussian integrals

Multivariate Gaussian integrals are generalisations of the one-dimensional Gaussian integrals of section B.2. In this section, the matrix $\mathbf{\Sigma}$ stands for a positive definite symmetrical matrix. All solutions can be reduced to one-dimensional integrals by diagonalising $\mathbf{\Sigma}$ and applying the formulae given in the previous section.

$$\int_{-\infty}^{\infty} \exp\left\{-\frac{1}{2}\boldsymbol{x}\cdot\mathbf{\Sigma}^{-1}\cdot\boldsymbol{x} - \boldsymbol{b}\cdot\boldsymbol{x}\right\} d\boldsymbol{x} = \sqrt{\det(2\pi\mathbf{\Sigma})}\exp\left\{\frac{1}{2}\boldsymbol{b}\cdot\mathbf{\Sigma}\cdot\boldsymbol{b}\right\}, \tag{B.6a}$$

$$\int_{-\infty}^{\infty} \exp\left\{-\frac{1}{2}(\boldsymbol{x}-\boldsymbol{m})\cdot\mathbf{\Sigma}^{-1}\cdot(\boldsymbol{x}-\boldsymbol{m})\right\} d\boldsymbol{x} = \sqrt{\det(2\pi\mathbf{\Sigma})}, \tag{B.6b}$$

$$\int_{-\infty}^{\infty} \mathbf{A}\boldsymbol{x} \exp\left\{-\frac{1}{2}(\boldsymbol{x}-\boldsymbol{m})\cdot\mathbf{\Sigma}^{-1}\cdot(\boldsymbol{x}-\boldsymbol{m})\right\} d\boldsymbol{x} = \sqrt{\det(2\pi\mathbf{\Sigma})}\mathbf{A}\boldsymbol{m}, \tag{B.6c}$$

$$\int_{-\infty}^{\infty} \boldsymbol{x}\cdot\mathbf{A}\cdot\boldsymbol{x} \exp\left\{-\frac{1}{2}(\boldsymbol{x}-\boldsymbol{m})\cdot\mathbf{\Sigma}^{-1}\cdot(\boldsymbol{x}-\boldsymbol{m})\right\} d\boldsymbol{x} = \sqrt{\det(2\pi\mathbf{\Sigma})}\left[\mathrm{Tr}(\mathbf{A}\mathbf{\Sigma}) + \boldsymbol{m}\cdot\mathbf{A}\cdot\boldsymbol{m}\right], \tag{B.6d}$$

$$\int_{-\infty}^{\infty} \boldsymbol{x}\otimes\boldsymbol{x} \exp\left\{-\frac{1}{2}(\boldsymbol{x}-\boldsymbol{m})\cdot\mathbf{\Sigma}^{-1}\cdot(\boldsymbol{x}-\boldsymbol{m})\right\} d\boldsymbol{x} = \sqrt{\det(2\pi\mathbf{\Sigma})}\left[\mathbf{\Sigma} + \boldsymbol{m}\otimes\boldsymbol{m}\right]. \tag{B.6e}$$

Other useful formula are

$$-\frac{1}{2}\boldsymbol{x}\cdot\mathbf{A}\cdot\boldsymbol{x} + \boldsymbol{b}\cdot\boldsymbol{x} = -\frac{1}{2}(\boldsymbol{x}-\mathbf{A}^{-1}\boldsymbol{b})\cdot\mathbf{A}\cdot(\boldsymbol{x}-\mathbf{A}^{-1}\boldsymbol{b}) + \frac{1}{2}\boldsymbol{b}\cdot\mathbf{A}^{-1}\cdot\boldsymbol{b}, \tag{B.7a}$$

$$-\frac{1}{2}(\boldsymbol{x}-\boldsymbol{m}_1)\cdot\mathbf{A}_1\cdot(\boldsymbol{x}-\boldsymbol{m}_1) - \frac{1}{2}(\boldsymbol{x}-\boldsymbol{m}_2)\cdot\mathbf{A}_2\cdot(\boldsymbol{x}-\boldsymbol{m}_2) = -\frac{1}{2}(\boldsymbol{x}-\boldsymbol{m}_c)\cdot\mathbf{A}_c\cdot(\boldsymbol{x}-\boldsymbol{m}_c) + C. \tag{B.7b}$$

It the latter, the relations for $\mathbf{A}_c$, the mean $\boldsymbol{m}_c$ and the constant C are given by

$$\begin{aligned}
\mathbf{A}_c &= \mathbf{A}_1 + \mathbf{A}_2, \\
\boldsymbol{m}_c &= (\mathbf{A}_1 + \mathbf{A}_2)^{-1}(\mathbf{A}_1\boldsymbol{m}_1 + \mathbf{A}_2\boldsymbol{m}_2), \\
C &= \frac{1}{2}(\mathbf{A}_1\boldsymbol{m}_1 + \mathbf{A}_2\boldsymbol{m}_2)\cdot(\mathbf{A}_1 + \mathbf{A}_2)^{-1}\cdot(\mathbf{A}_1\boldsymbol{m}_1 + \mathbf{A}_2\boldsymbol{m}_2) \\
&\quad - \frac{1}{2}(\boldsymbol{m}_1\cdot\mathbf{A}_1\cdot\boldsymbol{m}_1 + \boldsymbol{m}_2\cdot\mathbf{A}_2\cdot\boldsymbol{m}_2).
\end{aligned}$$

Section B.4 — The discrete Fourier transform in lattice representation

For many physicists, Fourier transforms are automatically connected to the Continuous Fourier Transform (CFT). Computationally, however, the continuous function is sampled in a set of discrete points. To approximate the CFT, the integral is replaced by a finite sum creating the Discrete Fourier Transform (DFT).

Consider a set of $2m+1$ complex numbers $\{\mathscr{X}_p = \mathscr{X}(x_p), p = -m,\ldots,m\}$, where space is discretised over

$$x_p = \frac{Tp}{2m+1}, \qquad p = -m,\ldots,m.$$

The DFT of this discrete set is given by

$$\mathscr{F}_q = \mathscr{F}(\omega_q) = \sum_{p=-m}^{m} \mathscr{X}_p e^{-ix_p\omega_q}, \tag{B.8}$$

and is the discrete representation of $\mathscr{X}_p$ in reciprocal space. The discretisation of the reciprocal space is given by

$$\omega_q = \frac{2\pi n}{T}, \qquad q = -m,\ldots,m.$$

As with CFTs, the DFT has an inverse transformation recovering the set of $\mathscr{X}_p$'s exactly and is

$$\mathscr{X}_p = \frac{1}{2m+1}\sum_{q=-m}^{m} \mathscr{F}_q e^{ix_p\omega_q}. \tag{B.9}$$

This is readily confirmed by substitution of Eq. (B.8) in Eq. (B.9) and employing the orthogonality relation [Arf95]

$$\sum_{q=-m}^{m} e^{ix_p\omega_q} = (2m+1)\sum_{p=-\infty}^{\infty}\delta_{q,(2m+1)p}. \tag{B.10}$$

Multidimensional DFTs are given by

$$\mathscr{F}_{\boldsymbol{q}} = \sum_{p_1=-m}^{m}\cdots\sum_{p_d=-m}^{m}\mathscr{X}_{\boldsymbol{p}}e^{-i\boldsymbol{x}_p\cdot\boldsymbol{\omega}_q}, \tag{B.11a}$$

$$\mathscr{X}_{\boldsymbol{p}} = \frac{1}{(2m+1)^d}\sum_{q_1=-m}^{m}\cdots\sum_{q_d=-m}^{m}\mathscr{F}_{\boldsymbol{q}}e^{i\boldsymbol{x}_p\cdot\boldsymbol{\omega}_q}, \tag{B.11b}$$

where the values of $\mathscr{X}_{\boldsymbol{p}}$ and $\mathscr{F}_{\boldsymbol{q}}$ are functional values taken on lattice in normal or reciprocal space. The lattice points are given by the lattice vectors

$$\boldsymbol{x}_p = \frac{T}{2m+1}\boldsymbol{p}, \qquad p_j = -m,\ldots,m, \tag{B.12a}$$

$$\boldsymbol{\omega}_q = \frac{2\pi}{T}\boldsymbol{q}, \qquad q_j = -m,\ldots,m. \tag{B.12b}$$

The above formula (B.11) are now easily transformed in the language of Bravais lattices. Since the Bravais lattice vectors $\boldsymbol{R}$ are generated by the primitive vectors $\boldsymbol{a}_1$, $\boldsymbol{a}_2$ and $\boldsymbol{a}_3$ as

$$\boldsymbol{R} = p_1\boldsymbol{a}_1 + p_2\boldsymbol{a}_2 + p_3\boldsymbol{a}_3 = \mathbf{B}\boldsymbol{p},$$

the reciprocal lattice vectors given by

$$\boldsymbol{K} = q_1\boldsymbol{b}_1 + q_2\boldsymbol{b}_2 + q_3\boldsymbol{b}_3,$$

with

$$\boldsymbol{b}_1 = 2\pi\frac{\boldsymbol{a}_2\times\boldsymbol{a}_3}{\boldsymbol{a}_1\cdot(\boldsymbol{a}_2\times\boldsymbol{a}_3)},$$
$$\boldsymbol{b}_2 = 2\pi\frac{\boldsymbol{a}_3\times\boldsymbol{a}_1}{\boldsymbol{a}_1\cdot(\boldsymbol{a}_2\times\boldsymbol{a}_3)},$$
$$\boldsymbol{b}_3 = 2\pi\frac{\boldsymbol{a}_1\times\boldsymbol{a}_2}{\boldsymbol{a}_1\cdot(\boldsymbol{a}_2\times\boldsymbol{a}_3)},$$

can be written as

$$\boldsymbol{K} = q_1\boldsymbol{b}_1 + q_2\boldsymbol{b}_2 + q_3\boldsymbol{b}_3 = 2\pi(\mathbf{B}^T)^{-1}\boldsymbol{q}.$$

Substituting these Bravais lattice vectors and Reciprocal lattice vectors in Eq. (B.11), they read

$$\mathscr{F}_K = \sum_{R\in\{\mathfrak{B}\}_m} \mathscr{X}_R e^{-\frac{i}{2m+1}R\cdot K}, \tag{B.13a}$$

$$\mathscr{X}_R = \frac{1}{(2m+1)^3} \sum_{K\in\{\mathfrak{R}\}_m} \mathscr{F}_K e^{\frac{i}{2m+1}R\cdot K}, \tag{B.13b}$$

where $\mathfrak{B}$ is the Bravais lattice with reciprocal lattice $\mathfrak{R}$. The notation $\{\mathfrak{Q}\}_m$, refers to the set of lattice vectors $\boldsymbol{q}$ of lattice $\mathfrak{Q}$, given by

$$\boldsymbol{q} = n_1\boldsymbol{v}_1 + n_2\boldsymbol{v}_2 + n_3\boldsymbol{v}_3, \qquad n_k = -m,\ldots,m,$$

where $\boldsymbol{v}_1$, $\boldsymbol{v}_2$ and $\boldsymbol{v}_3$ the primitive vectors are of lattice $\mathfrak{Q}$. By embedding the factor $1/2m+1$ into the reciprocal lattice vectors $\boldsymbol{K}$ as $\boldsymbol{K} = (2m+1)\boldsymbol{k}$, it can be written that

$$\mathscr{F}_k = \sum_{R\in\{\mathfrak{B}\}_m} \mathscr{X}_R e^{-i\boldsymbol{R}\cdot\boldsymbol{k}}, \tag{B.14a}$$

$$\mathscr{X}_R = \frac{1}{(2m+1)^3} \sum_{\boldsymbol{k}\in\{\mathfrak{R}\}'_m} \mathscr{F}_k e^{i\boldsymbol{R}\cdot\boldsymbol{k}}. \tag{B.14b}$$

The notation $\{\mathfrak{R}\}'_m$ refers to the set of vectors $\boldsymbol{k}$ contained within the Brillouin zone of Bravais lattice $\mathfrak{B}$.

The discretisation of the CFT leads towards a DFT, hence it also works in the other way. The more points taken, the closer the DFT tends to the CFT. When m tends to infinity the CFT reads

$$\mathscr{F}(\boldsymbol{k}) = \sum_{\boldsymbol{R}\in\mathfrak{B}} \mathscr{X}(\boldsymbol{R}) e^{-i\boldsymbol{R}\cdot\boldsymbol{k}}, \tag{B.15a}$$

$$\mathscr{X}(\boldsymbol{R}) = \frac{1}{V_{BZ}} \int_{V_{BZ}} \mathscr{F}(\boldsymbol{k}) e^{i\boldsymbol{R}\cdot\boldsymbol{k}} d\boldsymbol{k}. \tag{B.15b}$$

Section B.5 The Jacobi Theta functions

Theta functions were first systematically studied by C. G. J. Jacobi in his great treatise on Elliptical functions [Jac29] where he obtained their properties by purely algebraical methods. This section restricts itself to some of their fundamental properties.

A nice overview of these functions can be found in the work of Whittaker and Watson [Whi63] as well as the work of Bellman [Bel61] and the Tata lectures on theta [Mum83]. Further information can be found in Gradshteyn and Ryzhik [Gra07] as well as Abramowitz and Stegun [Abr72]. The convention employed here, is the one of Tannery and Molk [Tan02, Whi63].

Let τ be a complex number whose imaginary part is positive and define the nome q as $q = \exp(i\pi\tau)$, so that $|q| < 1$. Using these, the four theta functions are defined as the sum of the following series

$$\vartheta_1(z) = \frac{1}{i}\sum_{n=-\infty}^{\infty}(-1)^n q^{(n+\frac{1}{2})^2} e^{(2n+1)iz} = 2\sum_{n=1}^{\infty}(-1)^{n+1} q^{(n-\frac{1}{2})^2}\sin(2n-1)z, \tag{B.16a}$$

$$\vartheta_2(z) = \sum_{n=-\infty}^{\infty} q^{(n+\frac{1}{2})^2} e^{(2n+1)iz} = 2\sum_{n=1}^{\infty} q^{(n-\frac{1}{2})^2}\cos(2n-1)z, \tag{B.16b}$$

$$\vartheta_3(z) = \sum_{n=-\infty}^{\infty} q^{n^2} e^{2niz} = 1 + 2\sum_{n=1}^{\infty} q^{n^2}\cos 2nz, \tag{B.16c}$$

$$\vartheta_4(z) = \sum_{n=-\infty}^{\infty}(-1)^n q^{n^2} e^{2niz} = 1 + 2\sum_{n=1}^{\infty}(-1)^n q^{n^2}\cos 2nz. \tag{B.16d}$$

For brevity, the nome q will usually not be specified, so that $\vartheta_n(z)$ will be written for $\vartheta_n(z,q)$. When it is desired to exhibit the dependence on the parameter τ, it will be written as $\vartheta_n(z|\tau)$. From the above definitions it is obvious that $\vartheta_1(z)$ is an odd function while the others are even.

It is readily seen that the Theta-functions satisfy the partial differential equation

$$\frac{1}{4}\pi i\frac{\partial^2\vartheta_n(z|\tau)}{\partial z^2} + \frac{\partial\vartheta_n(z|\tau)}{\partial\tau} = 0. \tag{B.17}$$

By means of their definitions, all theta functions can be related to one another by the appropriate addition of $\frac{\pi}{2}$ or $\frac{\pi\tau}{2}$. They are related as

$$\vartheta_1(z) = -\vartheta_2(z+\tfrac{\pi}{2}) = -iM\vartheta_4(z+\tfrac{\pi\tau}{2}) = -iM\vartheta_3(z+\tfrac{\pi}{2}+\tfrac{\pi\tau}{2}), \tag{B.18a}$$

$$\vartheta_2(z) = \vartheta_1(z+\tfrac{\pi}{2}) = M\vartheta_3(z+\tfrac{\pi\tau}{2}) = M\vartheta_4(z+\tfrac{\pi}{2}+\tfrac{\pi\tau}{2}), \tag{B.18b}$$

$$\vartheta_3(z) = \vartheta_4(z+\tfrac{\pi}{2}) = M\vartheta_2(z+\tfrac{\pi\tau}{2}) = M\vartheta_1(z+\tfrac{\pi}{2}+\tfrac{\pi\tau}{2}), \tag{B.18c}$$

$$\vartheta_4(z) = \vartheta_3(z+\tfrac{\pi}{2}) = -iM\vartheta_1(z+\tfrac{\pi\tau}{2}) = iM\vartheta_2(z+\tfrac{\pi}{2}+\tfrac{\pi\tau}{2}), \tag{B.18d}$$

with $M = q^{1/4}e^{iz}$. The above relations imply that the theta functions are quasi doubly-periodic, i.e.

$$\vartheta_1(z) = -\vartheta_1(z-\pi) = -N\vartheta_1(z-\pi\tau), \tag{B.19a}$$
$$\vartheta_2(z) = -\vartheta_2(z-\pi) = N\vartheta_2(z-\pi\tau), \tag{B.19b}$$
$$\vartheta_3(z) = \vartheta_3(z-\pi) = N\vartheta_3(z-\pi\tau), \tag{B.19c}$$
$$\vartheta_4(z) = \vartheta_4(z-\pi) = -N\vartheta_4(z-\pi\tau), \tag{B.19d}$$

with $N = q^{-1}e^{-2iz}$.

The roots of the theta-functions are easily obtained through their quasi double-periodic structure. Each theta-function has zeros at

$$z_0 + m\pi + n\pi\tau,$$

where z_0 is easily obtained through the functional relations (B.18). Since one zero of $\vartheta_1(z)$ is obviously $z = 0$, it follows that the roots of $\vartheta_1(z)$, $\vartheta_2(z)$, $\vartheta_3(z)$ and $\vartheta_4(z)$ are the points congruent to 0, $\frac{\pi}{2}$, $\frac{\pi}{2} + \frac{\pi\tau}{2}$ and $\frac{\pi\tau}{2}$, respectively.

Finally, the relations connecting the theta functions with period-ratios of τ and $-1/\tau$, referenced as the modular transformation, are obtained by means of the Poisson summation formula and read

$$(-i\tau)^{\frac{1}{2}}\vartheta_1(z|\tau) = -i\exp\left(\frac{z^2}{i\pi\tau}\right)\vartheta_1\left(-\frac{z}{\tau}\middle|-\frac{1}{\tau}\right), \tag{B.20a}$$
$$(-i\tau)^{\frac{1}{2}}\vartheta_2(z|\tau) = \exp\left(\frac{z^2}{i\pi\tau}\right)\vartheta_4\left(-\frac{z}{\tau}\middle|-\frac{1}{\tau}\right), \tag{B.20b}$$
$$(-i\tau)^{\frac{1}{2}}\vartheta_3(z|\tau) = \exp\left(\frac{z^2}{i\pi\tau}\right)\vartheta_3\left(-\frac{z}{\tau}\middle|-\frac{1}{\tau}\right), \tag{B.20c}$$
$$(-i\tau)^{\frac{1}{2}}\vartheta_4(z|\tau) = \exp\left(\frac{z^2}{i\pi\tau}\right)\vartheta_2\left(-\frac{z}{\tau}\middle|-\frac{1}{\tau}\right). \tag{B.20d}$$

Next to the summation formula for the Theta functions, i.e. Eqs. (B.16), there are

also Jacobi's expressions for the Theta-functions as infinite products. They read

$$\vartheta_1(z) = 2q^{1/4}\sin(z)\prod_{n=1}^{\infty}(1-2q^{2n}\cos(2z)+q^{4n})\prod_{n=1}^{\infty}(1-q^{2n}), \tag{B.21a}$$

$$\vartheta_2(z) = 2q^{1/4}\cos(z)\prod_{n=1}^{\infty}(1+2q^{2n}\cos(2z)+q^{4n})\prod_{n=1}^{\infty}(1-q^{2n}), \tag{B.21b}$$

$$\vartheta_3(z) = \prod_{n=1}^{\infty}(1+2q^{2n-1}\cos(2z)+q^{4n-2})\prod_{n=1}^{\infty}(1-q^{2n}), \tag{B.21c}$$

$$\vartheta_4(z) = \prod_{n=1}^{\infty}(1-2q^{2n-1}\cos(2z)+q^{4n-2})\prod_{n=1}^{\infty}(1-q^{2n}). \tag{B.21d}$$

These formula are useful in obtaining an infinite series for $\vartheta_n'(z)/\vartheta_n(z)$ where $\vartheta_n'(z) = \partial\vartheta_n(z|\tau)/\partial z$. To this end, the logarithm of Eqs (B.21) are taken. Under the conditions that $|\Im\mathrm{m}\, z| < \pi\,\Im\mathrm{m}\, t/2$ these derivatives are written as

$$\frac{\vartheta_1'(z)}{\vartheta_1(z)} = \cot(z) + 4\sum_{n=1}^{\infty}\frac{q^{2n}\sin(2nz)}{1-q^{2n}}, \tag{B.22a}$$

$$\frac{\vartheta_2'(z)}{\vartheta_2(z)} = -\tan(z) + 4\sum_{n=1}^{\infty}\frac{(-1)^n q^{2n}\sin(2nz)}{1-q^{2n}}, \tag{B.22b}$$

$$\frac{\vartheta_3'(z)}{\vartheta_3(z)} = 4\sum_{n=1}^{\infty}\frac{(-1)^n q^{n}\sin(2nz)}{1-q^{2n}}, \tag{B.22c}$$

$$\frac{\vartheta_4'(z)}{\vartheta_4(z)} = 4\sum_{n=1}^{\infty}\frac{q^{n}\sin(2nz)}{1-q^{2n}}. \tag{B.22d}$$

Section B.6 The Riemann Theta function

Up to this point, Theta functions of one complex variable have been established, the general form of a theta function of several complex variables is, in matrix notation, written compactly as

$$\vartheta(\boldsymbol{z}|\mathbf{T}) = \sum_{\boldsymbol{n}}\exp\left(i\pi\boldsymbol{n}\cdot\mathbf{T}\cdot\boldsymbol{n} + 2i\boldsymbol{z}\cdot\boldsymbol{n}\right), \tag{B.23}$$

where the summation happens over all integral vectors $\boldsymbol{n}$. The matrix $\mathbf{T}$ is complex symmetric such that $\mathbf{T}' = -i\mathbf{T}$ is positive definite.

The quasi double-periodicity is seen by means of the unit vector $\boldsymbol{e}_k$ where all components are zero except for a one which occurs in the kth place. Using this it reads

$$\vartheta(\boldsymbol{z}|\mathbf{T}) = \vartheta(\boldsymbol{z} + \pi\boldsymbol{e}_k|\mathbf{T}) = \exp(i\pi\boldsymbol{e}_k \cdot \mathbf{T} \cdot \boldsymbol{e}_k + 2i\boldsymbol{e}_k \cdot z)\vartheta(\boldsymbol{z} + \pi\mathbf{T}\boldsymbol{e}_k|\mathbf{T}). \tag{B.24}$$

Finally the Poisson summation formula leads to the following modular transformation

$$\sqrt{\det(-i\mathbf{T})}\vartheta(\boldsymbol{z}|\mathbf{T}) = \exp\left(\frac{\boldsymbol{z} \cdot \mathbf{T}^{-1} \cdot \boldsymbol{z}}{i\pi}\right)\vartheta(\mathbf{T}^{-1}\boldsymbol{z}| - \mathbf{T}^{-1}). \tag{B.25}$$

C

GAUSSIAN WAVE PACKETS AND RELATED INTEGRALS

ABSTRACT

This appendix introduces the basic properties of Gaussian wave packets by means of analytical derivations. Not only its mean positions and spread but also the equations of motion. Special attention is given those equations physical interpretation.

Section C.1 Representation of the Gaussian wave packet

A general unnormalised Gaussian wave packet $|\mathbf{A}\boldsymbol{b}\rangle$ has the following representations in coordinate and momentum space.

$$\langle \boldsymbol{x}|\mathbf{A}\boldsymbol{b}\rangle = \exp\left\{-\frac{1}{2}(\boldsymbol{x}-\boldsymbol{b})\cdot\mathbf{A}^{-1}\cdot(\boldsymbol{x}-\boldsymbol{b})\right\}, \tag{C.1}$$

$$\langle \boldsymbol{k}|\mathbf{A}\boldsymbol{b}\rangle = \sqrt{\det(\mathbf{A})}\exp\left\{-\frac{1}{2}\boldsymbol{k}\cdot\mathbf{A}\cdot\boldsymbol{k} - i\boldsymbol{b}\cdot\boldsymbol{k}\right\}. \tag{C.2}$$

The matrix $\mathbf{A}$ is positive definite symmetric and couples all coordinates. The vector $\boldsymbol{b}$ is a phase-space vector which, as will be seen later on, can be associated with the mean position in phase space.

When $\mathbf{A} = a\mathbf{I}$, the Gaussian wave packet has a spherical nature and decouples the

various coordinates. It is written as $|a\boldsymbol{b}\rangle$ with the representations

$$\langle \boldsymbol{x}|a\boldsymbol{b}\rangle = \exp\left\{-\frac{(\boldsymbol{x}-\boldsymbol{b})^2}{2a}\right\}, \tag{C.3}$$

$$\langle \boldsymbol{k}|a\boldsymbol{b}\rangle = a^{d/2}\exp\left\{-\frac{a\boldsymbol{k}^2}{2} - i\boldsymbol{b}\cdot\boldsymbol{k}\right\}, \tag{C.4}$$

where d represents the spatial dimensionality of the system. The variance of the system is a which has a positive real value, i.e. $\Re\mathrm{e}\, a > 0$.

Section C.2 Overlap, mean positions and variance

Matrix elements of Gaussian wave packets can often be written in a closed analytical form. The latter can be obtained by making use of the expressions in appendix B. This way, the results for the spatial overlap, the mean position and the mean momentum can formally be deduced.

The spatial overlap of two Gaussian wave packets, throughout this work referenced as $\mathscr{R}_{pq}$, reads

$$\begin{aligned}\mathscr{R}_{pq} = \left\langle \mathbf{A}_p\boldsymbol{b}_p|\mathbf{A}_q\boldsymbol{b}_q\right\rangle &= \sqrt{\det(2\pi\mathbf{A}_p^\dagger(\mathbf{A}_p^\dagger+\mathbf{A}_q)^{-1}\mathbf{A}_q)} \\ &\times\exp\left\{-\frac{1}{2}(\boldsymbol{b}_p^\star-\boldsymbol{b}_q)\cdot(\mathbf{A}_p^\dagger+\mathbf{A}_q)^{-1}\cdot(\boldsymbol{b}_p^\star-\boldsymbol{b}_q)\right\}.\end{aligned} \tag{C.5}$$

Analogously, the one-body matrix elements of the operators $\hat{\boldsymbol{x}}$ and $\hat{\boldsymbol{k}}$ lead to

$$\langle \mathbf{A}_p\boldsymbol{b}_p|\hat{\boldsymbol{x}}|\mathbf{A}_q\boldsymbol{b}_q\rangle = \left[\mathbf{A}_q(\mathbf{A}_p^\dagger+\mathbf{A}_q)^{-1}\boldsymbol{b}_p^\star + \mathbf{A}_p^\dagger(\mathbf{A}_p^\dagger+\mathbf{A}_q)^{-1}\boldsymbol{b}_q\right]\cdot\mathscr{R}_{pq}, \tag{C.6}$$

$$\langle \mathbf{A}_p\boldsymbol{b}_p|\hat{\boldsymbol{k}}|\mathbf{A}_q\boldsymbol{b}_q\rangle = i(\mathbf{A}_p^\dagger+\mathbf{A}_q)^{-1}(\boldsymbol{b}_p^\star-\boldsymbol{b}_q)\cdot\mathscr{R}_{pq}. \tag{C.7}$$

With this the following definitions can be introduced

$$\boldsymbol{r}_{pq} = \frac{\langle \mathbf{A}_p\boldsymbol{b}_p|\hat{\boldsymbol{x}}|\mathbf{A}_q\boldsymbol{b}_q\rangle}{\langle \mathbf{A}_p\boldsymbol{b}_p|\mathbf{A}_q\boldsymbol{b}_q\rangle}, \qquad \boldsymbol{p}_{pq} = \frac{\langle \mathbf{A}_p\boldsymbol{b}_p|\hat{\boldsymbol{k}}|\mathbf{A}_q\boldsymbol{b}_q\rangle}{\langle \mathbf{A}_p\boldsymbol{b}_p|\mathbf{A}_q\boldsymbol{b}_q\rangle}.$$

The mean position and momenta of a single Gaussian wave packet are thus defined by $\boldsymbol{r}_p \equiv \boldsymbol{r}_{pp}$ and $\boldsymbol{p}_p \equiv \boldsymbol{p}_{pp}$. For a Gaussian wave packet, these relations can be related to the mean position in phase space $\boldsymbol{b}$ by $\boldsymbol{b} = \boldsymbol{r} + i\mathbf{A}\boldsymbol{p}$.

The spreading of the wave packet in phase space is determined by means of the operators $(\hat{\boldsymbol{x}} - \boldsymbol{r}_{pq})^2$ and $(\hat{\boldsymbol{k}} - \boldsymbol{p}_{pq})^2$. The matrix elements read

$$(\Delta \boldsymbol{r}_{pq})^2 = \frac{\langle \mathbf{A}_p \boldsymbol{b}_p | (\widehat{\boldsymbol{x}} - \boldsymbol{r}_{pq})^2 | \mathbf{A}_q \boldsymbol{b}_q \rangle}{\langle \mathbf{A}_p \boldsymbol{b}_p | \mathbf{A}_q \boldsymbol{b}_q \rangle} = \mathrm{Tr}\left(\mathbf{A}_p^\dagger (\mathbf{A}_p^\dagger + \mathbf{A}_q)^{-1} \mathbf{A}_q \right), \tag{C.8}$$

$$(\Delta \boldsymbol{p}_{pq})^2 = \frac{\langle \mathbf{A}_p \boldsymbol{b}_p | (\widehat{\boldsymbol{k}} - \boldsymbol{p}_{pq})^2 | \mathbf{A}_q \boldsymbol{b}_q \rangle}{\langle \mathbf{A}_p \boldsymbol{b}_p | \mathbf{A}_q \boldsymbol{b}_q \rangle} = \mathrm{Tr}\left((\mathbf{A}_p^\dagger + \mathbf{A}_q)^{-1} \right), \tag{C.9}$$

where the variance of the wave packets are defined through $(\Delta \boldsymbol{r}_p)^2 \equiv (\Delta \boldsymbol{r}_{pp})^2$ and $(\Delta \boldsymbol{p}_p)^2 \equiv (\Delta \boldsymbol{p}_{pp})^2$.

For three-dimensional uncoupled circular Gaussian wave packets, i.e. $\mathbf{A} = a\mathbf{I}$, the expressions reduce to

$$\mathscr{R}_{pq} = \left(\frac{2\pi a_p^\star a_q}{a_p^\star + a_q} \right)^{d/2} \exp\left\{ -\frac{(\boldsymbol{b}_p^\star - \boldsymbol{b}_q)^2}{2(a_p^\star + a_q)} \right\}, \tag{C.10}$$

$$\boldsymbol{r}_{pq} = \frac{a_q \boldsymbol{b}_p^\star + a_p^\star \boldsymbol{b}_q}{a_p^\star + a_q}, \tag{C.11}$$

$$\boldsymbol{p}_{pq} = i \frac{\boldsymbol{b}_p^\star - \boldsymbol{b}_q}{a_p^\star + a_q}, \tag{C.12}$$

$$(\Delta \boldsymbol{r}_{pq})^2 = \frac{3 a_p^\star a_q}{a_p^\star + a_q}, \tag{C.13}$$

$$(\Delta \boldsymbol{p}_{pq})^2 = \frac{3}{a_p^\star + a_q}. \tag{C.14}$$

Section C.3 The equations of motion for a Gaussian wave packet

The equations of motion for a trial state, determined by the time-dependent variational principle, are given by Eq. (2.21). This section employs these equations to determine the time evolution of a Gaussian wave packet under the influence of a Hamiltonian $\mathcal{H}$. The positive definite matrix $\mathbf{A}$ is written as $\mathbf{A} = \sum_\alpha A_\alpha \mathbf{S}^\alpha$ in the symmetrical basis $\mathbf{S}^\alpha$. Here, the matrices $\mathbf{S}^\alpha$ are an orthonormal basis of symmetrical matrices, i.e. $\mathrm{Tr}(\mathbf{S}^\alpha \mathbf{S}^\beta) = \delta_{\alpha\beta}$.

The geometry of the parameter manifold on which the Gaussian wave packet lives, is determined by the metric **C**. This metric is evaluated through the knowledge of the derivatives of the overlap $n = \langle \mathbf{A}\boldsymbol{b}|\mathbf{A}\boldsymbol{b}\rangle$. They are

$$\frac{\partial^2 \ln n}{\partial \boldsymbol{b}^\star \partial \boldsymbol{b}} = (\mathbf{A}^\dagger + \mathbf{A})^{-1} \tag{C.15a}$$

$$\frac{\partial^2 \ln n}{\partial \boldsymbol{b}^\star \partial A_\beta} = -i(\mathbf{A}^\dagger + \mathbf{A})^{-1}\mathbf{S}^\beta \boldsymbol{p} \tag{C.15b}$$

$$\frac{\partial^2 \ln n}{\partial A^\star_\alpha \partial \boldsymbol{b}} = i\boldsymbol{p}^T \mathbf{S}^\alpha (\mathbf{A}^\dagger + \mathbf{A})^{-1} \tag{C.15c}$$

$$\frac{\partial^2 \ln n}{\partial A^\star_\alpha \partial A_\beta} = \frac{1}{2}\,\mathrm{Tr}[(\mathbf{A}^\dagger + \mathbf{A})^{-1}\mathbf{S}^\beta (\mathbf{A}^\dagger + \mathbf{A})^{-1}\mathbf{S}^\alpha] + \boldsymbol{p}\cdot\mathbf{S}^\alpha (\mathbf{A}^\dagger + \mathbf{A})^{-1}\mathbf{S}^\beta \cdot \boldsymbol{p} \tag{C.15d}$$

These values used in the equation of motion Eq. (2.21) lead to

$$i(\mathbf{A}^\dagger + \mathbf{A})^{-1}\dot{\boldsymbol{b}} + (\mathbf{A}^\dagger + \mathbf{A})^{-1}\dot{\mathbf{A}}\boldsymbol{p} = \frac{\partial \mathscr{H}}{\partial \boldsymbol{b}^\star}, \tag{C.16a}$$

$$-\boldsymbol{p}\cdot\mathbf{S}^\alpha (\mathbf{A}^\dagger + \mathbf{A})^{-1}\cdot\dot{\boldsymbol{b}} + \frac{i}{2}\,\mathrm{Tr}[(\mathbf{A}^\dagger + \mathbf{A})^{-1}\dot{\mathbf{A}}(\mathbf{A}^\dagger + \mathbf{A})^{-1}\mathbf{S}^\alpha] + i\boldsymbol{p}\cdot\mathbf{S}^\alpha (\mathbf{A}^\dagger + \mathbf{A})^{-1}\dot{\mathbf{A}}\cdot\boldsymbol{p} = \frac{\partial \mathscr{H}}{\partial A^\star_\alpha}. \tag{C.16b}$$

Substitution of Eq. (C.16a) into Eq. (C.16b), while multiplication with $\mathbf{S}^\alpha$ and summation over α leads to

$$\dot{\boldsymbol{b}} - i\dot{\mathbf{A}}\boldsymbol{p} = -i(\mathbf{A}^\dagger + \mathbf{A})\frac{\partial \mathscr{H}}{\partial \boldsymbol{b}^\star}, \tag{C.17a}$$

$$\frac{i}{2}\left(\frac{\partial \mathscr{H}}{\partial \boldsymbol{b}^\star}\otimes\boldsymbol{p} + \boldsymbol{p}\otimes\frac{\partial \mathscr{H}}{\partial \boldsymbol{b}^\star}\right) + \frac{i}{2}(\mathbf{A}^\dagger + \mathbf{A})^{-1}\dot{\mathbf{A}}(\mathbf{A}^\dagger + \mathbf{A})^{-1} = \sum_\alpha \frac{\partial \mathscr{H}}{\partial A^\star_\alpha}\mathbf{S}^\alpha. \tag{C.17b}$$

Here the following property was employed, $\sum_\alpha \mathrm{Tr}(\mathbf{B}\mathbf{S}^\alpha)\mathbf{S}^\alpha = (\mathbf{B} + \mathbf{B}^T)/2$. The equations of motion are now given by

$$i\dot{\boldsymbol{b}} = (\mathbf{A}^\dagger + \mathbf{A})\frac{\partial \mathscr{H}}{\partial \boldsymbol{b}^\star} - \dot{\mathbf{A}}\boldsymbol{p}, \tag{C.18a}$$

$$i\dot{\mathbf{A}} = (\mathbf{A}^\dagger + \mathbf{A})\left(2\sum_\alpha \frac{\partial \mathscr{H}}{\partial A^\star_\alpha}\mathbf{S}^\alpha - i\frac{\partial \mathscr{H}}{\partial \boldsymbol{b}^\star}\otimes\boldsymbol{p} - i\boldsymbol{p}\otimes\frac{\partial \mathscr{H}}{\partial \boldsymbol{b}^\star}\right)(\mathbf{A}^\dagger + \mathbf{A}). \tag{C.18b}$$

Section C.4 — Physical interpretation of the equations of motion for a Gaussian wave packet

Howbeit the equations of motion, stemming from the time-dependent variational principle, have been deduced in their most general form, their physical meaning is not obvious. A better understanding of the underlying physics can be obtained when investigating a one-dimensional system. In the one-dimensional case, the equations can be rewritten in a way better known in physics. To this end, a Taylor expansion of the Hamiltonian operator $\mathcal{H}(\hat{x},\hat{k})$ will be performed. For a one-dimensional system, the equations of motion (C.18) reduce to

$$i\dot{b} = (a^\star + a)\frac{\partial \mathscr{H}}{\partial b^\star} - \dot{a}p, \tag{C.19a}$$

$$i\dot{a} = 2(a^\star + a)^2\left(\frac{\partial \mathscr{H}}{\partial a^\star} - i\frac{\partial \mathscr{H}}{\partial b^\star}p\right). \tag{C.19b}$$

In order to proceed, only the derivatives of $\mathscr{H}$ with respect to $b^\star$ and $a^\star$ need to be evaluated. A Taylor expansion of $\mathcal{H}(\hat{x},\hat{k})$ leads to the following derivatives in Eqs. (C.19):

$$\frac{\partial}{\partial b^\star}\left\langle \frac{\hat{x}^m\hat{k}^n + \hat{k}^n\hat{x}^m}{2m!n!}\right\rangle, \qquad \frac{\partial}{\partial a^\star}\left\langle \frac{\hat{x}^m\hat{k}^n + \hat{k}^n\hat{x}^m}{2m!n!}\right\rangle. \tag{C.20}$$

Before evaluating these derivatives, it is of interest to deduce recurrence relations for $\langle\hat{x}^m\hat{k}^n\rangle$ and $\langle\hat{k}^n\hat{x}^m\rangle$ since the derivatives introduce higher powers in $\hat{x}$ and $\hat{k}$. The two expectation values can be written down as double integrals in coordinate and momentum space. That is to say

$$\langle\hat{x}^m\hat{k}^n\rangle = \frac{1}{\langle ab|ab\rangle}\iint \langle ab|\hat{x}^m|x\rangle\langle x|k\rangle\langle k|\hat{k}^n|ab\rangle dxdk, \tag{C.21a}$$

$$\langle\hat{k}^n\hat{x}^m\rangle = \frac{1}{\langle ab|ab\rangle}\iint \langle ab|\hat{k}^n|k\rangle\langle k|x\rangle\langle x|\hat{x}^m|ab\rangle dxdk. \tag{C.21b}$$

Making use of the recurrence relations indicated by Eq. (B.5b) the following recurrence relations can be deduced:

$$\langle \hat{x}^{m+1}\hat{k}^n\rangle = r\langle \hat{x}^m\hat{k}^n\rangle + \frac{maa^\star}{a+a^\star}\langle \hat{x}^{m-1}\hat{k}^n\rangle + i\frac{na^\star}{a+a^\star}\langle \hat{x}^m\hat{k}^{n-1}\rangle, \tag{C.22a}$$

$$\langle \hat{k}^n\hat{x}^{m+1}\rangle = r\langle \hat{k}^n\hat{x}^m\rangle + \frac{maa^\star}{a+a^\star}\langle \hat{k}^n\hat{x}^{m-1}\rangle - i\frac{na}{a+a^\star}\langle \hat{k}^{n-1}\hat{x}^m\rangle, \tag{C.22b}$$

$$\langle \hat{x}^m\hat{k}^{n+1}\rangle = p\langle \hat{x}^m\hat{k}^n\rangle + i\frac{ma^\star}{a+a^\star}\langle \hat{x}^{m-1}\hat{k}^n\rangle + \frac{n}{a+a^\star}\langle \hat{x}^m\hat{k}^{n-1}\rangle, \tag{C.22c}$$

$$\langle \hat{k}^{n+1}\hat{x}^m\rangle = p\langle \hat{k}^n\hat{x}^m\rangle - i\frac{ma}{a+a^\star}\langle \hat{k}^n\hat{x}^{m-1}\rangle + \frac{n}{a+a^\star}\langle \hat{k}^{n-1}\hat{x}^m\rangle. \tag{C.22d}$$

The evaluation of the derivatives of the Taylor coefficients of Eq. (C.20) is now straightforward but lengthy. The proper usage of the recurrence relations in Eq. (C.22) reveals the true nature of the equations of motion through the following derivatives:

$$\frac{\partial}{\partial b^\star}\langle \hat{x}^m\hat{k}^n\rangle = \frac{am}{a+a^\star}\langle \hat{x}^{m-1}\hat{k}^n\rangle + i\frac{n}{a+a^\star}\langle \hat{x}^m\hat{k}^{n-1}\rangle, \tag{C.23a}$$

$$\frac{\partial}{\partial b^\star}\langle \hat{k}^n\hat{x}^m\rangle = \frac{am}{a+a^\star}\langle \hat{k}^n\hat{x}^{m-1}\rangle + i\frac{n}{a+a^\star}\langle \hat{k}^{n-1}\hat{x}^n\rangle, \tag{C.23b}$$

$$\begin{aligned}\frac{\partial}{\partial a^\star}\langle \hat{x}^m\hat{k}^n\rangle = {}& \frac{m(m-1)a^2}{2(a+a^\star)^2}\langle \hat{x}^{m-2}\hat{k}^n\rangle - \frac{n(n-1)}{2(a+a^\star)^2}\langle \hat{x}^m\hat{k}^{n-2}\rangle \\ & + ip\frac{ma}{a+a^\star}\langle \hat{x}^{m-1}\hat{k}^n\rangle - p\frac{n}{a+a^\star}\langle \hat{x}^m\hat{k}^{n-1}\rangle \\ & + i\frac{mna}{(a+a^\star)^2}\langle \hat{x}^{m-1}\hat{k}^{n-1}\rangle,\end{aligned} \tag{C.23c}$$

$$\begin{aligned}\frac{\partial}{\partial a^\star}\langle \hat{k}^n\hat{x}^m\rangle = {}& \frac{m(m-1)a^2}{2(a+a^\star)^2}\langle \hat{k}^n\hat{x}^{m-2}\rangle - \frac{n(n-1)}{2(a+a^\star)^2}\langle \hat{k}^{n-2}\hat{x}^m\rangle \\ & + ip\frac{ma}{a+a^\star}\langle \hat{k}^n\hat{x}^{m-1}\rangle - p\frac{n}{a+a^\star}\langle \hat{k}^{n-1}\hat{x}^n\rangle \\ & + i\frac{mna}{(a+a^\star)^2}\langle \hat{k}^{n-1}\hat{x}^{m-1}\rangle.\end{aligned} \tag{C.23d}$$

Finally, inserting the above equations after Taylor expanding $\mathcal{H}(\hat{x},\hat{k})$ in Eq. (C.19),

the equations of motion obtain their classical form through $b = r + iap$ being

$$\dot{r} = \left\langle \frac{\partial \mathcal{H}}{\partial \hat{k}} \right\rangle, \tag{C.24a}$$

$$\dot{p} = -\left\langle \frac{\partial \mathcal{H}}{\partial \hat{x}} \right\rangle, \tag{C.24b}$$

$$i\dot{a} = a^2 \left\langle \frac{\partial^2 \mathcal{H}}{\partial \hat{x}^2} \right\rangle + 2ia \left\langle \frac{\partial^2 \mathcal{H}}{\partial \hat{x} \partial \hat{k}} \right\rangle - \left\langle \frac{\partial^2 \mathcal{H}}{\partial \hat{k}^2} \right\rangle. \tag{C.24c}$$

An identical approach can be followed for the coupled multivariate Gaussian wave packets. The recursion relation of choice, required for this deduction was obtained by Willink [Wil05] and replaces Eq. (B.5b). It reads

$$I_{n_1 \dots n_k+1 \dots n_d} = \boldsymbol{m}_k I_{n_1 \dots n_d} + \sum_{j=1}^{d} \boldsymbol{\Sigma}_{kj} n_j I_{n_1 \dots n_j - 1 \dots n_d}, \tag{C.25}$$

with

$$I_{n_1 \dots n_d} = \sqrt{\det(2\pi\boldsymbol{\Sigma})} \int \prod_{i=1}^{d} x_i^{n_i} \exp\left\{ -\frac{1}{2} (\boldsymbol{x} - \boldsymbol{m}) \cdot \boldsymbol{\Sigma}^{-1} \cdot (\boldsymbol{x} - \boldsymbol{m}) \right\} d\boldsymbol{x}.$$

The general equations of motion, given by Eq. (C.18), reduce now to their most elegant structure

$$\dot{\boldsymbol{r}} = \left\langle \frac{\partial \mathcal{H}}{\partial \hat{\boldsymbol{k}}} \right\rangle, \tag{C.26a}$$

$$\dot{\boldsymbol{p}} = -\left\langle \frac{\partial \mathcal{H}}{\partial \hat{\boldsymbol{x}}} \right\rangle, \tag{C.26b}$$

$$i\dot{\mathbf{A}} = \mathbf{A} \left\langle \frac{\partial^2 \mathcal{H}}{\partial \hat{\boldsymbol{x}} \partial \hat{\boldsymbol{x}}} \right\rangle \mathbf{A} - \left\langle \frac{\partial^2 \mathcal{H}}{\partial \hat{\boldsymbol{k}} \partial \hat{\boldsymbol{k}}} \right\rangle + i\mathbf{A} \left\langle \frac{\partial^2 \mathcal{H}}{\partial \hat{\boldsymbol{x}} \partial \hat{\boldsymbol{k}}} \right\rangle + i \left\langle \frac{\partial^2 \mathcal{H}}{\partial \hat{\boldsymbol{k}} \partial \hat{\boldsymbol{x}}} \right\rangle \mathbf{A}. \tag{C.26c}$$

Section C.5 The equation of motion in a damped harmonic oscillator

In sections C.3 and C.4, the time evolution of a Gaussian wave packet under the operation of a Hamiltonian $\mathcal{H}$ was discussed. Here, the peculiar situation of a damped

harmonic oscillator is considered. The Hamiltonian governing the particle is of the form

$$\mathcal{H} = \mathcal{T}(\hat{\boldsymbol{k}}) + \mathcal{V}(\hat{\boldsymbol{x}}) = \frac{\hat{\boldsymbol{k}}^2}{2m} + C + \boldsymbol{\Gamma}\cdot\hat{\boldsymbol{x}} + \frac{1}{2}\hat{\boldsymbol{x}}\cdot\mathbf{K}\cdot\hat{\boldsymbol{x}}.$$

Within this Hamiltonian, the potential contains a damping term $\boldsymbol{\Gamma}$ while the oscillator term is given by the real symmetric matrix $\mathbf{K}$. The mass of the particle, appearing in the kinetic energy, is represented by m. The expectation value of such a Hamiltonian is deduced by means of the equation (B.6d) and reads

$$\mathscr{T} = \frac{1}{2m}[\boldsymbol{p}^2 + (\Delta\boldsymbol{p})^2] \tag{C.27a}$$

$$\mathscr{V} = C + \boldsymbol{\Gamma}\cdot\boldsymbol{r} + \frac{1}{2}\boldsymbol{r}\cdot\mathbf{K}\cdot\boldsymbol{r} + \frac{1}{2}\mathrm{Tr}(\mathbf{K}\mathbf{A}(\mathbf{A}^\dagger + \mathbf{A})^{-1}\mathbf{A}^\dagger). \tag{C.27b}$$

Calculations of the derivatives with respect to the conjugate phase-space position $\boldsymbol{b}^\star$ and the conjugate variance matrix $\mathbf{A}^\dagger$ are required for the equations of motion (C.18). These derivatives translate into

$$\frac{\partial\mathscr{T}}{\partial\boldsymbol{b}^\star} = \frac{i}{m}(\mathbf{A}^\dagger + \mathbf{A})^{-1}\boldsymbol{p}, \tag{C.28a}$$

$$\frac{\partial\mathscr{V}}{\partial\boldsymbol{b}^\star} = (\mathbf{A}^\dagger + \mathbf{A})^{-1}\mathbf{A}(\boldsymbol{\Gamma} + \mathbf{K}\boldsymbol{r}), \tag{C.28b}$$

$$\sum_\alpha \frac{\partial\mathscr{T}}{\partial A^\star_\alpha}\mathbf{S}^\alpha = -\frac{(\mathbf{A}^\dagger + \mathbf{A})^{-1}}{m}\left(\frac{(\mathbf{A}^\dagger + \mathbf{A})^{-1}}{2} + \boldsymbol{p}\otimes\boldsymbol{p}\right), \tag{C.28c}$$

$$\sum_\alpha \frac{\partial\mathscr{V}}{\partial A^\star_\alpha}\mathbf{S}^\alpha = \frac{1}{2}(\mathbf{A}^\dagger + \mathbf{A})^{-1}\left[\mathbf{A}\mathbf{K}\mathbf{A} - \mathbf{A}(\boldsymbol{\Gamma} + \mathbf{K}\boldsymbol{r})\otimes(\boldsymbol{b}^\star - \boldsymbol{b}) - (\boldsymbol{b}^\star - \boldsymbol{b})\otimes(\boldsymbol{\Gamma} + \mathbf{K}\boldsymbol{r})\mathbf{A}\right](\mathbf{A}^\dagger + \mathbf{A})^{-1}, \tag{C.28d}$$

such that the equations of motion become

$$i\dot{\boldsymbol{b}} = \mathbf{A}\boldsymbol{\Gamma} + \mathbf{A}\mathbf{K}\boldsymbol{b}, \tag{C.29a}$$

$$i\dot{\mathbf{A}} = \mathbf{A}\mathbf{K}\mathbf{A} - \frac{1}{m}\mathbf{I}. \tag{C.29b}$$

Making use of the identity $\boldsymbol{b} = \boldsymbol{r} + i\mathbf{A}\boldsymbol{p}$, they transform into equations that adopt the same form as the classical ones

$$\dot{\boldsymbol{r}} = \frac{\boldsymbol{p}}{m}, \tag{C.30a}$$

$$\dot{\boldsymbol{p}} = \boldsymbol{\Gamma} + \mathbf{K}\boldsymbol{r}, \tag{C.30b}$$

$$\dot{\mathbf{A}} = \frac{i}{m}\mathbf{I} - \mathbf{A}\mathbf{K}\mathbf{A}. \tag{C.30c}$$

These equations are a natural result out of the physical formulation of the evolution equations (C.26).

Section C.6 The two-body-matrix element

Integrals involving Gaussians and polynomials are analytically solvable. This is advantageous when computing matrix elements and lead to fairly simple expressions for one- and two-body operators.

A two-body operator of the type $\mathcal{O}(\hat{\boldsymbol{x}}_1 - \hat{\boldsymbol{x}}_2)$ has matrix-elements written as $\mathscr{O}_{pqrs} = \langle \mathbf{A}_p \boldsymbol{b}_p, \mathbf{A}_r \boldsymbol{b}_r | \mathcal{O} | \mathbf{A}_q \boldsymbol{b}_q, \mathbf{A}_s \boldsymbol{b}_s \rangle$. When writing $\mathscr{O}_{pqrs}$ down in integral form and transforming the integration into the integration over relative $\boldsymbol{x} = \boldsymbol{x}_1 - \boldsymbol{x}_2$ and central coordinates $\boldsymbol{X} = \frac{1}{2}(\boldsymbol{x}_1 + \boldsymbol{x}_2)$, the integration over the central coordinate can readily be carried out. The matrix element reduces to

$$\mathscr{O}_{pqrs} = \frac{\mathscr{R}_{pq}\mathscr{R}_{rs}}{\sqrt{\det(2\pi \mathbf{A}_{pqrs})}} \int \mathcal{O}(\boldsymbol{x}) \exp\left\{ -\frac{1}{2} (\boldsymbol{x} - \boldsymbol{r}_{pqrs}) \cdot \mathbf{A}_{pqrs} \cdot (\boldsymbol{x} - \boldsymbol{r}_{pqrs}) \right\} d\boldsymbol{x}. \quad \text{(C.31)}$$

Here, a re-normalised variance is introduced as

$$\mathbf{A}_{pqrs} = \mathbf{A}_p^\dagger (\mathbf{A}_p^\dagger + \mathbf{A}_q)^{-1} \mathbf{A}_q + \mathbf{A}_r^\dagger (\mathbf{A}_r^\dagger + \mathbf{A}_s)^{-1} \mathbf{A}_s,$$

and a quantum mechanical displacement vector as $\boldsymbol{r}_{pqrs} = \boldsymbol{r}_{pq} - \boldsymbol{r}_{rs}$.

To end this section, a closed expression is given for the expectation values of a Gaussian potential and the Coulomb potential. The Gaussian operator $\mathcal{G}$ defined as

$$\mathcal{G}(\hat{\boldsymbol{x}}_1 - \hat{\boldsymbol{x}}_2) = \exp\left\{ -\frac{1}{2} (\hat{\boldsymbol{x}}_1 - \hat{\boldsymbol{x}}_2) \cdot \boldsymbol{\Gamma}^{-1} \cdot (\hat{\boldsymbol{x}}_1 - \hat{\boldsymbol{x}}_2) \right\},$$

has as matrix element $\mathscr{G}_{pqrs}$. This matrix element is obtained by means of Eq. (C.31) and reads

$$\mathscr{G}_{pqrs} = \mathscr{R}_{pq}\mathscr{R}_{rs} \sqrt{\det\left[\boldsymbol{\Gamma}(\boldsymbol{\Gamma} + \mathbf{A}_{pqrs})^{-1} \right]} \times \exp\left\{ -\frac{1}{2} \boldsymbol{r}_{pqrs} \cdot (\mathbf{A}_{pqrs} + \boldsymbol{\Gamma})^{-1} \cdot \boldsymbol{r}_{pqrs} \right\}. \quad \text{(C.32)}$$

This matrix element can be used to obtain the one for the Coulomb potential. The Coulomb potential $\mathcal{C}$ is defined as

$$\mathcal{C}(\hat{\boldsymbol{x}}_1 - \hat{\boldsymbol{x}}_2) = \frac{\alpha}{\sqrt{(\hat{\boldsymbol{x}}_1 - \hat{\boldsymbol{x}}_2)^2}}$$

and can be written in Gaussian form by means of Eq. (GR 3.471.15) from Gradshteyn and Ryzhik [Gra07]. Thus

$$\mathcal{C}(\hat{\boldsymbol{x}}_1 - \hat{\boldsymbol{x}}_2) = \frac{2\alpha}{\sqrt{\pi}} \int_0^\infty \frac{1}{(2\gamma)^{3/2}} \exp\left\{ -\frac{(\hat{\boldsymbol{x}}_1 - \hat{\boldsymbol{x}}_2)^2}{2\gamma} \right\} d\gamma.$$

A closed expression for the matrix element of $\mathcal{C}$ can be obtained for three-dimensional spherical wave packets ($\mathbf{A} = a\mathbf{I}$), and reads

$$\mathscr{C}_{pqrs} = \mathscr{R}_{pq}\mathscr{R}_{rs} \frac{1}{\sqrt{\boldsymbol{r}^2_{pqrs}}} \operatorname{erf}\left\{ \sqrt{\frac{\boldsymbol{r}^2_{pqrs}}{2a_{pqrs}}} \right\}. \tag{C.33}$$

D

The Wigner distribution of a Gaussian wave packet

Section D.1 Definition of the Wigner distribution

The Wigner distribution of a wave packet with normalised wave function ψ is denoted as $W(\boldsymbol{X},\boldsymbol{P})$ and is defined as [Wig32]

$$W(\boldsymbol{X},\boldsymbol{P}) = \frac{1}{\pi^d}\int \langle \boldsymbol{X}-\boldsymbol{S}|\psi\rangle \langle \psi|\boldsymbol{X}+\boldsymbol{S}\rangle \exp(2i\boldsymbol{P}\cdot\boldsymbol{S})d\boldsymbol{S}, \tag{D.1}$$

wherein $\boldsymbol{X}$ and $\boldsymbol{P}$ the phase-space coordinates represent. It has the remarkable property that when the distribution is integrated over the spatial variable $\boldsymbol{X}$ it gives the probability distribution in momentum space and vice versa.

$$\int W(\boldsymbol{X},\boldsymbol{P})d\boldsymbol{P} = \psi^\star(\boldsymbol{X})\psi(\boldsymbol{X}), \tag{D.2a}$$

$$\int W(\boldsymbol{X},\boldsymbol{P})d\boldsymbol{X} = \psi^\star(\boldsymbol{P})\psi(\boldsymbol{P}), \tag{D.2b}$$

and is therefore normalised over the entire space

$$\iint W(\boldsymbol{X},\boldsymbol{P})d\boldsymbol{X}d\boldsymbol{P} = 1. \tag{D.3}$$

The Wigner distribution is not identical to the classical phase-space distribution. The latter represents the joint probability that a particle has certain phase-space coordinates. Uncertainty relations prohibit this. Furthermore, it is hardly surprising that the distribution is not positive definite for an arbitrary wave function. However, when the wave function is composed of wave packets following well defined trajectories, the

negative terms become negligible and the naive interpretation of the Wigner distribution as a joint probability in phase space is permissible [Got89]. For more information on the Wigner distribution the following references are useful [Wig32, Tan07, Cas08].

Section D.2 The Wigner distribution of a one-dimensional Gaussian wave packet

For a one-dimensional normalised Gaussian wave packet $f|ab\rangle$, the Wigner distribution is given by

$$W(X,P) = \frac{1}{\pi}\exp\left\{-\frac{2}{a+a^\star}(X-r)^2 - \frac{2i(a-a^\star)}{a+a^\star}(X-r)(P-p) - \frac{2aa^\star}{a+a^\star}(P-p)^2\right\}. \quad \text{(D.4)}$$

Note that X and P are the phase-space coordinates, while r and p are the mean position and momentum. The equidensity contours of the Wigner distribution are thus ellipsoids centred in phase space at (r,p). The equations of these ellipses are given by

$$\frac{2}{a+a^\star}(X-r)^2 + 2i\frac{a-a^\star}{a+a^\star}(X-r)(P-p) + \frac{2aa^\star}{a+a^\star}(P-p)^2 = C, \quad \text{(D.5)}$$

with C a constant. For the further course of this discussion it will be of greater interest to represent the phase space dimensionless by rescaling it. Introducing the new coordinates $\bar{X} = (X-R)/\lambda$ and $\bar{P} = \lambda(P-p)$ the equation (D.5) becomes

$$\frac{2\lambda^2}{a+a^\star}\bar{X}^2 + 2i\frac{a-a^\star}{a+a^\star}\bar{X}\bar{P} + \frac{2aa^\star}{a+a^\star}\frac{\bar{P}^2}{\lambda^2} = C. \quad \text{(D.6)}$$

A quick look at this equation shows that the ellipse is rotated over an angle ϕ between the major axis and the X-axis and is determined by

$$\tan(2\phi) = \frac{i\lambda^2(a-a^\star)}{\lambda^4 - aa^\star}. \quad \text{(D.7)}$$

The length of the major and minor axis is the given by

$$2C\cdot\frac{\lambda^4 + aa^\star + \sqrt{(\lambda^4-a^2)(\lambda^4-a^{\star 2})}}{(a+a^\star)\lambda^2}, \quad \text{(D.8a)}$$

$$2C\cdot\frac{(a+a^\star)\lambda^2}{\lambda^4 + aa^\star + \sqrt{(\lambda^4-a^2)(\lambda^4-a^{\star 2})}}. \quad \text{(D.8b)}$$

From this it is visible that the surface of the ellipse is independent of a and reads πC^2. This indicates that under a certain orientation in phase space the particle is of minimal uncertainty, i.e. $\phi = \pi/2$ or a multiple of it.

Section D.3 The Wigner distribution of a free Gaussian wave packet

The equations of motion of a free Gaussian wave packet follow from Eqs. (C.30)

$$\dot{r} = \frac{p}{m}, \qquad \dot{p} = 0, \qquad \dot{a} = \frac{i}{m}. \tag{D.9}$$

This indicates that the particle travels on the classic path through phase space. The imaginary part of the variance, however, increases with time. This translates into a change in orientation of the Wigner distribution. There $a(t) = a_0 + \frac{it}{m}$ the scaling λ is taken to be $\sqrt{\mathfrak{Re}\, a_0}$ and a scaled time is introduced through

$$\bar{T} = \frac{t + \mathfrak{Im}\, a_0 m t}{\mathfrak{Re}\, a_0 m}.$$

With these, the equidensity contours are described by

$$\bar{X}^2 - 2\bar{T}\bar{X}\bar{P} + (1 + \bar{T}^2)\bar{P}^2 = C. \tag{D.10}$$

These contours are orientated over ϕ as

$$\tan(2\phi) = \frac{2}{\bar{T}}, \tag{D.11}$$

and have major and minor axis with length

$$2C \cdot (2 + \bar{T}^2 + \sqrt{\bar{T}^2 + 4}\bar{T}), \tag{D.12a}$$

$$2C \cdot \frac{1}{2 + \bar{T}^2 + \sqrt{\bar{T}^2 + 4}\bar{T}}. \tag{D.12b}$$

All this can be understood in the following way. During the time evolution of the free Gaussian wave packet, its mean position and momentum follow the classical path. During this evolution, the Wigner distribution orientates and elongates itself such that the wave packet evolves towards a plane wave. The latter is best understood by means of Eqs. (D.2). The projection on the momentum space becomes more narrow in time centred around p while the projection on coordinate space spreads out in time. In the end, the wave packet will have a well defined momentum p but will be completely uncertain in coordinate space.

Section D.4 The Wigner distribution for a Gaussian wave packet in a harmonic oscillator

The equations of motion for a Gaussian wave packet acting in a harmonic oscillator $\mathcal{V} = \frac{1}{2}m\omega^2\hat{x}^2$ are given by Eq. (C.30)

$$\dot{r} = p, \qquad \dot{p} = -m\omega^2 r, \qquad \dot{a} = \frac{i}{m} - im\omega^2 a^2. \tag{D.13}$$

It is clear that the equations for the mean position in phase space and the variance are decoupled while the solutions for the mean position and momentum indicate that the particle follows the classical phase-space path, i.e.

$$r(t) = r_0\cos(\omega t), \qquad p(t) = -r_0 m\omega\sin(\omega t), \tag{D.14}$$

with initial zero momentum and initial position r_0. The time evolution of the variance according to Eq. (D.13) shows the existence of a static solution for $a = 1/m\omega$. Wave packets with this variance evolving under influence of a harmonic oscillator are referred to as the coherent state of the harmonic oscillator. Other wave packets with a different variance are referred to as squeezed states and are well known to quantum optics [Ger05, Fox06].

The most general solution of the variance is given by

$$a(t) = \frac{m\omega a_0\cos(\omega t) + i\sin(\omega t)}{m\omega(\cos(\omega t) + im\omega a_0\sin(\omega t))}, \tag{D.15}$$

indicating it evolves periodically, but with half the period of the harmonic oscillator. As a result of Eq. (D.5), this periodicity will be incorporated in the Wigner distribution and manifests itself through a rigid rotation in phase space of the distribution. Introducing the scaled variables $\lambda = 1/\sqrt{m\omega}$, $\bar{T} = \omega t$ and $\epsilon = a_0 m\omega$, the contours of the Wigner distribution are defined by

$$\begin{aligned}(1+\epsilon-\epsilon^\star-\epsilon\epsilon^\star)\left(\bar{X}-r+i(\bar{P}-p)\right)^2 e^{2i\bar{T}} \\ +(1-\epsilon+\epsilon^\star-\epsilon\epsilon^\star)\left(\bar{X}-r-i(\bar{P}-p)\right)^2 e^{-2i\bar{T}} \\ +(2\epsilon\epsilon^\star+2)\left((\bar{X}-r)^2+(\bar{P}-p)^2\right) = 2C(\epsilon+\epsilon^\star).\end{aligned} \tag{D.16}$$

Using the previous defined contours, the evolution of the Wigner distribution of a particle in a harmonic oscillator can be better understood. As indicated earlier, the

initial coordinate of the packet was r_0 and $p_0 = 0$. Using Eq. (D.7) the orientation of the ellipse evolves linearly in time as $\phi(t) = \phi_0 - \bar{T}$. Here ϕ_0 is the initial orientation and differs from zero if a_0 is imaginary. This linear time evolution of the orientation angle indicates a steady rotation of the Wigner distribution in phase space.The length of the major and minor axis of the ellipses, according to Eqs. (D.8), are given by

$$2C \cdot \frac{1 + \epsilon\epsilon^\star + \sqrt{(\epsilon^2 - 1)(\epsilon^{\star 2} - 1)}}{\epsilon + \epsilon^\star}, \tag{D.17a}$$

$$2C \cdot \frac{\epsilon + \epsilon^\star}{1 + \epsilon\epsilon^\star + \sqrt{(\epsilon^2 - 1)(\epsilon^{\star 2} - 1)}}, \tag{D.17b}$$

and are time independent. This means that the rotation is rigid. Furthermore, as a side note, the above formula also indicate that for coherent states, i.e. $\epsilon = 1$, and in the scaled representation, the distribution is circular while for squeezed states they are not. Hence shedding a light on the origin of its name.

Concluding, it is clear that the Wigner distribution of a particle in a harmonic oscillator, moves along the classical trajectories rotating rigidly in phase space gaining and loosing uncertainty according to the projections on the phase-space coordinates. While coherent states will always have minimal uncertainty, the squeezed states will have this on specific times.

This page intentionally left blank

E

Matrix elements of antisymmetric wave functions

Abstract

In Fermionic molecular dynamics, one of the main ingredients for a solution of the equations of motion of the system, is the calculation of overlap-matrix elements and expectation values of operators with antisymmetric wave functions and their derivatives. This appendix provides the mathematical background to calculate these matrix elements.

Section E.1 The antisymmetric many-body wave function

In FMD, the many-body states live in the antisymmetric subspace of the A-body Hilbert space. The one-body Hilbert space $\mathcal{H}_1$ is a product of coordinate, spin- and isospin-space. The A-body Hilbert space adopts then the form

$$\mathcal{H}_A = \mathcal{H}_1 \otimes \cdots \otimes \mathcal{H}_1.$$

The wave functions corresponding with this Hilbert space are product states $|\psi_1\rangle \otimes \cdots \otimes |\psi_A\rangle$ given in coordinate space by

$$\langle x_1|\phi_1\rangle \cdots \langle x_A|\psi_A\rangle.$$

To project a state on the antisymmetric subspace we use the antisymmetrisation operator

$$\mathcal{A} = \frac{1}{\sqrt{A!}} \sum_{\mathcal{P}} \mathrm{sgn}(\mathcal{P})\mathcal{P},$$

where the operator $\mathcal{P}$ performs a permutation among the wave functions. This results in antisymmetric wave functions Ψ that can be written as Slater determinants [Sla29]

$$\langle x_1,\ldots,x_A|\Psi\rangle = \frac{1}{\sqrt{A!}}\det\begin{pmatrix}\langle x_1|\psi_1\rangle & \ldots & \langle x_1|\psi_A\rangle\\ \vdots & \ddots & \vdots\\ \langle x_A|\psi_1\rangle & \ldots & \langle x_A|\psi_A\rangle\end{pmatrix}. \tag{E.1}$$

When introducing the notation

$$\Psi(\boldsymbol{x}) \equiv \langle x_1,\ldots,x_A|\Psi\rangle$$

and removing from this wave function Ψ the coordinate x_i and single-particle wave function ψ_j, the remaining antisymmetric state is written as $\Psi_{ij}(\boldsymbol{x})$. The latter is proportional to the minor of the matrix in the right hand side of Eq. (E.1). Accordingly $\Psi(\boldsymbol{x})$ can be written as

$$\Psi(\boldsymbol{x}) = \sqrt{\frac{1}{A}}\sum_{j=1}^{A}(-1)^{i+j}\psi_j(x_i)\Psi_{ij}(\boldsymbol{x}). \tag{E.2}$$

This notation will be useful in the next sections.

Section E.2 The overlap-matrix element $\langle\Phi|\Psi\rangle$

Before embarking on the derivation of the expectation values of operators, it is necessary to determine the overlap of two Slater determinants $\langle\Phi|\Psi\rangle$. It will be shown, by means of induction, that $\langle\Phi|\Psi\rangle = \det\mathbf{n}$, where $\mathbf{n}$ is the overlap matrix with elements $\mathbf{n}_{ij} = \langle\phi_i|\psi_j\rangle$. It is clear that for $A = 1$ this is valid. Assume that it is valid for $A-1$. The overlap $\langle\Phi|\Psi\rangle$, written as

$$\langle\Phi|\Psi\rangle = \int \Phi^\star(\boldsymbol{x})\Psi(\boldsymbol{x})d\boldsymbol{x},$$

is expanded by developing the wave functions according to x_i. Using Eq. (E.2), the overlap obtains the form

$$\langle\Phi|\Psi\rangle = \frac{1}{A}\sum_{pq=1}^{A}(-1)^{2i+p+q}\int \phi_p^\star(x_i)\psi_q(x_i)\Phi_{ip}^\star(\boldsymbol{x})\Psi_{iq}(\boldsymbol{x})d\boldsymbol{x}.$$

Here Φ_{ip} and Ψ_{iq} are Slater determinants of $A-1$ particles and are independent of x_i. By means of their definition, the above equation can be rewritten as

$$\langle\Phi|\Psi\rangle = \frac{1}{A}\sum_{pq=1}^{A}(-1)^{p+q}\langle\phi_p|\psi_q\rangle\det(\mathbf{m}_{pq}),$$

where $\mathbf{m}_{pq}$ is the determinant of the overlap matrix created by Φ_{ip} and Ψ_{iq}. Algebraically, $\mathbf{m}$ represents the minor of $\mathbf{n}$, revealing the result

$$\langle\Phi|\Psi\rangle = \det\mathbf{n}. \tag{E.3}$$

Hence, the following relations can be set

$$\langle\Phi_{ip}|\Psi_{iq}\rangle = \mathbf{m}_{pq}, \tag{E.4}$$

$$\langle\Phi_{ip,jr}|\Psi_{iq,js}\rangle = \mathbf{m}_{pq,rs}. \tag{E.5}$$

For this we introduced $\mathbf{m}_{pq}$ as the (pq) primary minor of the overlap matrix $\mathbf{n}$, while $\mathbf{m}_{pq,rs}$ is the (pq,rs) secondary minor. These relations will be useful in the next sections.

Section E.3 The expectation value of a one-body operator

In this section we derive the expectation value of the one-body operator $\mathcal{B}_I$, which, in the single-particle description, is

$$\mathcal{B}_I = \sum_{i=1}^{A} \mathcal{B}_{I,i}(x_i),$$

where $\mathcal{B}_{I,i}(x_i)$ is the operator acting on coordinates x_i. After separation of the coordinate x_i in the total sum, the expectation value becomes

$$\langle\Phi|\mathcal{B}_I|\Psi\rangle = \sum_{ipq=1}^{A} (-1)^{2i+p+q} \int \phi_p^\star(x_i)\mathcal{B}_{I,i}(x_i)\psi_q(x_i)\Phi_{ip}^\star(\boldsymbol{x})\Psi_{iq}(\boldsymbol{x})d\boldsymbol{x}.$$

Introducing the minor $\mathbf{m}$ of the overlap matrix $\mathbf{n}$, this can written as

$$\langle\Phi|\mathcal{B}_I|\Psi\rangle = \frac{1}{A}\sum_{ipq=1}^{A} (-1)^{p+q}\langle\phi_p|\mathcal{B}_{I,i}|\psi_q\rangle\mathbf{m}_{pq}.$$

Using the relation between the inverse and the adjugate of a matrix, i.e.

$$\mathbf{A}^{-1} = \frac{1}{\det\mathbf{A}}\operatorname{adj}\mathbf{A},$$

with $(\operatorname{adj}\mathbf{A})_{ij} = (-1)^{i+j}(\min\mathbf{A})_{ji}$, this becomes

$$\langle\Phi|\mathcal{B}_I|\Psi\rangle = \det\mathbf{n}\sum_{pq=1}^{A}\langle\phi_p|\mathcal{B}_I|\psi_q\rangle\mathbf{o}_{qp}.$$

Here, the matrix **o** is defined as the inverse of the overlap matrix **n**. With this result, the expectation value of the one body operator $\mathcal{B}_I$ for the wave state Ψ is given by

$$\mathscr{B}_I = \frac{\langle\Psi|\mathcal{B}_I|\Psi\rangle}{\langle\Psi|\Psi\rangle} = \sum_{pq=1}^{A} \langle\psi_p|\mathcal{B}_I|\psi_q\rangle \mathbf{o}_{qp}. \tag{E.6}$$

Section E.4 The expectation value for a two-body operator

In this section, we derive the expectation value of a two-body operator. In the one-particle representation, the operator is written as

$$\mathcal{B}_{II} = \sum_{ij=1}^{A} \mathcal{B}_{II,ij}.$$

To start, some linear algebraic expressions will be proved. Assume that **A** is a $N \times N$ matrix, then

$$(\mathbf{A}^{-1}_{qp}\mathbf{A}^{-1}_{sr} - \mathbf{A}^{-1}_{qr}\mathbf{A}^{-1}_{sp}) \det \mathbf{A} = 2 \cdot (-1)^{p+q+r+s} \sigma_{pq,rs} \mathbf{M}_{pq,rs}, \tag{E.7}$$

where $\mathbf{M}_{pq,rs}$ is the (pq,rs) secondary minor of **A** and $\sigma_{pq,rs}$ is defined as

$$\sigma_{pq,rs} = \begin{cases} 1 & p > r, q > s \quad \text{or} \quad p < r, q < s \\ -1 & p > r, q < s \quad \text{or} \quad p < r, q > s \end{cases}$$

To prove this, remark that

$$\delta_{kp} = \sum_{m=1}^{N} \mathbf{A}_{km}\mathbf{A}^{-1}_{mp},$$

and implement the analytic definition of the inverse matrix through its primary minor. This leads to

$$\delta_{kp} \det \mathbf{A} = \sum_{m=1}^{N} (-1)^{m+p} \mathbf{A}_{km} \mathbf{M}_{pm}.$$

There the (pm) primary minor of **A** is, by definition, a determinant, the above equation is expanded, by similar means, as

$$\delta_{kp}\delta_{lr} \det \mathbf{A} = \sum_{\substack{mn=1 \\ m\neq n}}^{N} (-1)^{m+n+p+r} \mathbf{A}_{km}\mathbf{A}_{ln} \sigma_{pm,rn} \mathbf{M}_{pm,rn}.$$

The term $\sigma_{pm,rn}$ introduced here, corrects the sign. When subtracting from the above, the same formula with interchanged indices k and l, one obtains

$$(\delta_{kp}\delta_{lr} - \delta_{kr}\delta_{lp}) \det \mathbf{A} = \sum_{\substack{mn=1 \\ m\neq n}}^{N} (-1)^{m+n+p+r} (\mathbf{A}_{km}\mathbf{A}_{ln} - \mathbf{A}_{lm}\mathbf{A}_{kn}) \sigma_{pm,rn} \mathbf{M}_{pm,rn}.$$

Multiplication with $\mathbf{A}^{-1}_{qk}\mathbf{A}^{-1}_{sl}$ and summing over k and l leads to

$$(\mathbf{A}^{-1}_{qp}\mathbf{A}^{-1}_{sr} - \mathbf{A}^{-1}_{qr}\mathbf{A}^{-1}_{sp}) \det \mathbf{A} = \sum_{\substack{mn=1 \\ m\neq n}}^{N} (-1)^{m+n+p+r} (\delta_{qm}\delta_{sn} - \delta_{sm}\delta_{qn}) \sigma_{pm,rn} \mathbf{M}_{pm,rn},$$

which finally reduces to the desired result, i.e.

$$(\mathbf{A}^{-1}_{qp}\mathbf{A}^{-1}_{sr} - \mathbf{A}^{-1}_{qr}\mathbf{A}^{-1}_{sp}) \det \mathbf{A} = 2 \cdot (-1)^{p+q+r+s} \sigma_{pq,rs} \mathbf{M}_{pq,rs}.$$

Using this identity, the expectation value of the two-body operator can be easily deduced. Separation of the coordinates x_i and x_j, leads directly to

$$\begin{aligned} \langle \Phi | \mathcal{B}_{II} | \Psi \rangle = & \frac{1}{A(A-1)} \sum_{\substack{ij=1 \\ pqrs=1 \\ p\neq r, q\neq s}}^{A} (-1)^{2i+2j+p+q+r+s} \sigma_{pq,rs} \\ & \times \int \phi^{\star}_{p}(x_i) \phi^{\star}_{r}(x_j) \mathcal{B}_{II}(x_i, x_j) \psi_q(x_i) \psi_s(x_j) \Phi^{\star}_{ip,jr}(\boldsymbol{x}) \Psi_{iq,js}(\boldsymbol{x}) d\boldsymbol{x}. \end{aligned}$$

The integrals can be solved with Eq. (E.5) and simplifies the matrix element to

$$\langle \Phi | \mathcal{B}_{II} | \Psi \rangle = \frac{1}{A(A-1)} \sum_{\substack{ij=1 \\ pqrs=1 \\ p\neq r, q\neq s}}^{A} (-1)^{p+q+r+s} \sigma_{pq,rs} \langle \phi_p \phi_r | \mathcal{B}_{II} | \psi_q \psi_s \rangle \mathbf{m}_{pq,rs}. \tag{E.8}$$

Adopting Eq. (E.7) and summing over i and j shows that

$$\frac{\langle \Phi | \mathcal{B}_{II} | \Psi \rangle}{\langle \Phi | \Psi \rangle} = \frac{1}{2} \sum_{pqrs=1}^{A} \langle \phi_p \phi_r | \mathcal{B}_{II} | \psi_q \psi_s \rangle (\mathbf{o}_{qp}\mathbf{o}_{sr} - \mathbf{o}_{qr}\mathbf{o}_{sp}). \tag{E.9}$$

Using this expression, the expectation value of a two-body operator is given by

$$\mathscr{B}_{II} = \frac{\langle \Psi | \mathcal{B}_{II} | \Psi \rangle}{\langle \Psi | \Psi \rangle} = \frac{1}{2} \sum_{pqrs=1}^{A} \langle \psi_p \psi_r | \mathcal{B}_{II} | \psi_q \psi_s \rangle (\mathbf{o}_{qp}\mathbf{o}_{sr} - \mathbf{o}_{qr}\mathbf{o}_{sp}). \tag{E.10}$$

This page intentionally left blank

F

CIRCULANT MATRICES AND THEIR PROPERTIES

ABSTRACT

A short analysis is given of circulant structured matrices. Their eigenvalues, eigenvectors and inverse matrices are calculated, this for both mono- and bidirectional matrices.

Section F.1 Toeplitz and circulant matrices

When introducing TAPBC to a system of fermions, it is shown that the overlap matrix obtains a nested circulant structure. Analogously when extending this to PBC a Toeplitz structure appeared. Toeplitz systems arise in a variety of applications in mathematics, scientific computing and engineering. Differential equations, control theory, signal processing and image restoration are just a few of them. Since their introduction by Toeplitz [Toe11] and as a result of their broad range of applications, these Toeplitz systems have been meticulously studied. The following references addressing these structures are noteworthy [Gre84, Cha96, Gra06, Cha07].

A Toeplitz matrix $\mathbf{T}_n$ is an $n \times n$ matrix which is constant along its diagonals and hence can be defined by a sequence of complex numbers $\{t_i, i = -\infty, \ldots, \infty\}$ such

that $\mathbf{T}_{n,pq} = t_{p-q}$.

$$\mathbf{T}_n = \begin{pmatrix} t_0 & t_{-1} & \dots & t_{2-n} & t_{1-n} \\ t_1 & t_0 & t_{-1} & \dots & t_{2-n} \\ \vdots & t_1 & t_0 & \ddots & \vdots \\ t_{n-2} & \vdots & \ddots & \ddots & t_{-1} \\ t_{n-1} & t_{n-2} & \dots & t_1 & t_0 \end{pmatrix}. \tag{F.1}$$

A common special case of Toeplitz matrices is the circulant matrix $\mathbf{C}_n$ where the (p,q)th entry is only a function of $(p-q) \mod n$ and is hence a right cycle shift of the row above it, i.e.

$$\mathbf{C}_n = \begin{pmatrix} c_0 & c_{n-1} & \dots & c_2 & c_1 \\ c_1 & c_0 & c_{n-1} & \dots & c_2 \\ \vdots & c_1 & c_0 & \ddots & \vdots \\ c_{n-2} & \vdots & \ddots & \ddots & c_{n-1} \\ c_{n-1} & c_{n-2} & \dots & c_1 & c_0 \end{pmatrix}. \tag{F.2}$$

When defining the up-shift permutation matrix $\mathcal{C}_n$ by

$$\mathcal{C}_n = \begin{pmatrix} 0 & 1 & \dots & 0 & 0 \\ 0 & 0 & 1 & \dots & 0 \\ \vdots & 0 & 0 & \ddots & \vdots \\ 0 & \vdots & \ddots & \ddots & 1 \\ 1 & 0 & \dots & 0 & 0 \end{pmatrix}, \tag{F.3}$$

the sequence $\mathcal{C}_n^0, \dots, \mathcal{C}_n^{n-1}$ can be used as a non-orthogonal basis of circulant matrices. A general circulant matrix is then written as

$$\mathbf{C}_n = \sum_{m=0}^{n-1} c_{n-m} \mathcal{C}_n^m. \tag{F.4}$$

As will be seen in the next section, circulant matrices have important connections with discrete Fourier transforms. This means that products of circulant matrices with vectors can be solved under fast Fourier transforms. Such products, resembling convolutions, are ubiquitous in signal processing and other areas.

Section F.2 _ Eigendecomposition of a circulant matrix

Properties of circulant matrices are well known and easily derived [Gre84, Gra06]. The eigendecomposition of these matrices can easily be obtained by means of Eq. (F.4). When investigating the up-shift permutation matrix $\mathcal{C}_n$, it is clear that, when acting on a vector, it creates a cyclic shift upwards within the vector's elements. Hence, when performing n cyclic shifts, the vector has again its original value that indicates that $\mathcal{C}_n^n = \mathbf{I}_n$. This has as a direct consequence that the eigenvalues of this matrix are given by the nth roots of 1, i.e. ω_n^m with $\omega_n = \exp(2\pi i/n)$. The eigenvectors of $\mathcal{C}_n$ emerge then naturally out of the eigenvalue problem when taking the cyclic shift into account. They are given by

$$\boldsymbol{\nu}_m = \frac{1}{\sqrt{n}} \left(\omega_n^0, \omega_n^m, \omega_n^{2m}, \ldots, \omega_n^{(n-1)m}\right)^T. \tag{F.5}$$

The eigendecomposition of $\mathbf{S}_n$ can now be written by means of the unitary matrix $\mathbf{U}_n$, denoted as

$$\mathbf{U}_n = \frac{1}{\sqrt{n}} \cdot \begin{pmatrix} 1 & 1 & \ldots & 1 \\ 1 & \omega_n^1 & \ldots & \omega_n^{n-1} \\ \vdots & \vdots & \ddots & \vdots \\ 1 & \omega_n^{n-1} & \ldots & \omega_n^{(n-1)(n-1)} \end{pmatrix}.$$

Furthermore, through Eq. (F.4), the eigendecomposition of a circulant matrix can then be written as $\mathbf{C}_n = \mathbf{U}_n \mathbf{D}_n \mathbf{U}_n^\dagger$ where $\mathbf{D}_n$ is the diagonal matrix with elements $d_k = \sum_{m=1}^n c_{n-m} \omega_n^{km}$. The connection with discrete Fourier transforms is evident now. The diagonal matrix elements are discrete Fourier transforms of the sequence $\{c_i\}$ while the unitary matrix $\mathbf{U}_n$ is proportional to the Fourier matrix $\mathbf{F}_n$ and directly connected with fast Fourier transforms [Gol96].

When investigating bidirectional circulant matrices, an analogue approach can be used. Taking into account the fact that the indices of bidirectional matrices can be positive as well as negative and vary from $-n$ to n and the circulant structure is obtained through the sequence $\{c_k; k = -n, \ldots, n\}$, an identical eigendecomposition can be obtained. When defining the eigenvalues $\rho_n = \omega_{2n+1}$, the diagonal elements are written as $d_k = \sum_{m=-n}^n c_m \rho_n^{-km}$ while the the unitary matrix is given by

$$\mathbf{U}_n = \frac{1}{\sqrt{2n+1}} \cdot \begin{pmatrix} \rho_n^{n^2} & \rho_n^{n(n-1)} & \ldots & \rho_n^{-n^2} \\ \rho_n^{(n-1)n} & \rho_n^{(n-1)^2} & \ldots & \rho_n^{-(n-1)n} \\ \vdots & \vdots & \ddots & \vdots \\ \rho_n^{-n^2} & \rho_n^{-n(n-1)} & \ldots & \rho_n^{n^2} \end{pmatrix}.$$

Section F.3 Inverting a circulant matrix

The previous section introduced the eigendecomposition of a circulant matrix. Without a lot of difficulty it is possible to retrieve the inverse of such a matrix. Since $\mathbf{C}_n = \mathbf{U}_n \mathbf{D}_n \mathbf{U}_n^\dagger$, its inverse can be obtained as $\mathbf{C}_n^{-1} = \mathbf{U}_n \mathbf{D}_n^{-1} \mathbf{U}_n^\dagger$. The element (p,q) is easily obtained and reads

$$\mathbf{C}_{n,pq}^{-1} = \frac{1}{n} \sum_{k=0}^{n-1} \frac{\omega_n^{(p-q)k}}{\sum_{m=1}^{n} c_{n-m} \omega_n^{km}}. \tag{F.6}$$

From its structure it is obvious that the inverse of a circulant matrix is again circulant. The only requirement for a valid inversion is that $\mathbf{C}_n$ has no zeros as eigenvalue.

Likewise, the elements of the inverse of a bidirectional circulant matrix are given by

$$\mathbf{C}_{n,pq}^{-1} = \frac{1}{2n+1} \sum_{k=-n}^{n} \frac{\rho_n^{(p-q)k}}{\sum_{m=-n}^{n} c_m \rho_n^{-mk}}. \tag{F.7}$$

Section F.4 The block-circulant matrix

A block-circulant matrix is an $mn \times mn$ matrix in which a set of $m \times m$ matrices, i.e. $\{\mathbf{c}_i, i = 0, \ldots, n-1\}$, are ordered in a circulant structure. If $\mathbf{C}_{\mathcal{B},mn}$ is such a matrix, then it can be written as

$$\mathbf{C}_{\mathcal{B},mn} = \begin{pmatrix} \mathbf{c}_0 & \mathbf{c}_{n-1} & \cdots & \mathbf{c}_2 & \mathbf{c}_1 \\ \mathbf{c}_1 & \mathbf{c}_0 & \mathbf{c}_{n-1} & \cdots & \mathbf{c}_2 \\ \vdots & \mathbf{c}_1 & \mathbf{c}_0 & \ddots & \vdots \\ \mathbf{c}_{n-2} & \vdots & \ddots & \ddots & \mathbf{c}_{n-1} \\ \mathbf{c}_{n-1} & \mathbf{c}_{n-2} & \cdots & \mathbf{c}_1 & \mathbf{c}_0 \end{pmatrix}. \tag{F.8}$$

The properties of such a matrix are derived in an analogous way as for standard circulant matrices and by rewriting the matrix using the Kronecker product. The Kronecker product of an $m \times n$ matrix $\mathbf{A}$ and an $r \times q$ matrix $\mathbf{B}$, is an $mr \times nq$ matrix

$\mathbf{A} \otimes \mathbf{B}$ defined as

$$\mathbf{A} \otimes \mathbf{B} = \begin{pmatrix} A_{11}\mathbf{B} & A_{12}\mathbf{B} & \cdots & A_{1n}\mathbf{B} \\ A_{21}\mathbf{B} & A_{22}\mathbf{B} & \cdots & A_{2n}\mathbf{B} \\ \vdots & \vdots & \ddots & \vdots \\ A_{m1}\mathbf{B} & A_{m2}\mathbf{B} & \cdots & A_{mn}\mathbf{B} \end{pmatrix}.$$

Using this Kronecker product, a block-circulant matrix can be written by means of the up-shift permutation matrix $\mathcal{C}_n$ as

$$\mathbf{C}_{\mathcal{B},mn} = \sum_{k=0}^{n-1} \mathcal{C}_n^k \otimes \mathbf{c}_{n-k}. \tag{F.9}$$

Section F.5 — Eigendecomposition of a block-circulant matrix

In order to accomplish an inversion of a block-circulant matrix an identical approach is taken as for a circulant matrix and an eigendecomposition of the matrix is calculated. For the block structure a so called block-eigendecomposition is done. Meaning, the search for an $m \times m$ eigenblock $\mathscr{C}$ and an eigenvector of length n such that

$$\mathbf{C}_{\mathcal{B},mn} \left(\boldsymbol{\nu}_k \otimes \mathbf{I}_m \right) = \boldsymbol{\nu}_k \otimes \mathscr{C}_k. \tag{F.10}$$

Taking over the reasoning previously used for circulant matrices, the block-eigenproblem has analogue solutions. The eigenmatrix is given by

$$\mathscr{C}_k = \sum_{l=1}^{n} \omega_n^{kl} \mathbf{c}_{n-m}, \tag{F.11a}$$

while the eigenvector is written as

$$\boldsymbol{\nu}_m = \frac{1}{\sqrt{n}} \left(\omega_n^0, \omega_n^m, \omega_n^{2m}, \ldots, \omega_n^{(n-1)m} \right)^T. \tag{F.11b}$$

This eigenvector is identical to those of a normal circulant matrix. With this in mind it becomes possible to write the block-eigendecomposition by means of the unitary matrix $\mathbf{U}_{\mathcal{B},mn}$ and the block-diagonal matrix $\mathbf{D}_{\mathcal{B},mn}$ as $\mathbf{C}_{\mathcal{B},mn} = \mathbf{U}_{\mathcal{B},mn} \mathbf{D}_{\mathcal{B},mn} \mathbf{U}_{\mathcal{B},mn}^{\dagger}$, with

$$\mathbf{U}_{\mathcal{B},mn} = \mathbf{U}_n \otimes \mathbf{I}_m = \frac{1}{\sqrt{n}} \cdot \begin{pmatrix} \mathbf{I}_m & \mathbf{I}_m & \ldots & \mathbf{I}_m \\ \mathbf{I}_m & \omega_n^1 \mathbf{I}_m & \ldots & \omega_n^{n-1} \mathbf{I}_m \\ \vdots & \vdots & \ddots & \vdots \\ \mathbf{I}_m & \omega_n^{n-1} \mathbf{I}_m & \ldots & \omega_n^{(n-1)(n-1)} \mathbf{I}_m \end{pmatrix},$$

and the kth block of $\mathbf{D}_{\mathcal{B},mn}$ is given by $\mathscr{C}_k$.

The full eigendecomposition of the block-circulant matrix is then obtained through the eigendecomposition of the block-diagonal matrix $\mathbf{D}_{\mathcal{B},mn}$ or thus the matrices $\mathscr{C}_k$. The decomposition of the latter are given by $\mathscr{C}_k = \mathbf{W}_k \Lambda_k \mathbf{W}_k^{-1}$. The mn eigenvalues of $\mathbf{C}_{\mathcal{B},mn}$ are therefore given by λ_{kl} being the lth eigenvalue of $\mathscr{C}_k$ and has the eigenvector $\boldsymbol{v}_k \otimes \boldsymbol{w}_{kl}$ where $\boldsymbol{w}_{kl}$ is the eigenvector corresponding to λ_{kl} of $\mathscr{C}_k$. The result obtained here is in agreement with that obtained by Tee [Tee05].

This formalism can easily be mapped onto the block-eigendecomposition and eigendecomposition of the bidirectional block-circulant matrices. The block-eigendecomposition then reads $\mathbf{C}_{\mathcal{B},mn} = \mathbf{U}_{\mathcal{B},mn} \mathbf{D}_{\mathcal{B},mn} \mathbf{U}_{\mathcal{B},mn}^{\dagger}$. Here all matrices are $(2n+1)m \times (2n+1)m$ matrices constructed from $m \times m$ blocks. The kth block of $\mathbf{D}_{\mathcal{B},mn}$ is given by

$$\mathscr{C}_k = \sum_{l=-n}^{n} \rho_n^{-kl} \mathbf{c}_l, \tag{F.12a}$$

while the the unitary matrix is given by

$$\mathbf{U}_{\mathcal{B},mn} = \mathbf{U}_n \otimes \mathbf{I}_m = \frac{1}{\sqrt{2n+1}} \cdot \begin{pmatrix} \rho_n^{n^2}\mathbf{I}_m & \rho_n^{n(n-1)}\mathbf{I}_m & \cdots & \rho_n^{-n^2}\mathbf{I}_m \\ \rho_n^{(n-1)n}\mathbf{I}_m & \rho_n^{(n-1)^2}\mathbf{I}_m & \cdots & \rho_n^{-(n-1)n}\mathbf{I}_m \\ \vdots & \vdots & \ddots & \vdots \\ \rho_n^{-n^2}\mathbf{I}_m & \rho_n^{-n(n-1)}\mathbf{I}_m & \cdots & \rho_n^{n^2}\mathbf{I}_m \end{pmatrix}. \tag{F.12b}$$

Section F.6 Inverting a block-circulant matrix

Inverting block-circulant matrices is done in an identical way as for the circulant matrices and uses the block-eigendecomposition. For mono-directional matrices, the inverse is written as

$$[\mathbf{C}_{\mathcal{B},mn}^{-1}]_{PQ} = \frac{1}{n} \sum_{k=0}^{n-1} \omega_n^{(P-Q)k} \mathscr{C}_k^{-1}. \tag{F.13}$$

In this notation the indices P and Q reflect the block indices and the matrix $\mathscr{C}_k$ is defined as

$$\mathscr{C}_k = \sum_{l=1}^{n-1} \omega_n^{kl} \mathbf{c}_{n-l}. \tag{F.14}$$

It is obvious that each matrix $\mathscr{C}_k$ must be invertible and hence have a non-zero determinant.

Analogously, for bidirectional block-circulant matrices, the inverse is given by

$$[\mathbf{C}^{-1}_{\mathcal{B},mn}]_{PQ} = \frac{1}{n}\sum_{k=-n}^{n} \rho_n^{(P-Q)k} \mathscr{C}_k^{-1}. \tag{F.15}$$

with the eigenblocks

$$\mathscr{C}_k = \sum_{l=-n}^{n} \rho_n^{-kl} \mathbf{c}_l. \tag{F.16}$$

With this the inversion of block-circulant matrices is concluded. These results stem with those obtained by De Mazancourt [DM83].

This page intentionally left blank

NEDERLANDSTALIGE SAMENVATTING

Inleiding

Die het kleine niet eert, is het grote niet weerd. Dit spreekwoord vat samen hoe het universum met zijn grote verscheidenheid aan objecten en fenomenen moet bevat worden. Om hun dynamisch leven beter te begrijpen, is het noodzakelijk te kijken naar de bouwstenen en de krachten waaraan ze onderhevig zijn. Gravitationeel gebonden superclusters zijn opgebouwd uit miljarden sterrenstelsels. Sterren worden beheerst door de zwaartekracht inwerkend op de ontelbare kernen die door kernkrachten onderhouden worden. Een plaats in het universum waar alle krachten samenwerken en inwerken op de kleinste deeltjes, is een neutronenster.

Neutronensterren zijn zonder enige twijfel één van de meest dichte structuren in het universum. Gerezen uit de assen van massieve sterren, proppen ze ongeveer $1,4$ zonnemassa's samen in een straal van amper 12 km. Kernen worden samengeperst tot dichtheden van vijf, tien, zelfs twintig keer de nucleaire saturatiedichtheid. Dit leidt tot zeer extreme situaties die op aarde niet te vinden zijn. Fenomenen zoals hyperon-gedomineerde materie, onopgesloten quarkmaterie, supergeleiding en supervloeibaarheid met kritische temperaturen van 10^{10} K, alsook ondoorzichtigheid voor neutrino's en magnetische velden met sterktes tot 10^{13} Gauss zijn maar enkele van de situaties die kunnen voorkomen in neutronensterren. Alle fysica is vertegenwoordigd in neutronensterren, maar onder uitzonderlijke omstandigheden. Neutronensterren vormen dus een uitstekende test om theorieën aan te toetsen.

Eén van de interessantste gebieden in een neutronenster is de korst. Met dichtheden die lager zijn dan de nucleaire saturatiedichtheid en een dikte van ongeveer 1,6 km, speelt de korst een belangrijke rol in verschillende verschijnselen gerelateerd aan neutronensterren. Korstmaterie bepaalt het neutrinospectrum van een supernova en beheerst het koelingsscenario van neutronensterren. Indirect is de beschrijving van de neutronensterkorst ook gerelateerd aan de oorsprong van neutronenrijke kernen via

het zogenaamde r-procedé, alsook de rotatiestoringen van pulsars en de opwekking van gravitatiegolven. Het onderzoek naar de neutronensterkorst is dus van uitermate groot belang.

De opbouw en beschrijving van de neutronensterkorst

De neutronensterkorst is in principe eenvoudig te beschrijven. Aangezien de dichtheden onder de nucleaire saturatiedichtheid liggen, is het mogelijk de korst te beschrijven met behulp van technieken uit de kernfysica. Deze moeten echter gebruikt worden onder extreme omstandigheden waarvoor ze niet ontwikkeld zijn. Eveneens ten gevolge van deze *lage* dichtheden, is de korst opgebouwd uit neutronen, protonen en elektronen in een ladingsneutraal mengsel onder β-evenwicht.

De korst is opgebouwd uit drie delen: de buitenste en binnenste korst, en de mantel. De buitenste korst kan eenvoudig beschreven worden aan de hand van een roosterstructuur. Neutronenrijke kernen plaatsen zich in een kubisch ruimtelijk gecentreerde stapeling en zijn omgeven door een elektronengas. Naarmate de dichtheid groter wordt en we dieper in de korst binnendringen, worden de kernen groter en daalt hun proton-neutron verhouding. Wanneer de dichtheid de neutronendrupdichtheid overschrijdt, treden we de binnenste korst binnen. De neutronendichtheid is dan zo groot dat sommige neutronen ongebonden aanwezig zijn.

De mantel is de diepste zone en wordt aanzien als het overgangsgebied naar de uniforme buitenkern van de neutronenster. Dit overgangsgebied wordt getypeerd door abnormale geometrische structuren die de kernclusters aannemen ten gevolge van *frustratie* van het systeem. De dichtheid is zo groot dat de aantrekkende kernkracht en de afstotende Coulombkracht met elkaar in competitie treden. De natuur probeert altijd de energetisch meest voordelige toestand te kiezen. In dit geval zijn er echter een groot aantal quasi-equivalente toestanden die aan deze voorwaarde voldoen.

De mantel wordt dus gekenmerkt door frustratie en de complexe kernclusters die als *pasta's* worden omschreven. Bij stijgende dichtheid transformeren de sferische kernen (gehaktballen) in cilindrische (spaghetti) en planaire (lasagne) structuren. Daarna worden de rollen omgedraaid. De planaire structuren evolueren via cilindrische holten (ziti) naar sferische holten (Zwitserse kaas) om ten slotte over te gaan naar de uniforme kernmaterie (saus). Omdat deze gefrustreerde toestanden gevoelig zijn aan kleine veranderingen, is een dynamische beschrijving essentieel.

Moleculaire-dynamicatechnieken zijn hiervoor de uitgesproken simulatietechnieken. Deze laten toe de individuele deeltjes te traceren in de tijd aan de hand van bewegingsvergelijkingen. De klassieke aanpak is echter onvoldoende voor de beschrijving van de neutronensterkorst. Door de enorme dichtheden die in de korst gehaald worden, is het noodzakelijk om kwantummechanische aspecten in rekening te brengen. Vanuit het klassieke standpunt worden deeltjes aanzien als puntdeeltjes en zijn ze volledig gedefinieerd aan de hand van hun positie en snelheid. Het kwantummechanisch standpunt is net iets anders. Deeltjes worden niet gekarakteriseerd door hun positie en snelheid maar door een waarschijnlijkheidsdistributie in de faseruimte. Bovendien spelen ook hun spin en isospin een belangrijke rol en zijn ze onderhevig aan een karakteristieke statistiek. Voor de nucleonen in de korst is dit een fermionenstatistiek wat ervoor zorgt dat twee deeltjes niet dezelfde kwantummechanische toestand kunnen innemen.

Fermionische moleculaire dynamica

De uitgelezen techniek om fermionen op een dynamische manier te beschrijven is *Fermionische Moleculaire Dynamica* (FMD). Deze methode levert een klassiek raamwerk voor de beschrijving van fermionen en laat toe om naast de gemiddelde positie en impuls, eveneens de tijdsevolutie van de spin, isospin en waarschijnlijkheidsdistributie te bepalen. Hierbij wordt steeds het fermionenkarakter van het systeem behouden. De bewegingsvergelijkingen die door FMD aan het systeem opgelegd worden, hebben een Poissonkarakter en zijn sterk vergelijkbaar met de klassieke Hamiltonvergelijkingen.

Hoofdstuk 2 behandelt uitvoerig dit FMD formalisme en toont aan dat een matrixformalisme toelaat om een fermionensysteem te beschrijven. Dit laatste is een gevolg van het antisymmetrisch karakter dat het fermionensysteem met zich meedraagt. In het FMD formalisme wordt elk deeltje beschreven door een Gaussisch golfpakket wat voor FMD een individueel deeltjesbeschrijving met zich meebrengt. Voor de beschrijving van een fermionensysteem wordt een Slaterdeterminant gebruikt in combinatie met deze golfpakketten.

Hoewel FMD resulteert in een eenvoudig matrixformalisme, is het niet voor de hand liggend dit uit te breiden tot de beschrijving van onbegrensde fermionenmaterie. Eigenschappen van onbegrensde systemen kunnen worden bestudeerd aan de hand van studies op grote systemen waardoor randeffecten verwaarloosbaar worden. Dit is echter niet de gewenste weg die men wil inslaan. FMD wordt gekenmerkt als een computergericht N^4-probleem wat de behandeling van grote systemen uitermate

bemoeilijkt. Het denkpatroon dat gevolgd wordt bij klassieke moleculaire dynamica, met name het gebruik van periodieke randvoorwaarden (PRV), is maar een deel van de oplossing. PRV laten toe een onbegrensd systeem te beschrijven aan de hand van periodiek geplaatste kopieën van een klein systeem. Het laat ons evenwel in de kou staan als het op antisymmetrisatie aankomt. Het fermionenkarakter kan namelijk niet begrensd worden tot een welbepaalde groep deeltjes, het is een veeldeeltjescorrelatie waarin alle deeltjes meespelen. Hierbij slaat "alle" op het oneindig aantal.

De vraag hoe onbegrende fermionensystemen kunnen behandeld worden door middel van FMD in combinatie met PRV, wordt beschreven en ook beantwoord in hoofdstuk 3. Door gebruik te maken van concepten uit de vaste-stoffysica wordt aangetoond dat het FMD matrixformalisme voor de beschrijving van het oneindige fermionensysteem, een circulante structuur bezit ten gevolge van de PRV. De circulante structuur is een reflectie van het periodiek karakter en wordt wiskundig weerspiegeld door middel van Fourierreeksen. Door het Fouriergedrag uit te buiten, is het mogelijk het oneindig-dimensioneel matrixformalisme te herleiden tot een eindig-dimensioneel probleem. Dit formalisme heeft een gelijkaardige structuur als de matrixbeschrijving voor eindige fermionensystemen, maar is het uitgeïntegreerd in de duale roosterruimte.

In hoofdstuk 3 wordt dit formalisme toegepast op een aantal eenvoudige roosterconfiguraties. Uit deze toepassingen blijkt duidelijk dat het fermionenkarakter van de materie behouden blijft.

En wat nu?

Het doel van dit proefschrift was een formalisme te bepalen dat toelaat FMD te gebruiken bij de studie van de neutronensterkorst. Hoewel hier de eerste stappen gezet zijn, is vanuit een theoretisch perspectief de kous nog niet af. FMD is en blijft computergericht een zware techniek en de combinatie met PRV maakt het niet eenvoudiger. Het is dus sterk aan te raden op zoek te gaan naar vereenvoudigingen die het rekenkundig probleem aanpakken. Tegelijkertijd is er ook nood aan een goed integratieformalisme dat de differentiaalvergelijkingen efficiënt oplost en vooral het behoud van energie respecteert. Als laatste computergericht probleem is het ook noodzakelijk een antwoord te bieden voor de problemen die rijzen bij de implementatie van langedrachtinteracties zoals de Coulombinteractie. Tengevolge van de periodiciteit die aan het systeem wordt opgelegd, wordt dit periodiek karakter automatisch opgelegd aan de langedrachtsinteracties en dit kan tot afwijkingen leiden.

Praktisch gezien is het al mogelijk om FMD in combinatie met PRV te gebruiken om onderzoek te verrichten naar de neutronensterkorst. Met behulp van het Rayleigh-Ritz variatieprincipe is het mogelijk de grondtoestand van het systeem te onderzoeken. Hierbij kan een volledig dichtheidsspectrum doorlopen worden dat zowel de buitenkorst als de mantel beschrijft. Deze grondtoestanden en hun dynamisch karakter bij diverse temperaturen kunnen dan gebruikt worden bij de studie van neutrinotransport voor de koeling van neutronensterren en supernovae. Om dit alles mogelijk te maken, is er nood aan een goede beschrijving van de individuele interacties waaraan het fermionensysteem onderhevig is.

Het FMD verhaal is dus nog lang niet ten einde ...

This page intentionally left blank

Give credit where credit is due

BIBLIOGRAPHY

[Abr72] ABRAMOWITZ M & STEGUN I A. "*Handbook of Mathematical Functions with Formulas, Graphs, and Mathematical Tables*" (Dover Publications, New York, 1972), ninth dover printing, tenth GPO printing edition.

[Ada79] ADAMS D J. "*Computer simulation of ionic systems: the distorting effects of the boundary conditions*". *Chem. Phys. Lett.* **62**, pp. 329–332 (1979).

[Ada82] ADAMS D. "*Life, the Universe and Everything*", volume 3 of *The Hitchhiker's Guide to the Galaxy* (Pan Books, London, 1982).

[Aic86] AICHELIN J & STÖCKER H. "*Quantum molecular dynamics - a novel approach to n-body correlations in heavy ion collisions*". *Phys. Lett. B* **176**, pp. 14–19 (1986).

[Aic91] AICHELIN J. "*Quantum molecular dynamics - a dynamical microscopic n-body approach to investigate fragment formation and the nuclear equation of state in heavy ion collisions*". *Phys. Rep.* **202**, pp. 233–360 (1991).

[All91] ALLEN M P & TILDESLEY D J. "*Computer Simulations of Liquids*" (Clarendon, Oxford, 1991).

[And75] ANDERSON P W & ITOH N. "*Pulsar glitches and restlessness as a hard superfluidity phenomenon*". *Nature* **256**, pp. 25–27 (1975).

[Arf95] ARFKEN G B & WEBER H J. "*Mathematical Methods for Physicists*" (Academic Press, San Diego, 1995), fourth edition.

[Arn07] ARNOULD M, GORIELY S & TAKAHASHI K. "*The r-process of stellar nucleosynthesis: Astrophysics and nuclear physics achievements and mysteries*". *Phys. Rep.* **450**, pp. 97–213 (2007).

[Ash76] ASHCROFT N W & MERMIN N D. "*Solid State Physics*" (Saunders College, 1976).

[Baa34a] BAADE W & ZWICKY F. "*Supernovae and cosmic rays*". *Phys. Rev.* **45**, p. 138 (1934).

[Baa34b] BAADE W & ZWICKY F. "*On super-novae*". *Proc. National Acad. Sci.* **20**, pp. 254–259 (1934).

[Bay71a] BAYM G, BETHE H A & PETHICK C J. "*Neutron star matter*". *Nuclear Physics A* **175**, pp. 225–271 (1971).

[Bay71b] BAYM G, PETHICK C & SUTHERLAND P. "*The ground state of matter at high densities: Equation of state and stellar models*". *Astrophys. J.* **170**, pp. 299–317 (1971).

[Bay79] BAYM G & PETHICK C. "*Physics of neutron stars*". *Annu. Rev. Astro. Astrophys.* **17**, pp. 415–443 (1979).

[Bel61] BELLMAN R. "*A brief introduction to Theta functions*". Athena Series, selected topics in mathematics (Holt, Rinehart and Winston, New York, 1961).

[Blo29] BLOCH F. "*Über die Quantenmechanik der Elektronen in Kristallgittern*". *Z. Phys. A* **52**, pp. 555–600 (1929).

[Bor12] BORN M & VON KÁRMÁN T. "*Über Schwingungen in Raumgittern*". *Physik. Z.* **13**, pp. 297–309 (1912).

[Bra50] BRAVAIS A. "*Mémoire sur les systèmes formés par des points régulièrement distribues sur un plan ou dans l'espace*". *J. Ec. Polytech. Paris* **19**, pp. 1–128 (1850).

[Bri67] BRINK D M & BOEKER E. "*Effective interactions for Hartree-Fock calculations*". *Nucl. Phys. A* **91**, pp. 1–26 (1967).

[Bri73] BRINK D M & CASTRO J J. "*Alpha clustering effects in nuclear matter*". *Nucl. Phys. A* **216**, pp. 109–124 (1973).

[Bro88] BROECKHOVE J, LATHOUWERS L, KESTELOOT E & VAN LEUVEN P. "*On the equivalence of time-dependent variational principles*". *Chem. Phys. Lett.* **149**, pp. 547–550 (1988).

[Bro89] BROECKHOVE J, LATHOUWERS L & VAN LEUVEN P. "*Time-dependent variational principles and conservation laws in wavepacket dynamics*". *J. Phys. A* **22**, pp. 4395–4408 (1989).

[Buc71] BUCHLER J R & BARKAT Z. "*Properties of low-density neutron-star matter*". *Phys. Rev. Lett.* **27**, pp. 48–51 (1971).

[Bur06] BURROWS A, REDDY S & THOMPSON T A. "*Neutrino opacities in nuclear matter*". *Nucl. Phys. A* **777**, pp. 356–394 (2006).

[Cas08] CASE W B. "*Wigner functions and Weyl transforms for pedestrians*". *Am. J. Phys.* **76**, pp. 937–946 (2008).

[Cau82] CAURIER E, GRAMMATICOS B & SAMI T. "*The time dependent cluster model*". *Phys. Lett. B* **109**, pp. 150–154 (1982).

[Cha32] CHADWICK J. "*Possible existence of a neutron*". *Nature* **129**, p. 312 (1932).

[Cha96] CHAN R H F & NG M K. "*Conjugate gradient methods for Toeplitz systems*". *SIAM Rev.* **38**, pp. 427–482 (1996).

[Cha07] CHAN R H F & JIN X Q. "*An introducion to iterative Toeplitz solvers*". Fundamentals of algorithms (SIAM, Philadelphia, 2007).

[Cha08] CHAMEL N & HAENSEL P. "*Physics of neutron star crusts*". *Living Rev. Relativity* **11**, art. 10 (2008).

[Coa90] COALSON R D & KARPLUS M. "*Multidimensional variational Gaussian wave packet dynamics with application to photodissociation spectroscopy*". *J. Chem. Phys.* **93**, p. 3919 (1990).

[Coo86] COOPER F, PI S Y & STANCIOFF P N. "*Quantum dynamics in a time dependent variational approximation*". *Phys. Rev. D* **34**, pp. 3831–3841 (1986).

[Cor91] CORIANÓ C, PARWANI R & YAMAGISHI H. "*On the use of the time-dependent Rayleigh-Ritz equations for heavy-ion collisions*". *Nucl. Phys. A* **522**, pp. 591–609 (1991).

[Cre83] CREUTZ M. "*Microcanonical monte carlo simulation*". *Phys. Rev. Lett.* **50**, pp. 1411–1414 (1983).

[DaP63] DA PROVIDÊNCIA J. "*Cluster expansion of operator averages for systems of many particles*". *Nucl. Phys.* **46**, pp. 401–412 (1963).

[Dir30] DIRAC P A M. "*Note on exchange phenomena in the Thomas-Fermi atom*". *Proc. Cambridge Philos. Soc.* **26**, pp. 376–385 (1930).

[Dir67] DIRAC P A M. "*The Principles of Quantum Mechanics*". The international series of monographs on physics (Clarendon, Oxford, 1967), fourth edition.

[dL80] DE LEEUW S W, PERRAM J W & SMITH E R. "*Simulation of electrostatic systems in periodic boundary conditions. I. Lattice sums and dielectric constants*". *Proc. R. Soc. Lond. A* **373**, pp. 27–56 (1980).

[DM83] DE MAZANCOURT T & GERLIC G. "*The inverse of a block-circulant matrix*". *IEEE Trans. Antenn. Propag.* **AP-31**, pp. 808–810 (1983).

[Dor87] DORSO C, DUARTE S & RANDRUP J. "*Classical simulation of the fermi gas*". *Phys. Lett. B* **188**, pp. 287–294 (1987).

[Dou01] DOUCHIN F & HAENSEL P. "*A unified equation of state of dense matter and neutron star structure*". *Astron. Astrophys.* **380**, pp. 151–167 (2001).

[Ehr27] EHRENFEST P. "*Bemerkung über die angenäherte Gültigkeit der klassischen Mechanik innerhalb der Quantenmechanik*". *Z. Phys. A* **45**, pp. 455–457 (1927).

[Ewa21] EWALD P P. "*Die Berechnung optischer und elektrostatischer Gitterpotentiale*". *Ann. Phys. (Leipzig)* **369**, pp. 258–287 (1921).

[Fao06] FAOU E & LUBICH C. "*A Poisson integrator for Gaussian wavepacket dynamics*". *Comput. Visual. Sci.* **9**, pp. 45–55 (2006).

[Fel90] FELDMEIER H. "*Fermionic molecular dynamics*". *Nucl. Phys. A* **515**, pp. 147–172 (1990).

[Fel95] FELDMEIER H, BIELER K & SCHNACK J. "*Fermionic molecular dynamics for ground states and collisions of nuclei*". *Nucl. Phys. A* **586**, pp. 493–532 (1995).

[Fel97] FELDMEIER H & SCHNACK J. "*Fermionic molecular dynamics*". *Prog. Part. Nucl. Phys.* **39**, pp. 393–442 (1997).

[Fel98] FELDMEIER H, NEFF T, ROTH R & SCHNACK J. "*A unitary correlation operator method*". *Nucl. Phys. A* **632**, pp. 61–95 (1998).

[Fel00] FELDMEIER H & SCHNACK J. "*Molecular dynamics for fermions*". *Rev. Mod. Phys.* **72**, pp. 655–688 (2000).

[Flo83] FLOQUET M G. "*Sur les équations différentielles linéaires à coefficients périodiques*". *Ann. École Norm. Sup.* **2**, pp. 47–88 (1883).

[Fox06] FOX M. "*Quantum Optics: An Introduction*". Oxford Master Series in Physics (Oxford University, Oxford, 2006).

[Fre34] FRENKEL J I. "*Wave Mechanics: Advanced General Theory*" (Clarendon Press, Oxford, 1934), p. 435.

[Gae06] GAENSLER B M, CHATTERJEE S, SLANE P O, VAN DER SWALUW E, CAMILO F, & HUGHES J P. "*The X-ray structure of the pulsar bow shock G189.22+2.90 in the supernova remnant IC 443*". *Astrophys. J.* **648**, pp. 1037–1042 (2006).

[Ger22a] GERLACH W & STERN O. "*Der experimentelle Nachweis der Richtungsquantelung im Magnetfeld*". *Z. Phys.* **9**, pp. 349–352 (1922).

[Ger22b] GERLACH W & STERN O. "*Das magnetische Moment des Silberatoms*". *Z. Phys.* **9**, pp. 353–355 (1922).

[Ger83] GERJUOY E, RAU A R P & SPRUCH L. "*A unified formulation of the construction of variational principles*". *Rev. Mod. Phys.* **55**, pp. 725–774 (1983).

[Ger05] GERRY C C & KNIGHT P L. "*Introductory Quantum Optics*" (Cambridge University, Cambridge, 2005).

[Gle92] GLENDENNING N K. "*First-order phase transitions with more than one conserved charge: Consequences for neutron stars*". *Phys. Rev. D* **46**, pp. 1274–1287 (1992).

[Gle00] GLENDENNING N K. "*Compact Stars: Nuclear Physics, Particle Physics, and General Relativity*". Astronomy and Astrophysics Library (Springer, Berlin, 2000), second edition.

[Gol68] GOLD T. "*Rotating neutron stars as the origin of the pulsating radio sources*". *Nature* **218**, pp. 731–732 (1968).

[Gol96] GOLUB G H & VAN LOAN C F. "*Matrix computations*" (Johns Hopkins University, Baltimore, 1996), third edition.

[Gor05a] GORIELY S, DEMETRIOU P, JANKA H T, PEARSON J & SAMYN M. "*The r-process nucleosynthesis: a continued challenge for nuclear physics and astrophysics*". *Nucl. Phys. A* **758**, pp. 587–594 (2005).

[Gor05b] GORIELY S, SAMYN M, PEARSON J & ONSI M. "*Further explorations of Skyrme-Hartree-Fock-Bogoliubov mass formulas. IV: Neutron-matter constraint*". *Nucl. Phys. A* **750**, pp. 425–443 (2005).

[Got89] GOTTFRIED K. "*Quantum Mechanics Volume I: Fundamentals*" (Addison Wesley, California, 1989).

[Gou07] GOULD H, TOBOCHNIK J & CHRISTIAN W. "*An Introduction to Computer Simulation methods: applications to physical systems*" (Addison Wesley, San Francisco, 2007).

[Gra06] GRAY R M. "*Toeplitz and circulant matrices: A review*". *Found. Trends Commun. Inform. Th.* **2**, pp. 155–239 (2006).

[Gra07] GRADSHTEYN I S & RYZHIK I M. "*Table of Integrals, Series, and Products*" (Academic Press, London, 2007), seventh edition. Edited by Alan Jeffrey and Daniel Zwillinger.

[Gre84] GRENANDER U & SZEGÖ G. "*Toeplitz forms and their applications*" (Chelsea publishing, New York, 1984), second edition.

[Hae94] HAENSEL P & PICHON B. "*Experimental nuclear masses and the ground state of cold dense matter*". *Astron. Astrophys.* **283**, pp. 313–318 (1994).

[Hae07] HAENSEL P, POTEKHIN A Y & YAKOVLEV D G. "*Neutron Stars 1: Equation of State and Structure*", volume 326 of *Astrophysics and Space Science Library* (Springer, Berlin, 2007).

[Hai06] HAIRER E, LUBICH C & WANNER G. "*Geometric Numerical Integration: Structure-Preserving Algorithms for Ordinary Differential Equations*", volume 31 of *Springer Series in Computational Mathematics* (Springer, Berlin, 2006), second edition.

[Ham34] HAMILTON W R. "*On a general method in dynamics; by which the study of the motions of all free systems of attracting or repelling points is reduced to the search and differentiation of one central relation, or characteristic function*". *Philos. Trans. Roy. Soc. London* **124**, pp. 247–308 (1834).

[Ham35] HAMILTON W R. "*Second essay on a general method in dynamics*". *Philos. Trans. Roy. Soc. London* **125**, pp. 95–144 (1835).

[Han79] HANSEN J P, LEVESQUE D & WEIS J J. "*Self-diffusion in the two-dimensional, classical electron gas*". *Phys. Rev. Lett.* **43**, pp. 979–982 (1979).

[Has84] HASHIMOTO M A, SEKI H & YAMADA M. "*Shape of nuclei in the crust of neutron star*". *Prog. Theor. Phys.* **71**, pp. 320–326 (1984).

[Hei27] HEISENBERG W. "*Über den anschaulichen Inhalt der quantentheoretischen Kinematik und Mechanik*". *Z. Phys.* **43**, pp. 172–198 (1927).

[Hei00] HEISELBERG H & PANDHARIPANDE V. "*Recent progress in neutron star theory*". *Annu. Rev. Nucl. Part. Sci.* **50**, pp. 481–524 (2000).

[Hel75] Heller E J. "*Time-dependent approach to semiclassical dynamics*". *J. Chem. Phys.* **62**, pp. 1544–1555 (1975).

[Hel76a] Heller E J. "*Time dependent variational approach to semiclassical dynamics*". *J. Chem. Phys.* **64**, pp. 63–73 (1976).

[Hel76b] Heller E J. "*Classical s-matrix limit of wave packet dynamics*". *J. Chem. Phys.* **65**, pp. 4979–4989 (1976).

[Hew68] Hewish A, Bell S J, Pilkington J D H, Scott P F & Collins R A. "*Observation of a rapidly pulsating radio source*". *Nature* **217**, pp. 709–713 (1968).

[Hor04a] Horowitz C J, Pérez-García M A, Carriere J, Berry D K & Piekarewicz J. "*Nonuniform neutron-rich matter and coherent neutrino scattering*". *Phys. Rev. C* **70**, art. 065806 (2004).

[Hor04b] Horowitz C J, Pérez-García M A & Piekarewicz J. "*Neutrino-pasta scattering: The opacity of nonuniform neutron-rich matter*". *Phys. Rev. C* **69**, art. 045804 (2004).

[Hor08] Horowitz C J & Berry D K. "*The shear viscosity and thermal conductivity of nuclear pasta*". *Phys. Rev. C* **78**, art. 035806 (2008).

[Hor09] Horowitz C J & Kadau K. "*Breaking strain of neutron star crust and gravitational waves*". *Phys. Rev. Lett.* **102**, art. 191102 (2009).

[Hul75] Hulse R A & Taylor J H. "*Discovery of a pulsar in a binary system*". *Astrophys. J.* **195**, pp. L51–L53 (1975).

[Jac29] Jacobi C G J. "*Fundamenta nova theoriae functionum ellipticarum*" (sumtibus fratrum Borntræger, 1829).

[Jan07] Janka H, Langanke K, Marek A, Martínez-Pinedo G & Müller B. "*Theory of core-collapse supernovae*". *Phys. Rep.* **442**, pp. 38–74 (2007).

[Jog82] Jog C J & Smith R A. "*Mixed lattice phases in cold dense matter*". *Astrophys. J.* **253**, pp. 839–841 (1982).

[KE01] Kanada-En'yo Y & Horiuchi H. "*Structure of light unstable nuclei studied with antisymmetrized molecular dynamics*". *Prog. Theor. Phys. Suppl.* **142**, pp. 205–263 (2001).

[KE03] Kanada-En'yo Y, Kimura M & Horiuchi H. "*Antisymmetrized molecular dynamics: a new insight into the structure of nuclei*". *C. R. Physique* **4**, pp. 497–520 (2003).

[Ker76] KERMAN A K & KOONIN S E. "*Hamiltonian formulation of time-dependent variational principles for the many-body system*". *Ann. Phys. (NY)* **100**, pp. 332–358 (1976).

[Kid97] KIDERLEN D & DANIELEWICZ P. "*Fragments in gaussian wave-packet dynamics with and without correlations*". *Nucl. Phys. A* **620**, pp. 346–362 (1997).

[Kra80] KRATKY K W. "*New boundary conditions for computer experiments of thermodynamic systems*". *J. Comput. Phys.* **37**, pp. 205–217 (1980).

[Kra81] KRAMER P & SARACENO M. "*Geometry of the Time-Dependent Variational Principle in Quantum Mechanics*", volume 140 of *Lecture Notes in Physics* (Springer, Berlin, 1981).

[Kra82] KRATKY K W & SCHREINER W. "*Computeration techniques for spherical boundary conditions*". *J. Comput. Phys.* **47**, pp. 313–320 (1982).

[Lag68] LAGRANGE G L. "*Œuvres de Lagrange*", volume 2 (Gauthier - Villars, Paris, 1868). *Miscellanea Taurinesia IV*, 1766–1769.

[Lan32] LANDAU L D. "*On the theory of stars*". *Phys. Z. Sowjetunion* **1**, pp. 285–288 (1932).

[Lan72] LANGHOFF P W, EPSTEIN S T & KARPLUS M. "*Aspects of time-dependent pertubation theory*". *Rev. Mod. Phys.* **44**, pp. 602–644 (1972).

[Lan06] LANGANKE K. "*Neutrino nucleus reactions in core-collapse supernovae*". *Prog. Part. Nucl. Phys.* **57**, pp. 324–333 (2006).

[Las87] LASSAUT M, FLOCARD H, BONCHE P, HEENEN P H & SURAUD E. "*Equation of state of hot dense matter*". *Astron. Astrophys.* **183**, pp. L3–L6 (1987).

[Lat77] LATTIMER J M, MACKIE F, RAVENHALL D G & SCHRAMM D N. "*The decompression of cold neutron star matter*". *Astrophys. J.* **213**, pp. 225–233 (1977).

[Lat04] LATTIMER J M & PRAKASH M. "*The physics of neutron stars*". *Science* **304**, pp. 536–542 (2004).

[Lie86] LIEBMANN R. "*Statistical Mechanics of Periodic Frustrated Ising Systems*", volume 251 of *Lecture Notes in Physics* (Springer, Berlin, 1986).

[Lor93] LORENZ C P, RAVENHALL D G & PETHICK C J. "*Neutron star crusts*". *Phys. Rev. Lett.* **70**, pp. 379–382 (1993).

[Lub08] LUBICH C. "*From Quantum to Classical Molecular Dynamics: Reduced Models and Numerical Analysis*". Zurich Lectures in Advanced Mathematics (European Mathematical Society, Zürich, 2008).

[Mac33] MACDONALD J K L. "*Successive approximations by the Rayleigh-Ritz variation method*". *Phys. Rev.* **43**, pp. 830–833 (1933).

[Mal69] MALFLIET R A & TJON J A. "*Solution of the Faddeev equations for the triton problem using local two-particle interactions*". *Nucl. Phys. A* pp. 161–168 (1969).

[Man76] MANDELL M J. "*On the properties of a periodic fluid*". *J. Stat. Phys.* **15**, pp. 299–305 (1976).

[Man05] MANCHESTER R N, HOBBS G B, TEOH A & HOBBS M. "*The Australia telescope national facility pulsar catalogue*". *Astron. J.* **129**, pp. 1993–2006. URL `http://www.atnf.csiro.au/research/pulsar/psrcat` (2005).

[Mar96] MARUYAMA T, NIITA K & IWAMOTO A. "*Extension of quantum molecular dynamics and its application to heavy-ion collisions*". *Phys. Rev. C* **53**, pp. 297–304 (1996).

[Mar05] MARUYAMA T, TATSUMI T, VOSKRESENSKY D N, TANIGAWA T & CHIBA S. "*Nuclear "pasta" structures and the charge screening effect*". *Phys. Rev. C* **72**, art. 015802 (2005).

[McL64a] MCLACHLAN A D. "*A variational solution of the time-dependent schrodinger equation*". *Mol. Phys.* **8**, pp. 39–44 (1964).

[McL64b] MCLACHLAN A D & BALL M A. "*Time-dependent hartree-fock theory for molecules*". *Rev. Mod. Phys.* **36**, pp. 844–855 (1964).

[Met53] METROPOLIS N, ROSENBLUTH A W, ROSENBLUTH M N & TELLER A H. "*Equation of state calculations by fast computing machines*". *J. Chem. Phys.* **21**, pp. 1087–1092 (1953).

[Mig90] MIGDAL A B, SAPERSTEIN E E, TROITSKY M A & VOSKRESENSKY D N. "*Pion degrees of freedom in nuclear matter*". *Phys. Rep.* **192**, pp. 179–437 (1990).

[Mis73] MISNER C W, THORNE K S & WHEELER J A. "*Gravitation*" (W.H. Freeman and Company, New York, 1973).

[Moc73] MOCCIA R. "*Time-dependent variational principle*". *Int. J. Quantum Chem.* **7**, pp. 773–783 (1973).

[MP06] MARTÍNEZ-PINEDO G, LIEBENDÖRFER M & FREKERS D. "*Nuclear input for core-collapse models*". *Nucl. Phys. A* **777**, pp. 395–423 (2006).

[Mul03] MULLIN W J & BLAYLOCK G. "*Quantum statistics: Is there an effective fermion repulsion or boson attraction?*". *Am. J. Phys.* **71**, pp. 1223–1231 (2003).

[Mum83] MUMFORD D. "*Tata Lectures on Theta I*", volume 28 of *Progress in Mathematics* (Birkhäser, Boston, 1983).

[Nak09] NAKAZATO K, OYAMATSU K & YAMADA S. "*Gyroid phase in nuclear pasta*". *Phys. Rev. Lett.* **103**, art. 132501 (2009).

[Nef03] NEFF T & FELDMEIER H. "*Tensor correlations in the unitary correlation operator method*". *Nucl. Phys. A* **713**, pp. 311–371 (2003).

[Nef08] NEFF T & FELDMEIER H. "*Clustering and other exotic phenomena in nuclei*". *Eur. Phys. J. Special Topics* **156**, pp. 69–92 (2008).

[Neg73] NEGELE J W & VAUTHERIN D. "*Neutron star matter at sub-nuclear densities*". *Nucl. Phys. A* **207**, pp. 298–320 (1973).

[New87] NEWTON I. "*Philosophiæ Naturalis Principia Mathematica*" (Jussu Societatis Regiæ ac Typis Josephi Streater, London, 1687).

[Ohn93] OHNISHI A & RANDRUP J. "*Statistical properties of anti-symmetrized molecular dynamics*". *Nucl. Phys. A* **565**, pp. 474–494 (1993).

[Ohn95] OHNISHI A & RANDRUP J. "*Incorporation of quantum statistical features in molecular dynamics*". *Phys. Rev. Lett.* **75**, pp. 596–599 (1995).

[Ono92a] ONO A, HORIUCHI H, MARUYAMA T & OHNISHI A. "*Fragment formation studied with antisymmetrized version of molecular dynamics with two nucleon collisions*". *Phys. Rev. Lett.* **68**, pp. 2898–2900 (1992).

[Ono92b] ONO A, HORIUCHI H, MARUYAMA T & OHNISHI A. "*Antisymmetrized version of molecular dynamics with two nucleon collisions and its application to heavy ion reactions*". *Prog. Theor. Phys.* **87**, pp. 1185–1206 (1992).

[Ono96] ONO A & HORIUCHI H. "*Antisymmetrized molecular dynamics of wave packets with stochastic incorporation of vlasov equation*". *Phys. Rev. C* **53**, pp. 2958–2972 (1996).

[Ono04] ONO A & HORIUCHI H. "*Antisymmetrized molecular dynamics for heavy ion collisions*". *Prog. Part. Nucl. Phys.* **53**, pp. 501–581 (2004).

[Ons08] Onsi M, Dutta A K, Chatri H, Goriely S, Chamel N & Pearson J M. "*Semiclassical equation of state and specific-heat expressions with proton shell corrections for the inner crust of a neutron star*". *Phys. Rev. C* **77**, art. 065805 (2008).

[Oya84] Oyamatsu K, aki Hashimoto M & Yamada M. "*Further study of the nuclear shape in high-density matter*". *Prog. Theor. Phys.* **72**, pp. 373–375 (1984).

[Oya93] Oyamatsu K. "*Nuclear shapes in the inner crust of a neutron star*". *Nucl. Phys. A* **561**, pp. 431–452 (1993).

[Pac67] Pacini F. "*Energy emission from a neutron star*". *Nature* **216**, pp. 567–568 (1967).

[Pag06] Page D, Geppert U & Weber F. "*The cooling of compact stars*". *Nucl. Phys. A* **777**, pp. 497–530 (2006).

[Pau25] Pauli W. "*Über den Zusammenhang des Abschlusses der Elektronengruppen im Atom mit der Komplexstruktur der Spektren*". *Z. Phys.* **31**, pp. 765–783 (1925).

[Pet95] Pethick C J & Ravenhall D G. "*Matter at large neutron excess and the physics of neutron-star crusts*". *Annu. Rev. Nucl. Part. Sci.* **45**, pp. 429–484 (1995).

[Pra97] Prakash M, Bombaci I, Prakash M, Ellis P J, Lattimer J M & Knorren R. "*Composition and structure of protoneutron stars*". *Physics Reports* **280**, pp. 1–77 (1997).

[Ram01] Ramos A, Schaffner-Bielich J & Wambach J. "*Kaon condensation in neutron stars*", volume 578 of *Lecture Notes in Physics* (Springer, Berlin, 2001), pp. 175–202.

[Rav83] Ravenhall D G, Pethick C J & Wilson J R. "*Structure of matter below nuclear saturation density*". *Phys. Rev. Lett.* **50**, pp. 2066–2069 (1983).

[Rit08] Ritz W. "*Über eine neue Methode zur Lösung gewisser Variationsprobleme der mathematischen Physik*". *J. Reine Angew. Math.* **135**, pp. 1–61 (1908).

[Rud91] Ruderman M. "*Neutron star crustal plae tectonics. i. magnetic dipole evolution in millisecond pulsars and low-mass x-ray binaries*". *Astrophys. J.* **366**, pp. 261–269 (1991).

[Rüs06] Rüster S B, Hempel M & Schaffner-Bielich J. "*Outer crust of nonaccreting cold neutron stars*". *Phys. Rev. C* **73**, art. 035804 (2006).

[Sar83] SARACENO M, KRAMER P & FERNANDEZ F. "*Time-dependent variational description of $\alpha\alpha$ scattering*". *Nucl. Phys. A* **405**, pp. 88–108 (1983).

[Sch26a] SCHRÖDINGER E. "*Quantisierung als Eigenwertproblem (Erste Mitteilung)*". *Ann. Phys. (Leipzig)* **384**, pp. 361–376 (1926).

[Sch26b] SCHRÖDINGER E. "*Quantisierung als Eigenwertproblem (Zweite Mitteilung)*". *Ann. Phys. (Leipzig)* **384**, pp. 489–527 (1926).

[Sch26c] SCHRÖDINGER E. "*Quantisierung als Eigenwertproblem (Dritte Mitteilung)*". *Ann. Phys. (Leipzig)* **385**, pp. 437–490 (1926).

[Sch26d] SCHRÖDINGER E. "*Quantisierung als Eigenwertproblem (Vierte Mitteilung)*". *Ann. Phys. (Leipzig)* **386**, pp. 109–139 (1926).

[Sch93] SCHNACK J. "*Untersuchungen zur Fermionischen Molekulardynamik*". masterthesis, Technische Hochschule Darmstadt. GSI-report GSI-93-21 (1993).

[Sch96] SCHNACK J & FELDMEIER H. "*Statistical properties of fermionic molecular dynamics*". *Nucl. Phys. A* **601**, pp. 181–194 (1996).

[Sch97] SCHNACK J & FELDMEIER H. "*The nuclear liquid-gas phase transition within fermionic molecular dynamics*". *Phys. Lett. B* **409**, pp. 6–10 (1997).

[Sha04] SHAPIRO S L & TEUKOLSKY S A. "*Black Holes, White Dwarfs and Neutron Stars: The Physics of Compact Objects*" (Wiley-VCH, Weinheim, 2004), second edition.

[Sla29] SLATER J C. "*The theory of complex spectra*". *Phys. Rev.* **34**, pp. 1293–1322 (1929).

[Str05] STROHMAYER T E & WATTS A L. "*Discovery of fast x-ray oscillations during the 1998 giant flare from sgr 1900+14*". *Astrophys. J.* **632**, pp. L111–L114 (2005).

[Sum95] SUMIYOSHI K, OYAMATSU K & TOKI H. "*Neutron star profiles in the relativistic Brueckner-Hartree-Fock theory*". *Nucl. Phys. A* **595**, pp. 327–345 (1995).

[Suz85] SUZUKI M. "*Decomposition formulas of exponential operators and lie exponentials with some applications to quantum mechanics and statistical physics*". *J. Math. Phys.* **26**, pp. 601–612 (1985).

[Tak93] TAKATSUKA T, TAMAGAKI R & TATSUMI T. "*Characteristic aspects of pion-condensed phases*". *Prog. Theor. Phys. Suppl.* **112**, pp. 67–106 (1993).

[Tan02] TANNERY J & MOLK J. "*Elements de la Theorie des Fonctions Elliptiques*" (Gauthier-Villars, Paris, 1893–1902). Four volumes.

[Tan07] TANNOR D J. "*Introduction to quantum mechanics: a time-dependent perspective*" (University Science Books, Sausalito, California, 2007).

[Tee05] TEE G J. "*Eigenvectors of block circulant and alternating circulant matrices*". *Res. Lett. Inf. Math. Sci.* **8**, pp. 123–145 (2005).

[Toe11] TOEPLITZ O. "*Zur Theorie der quadratischen und bilinearen Formen von unendlichvielen Veränderlichen. i. Teil: Theorie der L-Formen*". *Math. Ann.* **70**, pp. 351–376 (1911).

[Vol65] VOLKOV A B. "*Equilibrium deformation calculations of the ground state energies of 1p shell nuclei*". *Nucl. Phys.* **74**, pp. 33–58 (1965).

[Wan37] WANNIER G H. "*The structure of electronic excitation levels in insulating crystals*". *Phys. Rev.* **52**, pp. 191–197 (1937).

[Wan72] WANG S S & KRUMHANSL J A. "*Superposition assumption II. high density fluid argon*". *J. Chem. Phys.* **56**, pp. 4287–4290 (1972).

[Wat03a] WATANABE G & IIDA K. "*Electron screening in the liquid-gas mixed phases of nuclear matter*". *Phys. Rev. C* **68**, art. 045801 (2003).

[Wat03b] WATANABE G, SATO K, YASUOKA K & EBISUZAKI T. "*Structure of cold nuclear matter at subnuclear densities by quantum molecular dynamics*". *Phys. Rev. C* **68**, art. 035806 (2003).

[Wat05] WATANABE G, MARUYAMA T, SATO K, YASUOKA K & EBISUZAKI T. "*Simulation of transitions between "pasta" phases in dense matter*". *Phys. Rev. Lett.* **94**, art. 031101 (2005).

[Wat06] WATTS A L & STROHMAYER T E. "*Detection with RHESSI of high-frequency X-ray oscillations in the tailof the 2004 hyperflare from SGR 1806-20*". *Astrophys. J.* **637**, pp. L117–L120 (2006).

[Wat07] WATANABE G. "*Understanding nuclear "pasta": current status and future prospects.*". *AIP Conf. Proc.* **891**, pp. 373–381 (2007).

[Wat09] WATTS A L. private communication. Hirschegg 2009: Nuclear Matter at High Density (2009).

[Whi63] WHITTAKER E T & WATSON G N. "*A course of Modern Analysis*" (Cambridge University Press, Cambridge, 1963), fourth edition.

[Wig32] WIGNER E P. "*On the quantum correction for thermodynamic equilibrium*". *Phys. Rev.* **40**, pp. 749–759 (1932).

[Wil85] WILLIAMS R D & KOONIN S E. "*Sub-saturation phases of nuclear matter*". *Nucl. Phys. A* **435**, pp. 844–858 (1985).

[Wil05] WILLINK R. "*Normal moments and hermite polynomials*". *Stat. Probabil. Lett.* **73**, pp. 271–275 (2005).

[Yak99] YAKOVLEV D G, LEVENFISH K P & SHIBANOV Y A. "*Cooling of neutron stars and superfluidity in their cores*". *Uspekhi Fiz. Nauk* **169**, pp. 825–868. (English trans. Physics - Uspekhi 42, 737–778) (1999).

[Yak01] YAKOVLEV D G, KAMINKER A D, GNEDIN O Y & HAENSEL P. "*Neutrino emission from neutron stars*". *Phys. Rep.* **354**, pp. 1–155 (2001).

[Yak04] YAKOVLEV D G & PETHICK C J. "*Neutron star cooling*". *Annu. Rev. Astro. Astrophys.* **42**, pp. 169–210 (2004).